DEVELOPMENT AND PERFORMANCE EVALUATION OF A DIURNAL PASSIVE RADIATIVE COOLING SYSTEM FOR APPLICATION IN BUILDINGS

By

OKORO, HUMPHREY OGBONNIA

(B.Eng., M.Eng.)

Reg. No.: 20184153428

A Ph.D. DISSERTATION SUBMITTED TO THE POSTGRADUATE SCHOOL

FEDERAL UNIVERSITY OF TECHNOLOGY OWERRI

IN PARTIAL FULFILMENT OF THE REQUIREMENT FOR THE AWARD OF DOCTOR OF PHILOSOPHY (Ph. D) DEGREE IN MECHANICAL ENGINEERING, ENERGY AND POWER ENGINEERING OPTION

FEBRUARY, 2024

CERTIFICATION

This is to certify that this dissertation: **"DEVELOPMENT AND PERFORMANCE EVALUATION OF DIURNAL PASSIVE RADIATIVE COOLING SYSTEM FOR APPLICATION IN BUILDING"** was an original work carried out by Okoro, Humphrey Ogbonnia (Reg. No: 20184153428) a postgraduate student in the Department of Mechanical Engineering, School of Engineering, Federal University of Technology, Owerri.

ENGR. PROF. E.E. ANYANWU Principal Supervisor	26/02/2024 **Date**
ENGR. DR. G.N. NWAJI Co-supervisor 1	26/02/24 **Date**
ENGR. Prof. N.V.OGUEKE Co-supervisor 2	26/02/2024 **Date**
ENGR. DR. C.A. OKORONKWO Co-supervisor 3	26/02/2024 **Date**
ENGR. DR. G.O. ONUOHA Heat of Department	26/02/2024 **Date**
ENGR. PROF. REMY UCHE Dean, School of Engineering	23/4/24 **Date**
PROFESOR B.O. ESONU Dean, Postgraduate School	**Date**
ENG. PROF. F. ABAM External Examiner	06/03/2024 **Date**

DEDICATION

This work is dedicated to my Lord and Saviour Jesus Christ. To my lovely wife and children.

ACKNOWLEDGEMENTS

My rare excitement for the successful completion of this work was made possible through the immeasurable contributions of some individuals, to whom I need to express my appreciation.

My special thanks go to my principal supervisor, Engr. Prof. E.E. Anyanwu, who unreservedly gave his time, attention, effort, and resources to ensure that this work came to this end on time. His fatherly disposition and resolve in mentoring the young generation to successfully actualize their dreams make him distinguished and rare. He checked on me at every stage committedly, patiently, and painstakingly read through the work and corrected/recast all my errors- which was a surprise to me. I came into this program vague in research but now, I can confidently say that I am made through him.

This appreciation will be meaningless if I don't recognize my co- and second supervisor, Engr. Dr. G.N. Nwaji whose commitment, encouragement, and sacrifice cannot be overestimated. He stood by me virtually all the time and was a tool in the hand of Prof. Anyanwu for me to achieve this great feat. He encourage me at my most discouraged moments. I simply say, may the good Lord reward you immensely. The advice and kind disposition my other co-supervisors, Engr. Prof. N.V. Ogueke and Engr. Prof. C.A. Okoronkwo, to offer councel at all times are also appreciated. Also, I want to thank the Head of the department, Engr. Dr. G. O. Onuoha, the PG coordinator, Dr. O. C. Nwufo, the Dean School of Engineering, Engr. Prof. Remi Uche, Dean School Postgraduate School, Prof. B.O. Esonu, and all Lecturers and other non-teaching staff of the Department of Mechanical Engineering, Federal University of Technology, Owerri for their support and encouragement.

This appreciation will not be complete without mentioning my lovely wife, Mrs Grace Nkeiruka Okoro, and children, Hephzibah, Alfred, Peace, and Daniella Okoro for their understanding and support. My unalloyed thanks go to my big brother and father, Pastor Emmanuel E. Okoro, and his family. Their presence in Owerri made the whole program seamless. To all my sibling, I remain grateful for their prayers.

My sincere appreciation goes to the Commonwealth Scholarship Commission, UK **(No. NGCN-2021-241)**, and Tertiary Education Trust Fund, Nigeria for their financial support for bench work at the University of Hull, UK during February 2022 to March 2023. I also wish to appreciate Namiroch Nigerian Limited for fabricating the systems.

Finally, I must remain grateful to God Almighty- the giver of inspiration and wisdom- for His mercy and sustenance

Table of Contents

CHAPTER 3 METHODOLOGY

CHAPTER 4 RESULTS AND DISCUSSION

List of Tables

List of Figures

NOMENCLATURE

C_p	Specific heat capacity
g	gravitational constant
G_{sc}	Solar constant
G_{on}	Extraterrestrial radiation on the horizontal surface
I	Total horizontal solar radiation
I_b	Beam solar radiation
I_d	Diffused solar radiation
α	Tilt angle
δ	Declination angle
τ	Transmittance
τ_b	Atmospheric transmittance
τ_A	Ratio of diffused radiation to extraterrestrial radiation
λ	wavelength of the material
η	Refractive index of the material
ε	Emisivity
σ	Boltzmann constant
P_w	Partial pressure of water
P_{ws}	Water vapour saturation pressure
RH	Relative humidity
ε_s	Sky emissivity of the material
ε_g	Ground emissivity
ρ	Reflectivity of the material
ρ_g	Ground surface reflectivity
T_g	Ground temperature
T_c	Temperature of the radiative cooler

T_{amb} Ambient temperature

T_{sky} Sky temperature

T_{db} Dry bulb temperature

P_{cool} Cooling power

P_{rad} Radiation from the cooler

P_{sun} Radiation from the sun

P_{atm} Radiation from the atmosphere

$P_{cond+conv}$ Heat loss due to conduction and convection

h Hour angle

d Thickness of the material

n Day number

A Altitude of the study location

R_b Beam radiation tilt actor

k Thermal conductivity [W/mK]

K Extinction coefficient of the material

F' View factor

θ_i Angle of incidence

A_{zs} Solar altitude angle

Abbreviations

TPX	Polymethyl pentene
PDMS	Polydimethylsiloxane
PET	Polyethylene
AEMT	Asymmetric Electromagnetic Transmission
HVAC	Heating Ventilation and Air-Conditioning
CAD	Computer Aided Design
MPEA	Mesoporous Polyethylene Aerogel

$BaSO_4$	Barium Sulphate
PVF	Polyvinyl fluoride
PVC	Polyvinyl chloride
P(VdF-HFP)HP	Poly(vinylidene fluoride-co-hexafluoropentane)
PMSQ	Polymethyl silsesquioxane
P(VdF-HFP)	Poly(vinylidene difluoride-co-hexafluoropropylene)
TSSS	Sensitive spectrally selective
TCPCS	Temperature-controlled phase change structure
CMM	Conical metamaterial
PTX	Polymethyl pentane
MIM	Metal-insulator-metal
PCSUVA	Photonic crystal structures on a UV-curable adhesive
ESR	Enhanced specular reflector
$PMMA_{PHA}$	poly methyl methacrylate

ABSTRACT

Space cooling for thermal comfort consumes significant amount of energy, and this has continued to be a major global challenge. However, space cooling needs are increasing in the tropics due to increase in energy intensive lifestyles, population increases, and incessant increases in ambient temperature. Global warming and climate change issues associated with convectional energy usage are increasingly informing investments in sustainable and clean energy systems. Accordingly, the development and performance evaluation of a diurnal passive radiative cooling system for space cooling application in buildings are hereby presented. Two diurnal passive radiative coolers using dual-layer mesoporous polyethylene aerogel and ultra-white barium sulphate on silver substrates as selective reflective surfaces were designed and fabricated. This test rig is a rectangular box with two compartments in which the coolers are installed for investigation. The top of the test rig is covered with a low density polyethylene windscreen, which is transparent to radiation in all wavelengths. Thermocouples are inserted underneath and outside the coolers to record the temperatures of the coolers and the ambient respectively. Extensive field investigations were conducted with these photonic coolers under direct solar irradiance in three different locations under Nigerian climatic conditions, namely, Abuja, Afikpo, and Owerri. The experimental results for a 24-hour test show that the diurnal passive radiative system achieved significant cooling performances with sub-ambient temperatures of about 3-5, 3-6, and 2-6^{o}C during the daytime and 1-2, 0-1, and 0.5-2^{o}C at night, for Abuja, Afikpo, and Owerri respectively for Mesoporous polyethylene aerogel cooler. For the barium sulphate cooler, sub-ambient temperatures of 2-3, 1.5-3.5, and 1-3.5^{o}C during the daytime and 0-1.5, 0-0.5, and 0-1^{o}C at night were reported. Average cooling powers of 108.84, 84.99, and 101.06W/m^2 were recorded in Abuja, Afikpo, and Owerri respectively with the mesoporous polyethylene Aerogel, while 120.29, 89.81, and 106.74W/m^2 were recorded with the barium sulphate in Abuja, Afikpo, and Owerri, respectively, during the investigation. Also, a theoretical model was developed and used to numerically predict the thermal performances of the coolers in six locations, namely, Abuja, Yola, Afikpo, Ado-Ekiti, Kaduna, Owerri, and Warri, representing the different geopolitical zones in Nigeria. The model equations were discretized using finite element numerical scheme for ease of implementation on a digital computer. The system behaviour was simulated with the developed model using a code written with FlexPDE Finite Element Model Builder and Numerical Solver Version 7.12. The numerical results obtained from the models were compared with experimental results and other similar data from the literature. The deviations of the model and experimental temperatures were recorded as ±2.73^{o}C for Mesoporous polyethylene aerogel and ±1.81^{o}C for barium sulphate. Thus, for the numerical performance evaluation, the model results closely matched experimental results with total standard uncertainties of 0.64 for Mesoporous polyethylene aerogel and 0.37 for barium sulphate. These deviations are less than 1, which is a necessary condition for model accuracy. Sensitivity analyses show that the optimal performance parameters are 15mm, 30^{o}, and 5, for the cooler thickness, orientation and number of windscreens, respectively. Therefore, further material development, extended field investigation, and possible deployment of passive radiative cooling system for use in residential buildings are recommended.

Keywords: Thermal comfort, sub-ambient cooling, diurnal radiative cooling, numerical simulation, thermal insulation, solar absorption.

CHAPTER 1

INTRODUCTION

1.1 Background Information

Space cooling in the tropics, a substantial energy end-use globally and a key factor in peak electricity demand plays an inestimable role in human life. It is necessary for human comfort and preservation of agricultural materials including processing of industrial products. Generally, energy utilization in the globe depends heavily on fossil resources (oil and gas products) and constitutes a serious threat to environmental sustainability because of the emission of greenhouse gases from these fossil resources (Chao, 2010). Furthermore, the possibility of exhaustion of fossil resources is also a major concern. These, therefore, have become contending challenges globally. Consequently, renewable and sustainable energy has gained serious attention in recent times through research and technological investments (Nwaji, 2019). Through renewable energy technology, energy is generated by converting natural occurrences (or resources) into usable energy forms and it is strongly believed to be one of the promising solutions to the identified energy security challenges.

Energy utilization in recent times for space cooling, especially in the tropical climates is fast growing, almost astronomically more than any other end use in building. Using electricity to achieve space cooling is a major contributor to global energy demand. For instance, using air conditioning systems (AC) to keep indoor space temperatures at comfort level and keeping them running consumes over 2000 terawatts hours (TWh) of electricity annually in the US as their energy efficiencies vary enormously. All over the world today, using air conditioner and electric fan to achieve cooling account to about 20% of the total electricity use in building (International Energy Agency, 2018). The electricity requirement for cooling in buildings could

increase by as much as 40% globally by year 2030 if there is no major effort towards improvements in the efficiency of cooling gargets (International Energy Agency, 2020).

In most countries like Philadelphia and Nigeria, the peak electricity consumption for cooling was 74% and 80%, respectively on a very hot day (Waite, et al 2017). Fig 1.1 represents the global energy consumption patterns indicating that residential/household has the greatest energy consumption of about 80%.

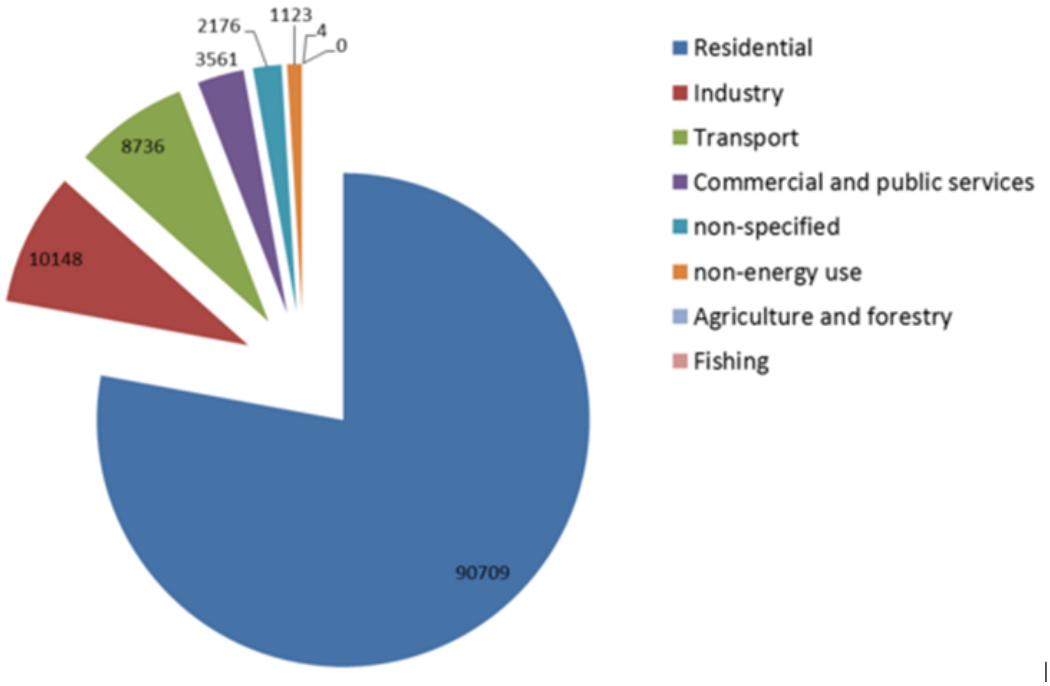

Fig 1.1 Energy consumption by economic sector in Ktoe (Waite et al (2017)

According to the report of Thibaut et al (2021), about 16% of final electricity consumption in 2020 (about 1 885 TWh) was used for space cooling in the building sector with operational residential units consuming nearly 70%. The rise in the demand for space cooling doubles that for lighting or water heating. Also, Bezerra et al (2021), reported that energy use within the building sector for space cooling represents nearly 28% of total energy utilization globally. This rapidly growing energy end-use has a high carbon dioxide (CO_2) emissions propensity. Going forward, the amount of energy consumed in buildings, especially in tropical and highly humid climates such as Nigeria for cooling needs urgent attention. This is

because the final energy consumption in the structures will be considerably influenced by the cooling demand in such climes. More energy demand in these structures results from rising living standards and population growth in emerging nations, which has a detrimental impact on the environment because of greenhouse gas emissions. In Nigeria, the residential sector accounts for roughly 65% of all energy use annually, whereas buildings account for about 40% of all energy use globally and produce about 33% of CO_2 emissions. (Olanrewaju and Adegun, 2021). Over 50% of the energy used in buildings in tropical climates arises from energy-intensive vapour compression systems, which can rise to 80% at peak times when the demand is high.

Even though it is only needed for a brief period of time, maintaining and operating electricity capacity to satisfy peak energy demand is quite expensive. This growing demand for cooling is driven by economic and population growth in the tropical regions, where the demand for cooling is peak. The worldwide energy and space cooling demand needed to provide the cooling will continue to increase for decades unless an alternative and innovative methods to achieve cooling are presented. Therefore, with rapidly expanding environmental awareness, which pays particular attention to energy consumption and environmental protection, space cooling has thus been receiving significant attention. The conventional cooling technologies, including air conditioners (AC), typically require a large amount of energy and leave a considerable carbon footprint, which gave rise to environmental protection issue. The utilization of solar energy (for space heating and cooling) has increased recently as a result of the dwindling fossil fuel supplies and environmental worries about climatic change and global warming. Passive radiative cooling appears a viable option for resolving the issue of energy consumption in buildings and consequent environmental pollution. It would be worthwhile to design and develop an energy-saving and ecologically friendly cooling method. The exploitation of the freely available passive cooling features that cool without the

need for electricity is currently generating more interests worldwide. These techniques could have a substantial impact on future global energy usage. A temperature that is lower than the ambient air temperature must be attained and maintained in order to achieve passive cooling. By using the surroundings as heat sink to dissipate the heat from the body, a cooler is utilized in passive radiative cooling systems to achieve cooling (Hossain and Gu, 2016). Despite the fact that solar electricity is expensive when compared to conventional energy sources like natural gas, its overall cost is declining as a result of technological advancements. An overview of several passive cooling strategies for buildings was presented by Geetha and Velraj in 2012. They divided potential passive cooling strategies into three major groups:

(i) solar and heat protection techniques (such as shading) to reduce heat gains;

(ii) heat modulation or amortization techniques (such as thermal massing) to modify gains; and

(iii) heat dissipation techniques (such as natural ventilation and radiative cooling) to remove gains.

A more promising way to cut down on cooling energy use is to employ modern passive cooling techniques to use ambient air and other natural heat sinks. In general, passive radiative cooling and active radiative cooling are the two ways to use radiative cooling in buildings (Argiriou, 2013). The roof of the structure radiates towards the sky in passive radiative cooling, and the lowered roof surface temperature helps to lower conductive heat gains from the outside. Raeissi and Taheri (2000) suggested utilizing mobile insulation as a passive radiative cooling approach when the water in clear plastic bags was placed on the roof of a house. Polyurethane insulating boards shielded the water bags from the sun's rays during warm days so as to achieve reasonable cooling.

Dedicated radiative panels that are typically not a part of the building envelope are used in conjunction with a heat transfer medium (such as air or water) in active hybrid radiative

cooling to provide cooling to specific interior rooms. The effectiveness of an air-based radiative cooling system was investigated by Mihalakakou et al. in 1998. This method involved cooling the air after it circulated under a metallic radiator and then directing the cooled air to the inside of the building for cooling. In summary, a switch from electricity and gas to solar cooling could strongly reduce fossil fuel consumption and CO_2 emissions. Through the exploitation of diurnal passive radiative cooling concepts, drastic reductions in household energy consumption could be achieved.

1.2 Problem Statement

Fossil fuel, including natural gas-driven grid-connected electricity, is currently used to provide space cooling for buildings. Ogueke et al. (2009) found that space cooling requirements seem to be highest during the midday when the solar irradiance is peak. In addition to being limited, these fossil fuel supplies are also thought to be the cause of the twin threats of global warming and climate change, which are currently the two most contentious political concerns in the world. Global atmospheric temperature is increasing, mostly during dry seasons of the year when the ambient temperature is higher than what is comfortable for people. This rise in temperature makes comfort cooling in tropical and humid climates inevitable, hence, increasing demand on grid electricity to drive the conventional air conditioning systems (Ogueke et al, 2011).

The immediate effects of conventional energy usage to suit human requirements include steadily rising energy supply costs and damaging emissions into the environment. Population, especially in developing nations, is also on the increase thereby placing a more increased burden on energy demand. Therefore, there is a need for nations to develop and provide energy systems commensurate with the growing population but free from adverse environmental effects. In most developing nations where the electricity supply is inadequate, during the times when cooling is most needed, either no electricity is available or parts of the

country are completely cut off due to a lack of grid supplies. As a result, the most seemingly convenient way to lessen these issues is to stop using electricity for cooling purposes, and it is predicted that using ambient energy will considerably reduce the issues. The development of energy-efficient and ecologically friendly cooling methods is ideal, and passive radiative cooling is one appealing solution to the issues of excessive energy use and environmental contamination. Therefore, by effectively utilizing the concepts of diurnal passive radiative cooling, the demand placed on traditional energy use for comfort cooling will be considerably reduced, and this will result in a reduction in energy expenses.

During the day, surfaces exposed to the open sky are heated up because of the high solar radiation and hence, reflecting greater part, if not, all of these radiations will help keep the body cool. Several materials to achieve sub-ambient cooling under direct sunlight abound which include polydimethylsiloxane (PDMS), Hierarchically porous polymethylmetacrylate (PMMA), hafnium dioxide (HfO_2), Silicon Dioxide (SiO_2), Titanium Dioxide (TiO_2), Metal dielectric conical metamaterial pillars, etc. Thus, if the roof of a building is coupled to a cooler with high reflectance and high emittance, diurnal cooling can be achieved to keep it cool and provide comfort throughout the day. In the daytime, the temperature is peak and heats the systems causing discomfort to human existence and hence the urgent need to harness diurnal cooling resources to supplement our cooling needs cannot be overemphasized.

Accordingly, Raman et al (2014) experimentally demonstrated diurnal radiative cooling to nearly 5^oC below the ambient air temperature, using a thermal photonic approach. Unlike the nocturnal radiation cooling system (NRCS), works in diurnal radiation cooling systems (DRCS) have remained at the laboratory experimental stage with only very few field experiments in certain tropical climates such as California, Hong Kong, Singapore, etc. No field experiments have ever been reported in tropical and humid climates of Africa.

Accordingly, the demand placed on conventional energy utilization for comfort cooling can be greatly reduced by the effective exploitation of the concepts of diurnal passive radiative cooling. This is expected to significantly reduce building energy use costs.

1.3 Objectives of Study

The main objective of the research work is development and performance evaluation of a diurnal passive radiative cooling system for application in buildings. To achieve the main objective, the specific objectives include:

(i) To design a diurnal passive radiative cooling test facility (rig) using Owerri, Nigeria climatic conditions.
(ii) To fabricate and assemble the diurnal passive radiative cooling facility.
(iii) To experimentally investigate the performance of the diurnal passive radiative cooling facility.
(iv) To develop a theoretical model to predict the performances of the system in different climatic conditions.
(v) To validate the model with the experimental results from (iii) above
(vi) To carry out a sensitivity analysis on the effects of thermophysical and material properties, and climatic conditions to ascertain optimal performance characteristics of the system

1.4 Justification of study

The effects of energy use on the environment and the rise in fossil fuel prices as well as the finite nature of fossil fuel have directed global attention to renewable energy sources. The solar water heating market had already started booming though truncated by the oil boom (when natural gas and oil were discovered). However, the oil crisis of 1973 sparked a renewed global interest in solar energy. The rise in oil price and the use of solar power in the space program brought about serious research into solar thermal energy and hence a renewed global interest in solar cooling technologies.

Globally, the solar industry has continued to be the vanguard of the energy revolution helping to facilitate the switch from a fossil-driven economy to a renewable energy-driven future.

This has become imperative to address the political issues of global warming and climate change. Space cooling forms a significant part the of energy consumption of many countries and especially a country like Nigeria and have been accomplished greatly using electricity and natural gas. Where consumption data are available, for instance, in the United States, Europe and Japan, statistics show that households' energy use for just water heating accounts for roughly 15% of energy use in Europe, 20% in the United States, up to 30% in Japan, and about 80% in countries with tropical climates like Nigeria. Also, available statistical data for building energy consumption show that the heating, ventilation, and air conditioning (HVAC) component, primarily provided by the mechanical vapour compression systems, accounts for as much as 70% of the total energy utilization. Hence, switching from electricity and gas to solar cooling could strongly reduce fossil fuel consumption and CO_2 emissions (Nwaji, et al, 2020). The exploitation of passive cooling techniques using diurnal passive radiative cooling concepts could help achieve drastic reductions in household energy consumption.

1.5 Scope of Study

The scope of this study covers the experimental and numerical investigation of diurnal passive radiative cooling. The research also center on prototype development, optimization and performance evaluation only. The prototype comprised a cooler with efficient emitters, and reflectors to suppress the effect of climatic factors that militate against sub-ambient temperature reduction. The fabrication of the radiative cooler was done using a thermally induced phase separation method (TIPS). A simple theoretical model was developed and analyzed using FlexPDE finite element model builder and numerical solver to ascertain the appropriate design that gives an efficient sub-ambient cooling.

CHAPTER 2

LITERATURE REVIEW

2.1 Historical Perspectives

This chapter centers on the review of the state-of-the-art knowledge of passive radiative cooling (PRC), including the pertinent applications of various structures in real life scenarios. It details the general principles and the different materials of PRC structures for nighttime and daytime applications. It also considers the current geographical spread of diurnal passive radiative cooling (DPRC) and their performances as well as configurations for building integration.

There is an increasing demand for space cooling to provide thermal comfort in homes, hotels, and many other industrial facilities in hot climates. In order to reduce local and global energy consumption during the warmest (summer and dry) seasons of the year, there is a demand for energy-efficient cooling (air conditioning) systems. Even the building sector may make a significant contribution to the transition to a system that uses less energy. Energy consumption reduction has tremendous potential when profitable solutions that lower costs on both an economic and environmental level are taken into account. According to the International Energy Agency (2018), buildings account for around 80% of household energy usage in Nigeria and 40% of all energy use in the European Union (EU) (Vall and Castell, 2017). Reversible heat pumps, which utilize a lot of energy (electricity) for space air conditioning, are used in the majority of buildings in nations with hot climates. In order to further reduce the usage of such conventional energy, there are various renewable resources that can be used in technological systems to provide the desired temperature level with zero or very little conventional electrical energy use. Solar energy is one of the resources that has been extensively investigated although the use of absorption heat pumps limits its use for cooling. Most buildings today only use mechanical systems to provide indoor comfort and cooling.

With mechanical cooling systems, electricity-powered equipment like room air conditioners, packaged air conditioners, and chillers are typically the only cooling source. Mechanical cooling equipment is appropriate as long as it can run consistently to maintain space thermal comfort, however they are significant energy consumers for buildings. Further efforts are required to use passive cooling techniques to replace, at least in part, the mechanical cooling energy demand in order to reduce the energy used for space cooling.

Another method that has been developed to achieve cooling and replace the use of heat pumps is radiant cooling. A terrestrial body emits long-wave thermal radiation toward space through the infrared atmospheric transparency window between 8 and 13μm wavelengths as part of the radiative cooling process. Without using any external active devices, passive radiative cooling absorbs heat from the surface and emits infrared radiation into the frigid universe through the atmospheric transparency window (8-13μm). Daytime radiative cooling is useful as there is peak cooling demand in the daytime but it is still a challenge as a result of solar absorbance (Zhu, et al, 2021). Certain infrared radiations can flow through the atmosphere through this window (the dynamic behaviour of the earth's atmosphere) without being absorbed or heating the atmosphere. The majority of radiation is produced in the infrared spectrum at room temperature because a body's ability to emit electromagnetic radiation at a particular wavelength is temperature-dependent. In order to reach a temperature below ambient, the properties are used to create a cooling net balance between the thermal radiation that is emitted from the terrestrial surface and that that is received from the atmosphere. Thus, there will be a significant reduction in energy use when using this radiative cooling technology for cooling. Since the radiative cooler's performance is influenced by its material qualities and the environment, special consideration must be given to both its material qualities and the environment, special consideration must be given to both of these factors.

Nocturnal radiative cooling, which requires utilizing a device exposed to the sky to radiate heat to outer space through a transparent window in the atmosphere (8–13 m), has been used to demonstrate passive cooling below ambient air temperature at night. Peak cooling demand occurs during the day, and it has remained extremely difficult to achieve daytime radiative cooling of a surface exposed to direct sunlight to a temperature below ambient.

Raman et al. (2014) used an integrated photonic solar reflector and thermal emitter composed of two parts, the upper three thick hafnium dioxide (HfO_2) in alternation with silicon dioxide (SiO_2) layers of varying thicknesses, which could reflect 97% of incident sunlight while emitting strongly and selectively in the atmospheric transparency window, to show that adequate radiative cooling effects were possible. They were able to reduce the temperature by 5^oC below ambient temperature by using the photonic technique. The investigation carried out in Hong Kong by Tso, et al. (2017) proved this to be impossible because daytime sky access heated the radiative cooler by the Sun. However, a reasonable temperature drop was obtained at night.

Under direct sunlight with irradiation of up to $860W/m^2$, a dual-layer radiative emitter could cool to 4.9^0C below the ambient air temperature using a basic experimental setup. Researchers suggested a straightforward dual-layer emitter that was deposited onto two separate substrates and had strong solar irradiance reflectivity as well as near-black mid-infrared absorptivity. They found that the emitters put onto two distinct substrates have the same potential cooling performance without a windshield and they are not sensitive to the substrates, resulting in a considerable daytime radiative cooling performance. (Zhu, et al, 2021)

A clear knowledge of the electromagnetic spectrum which has a range of wavelengths within the atmosphere of the Earth is critical to the concept of radiative cooling. This range of

wavelengths is called the atmospheric window. It is the region where atmospheric gases absorb relatively little terrestrial thermal radiation within the Infrared spectrum. The region of this window is between 8 and 14μm as shown in figure 2.1 with the Short wavelength infrared (SWIR), Mid-wavelength infrared (MWIR) and Long-wavelength infrared (LWIR) clearly represented. The humidity of different places and times makes the window narrow or even closed brought about by the obstructions by the cloud (Nibir et al, 2013).

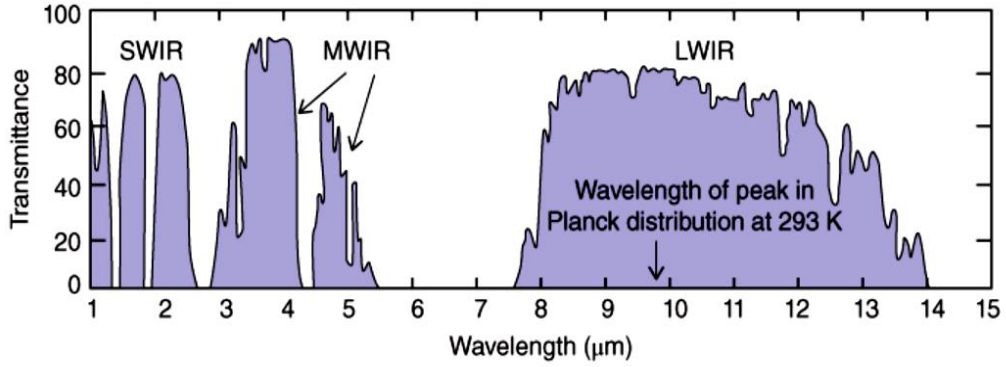

Fig. 2.1 Average atmospheric transmission for wavelengths between 1 and15μm (Nibir et al, 2013).

Our atmosphere is opaque to several wavelengths in the infrared spectrum and so does not allow electromagnetic radiation to pass through it. There is a band of frequencies or wavelengths called atmospheric windows within the earth's atmosphere where this radiation can be allowed to pass. The absorption band is the region of the electromagnetic spectrum that is blocked by the atmosphere, whereas the atmospheric window is merely the fraction of the electromagnetic spectrum that may be transmitted through it. The atmospheric window could be visible or optical atmospheric window (includes visible light), near infrared atmospheric window (this is responsible for daylight), radio atmospheric window (radio frequency range) and infrared atmospheric window (varies with time and place). This window can be likened to Holes in a curtain where only specific bands such as visible light and near-infrared light can freely permeate through them to the surface of the earth whereas other wavelengths (absorption bands) like gamma rays are blocked. The window

transparency determines the observed variations, and which itself is affected by higher altitudes. This underscores the reason for the use of high altitudes for practical purposes and locating observatories. Dry air (clear sky) helps in improving the transparency of the window for astronomical use whereas several gases such as water vapor in air (cloudiness), carbon dioxide, and ozone increase the opaque nature of the window. The uniqueness of the atmospheric windows cannot be overestimated as how the atmosphere behave in terms of weather and climate depends on it. Therefore, the greenhouse effect, which is how the sun heats up the earth and the earth's cooling the balances it, is influenced by the atmospheric window (cotton and Pielke (2007).

2.2 Radiative cooling concept

Every physical body possesses the tendency to spontaneously and continuously emit electromagnetic radiation. This process by which bodies lose more energy (heat) through thermal radiation than that is absorbed is called radiative cooling. Everywhere on Earth experiences radiative cooling, which is more likely to happen at night and is essential to maintaining the planet's energy balance. The tropospheric temperature and the atmospheric transparency window are two facts that make radiative cooling a real and important occurrence. The troposphere represents the first and lowest layer of the earth's atmosphere and contains 75% of the total mass of the atmosphere. The tropospheric temperature in most regions of the world is below the ambient, hence acting as a cooling reservoir. Atmospheric transparency window (within the wavelength range of 8-13μm) on the hand allows an emitting object to emit thermal radiations to the low-temperature troposphere.

In the daytime, there is usually a thermal imbalance as the amount of the incoming radiant energy exceeds the outgoing energy from the ground. This makes the temperature of the ground surface rise as shown in figure 2.2a below. But at night, the sun does not radiate anymore but the ground does continuously radiate away heat into outer space resulting in a

drop of its temperature (Figure 2.2b). This night-time cooling where there is a net energy loss by the ground is results in radiative cooling.

(a) (b)

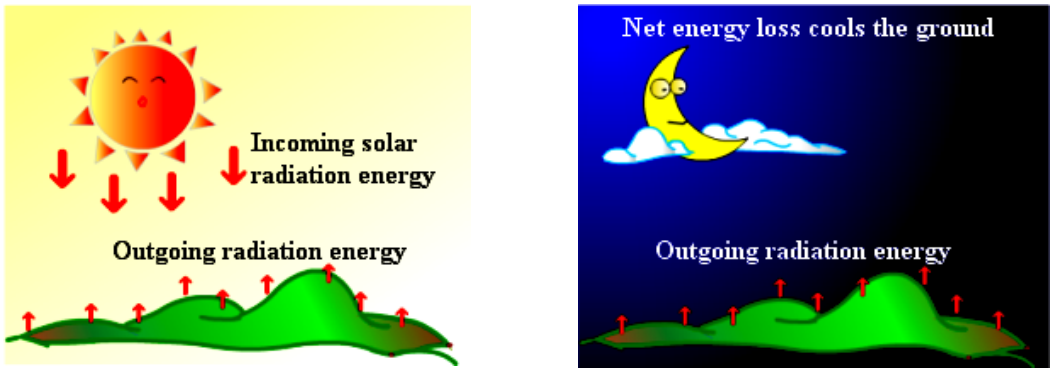

Fig.2.2 daytime heating of the ground surface and Night-time radiative cooling (Hong Kong Observatory, 2022)

The rate of radiant energy loss is determined by cloud cover, wind strength and humidity (dry conditions) and hence, it is necessary for achieving maximum cooling. The cloud cover prevents the radiation of heat energy from the ground to the universe the same way wrapping our body with a blanket to keep warm. Thus, temperature drop under cloudy conditions is less than that under clear skies.

The role light winds play in radiative cooling is noticed as they tend to locally confine the cool air by mixing it with the surrounding air and, hence, preventing it from getting warm. In like manner, heat on the ground is prevented from radiating away by moisture in the air, slowing down cooling rate under the condition of high humidity. The effect of cloud cover and other factors affecting radiative cooling is shown in figure 2.3.

(a) (b)

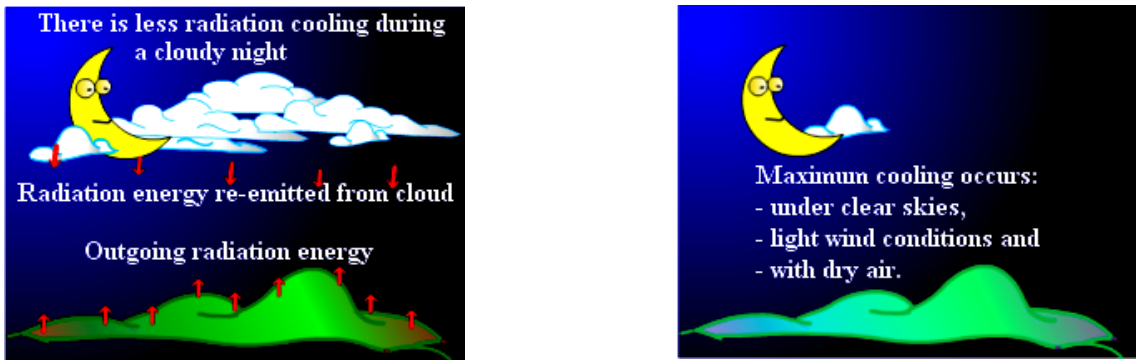

Fig. 2.3 Factors affecting the extent of cooling during radiative sky cooling (Hong Kong Observatory, 2022)

This radiative cooling is termed passive radiative cooling if there is no extra energy input is needed to achieve it. As a result, passive radiative cooling does not require any additional energy input. Instead, it merely makes use of a device or material to radiate heat to space through the transparency window in the atmosphere between 8 and 13 m band, allowing thermal emission from an emitting object to connect with the low-temperature troposphere.

By the development of several materials with high emissivity in the wavelength range of 8–13 μm, the idea of passive radiative cooling has been put up and explored by numerous researchers over the past century. As an alternative to an active cooling strategy, passive radiative cooling can cool materials even below the surrounding temperature. The spectral emission and absorption at various wavelength intervals are tailored in passive radiative cooling systems. This approach can be divided into nighttime or daytime cooling design concepts based on the targeted operation times. Radiative cooling for nighttime operations has been studied extensively in the literature and high cooling performances was reported.

Even though it has been researched, passive radiative cooling during the day is a relatively recent field of study in comparison to radiative cooling during the night. Achieving daytime radiative cooling to a temperature below ambient under sunshine is a difficult task since the incoming solar radiation is strong and can easily offset the exiting thermal radiation to outer

space. During the day, solar radiation, which is intense in the visible and near-infrared spectrums, must be effectively reflected. As a result, daytime passive radiative cooling offers a fresh, environmentally beneficial solution to the problem of the high energy requirement for building space cooling.

2.3 Materials for Passive Radiative Cooling

2.3.1: Base Materials

Building materials may be designed with a surface that emits the desired spectrum. Because of their excellent absorption properties, rare earth metals are regarded as selective emitters in the infrared spectrum (Family and Mengue, 2017) They reported basic materials for radiative cooling along with their benefits as shown in table 2.1.

Table 2.1: Base materials used for nighttime and daytime radiative cooling (Family and Mengue, 2017)

Name	Advantage
Silicon	Over a thermal wavelength, they have a small absorption coefficient
A-quartz	They have high emissivity, are transparent over visible wavelength and have double phonon polariton resonances.
ZnS	They are very strong mechanically, undamaged by solar ultraviolet and very transparent in the atmoapheric window.
PPO (Polyphonyoxide) resin	They can endure exposure to humidity and temperature over 100^{o}C
Silicon Oxynitride	Their absorption primarily declines within the transparency window, and as a result of their chemical composition, they can change from the SiO_2 absorption band to the Si_3N_4 band.
CdS	They exhibit a high range transmittance of irradiance (0.80) and a low band reflectance over the atmospheric window (below 0.02)

These materials cool down to form porous structures that are widely employed as building materials because they have the requisite low conductivity qualities.

2.3.2: Paints

The use of paints pigments with high reflectivity together with high absorptivity and emissivity in radiative cooling are favourable. These pigments are transistors and metal oxides. Carbon, FeOx, Melanin (natural pigment), Zn powder, PbS, Silicon, Organic soot, TiO_2, and FeMnOx are just a few of the pigments that could be utilized for radiative cooling.

2.3.3: Coatings

Coatings have similar emission-controlling capabilities as paints. Metal films are an outstanding example of coatings for radiative cooling applications due to their strong infrared reflectance and semitransparency in the visible range. Additional coatings include thin-film coatings made of silicon oxides, nitrides, oxynitrides, and oxides. Coatings used for radiative cooling applications and their advantages are listed in table 2.2.

Table 2.2: Coating materials for nighttime and daytime radiative cooling (Family and Mengue, 2017)

Name	Advantage
Polished aluminium coated with evaporated SiO_2 and Si_3N_4	When the air is dry and not humid, these surfaces have the advantage of low downward radiation in the atmospheric window.
Glass covered with SnO_2	The window's transparency and the buildup of frost may both be prevented by the low emittance coating.
Silicon oxinitride (SiO_2+Si_3N_4)	A highly promising technique to improve the performance of the gadget is through the interface contributions of the multilayered structures.
Pigmented Polyethylene foils (with ZnS or ZnO) with thin films of PbO	Polymeric foils with non-absorbing pigment can increase the solar radiation's reflection while also increasing its transmission through the atmospheric window. In the IR range, pigmented polyethylene films can exhibit strong solar reflection while being highly transparent.
PbS and PbSe onto Polyethylene foils	Low band gap semiconductors are predicted to block solar radiation and indicate high reflectivity by appearing transparent in the window.

2.4 Structures for Nocturnal Passive radiative cooling

The application of most of the designs of passive radiative cooling structures for nocturnal cooling has been widely investigated with a remarkable output. Several materials have been investigated for nocturnal radiative cooling and include the following are fully discussed below.

2.4.1 Polymers

The first structures using polymer film-based materials have been used for nocturnal radiative cooling (Zhao et al, 2019a). On the basis of earlier literature, they provided an adequate overview of the state of the art for radiative cooling technology today. Basic concepts, cutting-edge materials and architectures, prospective application growth, and passive radiative cooling prospects. The use of polymers to take advantage of the atmospheric window for radiative cooling has been widely researched. At the early stage, Trombe (1967) and Bartoli (1977) used polyvinyl fluoride (PVF) deposited on an aluminium reflector to investigate whether the radiative cooling of surfaces exposed to a clear sky can be used as an energy source, the polymers films used were coated on an aluminium substrate and primarily composed of polyvinyl chloride (PVC). Along with providing a potential practical application example and some measurements of the new selective surface's radiative power, they also demonstrated how selective surfaces connected to the atmospheric transparency window can be used to achieve useful temperatures and cooling powers. Subsequently, Grenier (1979) studied the development of passive radiative cooling technology using polymethyl pentene (TPX) thin films as shown in figure 2.4 and the

determined that a sub-ambient cooling was feasible under the nocturnal hours of the day.

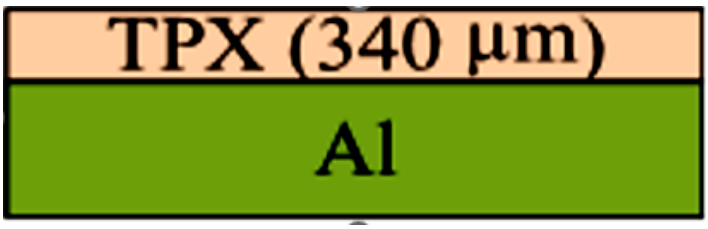

Figure 2.4: Schematic of film coated with polymethyl pentene (TPX) on an aluminium substrate (Greinier, 1979)

In the same vein, Muselli et al. (2002) developed a low-cost radiative condenser for gathering atmospheric vapour using polymethyl methacrylate (PMMA) on aluminium as a reflector.

It is anticipated that this portable condenser design will prove to be an effective water supply in areas without fog or rain. Despite Ajaccio having just a 45% annual occurrence of dew, the condenser was used to gather roughly 770L of dew in 16 months of operation. Meir et al. (2002) constructed a radiative cooling system using reservoirs, unglazed flat plate radiators, and water as a heat transfer medium. The radiators were designed as inexpensive roof integrated modules and were manufactured of twin-wall sheets of a modified PPO (Polyphenylenoxid) resin. The impact of the tilt angle, aperture area, and reservoir volume on cooling performance was examined through simulations, and the viability of modelling a radiative cooling system created for a single-family home was examined. These polymers were used as spectrally selective cooling materials and outperformed non-selective surfaces in terms of performance. Hu et al. (2016) created a composite surface using a titanium-based solar absorber and polyethylene terephthalate (PET) material, and on a clear night they

measured a net cooling power of 50.3W/m2. Similar to this, a PDMS-based selective emitter was created with SiC nanoparticles inserted, as shown in figure 2.5, and proved under direct sunshine to produce a sub-ambient temperature drop of 12oC. (Czepla et al, 2017).

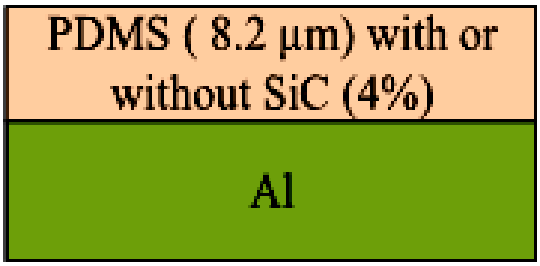

Figure 2.5: Schematic of Thin coating of polydimethylsiloxane (PDMS) placed onto an aluminium substrate (Czepla et al, 2017)

The polymer-based film generally has the advantage of mass production for commercial purposes.

2.4.2 Paints

Paints with a high degree of thermal selectivity that are primarily composed of titanium dioxide (TiO2) layers have a remarkable capacity for radiative cooling during the night when applied to an aluminum substrate. Under a clear sky, Harrison et al.'s 1978 study using white paints that contained TiO2 on an aluminum plate revealed a sub-ambient temperature of 15 °C. A specific focus of the study was to examine the impact of atmospheric absolute humidity in the 8–13-µm window. According to the experimental findings, the amount of cooling that could be achieved was reliant on the relative humidity of the earth's surface air. The setup of the TiO2-based white paint applied to an aluminum substrate is depicted in Figure 2.6.

Figure 2.6: Schematic of Coating aluminum substrate with white paint based on TiO_2 (Harrison and Walton, 1978)

A cooling power of 22 W/m2 and a temperature of roughly 5 oC lower than the ambient were obtained from a hut with the painted roof, which was marginally better than that with the "Tedlar" covered roof, when the study on TiO_2-based white paints was further investigated on galvanized steel by Michell and Biggs (1979). Their experiments proved that a stream of air within a room can be cooled by thermal transfer between the air and a surface radiating to a clear sky. When Kimball compared TiO_2-based white paints to black paints in 1985, he found that the white paints had an 11^oC temperature drop. In the same vein, Orel (1993), added $BaSO_4$ to TiO_2-based paints because of the enhanced absorption of SO_4 stretching vibrations so as to achieve improved effects with a temperature reduction of 14.2^oC increase compared to the one with only TiO_2. Figure 2.7 represents the structure.

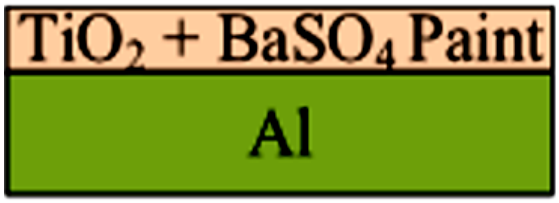

Figure 2.7: Schematic of BaSO4 and SiO2 as component in white paint applied in aluminum pannel (Orel et al, 1993)

For practical applications, pigmented paints are the most widely used and efficient cooling design due to their adaptability for roof retrofitting. TiO2 pigment, which affects paints' near-unity and broadband emittance of roughly 0.95, is commonly found in all paints. However, for the best TiO2-based paints, the optimized solar reflectance is less than 0.86 due to the absorption of ultraviolet and near-infrared solar radiation by polymer binders, which prevents the pigmented paints from actually experiencing diurnal radiative cooling in direct sunlight (Mandal et al, 2020). Additionally, cool-colored materials with high near-infrared reflectance

in the near-infrared range (700-2500nm) can be used to make non-white-colored pigments stay cool under the sun (Synnefa et al 2007). When examining the effect of cool roof coatings on the cooling and heating loads, they estimated the indoor thermal comfort conditions of residential buildings at different climatic conditions based on their investigation. It has been demonstrated that increasing the roof solar reflectance reduces cooling loads by 18–93% as well as the peak cooling demand in air-conditioned buildings by 11-27%. Additionally, the maximum temperatures in residential buildings without air conditioning were lowered by 1.2 to 3.3 oC, and the hours of discomfort were decreased to improve the indoor thermal comfort conditions. It has been determined that cool roof coatings, due to their ease of use, low cost, and effectiveness, are a technique that improves building thermal comfort and energy efficiency.

2.4.3 Inorganic materials

The films related to silicon that are applied to aluminum substrates make up the majority of the inorganic materials used for nocturnal radiative cooling. A magnesium oxide coating on aluminum foil outperforms PVF materials with a net cooling power of 85 W/m2, according to Berdahl's (1984) research. Once more, an examination of the characteristics of SiO film deposited on an aluminum substrate revealed a robust infrared emission within the atmospheric transparency window (8–13μm), resulting in a temperature that was 14oC lower than the ambient (Granqvis et al, 1981). To show efficient radiative cooling, the surface radiated predominantly within the atmospheric transparency window, which was because of strong lattice absorption in the spectral range that combines with destructive interference to yield a low reflectance (i.e., high emittance). It is anticipated that efficient ambient temperature is possible if the surface is only observed from a near-zenith angle and if heat inputs from conduction, convection, and solar radiation are minimal enough. The structure of

the SiO_2-based film on aluminum substrate is shown in figure 2.8a below. Subsequently, Granqvist (1982) proposed a Si_3N_4 film-based radiator with stronger and better thermal selectivity as shown in figure 2.8b, which was evaporated onto an aluminum substrate. The showed that selective infrared radiation-emitting surfaces are required to fully realize the potential of this cooling technique and appears to give prospects for several practical applications by deploying the use of the atmospheric window (8-13um).

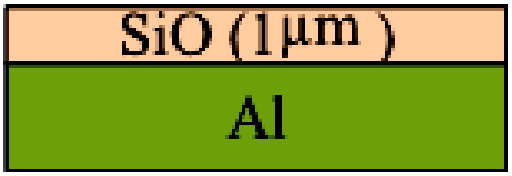

Figure 2.8a: Schematic of SiO2-based film on aluminum substrate (Granqvist and Hjortsberg, 1980)

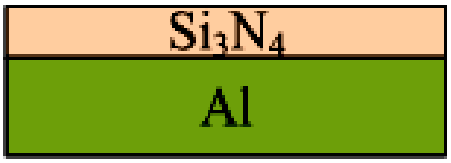

Figure 2.8b: Si3N4 film coated on aluminum substrate (Granqvist et al, 1982)

Furthermore, SiO_2- and $SiO_{0.25}N_{1.52}$ bilayers coated on an aluminum substrate with selective thermal emission, as well as thin films of silicon oxynitride ($SiO_{0.6}N_{0.2}$) with a thickness of 1.34μm, were proposed by Eriksson et al. (1984 and 1985, respectively). With his proposal of three kinds of silica and silica oxynitride-based multilayer for passive radiative cooling application, Diatezua et al. (1996) predicted a temperature drop ranging from 48ºC to 56ºC as well as the cooling power from 118, 119, to 125W/m^2. It was found that silicon oxynitride is a desirable material for radiative cooling because of its superior optical properties. Multilayered configurations show great promise in improving device performances due to their interface contributions. The structure is shown in figure 2.9.

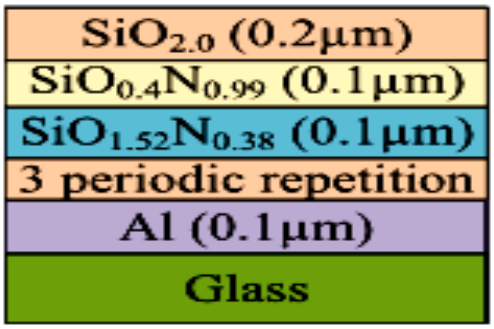

Figure 2.9: Schematic of SiO2 and SiO0.4N0.99 multibilayer deposited on aluminum substrate (Diatezua et al, 1996)

Gentle and Smith (2010) achieved a sub-ambient temperature of 17 °C in an experiment that was consistent with the calculated value of 18.5 °C. This was due to the surface photon resonance of the nanoparticles, which were composed of 5% SiC and 5% SiO_2 by volume in polyethylene films, deposited on an aluminum substrate. The structure is as shown in figure 2.10.

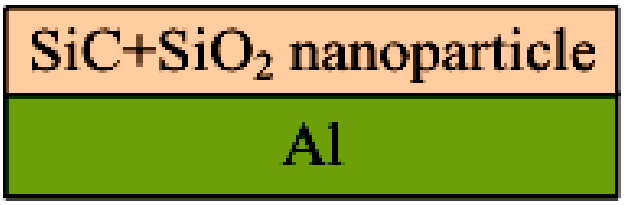

Figure 2.10: Schematic of Polyethylene films + crystalline SiC and SiO_2 nanoparticles are deposited on an aluminum substrate. (Gentle and Smith, 2010)

2.5 Structures for diurnal passive radiative cooling

Daytime radiative cooling is an emerging major player in complementing conventional cooling systems like air conditioning (AC) so as to reduce energy consumption. In many real-world situations, such as energy-efficient building cooling systems, individual thermal control, etc., passive radiative cooling materials and systems are anticipated to be used. The materials and structure design are important factors to consider in order to obtain a reasonable cooling effect using the passive radiative cooling method. Much research has been carried out right from ancient times to explore the feasibility of cooling buildings and desalinating water. The application of most of the designs of passive radiative cooling structures for diurnal cooling is restricted by their poor solar reflection despite their excellent selective thermal emission. However, their application for nocturnal cooling is widely investigated with a remarkable output.

This section presents recent reports on materials, devices, and systems for daytime radiative cooling. Only sub-ambient temperature under direct sunlight would be achievable with selective materials that could not present both very high reflectivity and high emissivity in the

solar spectrum and atmospheric window, respectively. Hence, available literature on passive daytime radiative cooling has been reviewed and grouped based on the approaches adopted by the researchers. These approaches cover polymeric and nano photonic structures as well as paint coatings for achieving sub-ambient cooling during the diurnal hours of the day. Using a bottom layer of silver film to meet the spectral requirements of extremely high solar reflection and selective thermal emission in the vicinity of the atmospheric transparency window, diurnal passive radiative cooling has been experimentally demonstrated thanks to advancements in nanophotonic technology (Raman et al, 2014).

Achieving diurnal radiative cooling requires eliminating solar absorption because more than 10% of absorbed solar energy may result in a difference in the radiative cooling power generated. To do this, there is a need to stop solar radiation from reaching the radiative cooling system. This is done by making use of IR transparent solar reflective materials (which have high solar reflectance and IR transmission) above the selective emitter. A lot of designs were done earlier where inorganic materials were doped with polyethylene films as a shield. Andretta et al, (1981), Nelson and Niklasson (1995), Dobson et al (2003), and Benlattar et al (2005) respectively investigated diurnal passive radiative cooling using TiO2 pigments and carbon particles, ZnS, semiconductors of PbS and PbSe and CdTe. Due to the challenging spectral requirements of high solar reflectance and IR transmittance, these designs did not demonstrate any cooling performance during the diurnal periods of the day. Nevertheless, diurnal cooling has been successfully demonstrated by other recent material designs, as reported by Leroy et al. (2019) and Torgerson and Hellhake (2020). The use of back solar reflectors at the bottom of solar transparency to create IR selective emitters with spectrally selective characteristics is a novel approach in the field of nanophotonics and metamaterials-based fabrication techniques, which is another encouraging development. Large extinction coefficient metals, such as aluminum (Al) and silver (Ag), are utilized in

back solar reflectors because they are thought to have superior reflective qualities. For a full wavelength range, silver has a high solar reflectance of 97% (Palik, 1998). Moreover, Mandal et al (2018) and Mandal et al (2020) demonstrated adequate diurnal radiative cooling potential using novel designs where micro-particles and nano-pore were used in polymer materials to backscatter sunlight and at the same time emit thermal radiation.

2.5.1 Polymeric Structures

Polymeric photonic structures are presented in this section as a potential solution for diurnal radiative cooling. To get a high emissivity in the atmospheric window, nanomaterials-resonators are usually doped with polymers (Santamouris and Feng, 2018).

Nanoporous polyethylene cloth was designed by Hsu et al (2016) which transmitted mild-infrared human radiation with no visible light where he used fabrics with embedded metal nanowires to present a personal thermal management system. The high thermal insulation properties of the nanowires combined with their conductive network formation allowed them to provide a joule heating to complement passive insulation layers. The developed fabrics can improve radiative cooling performance while still having the ability to breathe, absorb water and resist wear by their mechanical strength as a result of the porous nature of the nanowires.

Kou et al. (2017) used only a polymer-silica-mirror, which is made up of a fused silica wafer coated with a polymer top layer and a silver back reflector, to demonstrate passive radiative cooling in direct sunlight and at night. This straightforward plan was able to achieve cooling temperature differentials during the day of 8.2°C in direct sunlight and 8.4°C at night, which is almost 3°C more than the nanophotonic structure was able to achieve during the day. Their work demonstrated that radiative cooling during the day can be achieved at a low cost without requiring intricate photonic structures. By coating a 4 in. fused silica wafer of

500µm thickness with a 100µm thick polydimethylsiloxane (PDMS) film as a top layer and a 120nm thick silver film as a back reflector, they experimentally investigated the radiative cooling performance of the polymer-silica-mirror, as illustrated in figure 2.11.

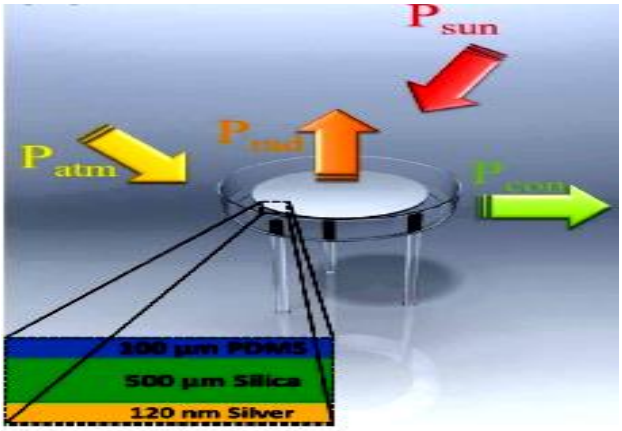

Fig 2.11: Schematic setup of the cooler (Kou, et al, 2017)

According to the results, it performs almost 3°C better than a multilayer thin film stack made with vacuum deposition techniques. They calculated further that the cooler's daytime average net cooling power is roughly 127 W/m^2. Drawing inspiration from earlier cool-roof paints (CRPs), Mandal et al. (2018) created an affordable hierarchically porous polymer P(VdF-HFP)HP coating for daytime radiative cooling by substituting light scattering air voids for the dielectric pigment in CRPs. In their report, they described a straightforward method for creating hierarchically porous Poly(vinylidene fluoride-co-hexafluoropentane) (P(VdF-HFP)HP) coatings using the polymer-based radiative cooling material. Because the coatings can be sprayed, dip-coated, or painted on a variety of substrates, including wood, plastic, and metal, (P(VdF-HFP)HP) coatings can be used extensively as exterior building paints. Due to the various vibrations in its molecular structure, the P(VdF-HFP)HP exhibits multiple emission peaks and minimal intrinsic solar absorption. Because P(VdF-HFP)HP is resistant to weathering, contamination, and UV radiation, it can be left outside for extended periods of time without losing any of its optical qualities. The P(VdF-HFP)HP's high long-wave infrared emissivity results in a hemispherical long-wave emissivity that is more than 10% higher than

previously reported values, while its high solar emissivity guarantees excellent reflection of sunlight from all incidences and does away with the need for silver reflectors used in previous designs. The outcome demonstrated that, with the high substrate-independent hemispherical solar reflectance of 0.96 and long-wave infrared (LWIR) emissivity of 0.97, it was possible to achieve sub-ambient temperature drops of roughly 6°C and cooling powers of roughly 96 W/m2 under solar intensities of 890 and 750 W/m2, respectively. Paints would become more environmentally friendly, though, if a water-based fluoropolymer were to take the place of these components (Mandal et al, 2020).

The application of an optically selective and thermally insulating (OSTI) polyethylene aerogel (PEA) cover for high-performance sub-ambient radiative cooling was developed and experimentally demonstrated by Leroy et al. (2019). As a straightforward method of lowering parasitic heat gain and solar absorption at the emitter, PEA was added to the top of a radiative cooling emitter. They examined the performance of PEA using a strong theoretical model, which provided insights into the trade-off between system performance and PEA thickness and made it possible to determine the ideal PEA thickness for a given system, set of weather conditions, and operating temperature. Passive cooling with a daytime temperature drop of up to 13°C and a cooling power of 96 W/m2 was accomplished around solar noon. The modular and easily integrable approach is expected to enhance the efficiency of current radiative cooling systems, including sorption-based water harvesting devices, passive refrigeration of food products, and radiative cooling water panels for building air conditioning units. It also showed how PEA's high solar reflectance allowed for the use of nonselective emitters with very little performance degradation, allowing for simpler designs and less expensive radiative coolers.

The highly size-selective lossless air pores in polyethylene were distributed evenly by Torgerson and Hellhake (2020), who created an all-polymer filter with high solar reflectance

and LWIR transparency. The enhanced optical characteristics of high solar reflection (0.95) and infrared transmission within the atmospheric transparency window (0.75) allowed for the achievement of cooling performance with the emitter. Radiative heat transfer to the cold sink of space during the day and night produced a sub-ambient temperature of up to 10^{o}C for the proposed polyethylene solar filter. Similarly, a surface under the solar filter was shown to have a cooling power of more than 110 W/m^2.

Jeong et al. (2020b) presented a plan for a passive daytime radiative cooler that is bio-inspired. It consists of a bottom solar reflective layer made of Ag that can provide solar reflection above 95% and top PDMS and SiO2 mid-infrared (MIR) emissive layers that can radiate strongly in the 8–13μm spectrums. Using polydimethylsiloxane, which has a very high emittance in the 8–13μm spectrum, and the thermoregulatory prismatic structure of Saharan silver ants, a geometrically modified polymer-based daytime radiative cooler was created. The optimization was centered on attaining the maximum emissivity within the intended MIR range (8–13μm), as emissivity plays a significant role in net radiative cooling efficiency. The advantage of the radiative cooler is due to the wide availability of SiO2 substrate wafer and the flexibility of the material property of PDMS, which can be shaped into desired geometries on the surface by a nano-imprinting process during fabrication. This enormous flexibility in PDMS shaping provides the chance to research how to improve optical characteristics, particularly emissivity in various configurations. The greatest numerical cooling power of 144w/m^2 is presented by a bio-inspired radiative cooler, according to the results. However, because of unfavorable sky conditions and low atmospheric transparency, the field investigation only revealed a net cooling power of 19.7W/m^2 and a temperature drop of 6.2^{o}C below ambient under direct sunlight. It showed that the cooling performance of the coolers deteriorated clearly in highly humid weather condition but can be successively enhanced by minimizing incoming solar irradiance.

Zhao et al. (2018) studied the viability and potential of employing radiative cooling technology to passively cool solar cells for standard PV modules. A 3.2mm glass was used in the investigation to encase a crystalline silicon solar cell. As a result, the glass's mid-infrared spectral emissivity was improved by applying a polydimethylsiloxane (PDMS) film to improve radiative cooling. The improved structure with PDMS film is illustrated in figure 2.12. The results of their comparative experiment indicated that there was only a 1.75K temperature difference between the solar cells in the commercial and modified structures. This suggests that improving the radiative cooling efficiency of a PV module did not significantly alter the cooling effect of the solar cells in real-world conditions. They also talked about and discovered the possibility of using radiative cooling as a substitute technique for controlling solar cell temperature in an extraterrestrial setting.

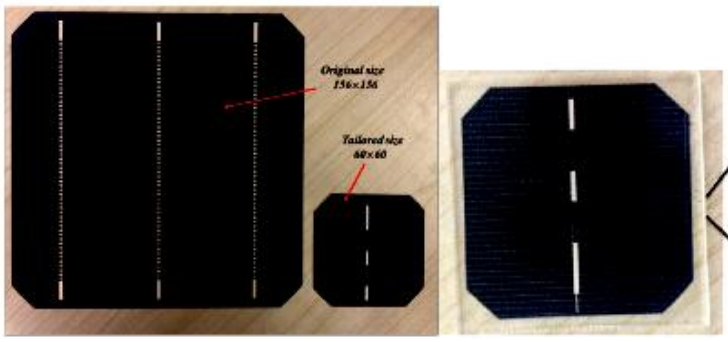

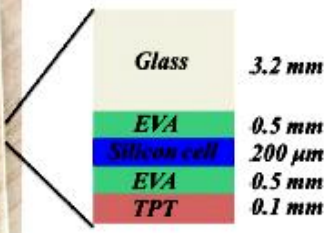

Fig. 2.12a: schematic cross-section of encapsulated silicon solar cell

Fig. 2.12b: schematic cross-section of modified silicon solar cell (Zhao, et al, 2018)

Lee and Luo (2019) demonstrated that chemically stable and reasonably priced polydimethylsiloxane (PDMS) can be a near-optimal thermal emitter for cooling flexible thin-film solar cells through theoretical calculation. They stated that although PDMS can be used as encapsulating materials in some situations, its potential as a radiative cooling substrate for solar cells has not been investigated. In their demonstration, it was discovered that a planar PDMS layer 200 nm thick can achieve a high emissivity of over 0.9 for the mid-infrared (IR) regime of 4-26μm. Yet, the emissivity can further increase to near-unity by

adding a pyramid structure to the surface in the 8-13μm range where the environmental radiation is negligible. The schematics for the planar PDMS and the pyramid-structured PDMS are shown in Figures 2.13a and 2.13b, respectively. Therefore, they hypothesized that, in comparison to the commonly used polyethylene terephthalate (PET) substrate, a pyramid-shaped PDMS layer can significantly lower the temperature of an organic solar cell by 11 °C; and that of a perovskite and a micro-crystalline (μc)-Si flexible solar cell by 11 °C, 12 °C, and 16 °C, respectively.

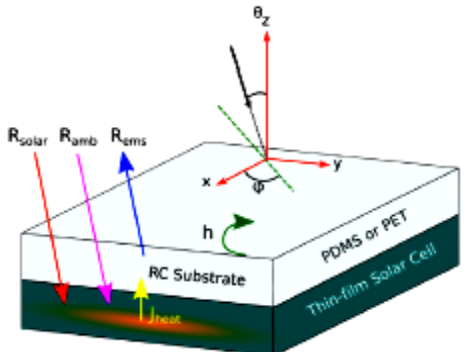

Fig 2.13a: Planar PDMS or PET

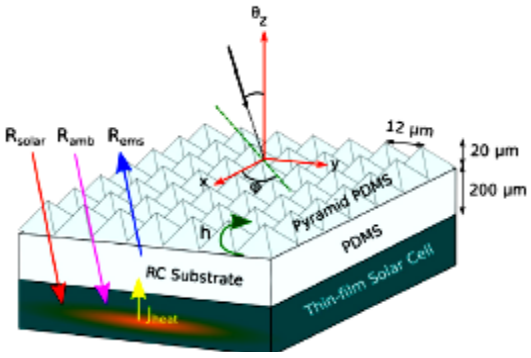

Fig.2.13b: Pyramid-structure PDMS radiative coolers (Lee and Luo, 2019)

Zhou et al. (2019) conducted experiments (both indoor and outdoor) using their low-cost planar PDMS/metal thermal emitter thin film structure, which is beneficial for large-scale, effective radiative cooling applications. They conducted experiments in the lab and outdoorconditionsous environmental conditions, and they found that, with an average cooling power of 120W/m2, they could reduce temperatures by 9.5oC and 11oC, respectively. They put their carefully thought-out selective structure into practice to reduce solar input and manage the thermal emission's divergence. On February 28, 2018, from 11:00 to 15:00, they conducted their outdoor test in three different locations on the UB campus in Buffalo, New York. The weather was clear and sunny with a 60% relative humidity. The beaming system reduced the temperature by 2-9^{o}C during the daytime 7-9^{o}C at night.

Fig.2.14: Schematic diagram of the planar PDMS/metal thermal emitter (Zhao, et al, 2019)

Carlorena et al. (2021) proposed and tested a polymer called polymethylsilsesquioxane (PMSQ) packed with silicon dioxide nanoparticles to create emissive layers for daytime radiative cooling on substrates made of aluminum and vikuiti. Prior to fabrication, they tested the proposed structures using simulation, and the study's material design gave them the crucial knowledge to adjust the material's thickness. Without focusing specifically on lowering radiative heat losses and relative humidity, the study's objective was to find daytime radiative cooling materials that are scalable but efficient for the built environment (moderate) in a range of weather scenarios. For radiative cooling applications on different surfaces, the study offered an x-ray of the materials' efficacy. According to test results, the DTRC design on aluminum yielded an emissivity of 0.34 in the atmospheric window and an average reflectance of 0.7 in the solar band, while the Vikuiti design produced values of 0.97 and 0.89. During the daytime solar irradiation in the testing, samples with the vikuiti substrate had an average temperature reduction of 2.7^{o}C below the ambient, while samples made of aluminum, with their emissive layer, were unable to demonstrate sub-ambient cooling throughout the day, even though their average surface temperature decreased by 1.7^{o}C. They justified their thesis by pointing out that the simple coatings—which required just that a bare substrate be sprayed with coating—provided significant radiative cooling in real climatic conditions.

Lin et al. (2021) proposed a daytime passive radiative cooling structure that is flexible, scalable, and reasonably priced in order to enhance mass manufacturing and reduce costs. The structure is a cooling sheet composed of layers of polydimethylsiloxane (PDMS) and a reflector, which can be used to simulate passive cooling during the day in Hong Kong's hot

and humid climate both experimentally and numerically. Under clear sky conditions, the proposed cooling sheet achieved a theoretical sub-ambient temperature of 4.7°C and a net cooling power of 68.3 W/m^2. Its average solar reflectivity was 92.1%, and its average solar emissivity was 94.5%, with a solar intensity of approximately 1000 W/m^2. In contrast, an experimental test that was conducted continuously for 48 hours without the use of windscreens or sun shields was able to achieve an average sub-ambient temperature of 2.4°C at noon, with a cooling power of 52.4 °W/m2. In addition, a 24-hour operation yielded a 1°C drop in air temperature, which was used to investigate the heat exchange between vented air and the suggested passive radiative air-cooling system. Because they prevent the cooler from accessing the clear sky, obstacles, high humidity, and parasitic heat loss rate are demonstrated to affect cooling performance in real-world applications. To investigate potential uses of radiative cooling in tropical environments, Han et al. (2022) distributed BaSO4 particles within a Poly (vinylidene difluoride-co-hexafluoropropylene) matrix [P (VdF-HFP)] to form a highly reflective polymeric structure. The single-layer structure, which can be on a variety of substrates, including wood and concrete, is made using a highly scalable and reasonably priced technique in addition to the coating's remarkable properties—hydrophobicity, flexibility, mechanical strength, and durability in wet weather conditions. The structure exhibits a high reflectivity of 97% and strong emission of 94.2%, indicating the coating's potential for radiative cooling. These properties are attributed to the coating's components, BaSO4 and P(VdF-HFP), and their inherent bond vibrations. The average surface temperature of the concrete coated with BaSO4-P(VdF-HFP) was consistently 5^{o}C lower than that of the commercial NIPPON SOLAREFLECT Si coating during field testing. Polymer-based coolers have gained a great deal of interest recently because of their excellent radiative qualities and scalability. The parasitic absorption of functional groups in polymers was used by Liu et al. (2022) to determine whether polymer materials are suitable for radiative cooling.

For all-day sub-ambient Radiative cooling, they created a dual-layer film made of an optically transparent ethylene-tetrafluoroethylene (ETFE) film, a layer of silver (Ag), and a layer of silica (SiO_2). According to their findings, polymer materials with thicknesses between 10 and 100 m emit large levels of infrared radiation, and as thickness increases, the cooler's increased parasitic sun absorption cancels out the radiative cooling effect. The structure's characterization revealed that the ETFE cooler's solar reflectivity and atmospheric thermal emissivity were 94% and 83%, respectively, making it a strong contender for all-day RC. Moreover, Hefei observed daytime temperature drops of about 3°C below ambient air and night-time temperature drops of almost 10°C.

2.5.2 Paint Coatings

The application of photonic crystals to achieve efficient radiative cooling has been limited by their high cost and fragile nature. The use of radiative cooling materials in the form of paint formats in radiative cooling is to reduce cost as expensive materials like silver are not used for the purpose and are presented in this section. Paints which are coatings on zero transparent surfaces are made up of pigments and resins and must be both highly reflective and absorptive. The composition and design of paints intended for radiative cooling is such that infrared selective metal is layered at the bottom and thickness-sensitive spectrally selective (TSSS) paints are layered on top. There is, therefore, the need for such materials as paints or polymer films whose preservation, transportation and application in different textures and geometries are appealing for real-world use.

Orel, et al (1993) proposed how selective paint radiators perform in real condition by pigmenting it with either $TiO_2/BaSO_4$ mixture or TiO_2/ZnS pigment mixture, having the same overall pigment-to-volume ratio. From their research work, the result showed that the NO_1 paints with greater emittance as a result of the absorption of BaSO4 extender in the spectral

range of 8-13µm recorded a greater temperature drop than those of the NO_2. It was also revealed that addition of barium sulphate extender into the paint coatings increased the cooling performance of the radiators with a small temperature drop.

The daytime radiative cooling under direct sunlight was demonstrated by Torgerson and Hellhake (2019) in their work on polymer solar filters. They used an all-polymer filter that shields solar irradiance while still maintaining high transmittance in the long wave infrared (LWIR). Over 99% of the solar irradiance can be blocked by this polymer film, known as STATIC (spectrally turned all-polymer technology for inducing cooling), which prevents solar heating while allowing the heat to be directed into space. Separating solar irradiance from the atmospheric transparency window allows for full-sun radiative cooling during the day with a solar filter. By placing an emissive surface beneath the filter, they obtained a cooling power of over 110W/m^2 and a temperature drop up to 10^{o}C during the daytime and nighttime.

Although paints, plastics, and even wood can be designed to stay cool in direct sunlight, Lim (2020) concluded that it is unclear how these materials will replace energy-hungry air conditioners in her study of the incredibly cool materials that transfer heat to the space. He noted the challenges in keeping cool so far recorded and the efforts made by different researchers to solve the problem. He also expressed his concern about whether or not consumers will embrace the idea of supercool materials, pointing out that their ability to function in a variety of climates and locations is still in question. After all, homeowners haven't even taken the basic step of replacing their old, worn-out roofs with reflective ones. He said that super-cool paints could double the energy savings over a white roof, even though it would still be purely theoretical. He came to the conclusion that one advantage of radiative cooling is that it prevents solar panels from losing efficiency. He also noted that passive

radiative cooling is the only technology that captures all waste heat and returns it to the space.

2.5.3 Nano photonic Materials for diurnal passive radiative cooling

Multilayer planar photonic radiative structures, which are typically composed of two parts, are presented in this section to achieve high reflectivity of a structure in the short wavelength range where silver (Ag) and aluminum (Al) are used, while at the same time increasing its absorption in the 8-13μm atmospheric window. Photonic structures can be engineered to produce thermal emissions that are both strongly and strictly selective. When paired with a solar reflector, they can effectively generate radiative power that surpasses incident solar and atmospheric radiations, potentially leading to net cooling effects. Recently, the obstacles of diurnal solar absorption have been effectively overcome through the fabrication of nano photonic-based cooling materials.

2.5.3.1 Single Layer Nanophotonic Structures

Experiment with a single layer nano photonic structure was carried out by Chen et al (2016) with sunshades, which blocked the incident sunlight, to demonstrate an extreme temperature reduction through radiative cooling. By using thermal emitters made of silicon nitride (Si_3N_4), amorphous silicon (Si), and aluminum layers deposited on top of a silicon wafer, which are highly selective within the atmospheric transparency window (8-13μm), it was possible to achieve radiative cooling to deep sub-freezing temperatures over the course of a 24-hour day-night cycle. By combining photonic and thermal design as shown in fig. 2.15, it is possible to minimize parasitic heat losses and achieve ultra-layer temperature reductions of up to 42^{o}C below ambient when the apparatus is exposed to peak solar irradiance. This results in a continuous passive cooling that occurs day and night.

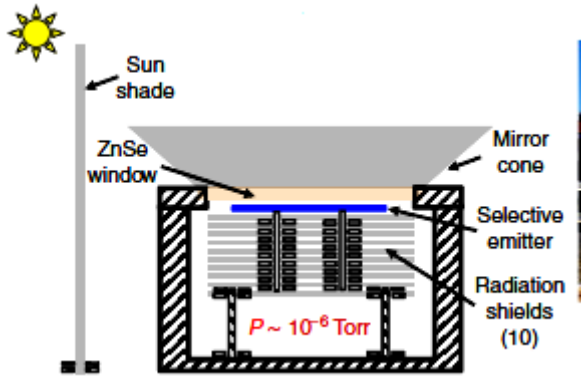

Fig 2.15: Schematic of the experimental setup (Chem, et al, 2016)

Lu, et al (2016) gave a comprehensive overview of passive radiative cooling (PRC) in buildings based on previous studies. The fundamentals were reviewed, and the development courses for passive radiative cooling systems were presented by examining trends in articles and applications that had been published. They analyzed and optimized strategies to increase the net radiative cooling effect using simple physical models. It has been noted that selective emitters work better for sub-ambient cooling, but high emittance radiative surfaces are preferred for high thermal load cooling. A significant amount of the incoming heat gain is accounted for by atmospheric radiation, which can be reduced by using heat mirror apertures or angular selective surfaces. The purpose of installing the windshield was to suppress the convective terms. The higher cooling power magnitude must be made up for by higher surface temperatures. They noted that the cooling magnitude from the nocturnal PRC experiment was typically maintained at 30–40 W/m^2 for distinctive cooling purposes. According to them, temperate and Mediterranean climates—which feature greater daily temperature swings, lower humidity, and less cloud cover—are the best places to implement nocturnal passive radiative cooling. Additionally, they claimed that, if done correctly, daytime passive radiative cooling—an emerging, highly significant free-energy technique—could replace traditional mechanical cooling and lessen the load on the grid during peak hours. Although it is still thought that daytime passive radiative cooling can be accomplished

under direct sun radiation on a clear winter day in the mid-and high-latitude regions, it was noted that daytime passive radiative cooling is unlikely to be implemented in periods and locations where daytime cooling is most needed. At last, they came to the conclusion that the development of novel optical materials will be crucial to the widespread application of passive radiative cooling systems. They also noted that the main challenges will be in the areas of cooling magnitude, product reliability, coating optical properties, cover durability, and building integration. The photonic cooler is schematically shown in figure 2.16.

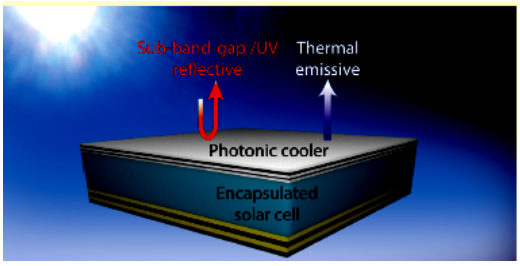

Fig 2.16: Schematics of photonic cooler (Lu, et al, 2016)

Li et al. (2019) developed Potassium Phosphate (AlPO4) powder through a precipitation process. This is a new type of inorganic passive radiative cooling material that has high mid-infrared emissivity and high solar reflectivity during the day. This was done by uniformly mixing together the aqueous solutions Aluminium and Phosphorus in a molar ratio 1:1, and used the Ammonium phosphate $(NH_4)_3PO_4 \cdot 3H_2O$ and aluminum chloride $AlCl_3 \cdot 6H_2O$ as reactants. They investigated the crystalline structures and optical characteristics of AlPO4 at various heat treatment temperatures in addition to testing the prepared AlPO4 powder material's passive radiative cooling capabilities. The findings demonstrated that AlPO4's reflectivity rises and its emissivity falls with increasing heat treatment temperature. These remarkable properties of tridymite-type AlPO4 (T-APO) suggest that it has a strong potential for passive radiative cooling during the day. Additionally, it was demonstrated that T-APO, which has a unique huge cavity channel structure, has an emissivity that is 0.90 higher than that of AlPO4 (C-APO), a type of cristobalite. The AlPO4 coating cools 4.2 °C below the

surrounding air temperature when exposed to direct sunlight, increasing people's comfort level.

An optically selective and thermally insulating (OSTI) polyethylene aerogel (PEA) cover was developed and experimentally demonstrated by Leroy et al. (2019) for high-performance sub-ambient radiative cooling. In order to lower parasitic heat gain and solar absorption at the emitter, PEA was added to the top of a radiative cooling emitter as a straightforward solution. In order to determine the ideal PEA thickness for a given system, weather, and operating temperature, they employed a strong theoretical model to study the performance of PEA. This model provided insights into the trade-off between system performance and PEA thickness. A passive cooling of up to 13°C below the surrounding air temperature during the day, approximately at solar noon, was accomplished, with a cooling power of 96 W/m^2. It is hoped that the approach, which is easily modularized and implemented in current systems, will contribute to the enhancement of current radiative cooling systems, including sorption-based water harvesting devices, passive refrigeration of food produce, and radiative cooling water panels for building air conditioning units. Additionally, it showed that PEA permitted the use of nonselective emitters with very little performance degradation due tots high solar reflectance and hence, enabling simpler-design and lower-cost radiative coolers.

To be able to assist radiative coolers in regulating their radiative cooling in accordance with the average ambient temperature, Xia et al. (2020) proposed and designed a temperature-controlled phase change structure (TCPCS). The cooler's structure was composed of a few long, thin sheets (15 cm x 1 cm x 1 mm) with two thin steel wires fastened to the sides. These thin sheets are always parallel to one another and are joined by four perforated plastic plates. The cooler can modify the cooling by altering the angle at which the sheet opens. This means that when the sheets are closed, or at an angle of 0 degrees Celsius, there is no cooling; however, the cooler begins to cool when the sheets are positioned vertically at an angle of 90

degrees Celsius. The transmissivity of the TCPCS and, consequently, the cooling, are determined by the opening angle. Accordingly, when the sheets are vertical or open, the radiative energy transmissivity increases from 0 (when the sheets are closed) to 1. Their findings then revealed that, in the event that the TCPCS is not used for the entire day, the cooler can permit a decrease in the maximum temperature difference from 19.6ºC to 9.7ºC. In order to further enhance the TCPCS, they created a v-shaped TCPCS that can use solar heating in the winter and space cooling in the summer.

In 2020, Yang and Zhang conducted research on the theory, practical uses, and financial evaluation of passive radiative cooling (PDRC). A surface that loses heat to space during the day because it absorbs less sunlight than it radiates has three characteristics that make it ideal for passive radiative cooling without the need for electricity: 100% reflectance, for example. 10% solar spectrum absorbtivity, 100% emittance in the atmosphere's long-wave length infrared transmission window (8–13μm), and 0% emittance outside the atmospheric transparency window (5-8μm and >13μm). It was found that when the aforementioned qualities were met, the cooler's net cooling power ranged from 150W/m2 at ambient temperatures between 20 and 30 degrees Celsius. They noted that in tropical regions with humidity levels above 60%, the air moisture content, or humidity, can drop to less than 50 W/m^2. A flat, reflective metal film, such as aluminum or silver (Al), combined with transparent mid-infrared emitter films that have low thermal emittance and high reflectance in the infrared spectrum was one of the two main design strategies they mentioned. The second method was to attain high reflectance by using optical scattering at the interface between two materials with different refractive indices. They also included a list of applications for this passive radiative cooling during the day, including solar power generation, building envelopes, cars, trucks, containers, and oil tankers. In the end, they evaluated the differences in net energy savings, coating costs for economic benefit, CO_2 reduction, system durability

(cooler), mechanical stability for porous structure, and PDRC device design and performance as major challenges. This allowed them to finally x-ray the economic and environmental benefits of PDRC.

In order to improve the passive radiative cooling characteristics of flexible class solar cells for space application, Banik et al. (2020) used single-layer silicon oxy carbonitride films. They examined and demonstrated the optical properties of this coating using a dip coating deposition method. They combined CIGS cells on polyimide substrates with commercial organiopolysilazane as a precursor. They created a 50%w/w solution in the sample preparation process by combining the organopolysilazane precursor, durazane 1800, with di-n-butyl ether solvent. After agitating the mixture for an hour at room temperature with a magnetic stirrer, they let it stand for roughly ten minutes before dipping it with an in-house dip counter that used a stepper motor connected to a linear actuator and motor controller. After curing a 3.2 μm layer of silicon oxycarbonitride coating, they demonstrated that the coating can be very suitable for cooling terrestrial photovoltaic modules. This can lower the module's temperature by 300C, increasing the maximum power output by 27% under full irradiation conditions. They also achieved a high emissivity, α of 0.72.

2.5.3.2 Dual-Layer Nanophotonic Structures

Subwavelength dielectric resonator metasurface can be considered efficient absorbers as they can support various resonance modes. Zou et al (2017) proposed a two-layer meta-surface to demonstrate diurnal cooling. The cooler was made of silver and n-type doped silicon resonators. Metal loading was applied to improve the experimental demonstration of the metasurface and achieve strong broadband thermal emission over a broad angle that spectrally matches the main IR atmospheric transparency window. Based on a simulation-based analysis of the cooling ability, they have reported the lowest temperature drop that can

be achieved at night (11.14K) and during the day (8.55K) at thermal equilibrium. Additionally, the corresponding measurement-based analysis revealed that during the nocturnal and diurnal hours, the minimum temperature dropped by 10.29 and 7.36K, respectively. When compared to other reported multilayer metamaterial structures, the fabrication of the proposed dual-layer structure is straightforward and reasonably affordable. Scalable fabrication that can be integrated with silicon photonics is feasible, making the design applicable to thermal emission control, and IR-sensing.

Huang and Ruan (2017) designed a double-layer coating consisting of carbon black as the bottom layer for thermal emission and titanium dioxide (TiO2) with acrylic resin embedded to achieve diurnal radiative cooling. Over 90% of solar radiation can be reflected and emitted when (TiO2) particles have an ideal size of 0.2μm, yielding a predicted net cooling power of 100W/m2. The outcome demonstrates that even with the possibility of continued conduction and convection heat exchange, the cooling effect was preserved. The sketch of the functional double-layer coating is shown in Fig 2.17.

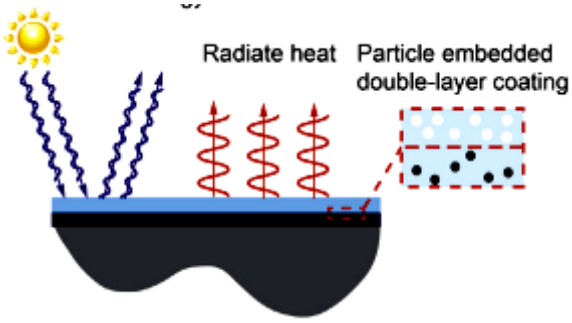

Figure 2.17: Sketch of a functional double-layer coating used for daytime radiative cooling Huang and Ruan (2017)

Moreover, Bao et al. (2017) developed a highly scalable nanoparticle-based double-layer coating with SiC particles in the bottom layer for thermal emission and TiO2 particles on top for solar reflection. In order to improve the cooling capabilities of substrates, the double-layer coatings were made up of SiO_2 or SiC nanoparticles that were tightly packed with TiO_2 particles. The structures were placed atop an aluminum substrate that exhibits an overall solar

spectrum reflectivity of 90.7% and an atmospheric transparency window emittance of 90.11%. As a result of direct solar radiation (AM1.5), the test result indicated that both the structures on the aluminum substrate and the TiO_2+SiC configuration achieved sub-ambient cooling, with temperature reductions of 8°C below ambient and roughly 10–11°C for the TiO_2+SiO_2 configuration. When the surface is coated with TiO_2+SiO_2, it can be made to reach a temperature of 5 °C below ambient during the night, which is 1-2 °C lower than TiO_2+SiC.

Subsequently, a follow-up investigation on a metasurface-based radiative cooler was carried out by Sun et al (2018) an al-doped zinc oxide (AZO) conducting box was developed. The structure had aluminum as the back reflector, optical solar reflector, and SiO_2 as the spacer all lying below the AZO box. A thermal emittance of 79% and absorptance of 0.16 was achieved for space cooling. In spite of the challenge of strict spectral selectivity and strong IR emittance, complex fabrication methods is still a major setback for 2-D photonic structures.

Zhu et al. in 2021 experimentally demonstrated that effective daytime radiative cooling can be achieved with the simple, easily-prepared dual-layer emitter shown in figure 2.18. This dual emitter shows a high reflectivity of 97.5 percent of solar irradiation and near-black absorptivity in the mid-infrared range. The researchers discovered that the cooling performance was influenced by the convective cloud cavern and the relative humidity. They also discovered that substrates had no effect on the emitters because they were still able to achieve the same potential cooling performance by exposing all of the structures to the sky. The structure's temperature can reduce by 3.3^{o}C in the absence of windshield during the day and a potential cooling power density of roughly 72.7W/m^2.

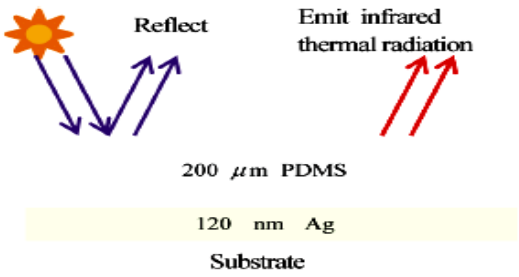

Fig 2.18: schematic of a dual-layer emitter for efficient daytime Radiative cooling (Zhu, et al, 2021)

Ong, et al. (2022) used a straightforward way to develope a dual-layer cooler using silver as the bottom layer and fluorocarbon resin (FEVE) as the top layer for daytime radiative cooling as shown in Fig 2.19. The FEVE was purchased, and it was dissolved in a butyl acetate solution using magnetic stirring at room temperature to thin down and spread the solute. This was done to prepare the FEVE-based coolers. This cooler has a reflectivity of 0.933 in the solar radiation band and an average emissivity of 0.945 in the atmospheric window. The proposed FEVE-based cooler's thermal stability, water resistance, weather resistance, and daytime cooling performance were all validated in outdoor trials. The constructed cooler's emissivity increased from 0.1 to 0.9 in the 8–10μm band, which is a clear sign that FEVE is the main cause of the emissivity increase. The cooling power under direct sunlight and at 27^{o}C ambient temperature was found to be 128.75 W/m^{2}, discounting non-radiative heat transfer. Additionally, 5.1^{o}C was recorded as the average temperature drops between 10:00 a.m. and 2:00 p.m. They deduced from the results that the sample's infrared radiation characteristics and solar radiation absorption were both influenced by the thickness of the FEVE layer.

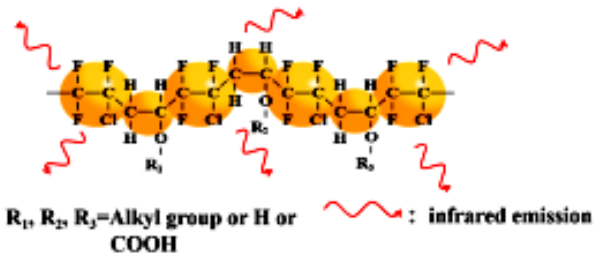

Figure 2.19: Schematic of FEVE molecular structure and vibration infrared emission

Huang et al. (2022b) used aluminium foil and scotch tape to demonstrate a straightforward, low-cost, and do-it-yourself design for a selectively emissive radiative cooler (Shown in Fig 2.20). This cooler can match state-of-the-art designs in terms of solar reflectance, long wavelength infrared emittance, and optical selectivity. The infrared optical properties of the cooler are excellent for the proposed radiative cooling concept, and this low-cost, efficient radiative cooler is easily constructed. Aluminum foil, used for the back, has a scotch tape emittance of 0.68 and a modest weighted solar reflectance of 0.83. However, this design may also achieve radiative cooling during the day by using silver as the rear reflector, which has a high solar reflectance (Rsolar=0.95). In the night, the results revealed a sub-ambient cooling of 11°C with a convection shield and 7°C without a convection shield, although utilizing silver as opposed to aluminium foil, a temperature reduction of up to 2°C under direct sunshine was reached without any convection shield, making it a strong choice for applications needing modest sub-ambient cooling. They stated that scotch tape may be put directly into the aluminium foil at a low cost, in contrast to other methods of creating radiative coolers, which call for expensive materials and fabrication techniques. It is used as a thermal emitter because it can be made into a repeatable radiative cooler by combining mass-produced, commercially available scotch tape with aluminum foil or vapor-deposited silver.

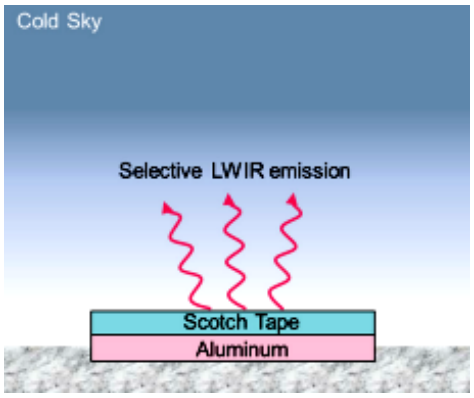

Fig 2.20 Schematic of the scotch tape radiative cooler with aluminium (Huang et al, 2022b)

Chen et al. (2022) reported the development of clean bi-layer porous coatings, as illustrated in Fig. 2.21, for efficient radiative cooling during the day. The cooler's enhanced daytime radiative cooling efficiency, scalability, and self-cleaning characteristics make the coating long-lasting for outdoor use in direct sunlight. The Daytime passive radiative cooling coating was made with reasonably priced, well-optimized NaCl. Water-soluble NaCl particles of the proper sizes were utilized as sacrificial templates to produce this covering of size-controlled holes. The solution enhances energy efficiency and scalable fabrication functionality and is readily recyclable. There was a 97% solar reflectance and 96% LWIR emissivity in the proposed super-hydrophobic bi-layer coating. During the outdoor experimental study with the coating, the temperature decreased by 4°C when the sun's irradiation was 774W/m2, and it even dropped to 4.7°C below the temperature of commercial coatings. The design was able to sustain an exceptional cooling performance of approximately 3.1oC even after particle contamination because rainwater can readily remove dust. The coatings are cleaned using this process without the need for energy or labor, which is beneficial for long-term practical applications.

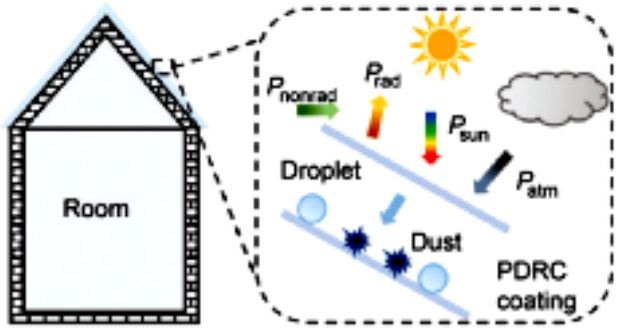

Figure 2.21: schematic of the super-hydrophobicity porous coating (Chen et al, 2022)

2.5.3.3 Multilayer Nano photonic structures

The multilayer structure are categorized into one dimensional (1-D), two dimensional (2-D) and metamaterials

Raman et al. (2014) used one-dimensional (1-D) planar photonic structure to experimentally demonstrate radiative cooling to nearly 5oC below the ambient air temperature under direct sunlight. This method introduced an integrated photonic solar reflector and thermal emitter that emits strongly and selectively in the atmospheric transparency window, reflecting 97% of incident sunlight through seven layers of varying thicknesses of HfO2 and SiO2. A 200 nm layer of Ag is deposited on top of a 200 mm silicon wafer, which is followed by these alternating layers of HfO_2 and SiO_2. When exposed to direct sunlight above 850 W/m2 on a rooftop, the photonic radiative cooler depicted in Figure 2.22 achieves a cooling power of 40.1 W/m2 and cools to a temperature that is 4.9oC below the ambient air temperature. Their findings show that new technological opportunities for energy efficiency can be made possible by the photonic approach. Furthermore, even in the hottest parts of the day, the chilly darkness of the universe can be exploited as a replenishable thermodynamic resource. They demonstrated that, even with an ideal selective emitter that emits only in the atmospheric transparency window, more than 90% of incident sunlight must be reflected in order for the temperature to remain at room temperature. In reality, a significant radiative

cooling during the day requires the reflection of more than 94% of the sun's energy, especially considering the variations in atmospheric conditions among various geographical locations. Peak sunlight irradiance of up to 890 W/m2 on the radiative cooler was ensured during the cold months of testing, and the entire apparatus was tilted 300 degrees southward. Better cooling performance would be anticipated for the same setup if the cooler were operated without the tilt, as this experimental constraint limits sky access for the purpose of thermal radiation. They exposed the photonic radiative cooler to the sky on a building rooftop during the day to show off its capabilities on a crisp, cold day. The temperature of the cooler was about 22.1^{o}C compared with the ambient air temperature of about 29^{o}C.

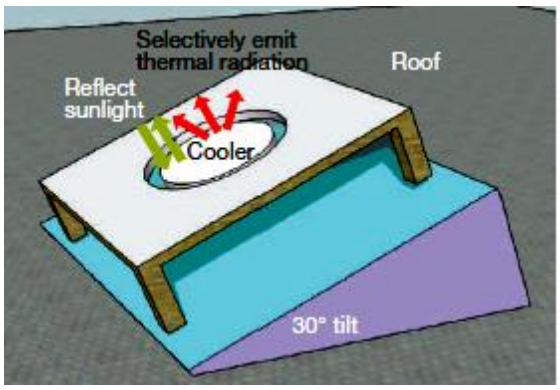

Fig 2.22: Schematic Diagram of a Radiative Photonic Cooler (Raman et al, 2014)

Li et al. (2017) presented a comprehensive photonic approach for solar cell cooling, which forms part of another set of one-dimensional nano photonic structures. They investigated the thermal radiation and solar absorption properties of silicon solar cells experimentally in order to achieve radiative cooling and selective solar energy utilization. The multilayered dielectric stacks used in their designed photonic cooler consist of n sub-layers of Al_2O_3/SiN/TiO_2/SiN on top of a single layer each of SiN, SiO_2, TiO_2, and Al_2O_2. It is a one-dimensional photonic film with significant solar spectrum reflection and strong heat radiation capabilities. In order to successfully reduce the temperature of the cell—roughly 5.7^{o}C—they suggested integrating the cooler into an already-existing solar panel.

Then, in 2018, Li et al presented a color preserving application with the introduction of material fabrication methods that included simulated annealing, needle optimization, jump method, and memetic algorithm which helped to precisely control the layer thickness so as to maximize the spectral properties.

Besides one-dimensional nanophotonic planar cooling materials, the property of spectral thermal selectivity can be tailored for a two-dimensional photonics. A metal-dielectric photonic structure that can provide radiative cooling throughout the day in outdoor environments was created by Raphaeli et al. in 2013. The two-dimensional photonic crystal employs a selective thermal radiation in conjunction with quartz and silicon carbide (SiC). Silver (Ag) was used as a substrate for the deposition of multilayers of titanium dioxide (TiO_2) and magnesium fluoride (MgF_2) with a dielectric reflector. Roll-to-roll nanoimprint lithography was used to create the radiative cooling system, which functions as a broadband mirror for solar light and the time emits strongly in the mid-IR within the atmospheric transparency window. The structure demonstrated a cooling persistence even in the presence of significant convective/conductive heat exchange and unfavorable atmospheric conditions, achieving a net cooling power of roughly $100W/m^2$ at ambient temperature.

Hossain, et al (2015) used 2-D photonic crystals as selective emitters to theoretically investigate the use of symmetrical conical metamaterial (CMM) pillars in daytime radiative cooling. The emissivity spectra value of the CMM pillars was found to be in the range of 0.8-0.99 for different bottom diameters of the CMM pillars. Their elementary metal–dielectric concept of CMM pillar consists of alternating layers of aluminum and germanium of thicknesses 30nm and 110nm respectively whose diameters decrease gradually from bottom to top which gives the structure a conical shape. The substrate of the CMM structure is aluminum of thickness, 150nm, which is by its optical property thickness can diminish any infrared transmission through the substrate. The result indicates that the structures can

achieve cooling of up to 12.2 °C below the ambient temperature at night-time and 9 °C below the ambient temperature during daytime operation. If the non-radiative heat exchange is further reduced, leading to Q = 1 W/m^2/K, then, an equilibrium temperature of 25 °C below the ambient temperature during the daytime can be realized, a remarkable low temperature approaching the freezing point of water. They demonstrated that to diminish the atmosphere radiation, the CMM acted like a metallic mirror with an absorptivity between 0.8-0.99 and that infrared radiation transmitting solar reflector is needed since CMM absorbs solar light extensively. The schematic of the conical shape of the multilayer metamaterial pillar array is shown in Fig 2.23.

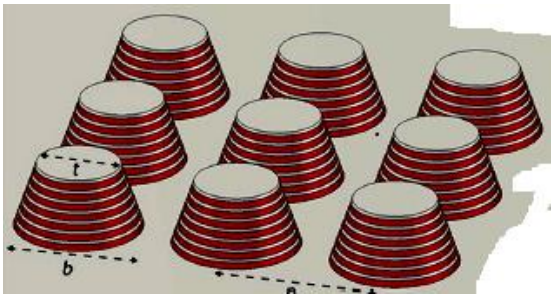

Fig 2.23: Schematic of conical shape of the multilayer metamaterial pillar array (Hossain, et al, 2015).

Since optimal radiative cooling for solar absorbers is dependent on a visibly transparent blackbody placed on a silicon absorber under sunlight, Zhu et al. (2015) used a thermosphotonic approach to demonstrate this experimentally. A polished silicon wafer measuring 100mm in diameter and 525μm in thickness makes up the solar absorber. Additionally, the absorber has a 200 nm thick aluminum reflector and a 75 nm thick layer of silicon nitride on top as an antireflection layer. Through passive radiative cooling, the blackbody contributed to bringing the temperature of the silicon absorber down to 13^{o}C while maintaining and even slightly increasing solar absorption. They therefore illustrated that radiative cooling concept can be in combination with solar absorber that was deposited on a 2-D silica photonic crystal.

In order to achieve a cooling power comparable to that of the more intricate 3D structure, Kecebas et al. (2017) proposed two different designs for 2D thin film coatings. This is because passive radiative cooling during the day requires an effective thermal emission in the 8–13 μm spectrum, and photonic structures can raise or lower thermal emission in 2D or 3D configurations of solar thermos photovoltaics. In order to improve the structure's cooling performance, their first alternative design modified the Raman et al., 2014 proposed structure by adding Al_2O_3 layers in addition to TiO_2 and SiO_2 layers, as shown in Figure 2.24. They also showed the second alternative configuration in which silver layers were used in the design with periodic segments of TiO_2 and SiO_2 (to obtain high reflectance in the visible and near-infrared spectrum). They showed that the second configuration with periodic segments significantly provided higher radiative cooling power, which is around $100W/m^2$.

Fig 2.24: Scheme for the implemented structure (Kecebas, et al, 2017)

In the demonstration of Zhai, et al (2017), polymethylpentane (PTX) metamaterials can be used as the cover of the building's exterior owing to their lightweight and outstanding flexibility. They fabricated a 50μm thick polymethylpentane film (TPX) that encapsulated random-distributed 8μm diameter SiO_2 microsphere as a metamaterial selective emitter to promote a high-throughput, economical roll-to-roll method for daytime radiative cooling. The schematic of the hybrid metamaterial backed with a thin silver film is as shown in figure

2.25. Here, heat from the sun can be avoided since both TPX and SiO_2 microparticles are transparent to solar light. When the metamaterial film was coated on a silver reflector to reflect incident radiation, it was observed that the optical properties of the metamaterials could only be affected by the diameter of the SiO2 microspheres. Approximately 4% of sunlight was captured. The exceptional mechanical and chemical resistance of PTX metamaterials makes them a promising option for daytime radiative cooling in buildings, with long-term potential.

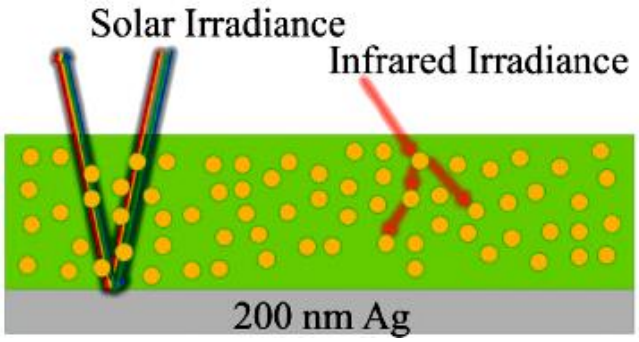

Fig 2.25: Schematic of the hybrid metamaterial backed with a thin silver film (Zhai, et al, 2017)

Zhang et al. (2018) presented a first-hand study on radiative cooling with metamaterial to give residential buildings affordable diurnal cooling, in line with the work done by Zhai et al. (2017). For diurnal cooling, the structure is made of a hybrid metamaterial consisting of randomized glass-polymer coated in silver. When combined with residential air conditioning systems, the hybrid diurnal radiative cooled-cold storage cooling system demonstrated significant financial and energy savings for a typical single-family home. The hybrid system was found to have an average daily cooling power of 110 W/m^2 and an average annual coefficient of performance increase of more than 39.4%.

Zhai et al. (2019a) developed a new application using materials similar to those used by Zhai et al. (2017). Under stationary conditions, water was cooled to 10.6oC below ambient at noon using the developed radiative cooled-cold collection module. They investigated the use of inexpensive, scalable-manufacturable radiative cooling metamaterials for radiative sky

cooling. In order to provide continuous day and night cooling, they constructed and demonstrated a kilowatt (KW) scale Radicold system with a radiative cooling surface area of 13.5 m^2. This system can provide a maximum cooling power of 1,296 W at night and an average of 607 W at noon. In their work, they presented how weather affects the radiative cooling performance of bilayer radicold metal films whose schematic is as presented in figure 2.26. It has been discovered that cloud cover has a complex effect on atmospheric radiation because of variations in cloud types, cloud heights, cloud composition, and cloud behaviors that vary over time and space. They demonstrated a clear relationship between rising cloud cover and falling radiative cooling power.

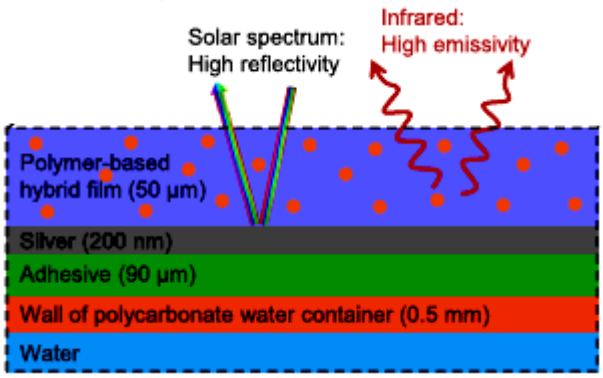

Fig 2.26: Schematic of the bilayer RadiCold metal film (Zhao, et al, 2019)

Titanium dioxide (TiO_2) particles basically have high solar reflectance and are usually doped with acrylic paints to boost their surface reflectivity property. However, increasing the TiO_2 particle sizes in pigments may impact the coatings negatively by decreasing their solar and visible light reflectance (song et al, 2014). Hence, an optimum particle size of approximately 0.2μm is should be maintained.

Using low-cost random photonic silica spheres, Atiganyanum et al. (2018) developed a method to extend the mile-stone. They did this by minimizing the photon transport mean path to alter the spectral absorption, potentially cooling a black substrate to 12oC below ambient temperature, as opposed to the 7.3oC that commercial solar reflective white paint reaches during periods of strong solar radiation. Their research demonstrated that the material, size,

and fill fraction of the microsphere can all be carefully chosen to optimize optical scattering power. From the demonstration result, a route to inexpensive coatings with exceptional radiative cooling efficiency is predicted.

In place of materials based on polymers, Li et al. (2019) created cooled wood with a superior mechanical strength (404.3 MPa) that may be utilized as building material. The materials can be continuously cooled below room temperature during the day and night by using cellulose nanofibres in the cooling woods to backscatter solar radiation and emit strongly mild-infrared wavelengths. A model that used cooling wood as the roof in different residential areas demonstrated that 20–60% of energy could be saved by using a cooling roof. Remarkably, three types of radiative cooling systems—air-based, water-based, and hybrid systems—are recognized.

(a) Systems that use air to transfer heat between the environment and the radiator are known as air-based cooling systems (Nwaigwe et al., 2012). The air is contained in the heat exchanger media. One benefit of air-based systems is that they are inexpensive and easy to set up. However, because these systems can only be used in detached homes, the top floor of duplexes, or multi-story buildings, their integration and implementation into buildings can be challenging. To reduce heat contact with air, the radiator needs to have air channels with a lot of surface area. One drawback of air-based systems is that it is not as effective and cannot be used in new ways.

(b) Similar to this, water-based systems cool buildings by using water as a heat-transfer fluid. Systems may be open or closed. An open water system functions by taking in heat from the interior and transferring it via radiation and evaporation to the nearby heat sink. A closed water-based system is made up of internal water-transporting pipes. There are fewer limitations and greater temperature control capabilities with this type of design. The contrast between achieving a lower outside temperature and pursuing a higher cooling performance

limits the technique application of the water-based system, which has a higher cooling power and better temperature control ability than the air-based system.

(c) Combining radiative cooling units with other energy-harvesting systems like radiative cooling and heat pump (RC-HP), radiative cooling and evaporative cooling (RC-EC), and radiative cooling and solar energy utilization (RC-SE), hybrid systems provide better cooling with higher power. The use of solar energy in conjunction with radiant cooling has garnered the most attention of all the combinations.

Tso et al. (2017) investigated the viability of using radiation for cooling in the hot and muggy climate of Hong Kong. In their work, they employed three distinct designs for passive radiative coolers. Three different designs were included: one with a single potassium chloride (KCl) IR-Pass window; one with seven KCl IR-Pass windows; and one without a vacuum. Figure 2.27 shows the schematic diagram and drawing of the passive radiative cooler inside the vacuum chamber. The coolers were tested in a variety of sky conditions, including clear, cloudy, and partly cloudy, as well as during day and night operations. The temperature differential between the ambient air and the radiative cooler served as the primary basis for their investigation. The experiment's findings demonstrated that, although the ambient air temperature was lowered by roughly 6-7^{o}C at night thanks to the passive radiative cooler with seven KCl windows and the cooler design without vacuum, the coolers were unable to generate a cooling effect during the day under any of Hong Kong's meteorological conditions. When the passive radiative cooler was used during the day with a single KCl window, the same outcomes were observed. Nonetheless, under a clear night sky, the passive

radiative cooler design's cooling capacity of 38 W/m2 was attained without a vacuum.

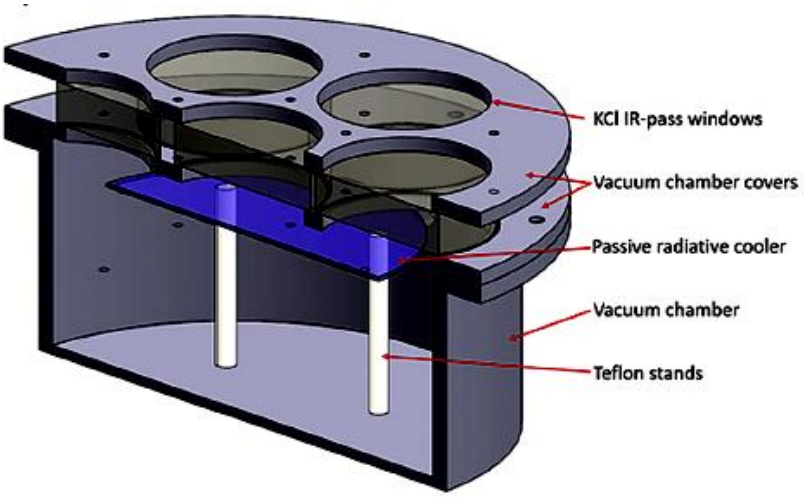

Fig. 2.27: schematic diagram and drawing of the passive radiative cooler inside the vacuum chamber (Tso, et al, 2017)

In order to achieve radiative cooling while simultaneously selectively utilizing the sunlight, Li et al. (2017) proposed a comprehensive photonic approach for solar cell cooling. They did this by experimentally characterizing the thermal radiation and solar absorption properties of silicon solar cells. Figure 2.28 depicts their designed photonic cooler, which is composed of a one-dimensional photonic film with n sub-layers of Al2O3/SiN/TiO2/SiN and a single layer each of SiN, SiO2, TiO2, and Al2O2. This film can radiate heat strongly and significantly reflect the solar spectrum. They suggested that the cooler can be integrated into an existing solar panel to efficiently cool the cell temperature, achieving a temperature reduction of about 5.7^{o}C.

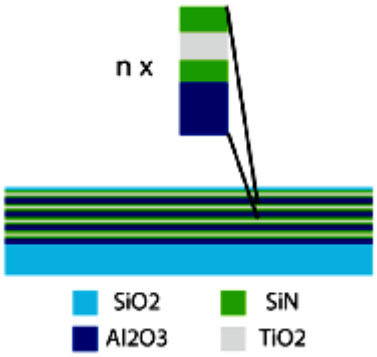

Fig 2.28: Schematic of a photonic cooler made of a multilayer dielectric stack, with n-sublayers (Li, el al, 2017)

According to spectral selectivity characteristics, Zhao et al. (2017) proposed a building-integrated PV–RC system (BIPV–RC) that uses nocturnal RC to achieve space cooling and diurnal PV conversion to generate electricity. In order to reduce the payback period, this system can also reduce the initial investment and installation areas in the building architecture. After demonstrating the perfect spectral selectivity of the selective plate and examining the BIPV–RC system's performance using a quasi-steady-state mathematical model, they contrasted the suggested system's performance with that of the traditional BIPV system. The system's effectiveness in PV conversion and RC was demonstrated by the results, which showed an annual electricity production of 156.74 kW h m−2 and a cooling energy gain of 579.91 MJ m−2. Once more, in comparison to the BIPV system, the electrical efficiency of the BIPV-RC system decreases more quickly as solar radiation rises. Their suggested BIPV-RC system, depicted in figure 2.29, has the potential to provide a total annual energy gain of 96.96% more than the BIPV system, allowing for nighttime space cooling. It was also found that the BIPV-RC system's performance was impacted by the inlet air temperature, wind speed, air mass flow rate, amount of precipitable water vapor, and insulator thickness. Therefore, since low water vapour correlates with a high nocturnal RC power, it has been established that a dry climate is ideal for this system's nocturnal RC.

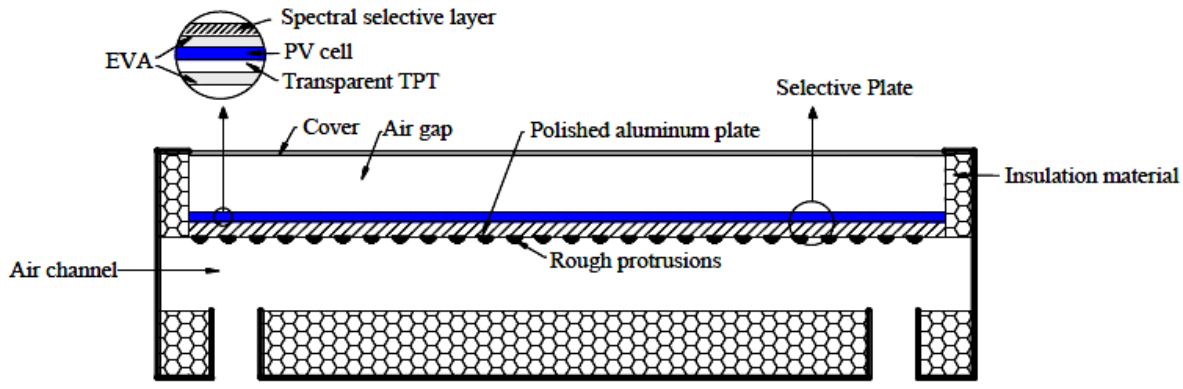

Fig 2.29: Cross section of the BIPV–RC module (Zhao, et al, 2017)

To restore cooling performance in a humid, subtropical environment, Ross et al. (2018) proposed integrating a radiative cooler with an asymmetric electromagnetic transmission window that permits outgoing radiative transmission and radiation at the same wavelengths. In their work, they explored the transmission, reflection, and absorption/emittance using finite difference time domain properties of the device, and they also discussed the working principle of asymmetric electromagnetic transmission (AEMT) enhanced radiative cooler quantitatively. First, they developed a theoretical model based on energy conservation to predict the radiative cooling power and steady-state temperature. They stated that an array of planar microstructures, such as corrugated metal surfaces, could be used to achieve asymmetric transmission, as demonstrated in different frequency regimes. As a result, they only offered one radiative cooling plan, and the ultra-broadband AEMT device serves as both an inspiration for numerous innovative engineering systems and a crucial passive daytime radiative cooler. A schematic diagram of the cooler with the AEMT window is shown in Fig. 2.30.

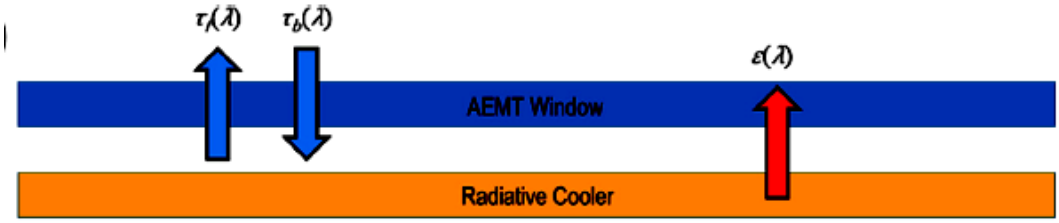

Fig 2.30: Schematic diagram of the AEMT cooler (Ross et al, 2018)

The peak cooling demand during the day cannot be satisfied by nocturnal radiative cooling, which depends on a clear night sky. The cooler is exposed to direct sunlight during the day, unlike at night. The inside air temperature rises above the outside air temperature due to the incapacity to reflect massive amounts of solar radiation (Jeong et al, 2018). The widespread use of passive cooling technologies in buildings has been limited due to these shortcomings. On the other hand, daytime radiative cooling does not experience the aforementioned flaws because it produces strong radiative power and a high level of sunlight reflection.

Maintaining a temperature below ambient is made feasible by this cooling scheme. Daytime passive cooling would be an interesting passive cooling strategy that, in the near future, will advance the design of energy and HVAC systems for smart green buildings due to its cooling efficacy in direct sunlight. Even though passive radiative cooling during the day can produce below-ambient temperatures in direct sunlight without the need for energy, its use in space cooling to reduce energy consumption is still not well understood.

By reflecting solar radiation and sending thermal radiation into the cold universe through an atmospheric window located between 8 and 13 μm in the electromagnetic spectrum, surfaces could be cooled below the ambient temperature when exposed to direct sunlight.

However, the sky emissivity can be raised significantly by both humidity and cloud coverage, hence, intensifying thermal emission within the 8–13μm spectrum (Wong et al, 2018). To recover the cooling performance in a humid climate, they recommended integrating the cooler with an asymmetric electromagnetic transmission (AEMT) window, which allows outgoing radiative transmission but reflects incoming radiation of the same wavelengths. Their objectives were to present a workable design of an AEMT device for radiative cooling applications and to quantitatively discuss the operation of an AEMT enhanced radiative cooler.

Santamouris and Feng (2018) presented and analyzed the main recent achievements that have taken place in daytime radiative cooling technologies. They emphasized that previous studies on radiative cooling had demonstrated a very small failure rate in the daytime compared to the success rate observed at night. Their primary goal was to showcase the latest developments in the field of radiative cooling during the day. As a result, they concentrated on the different surface technologies that have been developed, as well as their benefits, drawbacks, and possibilities for cooling built environments. The optical properties and characteristics, as well as the thermal performance, were analyzed and categorized into four

major technological clusters. These clusters included paints for radiative cooling, polymers for radiative cooling, multi-layer planar photonic structures, and meta-materials. Their results clearly showed that polyethylene has transmittance in the 8–13μ transparency window. Also, it was discovered that the use of vacuum technologies resulted in a giant drop of surface temperature below ambient air temperature.

In a 2018 numerical study, Jeong et al. combined a daytime passive radiative cooler with a traditional refrigeration cycle to create a novel method of space cooling in buildings. The integration of a daytime passive radiative cooler (DPRC) with a conventional refrigeration cycle in a one-loop system, as depicted in Figure 2.31, possesses a novel feature that enhances energy efficiency while significantly simplifying prior proposals.

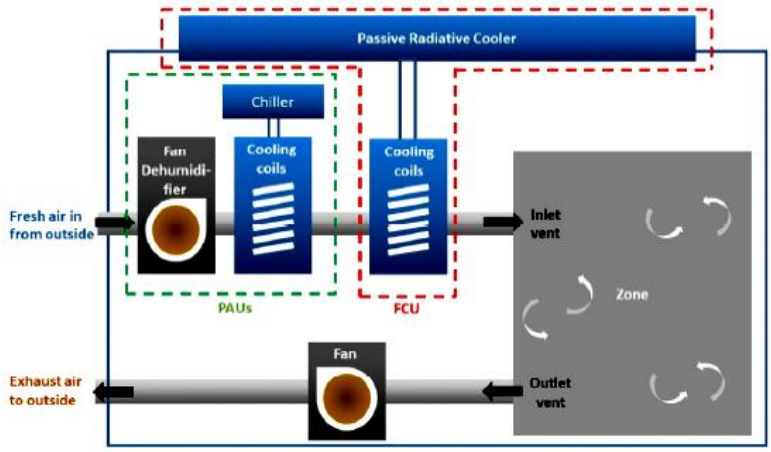

Fig 2.31: schemetic diagram of the radiative cooling panel intergrated with AVAC system (Jeong, et al, 2018)

Focus has been placed on the potential of using daytime passive radiative cooling as a solution to renewable energy in order to save energy required in cooling buildings. In their study, the most effective and simplified indoor cooling system with a daytime passive radiative cooler, was established, along with a new cooling performance analysis tool that can be used to estimate the indoor air temperature reduction and the cooling load. They investigated the effects of the following factors on the cooling performance of the daytime passive radiative cooler integrated HVAC system: the temperature of the supplied air to the

fan coil unit (FCU), the internal heat load, the exposed surface area of the passive radiative cooler, the thermal conductance of the channel, the volumetric flow rate of water and air, and the heat transfer coefficient of parasitic heat gain in their simulation.

Using spectrally selective surfaces for air conditioning and refrigeration systems, Bergman (2018) predicted the cooling performance of these surfaces in a passive operating mode and developed a novel concept of daytime radiative cooling using a system-level model. According to their predictions, existing refrigeration and air conditioning systems that functioned in the ADRC mode could be integrated with the suggested selective surface for PDRC, just like other surfaces. Among other potential benefits, they found that: the PDRC provided a lower cooling rate than the ADRC under the same cooling surface cooling; the ADRC's cooling rates are relatively unaffected by the temperature of the volume to be cooled; the PDRC needs a large surface area to meet a specific cooling load; the heat transfer from the warm, prevalent environment to the selective surface negatively affects the cooling capacity and thus necessitates insulating the surface from heat gains due to convection and conduction; the ADRC may lower global temperatures by increasing the amount of heat loss from Earth to deep space, thereby positively affecting the earth's energy balance.

In order to achieve sub-ambient cooling during the day, Bhatia et al. (2018) experimentally demonstrated a novel directional approach to passive radiative cooling using a straightforward, low-cost method. They proved that for emitters that are both reflective and absorptive in the solar spectrum, significant cooling below ambient temperatures can be achieved during the day. Their measurement, which was conducted at about midday, revealed a maximum cooling power of 45W/m2 and a temperature drop of 6^{o}C below the surrounding air. For simplicity and ease of use, they used easily accessible, reasonably priced materials such as polished aluminum, white polyethylene sheet, and commercial paint. A CAD drawing of the proof-of-concept demonstration is shown in figure 2.32.

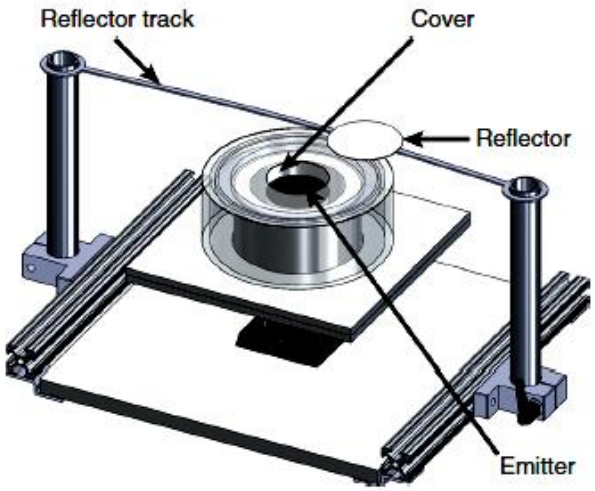

Fig 2.32: CAD drawing of the proof-of-concept demonstration (Bhatia, et al, 2018)

Lee, et al (2018) presented a photonic approach for fabricating a coloured daytime passive radiative cooler (CDPRC) for aesthetic purpose and is as shown in figure 2.33. They did this by encasing a metal-insulator-metal (MIM) subtractive cooler film beneath a Si3N4-based selective emitter (SE) layer. During testing in direct sunlight during the day, a multicolored CPRC with a silvery background to improve net cooling efficiency was shown to have exceptional sub-ambient cooling performance. They found that the scheme can be compared to small modern electronics where the flexible radiative cooling material could lower the device's surface temperature and thereby increase the device's battery efficiency by depositing the MIM and SE structure on a flexible foil. The result obtained from the theoretical and systematic experiments proved the feasibility of sub-ambient cooling through their system as it lowered the temperature to 3.9^{o}C below ambient air in the daylight.

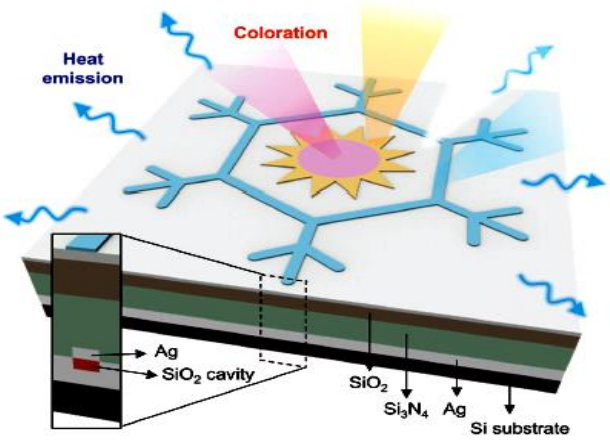

Fig. 2.33: Schematics a coloured passive radiative cooler (Lee, et al, 2018)

In order to generate electricity and cooling energy during the day, Zhao et al. (2018) proposed a hybrid PV/RC system. They also presented a comprehensive photonic approach for the selective plate, which involves placing a photonic structure on top of a monocrystalline silicon solar cell. As seen in figure 2.34, the intended photonic structure was made up of a 2D photonic crystal and a 1D multilayer stack. Its dual purposes were to decrease the selective plate's needless solar absorption and improve the RC process at the same time. The performance of the planned photonic structure on the nocturnal RC processes and diurnal PV conversion was then examined through a simulation.

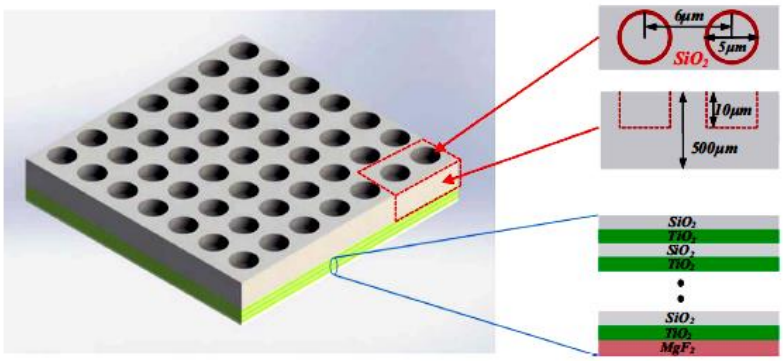

Fig. 2.34: Schematics of the photonic structure (Zhao, et al, 2018)

It was the objective for the photonic structure to meet several spectral requirements: it needed to maximize transmittance in the PV band (0.3–1.1 μm) to guarantee PV conversion of monocrystalline silicon solar cells; it needed to have high reflectivity in the vain band (1.1–

4.0 μm) to reflect part of the solar irradiance that cannot be converted to electricity, lowering the temperature of the solar cell; and, lastly, it needed to have high emissivity in the 4.0–25μm (or RC band) to maximize the RC process. Results demonstrated that this photonic structure has the enticing potential for the PV/RC hybrid system. It can not only effectively lower the cell operating temperature in the diurnal PV conversion, but it can also show a large net RC power in the nocturnal RC process. Additionally, they obtained more cooling energy from the suggested selective plate than from the current RC emitters.

Zhao, et al (2019c) carried out a study on radiative sky cooling in which they reviewed the fundamental principles, the recent advances made so far, the materials for radiative cooling, and the potential applications. In order to attain a net cooling effect during the day when exposed to direct sunlight, a radiative cooling material needs to reflect over 95% of the solar radiation. They also found that the effectiveness of radiative sky cooling was significantly impacted by local metrological conditions. These meteorological factors, which can have a negative impact on the system's efficiency, include humidity, sky clarity, wind speed locally, and unstable weather. They came to the conclusion that passive radiative sky cooling is currently the most promising approach to system integration because of its low maintenance requirements, low cost, and simplicity of the system. It is also expected to play a significant role in reducing building energy consumption, combating global warming, and resolving water and environmental issues.

Zhu, et al (2019) experimentally and theoretically demonstrated an improved thin film multilayer radiative emitter with high solar reflectance that can reduce remarkably the absorption of solar radiation in the ultraviolet region. Their design was tested on a six-story building's flat roof. It consisted of five layers: a 200-nm thick MgF2, a 36-nm thick TiO2, a 100-nm thick PDMS film coating on top of a 4-inch fused 500μm thick silica wafer, respectively, and a 120-nm thick Ag film on the back. The schematic of the multilayer thin

film structure is illustrated in figure 2.35. It was also shown that the addition of MgF2 and TiO2 thin film layers was responsible for the noticeable increase in solar reflectance in the ultraviolet spectrum, which enhanced the emitter's cooling capabilities. Hence, they showed that efficient daytime radiative cooling using macroscopically planar multilayer thin film emitter was feasible as indicated by the temperature reduction of 12.6^{o}C that was achieved.

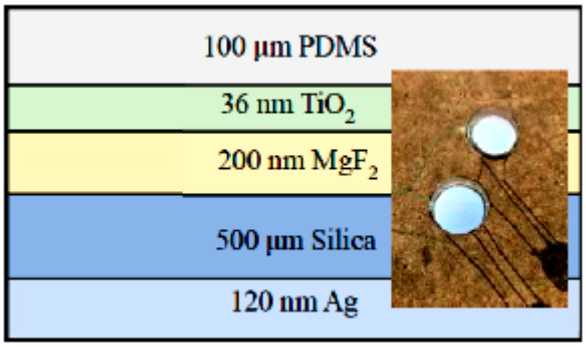

Fig 2.35: Schematic of multilayer thin film structure (Zhu, et al 2019)

Liu et al. (2019) examined the use of passive radiative cooling in greenhouses—artificial structures that protect crops from inclement weather. This harsh weather is caused by solar radiation (having UV, 100-400µm; VIS, 400-780nm, and NIR, 750-2500nm), which penetrates the greenhouse through the cladding to enable crops to grow. They noted that the greenhouse effect is exacerbated by extremely high temperatures, which make it difficult for people to work in greenhouses and make it difficult for plants to grow there. They integrated radiative cooling with greenhouse covering materials to reduce CO2 emissions, save energy, and control greenhouse temperature. Instead of employing complicated composition, they created the new greenhouse covering by combining non-metal oxide particles with a polyethylene matrix (made of polyethylene and hindered amine light stabilizers). To stop the film from aging too quickly, a light stabilizer was incorporated into their design. The result they obtained showed that under the environmental condition of 35^{o}C, a 2.2^{o}C temperature reduction of the simulated greenhouse with PE with added nonmetal oxide particles (PE@

1.0S) from that of the PE cladding and a 28W/m^2 net cooling power of the green house film developed was as a result of passive radiative cooling.

A polymethylpentane (TPX) thin film embedded with a silicon infrared emitting layer is the basis of the bi-layer selective emitter that Liu et al. (2019b) designed and created. On a silicon sheet, a 600 nm Ag was applied as the solar reflecting layer beneath the selective emitter layer. Figure 2.36 shows the schematic of the bi-layer selective emitter. After conducting a theoretical analysis of the samples' theoretical cooling performance, they found that, in a relatively dry ambient air, the samples' theoretical cooling performance during the day was 25.5oC below ambient air temperature under direct sunlight (AM1.5) and 60% relative humidity. Also, at nighttime, this bi-layer selective emitter provided a cooling performance of 36.7^{o}C below ambient temperature. From the result, they, to the best of their knowledge, proved that the cooling performance of the bi-layer emitter was better than the other published selective emitters. This excellent cooling performance of this emitter and its low cost presents it with great potential for practical purpose.

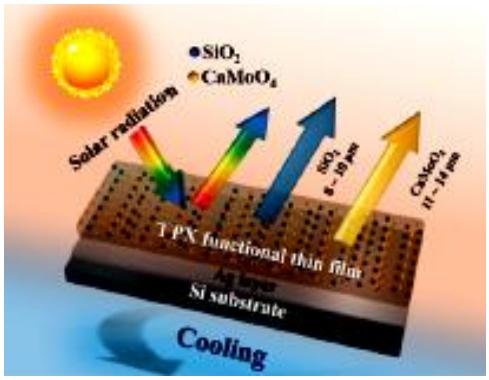

Fig 2.36: Schematic drawing of the bi-layer selective emitter (Liu, et al, 2019b)

Zhao, et al (2019d) proposed a general strategy to change the relative position between the radiative cooler and the sun so as to reduce the amount of solar radiation that reaches the coolers. The coolers being positioned against the sun (solar radiation) is a major feature of this proposed strategy. They used two identical coolers as illustrated in figure 2.37, one fixed against the sun and the other facing the sun directly.

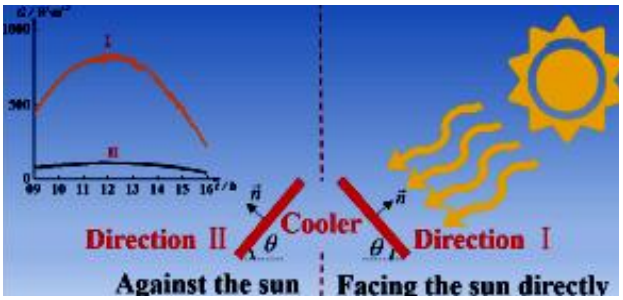

Fig 2.37: Schematic diagram of the strategy radiative cooler (Zhao, et al, 2019)

The average temperature drop below ambient for coolers A and B, positioned with their backs to the sun, was 7.4 ^{o}C and 3.2 ^{o}C, respectively, according to the results. Thus, with the cooler positioned against the sun, sub-ambient radiative cooling during the day is more likely to be accomplished.

Gao et al. (2019) designed a photonic crystal structure on a UV-curable adhesive (UVA) by using the ultraviolet (UV) nanoimprint method. Based on these optical constants and appropriately constructed photonic crystal structures, they simulated emittance in the 8–13 μm wavelength range, which resulted in the UVA exhibiting an emittance of 95% at an emissive angle of 70°. Since an Ag layer backs the photonic crystal structures on a UV-curable adhesive (PCSUVA)-based substrate, the cooler depicted in Figure 2.38 may be used to reflect solar light. They looked at the optical constants of a UVA, and the findings showed that the UVA could be considered a near-thermal blackbody within the atmospheric window (8–13 μm). Due to the Ag layer's ability to reflect sunlight and the PCSUVA's high emittance within the 8–13 μm wavelength range, it was discovered that the PCSUVA-PET-Ag combination could lower the temperature of the silicon wafer underneath by 7.7 ± 0.2 °C on a summer day. Because of its affordability, the suggested method might be a good option for a large-area, flexible, inexpensive, and angle-independent radiative cooler.

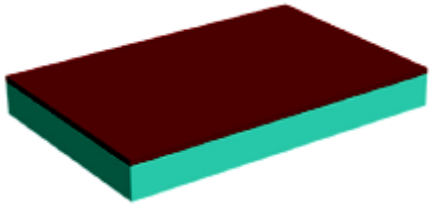

Fig 2.38: Schematic of fabrication of PCSUVA (Gao, et al 2019)

Han, et al, (2020) carried out a preliminary study of passive radiatve cooling under singapore's tropical climate as its latitude is very near to the equator. The study examined the impact of local solar radiation and humidity on the efficiency of radiative coolers during the day and at night, respectively, using both theoretical simulations and experimental data. It was discovered that the two main factors influencing daytime cooling performance were humidity and regional solar irradiance. Through a series of experimental investigations, the steady-stat temperatures of two radiative coolers and two reference aluminum (Al) plates were measured in three distinct weather conditions (sunny, partly cloudy, and cloudy skies) in Singapore. The results showed that the two radiative coolers' daytime cooling performance was not achievable due to high solar radiation and humidity. On the other hand, enhanced specular reflector (ESR) film with higher solar radiation reflectivity can be used to create sub-ambient temperatures on cloudy days. They were able to establish a steady- stat temperature 3.5^{o}C lower than the ambient for the photonic device and that of 5^{o}C for the ESR film. Figure 2.39 shows the cross-section schematic of the apparatus.

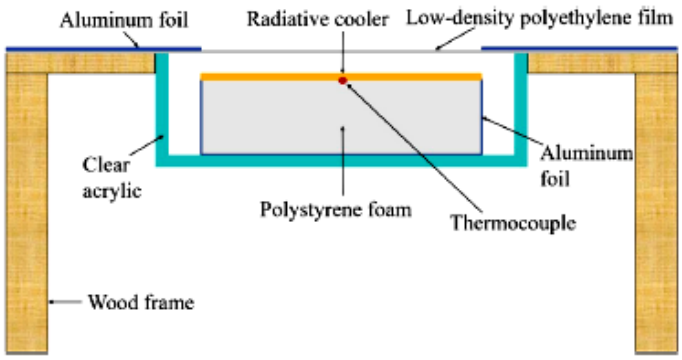

Fig 2.39: A cross-section schematic of the apparatus (Han, et al, 2020)

Jeong, et al (2020b) designed a high performing but cheap daytime radiative cooler with alternating TiO_2 and SiO_2 sub-layers for sub-tropical climates. In the study, they conducted analysis of optical property for optimization on different parameters such as volume fraction between TiO_2 and SiO_2 layers, thickness of each layer and number of layers in order to achieve the highest radiative net cooling power. A computational study was carried out in both a humid sub-tropical climate and a clear transparent sky to determine the temperature and net radiative cooling of their optimized TiO_2-SiO_2 multi-layered radiative cooler. Finally, field research conducted in the humid climate of Hong Kong was used to validate their simulated results. The study also revealed that because of the high humidity (H_2O concentration) and low transparency of the atmosphere, neither TiO_2 nor HfO2-based passive radiative cooler demonstrated any cooling effect. Their TiO_2- SiO_2 multi-layered daytime passive radiative cooler shown in figure 2.40 achieved an enhanced net cooling effect of 136.3w/m^2 which exceeds the highest reported net cooling power of 127W/m^2, generated by a PDMS polymer based radiative cooler. In a sub-tropical climate, they were able to demonstrate a temperature reduction of 7.2^{o}C below the ambient air temperature and a net cooling power of 14.3W/m^2 for the TiO_2-SiO_2 photonic daytime radiative cooler by externally shading the coolers (HfO_2-SiO_2 and TiO_2-SiO_2) to reflect the majority of the incident solar energy.

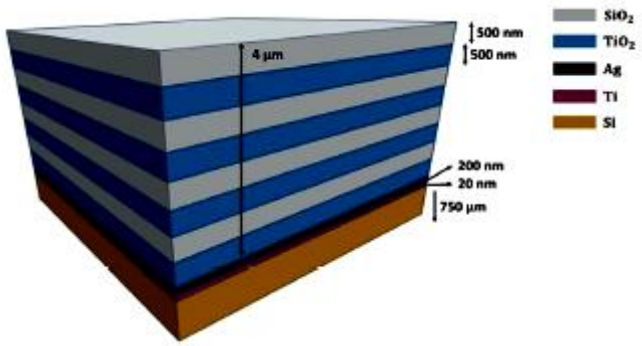

Fig 2.40: Schematic diagram of optimized multi-layered TiO_2-SiO_2 alternating radiative cooler Jeong, et al (2020).

A passive radiative cooler inspired by biotechnology was proposed by Jeong et al. (2020). It features PDMS and SiO2 mid-infrared (MIR) emissive layers on top that can radiate strongly in the 8–13 μm spectrum, and a bottom Ag solar reflective layer that can provide solar reflection above 95%. Using polydimethylsiloxane, which has a very high emittance in the 8–13μm spectrum, and the thermoregulatory prismatic structure of Saharan silver ants, a geometrically modified polymer-based daytime radiative cooler was created. The optimization was centered on attaining the maximum emissivity within the intended MIR range (8–13μm), as emissivity plays a significant role in net radiative cooling efficiency. The PDMS material property, which is flexible and can be shaped into desired geometries on the surface during fabrication through a nano-imprinting process, is what gives the radiative cooler its advantage over other materials. SiO2 substrate wafers are readily available. This enormous flexibility in PDMS shaping provides the chance to research how to improve optical characteristics, particularly emissivity in various configurations. The greatest numerical cooling power of 144w/m^2 is presented by a bio-inspired radiative cooler, according to the results. However, because of unfavorable sky conditions and low atmospheric transparency, the field investigation only revealed a net cooling power of 19.7W/m^2 and a temperature drop of 6.2^{o}C below ambient under direct sunlight. It showed that the coolers cooling performance deteriorated significantly in high humid weather condition but can be successively enhanced by minimizing incoming solar irradiance.

Wang et al. (2020) developed, improved, and built a radiatively cooled high-concentration photovoltaic system. In a paper they presented, they examined the radiactive cooling performance of concentrating photovoltaics (CPV) in three distinct cooling structures using lightweight, passive radiative cooling to improve CPV. These investigations were conducted with varying wind speeds and solar heat loads. They also carried out a number of outdoor experiments in both the best and worst environmental circumstances to assess the overall

effectiveness of radiative cooling. Depending on the working conditions, their experiment showed that radiative cooling can bring about 25% to 62% of the overall cooling power of a CPV system that has a flat plate heat sink without extra power consumption even with the added high weight. The results showed an average load of 5 to 6W on the solar cell, a temperature drop of Gasb cell at stead state of 5ºC-36ºC for worst and best scenarios respectively. Consequently, the large temperature drop of 36ºC and cooling power of 140W/m^2 was achieved through the experiment, which resulted in an 8% to 27% relative increase in the open-circuit voltage of their Gasb PV cell, which approximates to 28 to 75MV. Additionally, the temperature drop suggested that different kinds of solar cells could have longer lifetimes, which could lead to their application in additional CPV systems. They came to the conclusion that the CPV radiative cooling system's performance can vary greatly depending on the choice of cooling design and working environment. They quantitatively modeled the system's cooling performance using an opto-thermal simulation, and the results closely matched the experimental data. Three distinct cooling designs—a flat plate heat sink in an open chamber, an open chamber with fins, and a sealed chamber heat sink—were examined and quantitatively analyzed. A configuration of the experimental test rig with the cooler exposed to the sky is shown in Figure 2.41.

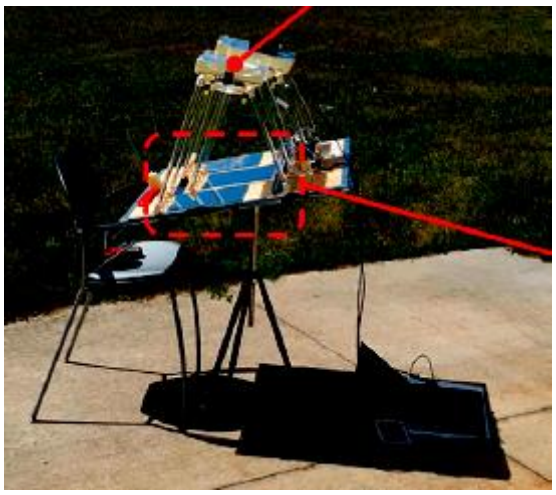

Fig 2.41: A Test rig of the experimental setup showing the cooler exposed to the sky (Wang, et al, 2020).

In 2020, Suhendri and colleagues conducted a review on the application of passive radiative cooling (RC) technology in buildings. The review comprised a wide range of topics, including the need for passive cooling in buildings and the global energy demand for cooling; the challenges associated with radiative cooling (technical and financial issues, geographical issues, etc.); the need for buildings to be kept cool during the day for building occupants; and, lastly, the improvement strategies for the application of RC technology in buildings. The improvement strategies they presented, for both nocturnal and diurnal conditions, covered emitter material, cover material, design, and combination improvement. According to their review, the development of new materials has revitalized the field of RC research and experimentation and led to the development of numerous high-performance RC materials. Research on coloured and transparent RC materials could widen the application of RC in buildings besides providing scalable and durable RC materials. The schematic of the typical radiative cooling (RC) panel design and heat transfer on the panel as illustrated by Suhendri et al (2020) is shown in figure 2.42. They showed that available materials have been implemented in various RC module designs and that a continued emphasis on combination of RC with other passive design strategies should be pursued. It should be noted that the effort to apply RC in buildings need to be integrated more into the architectural design of a real-life building, either existing or newly constructed.

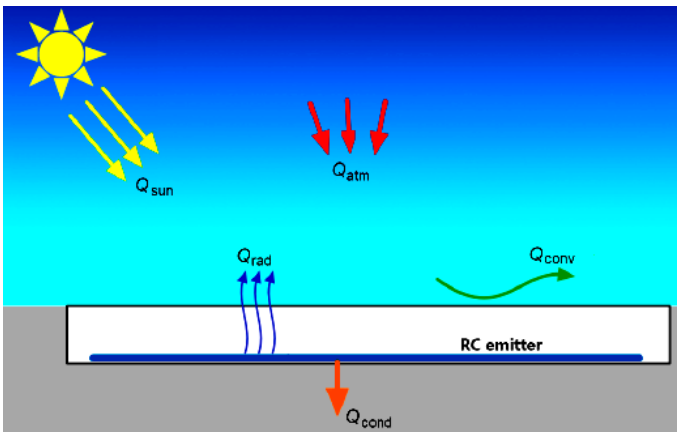

Fig 2.42: Typical radiative cooling (RC) panel design and heat transfer on the panel Suhendri, et al (2020)

Albergini et al (2020) designed, constructed and tested experimentally, a passive cooling device that could serve as an alternative technique for use in high humid or dusty environmental condition. The main idea underlying the concept is to develop a net cooling load that is generated by a salinity disparity between two aqueous solution of distilled water and brine, which can only exchange water vapour when only separated by a hydrophilic micro porous membrane. The proposed cooling system uses capillarity and gravity in its multistage, passive cooling process that is driven by a salinity difference. It is capable of storing cooling capacity intrinsically through a salinity difference. As a result, they can adapt to varying solar energy availability based on time and fluctuating cooling demands. The result showed a maximum cooling capacity of approximately 60W/m^2 and 100W/m^2 when extrapolated at varnishing temperature when 3.1mol/kg solution of aqueous NaCl salt was used. When an aqueous solution of $CaCl_2$ salt was used, a maximum cooling capacity of approximately 110W/m^2 and 170W/m^2 at varnishing temperatures. Finally, they were able to forecast the passive cooler's performance across a larger range of operating conditions by using the validated model.

Through a computational analysis that demonstrated the diurnal cooling effectiveness of a network of silica (SiO_2) fibres by reflecting sunlight via backscattering and emitting infrared thermal radiation, Yalcin et al. (2020) offer a novel strategy for midday radiative cooling based on a network of silica fibers. Utilizing this network would do away with the requirement for a binder, just as spheres that allow fibers to be suspended in midair do. Because silica fibers are widely produced for many common applications, they are a great option for radiative cooling applications during the day. Compared to other studies, they showed that silica fiber networks have one of the highest net radiative cooling values, at 178 W/m^2, and can serve as a coating that is nearly ideal for radiative cooling applications. Additionally, it was demonstrated that the almost isotropic directional emittance at the sky

window for coatings without a binder makes the avoidance of binder necessary to enhance scattering and avoid internal surface reflection between the coating and air.

Since the development of cooling technology was hampered by the high cost and subpar performance of serious RC materials, Liu et al. (2020) developed a simple and inexpensive RC material (clear epoxy resin (CER)) to attain daytime cooling performance. The weighted solar reflectivity and infrared emissivity within the atmospheric transparency window were found to be 93% and 92%, respectively, according to investigations of the spectral profile. Moreover, the suggested RC material can reach sub-ambient cooling performance even in hot and humid environments. With a maximum temperature decrease (MTD) of around 2.75°C on average during the day from 10:00 am to 2:00 pm and 8.1°C on average at night. The PE wind cover and back-to-sun tilt technique significantly improved the RC performance.

Wang, et al (2021) reported a hierarchically porous array of poly methyl methacrylate ($PMMA_{PHA}$) film that has an array of micropores on the surface that are closely packed together with abundant random monopore inside, for a highly efficient all day and nighttime passive radiative cooling. Their demonstration with the $PMMA_{-PHA}$ film is because of their sufficiently high solar reflectance of about 0.05 and excellent thermal emittance of 0.98 of long wave infrared radiation. They fabricated the $PMMA_{-PHA}$ by placing 5nm monodisperse SiO_2 microspheres on top of a glass sheet coated with a polydimethylsiloxane (PDMS) film and then rubbed with another PDMS substrate. They did not only discover a sub-ambient cooling of 8.2^{o}C in the night, 6.0^{o}C to 8.9^{o}C during the mid-day and under solar intensity of 900w/m^2, an average cooling power of 85w/m^2 , but also a sub-ambient temperature of 5.5^{o}C even under solar intensity of 930W/m^2 and relative humidity of 64% in hot and moist subtropical climate. Fig 2.43 shows a schematic illustration of the fabrication of $PMMA_{-HPA}$ with a hierarchically porous array.

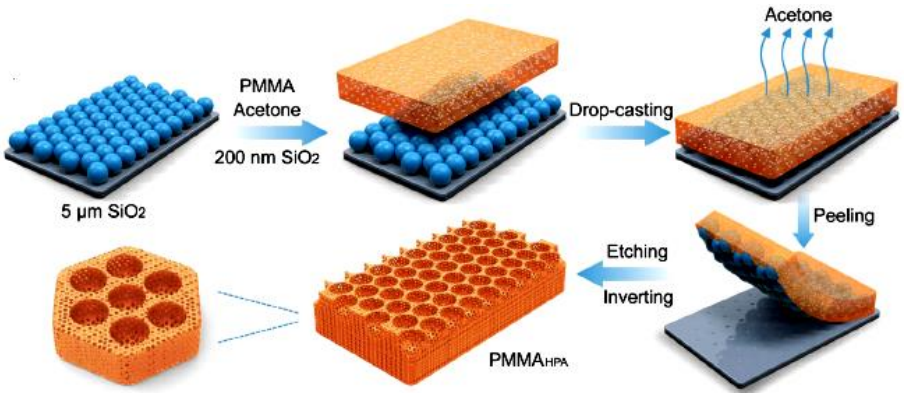

Fig 2.43: Schematic illustration of the fabrication of PMMA-HPA (Wang, et al, 2021)

Zhou et al. (2021) conducted experiments both indoors and outdoors to illustrate a double-sided architecture that uses solar spectrally reflecting mirrors made of metal to reroute thermal emission from an emitter that is aligned or arranged vertically, resulting in concentrated radiative cooling. As seen in Fig. 2.44, they built the absorption film on a glass substrate using ten stacked layers of co-sputtered Ag-SiO2 nano-composite films.

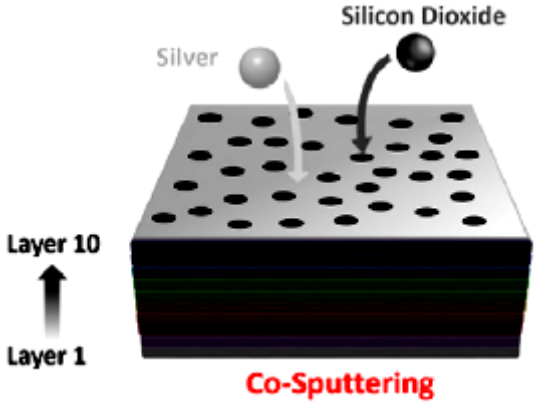

Fig 2.44: schematic of the carmet-based solar spectal selector (Zhou, et al, 2021)

In addition to functioning as a solar absorber, the solar selector here functioned as a thermal radiaton wave guide /mirror. The result obtained showed a very high local cooling power density of 273.3W/m^2 within the laboratory, which is double the previously reported cooling power density of single sky-facing surface. Also, temperature reduction of 14^{o}c and over 12^{o}C below ambient temperature in the laboratory and outdoor environment respectively were reported under standard atmospheric pressure. Their system as shown in figure 2.30 was able to absorb solar light efficiently and at the same strongly reflect thermal radiation from

the emitter. The v-shape configuration of the mirror helped to achieve two major benefits which are: absorption of incident solar energy on the two solar absorption mirrors and allowing additional solar heating effect without extra surface area and low equilibrium temperature as a result of double local cooling power density of the thermal emitter. Out of the over 80h of outdoor experiment they performed on selected sunny days in 2010 and 2020, it was discovered the relative humidity, wind speed and cloud cover effect the overall cooling performance.

Wang et al. (2021b) used a solvent exchange process to create a superhydrophobic DPRC composite film of ethylene-propylene-diene copolymer (EPDM) and SiO2 particles (EPDM/SiO2). They did this because they knew that in outdoor applications, water wetting and dust formation would affect the cooling performance of DPRC materials over time, resulting in lower reflectance and increased absorption of solar light. For practical applications, it is imperative to endow radiative cooling materials with superhydrophobic properties to prevent the cooling materials from getting wet by rain or discolored by dust. The film's solar reflectance reached 96% because of the effective light scattering caused by the porous structures and SiO2, and its emissivity reached 95% because of the SiO2 photon-polarization resonances in the atmospheric transparency window. According to the findings, the film was capable of achieving a sub-ambient temperature reduction of 12°C in sealed air and 7°C in the open air during bright sunlight. Because of its superhydrophobic self-cleaning ability, the film is shielded from contamination, preserving its cooling capacity for prolonged outdoor applications.

Daytime passive radiative cooling (DPRC), according to Chen et al. (2021), improves the release of heat to the cold environment without requiring any energy input or creating pollution, thereby reducing the effects of the energy crisis in tropical and subtropical climates and global warming. The strategies for obtaining PDRC that have previously been put into

practice were compiled, along with a number of PDRC technology implementations. Previous assessments, it has been noted, gave little attention to the sub-band spectrum designs from the solar spectrum (including coloured coatings) and LWIR spectrum (selected or angle-dependent coatings), as well as their dynamic switchable spectrum depending on the solar spectrum. They outlined the material and structural designs to improve thermal LWIR emittance and solar reflectance, went over the foundations of PDRC, and discussed the dynamic switchable regulations of cooling coatings from the solar spectrum or LWIR spectrum. Ultimately, a variety of PDRC applications were examined, including power generation, water harvesting from the atmosphere, cooling of solar cells, and cooling of space. For practical applications, additional characteristics of the radiative cooling system, such as cost, toughness, and low energy density, should also be seriously taken into account. The heat transfer process on the radiative cooler is shown in Fig 2.45.

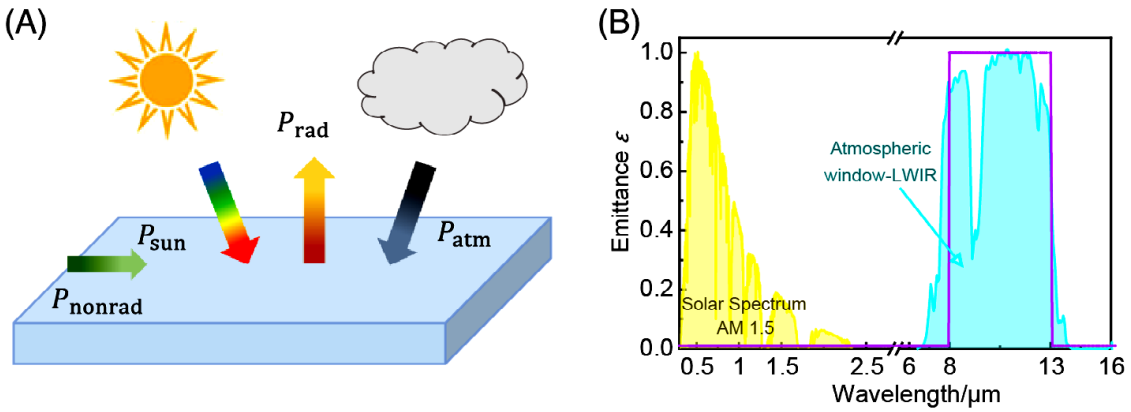

Fig 2.45: Schematic diagram and heat transfer processes of PDRC coatings (Chen et al, 2021)

Liu et al (2021) presented a Nano PE film, which was able to effectively scatter UV light in the solar band, increase solar reflectivity from 96% to 99%. They used Nano PE film with a thickness of 15μm to enhance the radiative cooling performance by reducing UV absorption. The experimental device was made of high-transparente polymethyl methacrylate (PMMA) and is shaped into a square box (30 cm by 30 cm by 4 cm). These thin nano PE films

outperform conventional PE films in terms of weather resistance and mechanical strength, and nano-PE films can scatter some visible light, reducing light pollution generation in practical applications. The experimental investigation performed in Tianjin, China's humid environments reveal that Nano-PE films can improve radiative cooling performance by 76% on a clear day and 120% on a cloudy day.

Lin et al (2021) developed a Solution-processed Inorganic Emitter with High Spectral Effectiveness for Efficient Daytime Radiative Cooling in Hot and Humid Climates. The strong solar reflection of 96% and high IR emission of 96.6% within an atmospheric window of device render the coating quite suitable for cooling radiatively in hot humid climates. By using spray coating or spinning coating during the fabrication process, a layer of Perhydropolysilazane (PHPS, 20 wt.%) was deposited onto a silicon or metal substrate coated with 20 nm of titanium and 120 nm of silver, with the thickness controlled by the concentration of PHPS and flow rate or rotational speed. The result of the experiment showed that a ttemperature drop of up to 5 °C below ambient air temperature was achievable in the subtropical coastal city of Hong Kong at noontime under high humidity, with the emitter directly exposed to the ambient.

Sun et al. (2022) examined recent advancements achieved in disordered media-based DPRC materials, with a focus on the selective management of the spectrum of disordered nanoparticles and disordered porous structures as well as their radiative cooling effects. Because of their randomly distributed dielectric particles, these structures are gradually emerging as one of the contenders for effective radiation heat dissipation and consequently DPRC. They have an advantage over metamaterials in that they have a much greater potential for mass production, popularisation, and application. In addition, their affordable, readily available raw materials, established technology, quick preparation, and effective cooling

effect make them materials to be sought after to offer solid support for space cooling. By adjusting the type and particle size of the disordered nanofillers, it is feasible to change both the spectrum of mid-infrared radiation and the spectrum of sunlight reflection separately. With materials exhibiting good cooling effects as a result of the development of DPRC technology, the viability of radiative cooling in direct sunlight was confirmed.

Yang et al (2022) presented an appealing thermal management technology on a "Geopolymer-based sub-ambient daytime radiative cooling coating" (SDRCC), which has significant potential for mitigating global warming and the urban heat island effect. They pointed out that the potential of sub-ambient daytime radiative cooling (SDRC) technology to cool the surface of an object below the ambient temperature under direct sunlight with zero energy consumption has garnered worldwide attention. Through the design of a surface in the sky transparent window that has a high solar reflectance as well as a high emittance (infrared atmospheric window), sub-ambient cooling can be achieved. Using a precursor material (metakaolin) and an alkali activator (AA) solution, the inorganic geopolymer-based daytime radiative cooling coating was made. The developed coating is environmentally friendly and can be formed and cured at room temperature. They found from the that the addition of $BaSO_4$ and nano-SiO_2 particles, as well as the hierarchical air pores formed in the Alkali Activator Geopolymer (AAGP) matrix, contributed to the AAGP coating's high sky window emissivity of 0.95 and 97.6% solar reflectance. Under direct sunlight, the optimized AAGP coating could achieve a sub-ambient cooling effect of up to 8.9 °C. The developed AAGP coating could maintain its performance even after mechanical wear and high temperature exposure, and it was waterproofed.

Luo and Zou (2022) researched UV-cured coatings for highly efficient passive all-day radiative cooling. Passive radiative cooling appears to be a promising way to reduce cooling energy consumption. It does, however, always necessitate stringent material designs or

manipulations that are neither cost-effective nor widely adaptable. The author presented a fast, low-cost, and scalable UV-curing method for producing porous polymer coatings via photopolymerization-induced phase separation. Using trimethylolpropane triacrylate (TMPTA) and vinyltriethoxysilane (VTES) as a formulation, the resulting poly (TMPTA-VTES) coating has a hierarchical pore structure, resulting in an excellent passive all-day radiative cooling capability.

2.6 Numerical Study of diurnal passive radiative cooling

The property of spectral thermal selectivity was tailored for two-dimensional (2-D) photonics to develop a metal-dielectric photonic structure capable of diurnal radiative cooling in outdoor conditions (Raphaeli et al., 2013). The multilayer structure of magnesium fluoride (MgF_2) and titanium dioxide (TiO_2) with a dielectric reflector deposited on silver (Ag) achieved a net cooling power of about 100W/m^2. The result of the structure shows a cooling persistence even in the presence of significant convective/conductive heat exchange and bad atmospheric conditions.

The use of symmetrical conical metamaterial (CMM) pillars in daytime radiative cooling where 2-D photonic crystals were used as selective emitters was theoretically investigated. The CMM pillar has a spectral emissivity value of 0.8-0.99 for different bottom diameters of the CMM pillars (Hossain et al., 2015). The optical properties of the aluminum substrate for the CMM structure can diminish any infrared transmission. The structures can achieve cooling of up to 12.2 °C and 9 °C below the ambient at night-time and during daytime operations respectively as well as a cooling power of 116.6W/m^2. A remarkably low temperature of 25 °C below the ambient during the daytime is feasible if non-radiative heat exchange is further reduced.

Subwavelength dielectric resonator metasurface can be considered efficient absorbers as they can support various resonance modes. Zou et al (2017) proposed a two-layer meta-surface to demonstrate diurnal cooling. The cooler was composed of n-type doped silicon resonators and silver. The experimental demonstration of the metasurface was enhanced by metal loading so as to obtain strong broadband thermal emission over a wide angle that spectrally matches the main IR atmospheric transparency window. They reported a minimum achievable temperature drop of 11.14 and 8.25K during the night-time and daytime operations at thermal equilibrium, respectively from the simulation-based analysis of the cooling ability. Also, the corresponding measurement-based analysis showed a minimum temperature drop of 10.29 and 7.36K during the nocturnal and diurnal hours respectively. The fabrication of the proposed dual-layer structure is simple and cost-effective compared to other reported multilayer metamaterial structures. Scalable fabrication that can be integrated with silicon photonics is feasible, making the design applicable to thermal emission control, and IR-sensing.

To achieve diurnal radiative cooling, Huang and Ruan (2017) developed a double-layer coating that comprised Titanium dioxide (TiO_2) with acrylic resin embedded and carbon black as the bottom layer for thermal emission. With the optimum particle size of 0.2μm for (TiO_2), over 90% of the solar radiation can be reflected and emitted, resulting in the predicted net cooling power of 100W/m^2. The result shows that the cooling effect was maintained though conduction and convection heat exchange could persist.

Also, a highly scalable nanoparticle with TiO_2 particles on top for solar reflection and SiC particles as the bottom layer for thermal emission was designed and recorded a theoretical temperature reduction of 5^oC below the ambient air temperature because of high solar reflectivity of over 90.7% and thermal emittance of 90.11% within the atmospheric

transparency window (Bao et al, 2017). To extend the milestone, low-cost random photonic silica spheres could potentially cool a black substrate to a temperature of $12^{o}C$ below the ambient under solar irradiation was developed by minimizing the photon transport mean path to alter the spectral absorption. Furthermore, a more complicated multilayer structure made of a dielectric micro-pyramid with nineteen (19) alternating aluminum oxide (Al_2O_3) and silica deposited on silver layers was proposed by Wu et al (2018). The result of their investigation showed that an enhanced net cooling power of $122W/m^2$ can be achieved.

Jeong et al (2018) carried out a numerical study of daytime passive radiative coolers for space cooling in buildings in which a new scheme integrated a daytime passive radiative cooler with a conventional refrigeration cycle. This system of integrating daytime passive radiative cooler (DPRC) with conventional refrigeration cycle in a one loop system has significant simplification of previous proposals and enhancing of energy efficiency as its novelty. In their study, the most efficient and simplified indoor cooling system with a daytime passive radiative cooler, new cooling performance analysis tool that can be employed to estimate the indoor air temperature reduction and the cooling load was established, hence, a focus on the potential of applying daytime passive radiative cooling a solution to renewable energy in order to save energy required in cooling in building application. In their simulation, heat transfer coefficient of parasitic heat gain, the exposed surface area of the passive radiative cooler, thermal conductance of the channel, the volumetric flow rate of water and air, the temperature of the supplied air to the fan coil unit (FCU) and the internal heat load were investigated to determine their influence on the cooling performance of the daytime passive radiative cooler integrated HVAC system.

Lee and Luo (2019) identified that, by the use of theoretical calculation, chemically stable and inexpensive polydimethylsiloxane (PDMS) can be a close-to-ideal thermal emitter for cooling flexible thin-film solar cells. They reported that the role of PDMS as a radiative

cooling substrate for solar cells has not been studied even though they can be used as encapsulating materials in some cases. In their demonstration, it was discovered that a 200nm-thick planar PDMS layer can achieve a high emissivity of over 0.9 for the mid-infrared (IR) regime of 4-26μm, but by adding a pyramid structure to the surface in the range of 8-13μm, where environment radiation is negligible, the emissivity can further increase to near-unity. Hence, they predicted that a pyramid-structured PDMS layer can significantly lower the temperature of an organic solar cell by 11^{o}C; and that of a perovskite and a micro-crystalline (μc)-Si flexible solar cell by 11 °C, 12 °C and 16 °C, respectively as compared to conventionally used polyethylene terephthalate (PET) substrate.

Liu, et al (2019b) designed and prepared a bi-layer selective emitter that has a polymethylpentane (TPX) thin film, which is embedded with Silicon infrared emitting layer. A 600nm Ag was deposited on silicon sheet as the solar reflecting layer at the bottom of the layer of the selective emitter. They theoretically analyzed the theoretical cooling performance of the samples used and the result showed a daytime cooling performance of 25.5^{o}C below ambient air temperature under direct sun light (AM1.5) and relative humidity of 60% when the ambient air was relatively dry. Also, at nighttime, this bi-layer selective emitter provided a cooling performance of 36.7^{o}C below ambient temperature. From the result, they, to the best of their knowledge, proved that the cooling performance of the bi-layer emitter was better than the other published selective emitters. This excellent cooling performance of this emitter and its low cost presents it with great potential for practical purposes.

Han, et al, (2020) carried out a preliminary study of passive radiative cooling under Singapore's tropical climate as its latitude is very near to the equator. The investigation was through both theoretical simulations and experiments where they discussed the effect of regional solar radiation and humidity on the performance of radiative coolers in the daytime

and nighttime respectively. It was found that regional solar irradiance and humidity mainly influenced daytime cooling performance. By measuring the steady-stat temperatures of two radiative coolers and two reference aluminum (Al) plates in three different weather conditions (clear, partly cloudy, and cloudy skies) in Singapore, with their series of experimental investigations, the daytime cooling performance of the two radiative coolers could not be achieved due to high solar radiation and humidity. However, cloudy, sub-ambient temperatures can be produced using enhanced specular reflector (ESR) film with higher solar radiation reflectivity. They were able to establish a steady- state temperature of 3.5^{o}C lower than the ambient for the photonic device and that of 5^{o}C for the ESR film.

Young *et al* (2020) proposed an optimized TiO_2 - SiO_2 alternating multilayered photonic daytime radiative cooler with an average emissivity of 0.84 within 8–13 μm which reflected 94% of incident solar energy. Its net cooling power was estimated to be 136.3 W/m^2 at an ambient air temperature of 27^{o}C. This shows an improvement of 90 W/m^2 compared to that of the HfO_2-SiO_2 photonic radiative cooler.

Bijarniya's (2021) research on the "Performance simulation of polymer-based nanoparticle and void dispersed photonic structures for radiative cooling", showed that passive radiative cooling is a new field that requires further material development. A computational approach for effective metamaterial design is crucial prior to the fabrication. They used the finite difference time domain (FDTD) method to investigate the interaction of electromagnetic waves with the material. Also, an algorithm for simulating the surface emissive properties of various material nanostructures in both the solar and thermal infrared spectrums was developed, followed by the estimation of cooling performance. In a typical hot summer clear day in Varanasi, India, the maximum cooling power of 162W/m^2 at ambient temperature was observed for Si_3N_4 with voids inline structure during evening time when solar gain reduces to zero, and 132W/m^2 cooling power was observed for SiO_2 with the silver layer in staggered

structure during peak solar radiation. A maximum temperature drops of 9.5°C below ambient during the night and 7.5°C during the daytime performance was observed in hot summer days with elevated ambient temperature.

Noro et al (2021) presented a work on "Energy and Economic Sustainability of a Trigeneration solar system using Radiative Cooling in Mediterranean Climate". They used a mathematical model previously validated against experimental data to numerically investigate different configurations of a hybrid photovoltaic radiative cooling (PVT-RC) system. Based on the basis of the test reference years, the annual energy, CO2 emissions, and economic sustainability of the system were examined in two typical Mediterranean climates. Glass PVT-RC is presented as better performance in terms of overall efficiency (electric + thermal) and cooling energy capacity, and it even performs even better when combined with a thicker insulation layer. Nonetheless, the average glass PVT module achieves performance comparable to the best. By combining the proposed glass PVT-RC collector with the inherent heating, ventilation, and air conditioning system in buildings, the proposed glass PVT-RC collector can cover a significant portion of the energy load in an environmentally friendly manner, providing an interesting primary energy saving capacity.

Liu et al (2021) presented a Nano PE film, which was able to effectively scatter UV light in the solar band, increase solar reflectivity from 96% to 99%. They used Nano PE film with a thickness of 15μm to enhance the radiative cooling performance by reducing UV absorption. The experimental device was made of high-transparente polymethyl methacrylate (PMMA) and is shaped into a square box (30 cm by 30 cm by 4 cm). These thin nano PE films outperform conventional PE films in terms of weather resistance and mechanical strength, and nano-PE films can scatter some visible light, reducing light pollution generation in

practical applications. The modelling results revealed that more than 95% of China's areas can achieve daytime cooling performance with nano PE films.

Zaite et al (2022) numerically investigated Night Cooling Technology by combining photovoltaic and solar thermal technologies using a PV/T collector in three different climates, as well as to improve the temperature and electrical efficiency of the PV cells. The temperatures obtained numerically and those obtained experimentally and available in the literature was compared performed in order to validate the model used in their work. a thermal grease was used between the plate and the PV module to ensure an efficient contact. The differences between the three selected climates of arid climate, semi-arid climate and Mediterranean hot-summer climate allowed us to investigate the effect of climate type on the performance of radiative cooling, electrical and thermal production. This was also used to improve the temperature and electrical efficiency of the PV cells of the same collector in climates where night radiative cooling was effective. The integration of night radiative cooling technology using a PV/T collector is not appropriate in the Mediterranean hot-summer climate due to the higher relative humidity. In the arid and semi-arid climates, the use of night radiative cooling has significantly reduced the temperature of the PV cells while increasing their electrical efficiency.

Huang, et al. (2022) conducted a study to give design principles for producing infrared transparent and thermally insulating mesoporous materials for continuous radiative cooling applications. For all-day radiative cooling applications, the effects of material type and microstructure on the transmission of infrared radiation through mesoporous materials were examined numerically. Particular focus was given to the impacts of particle size, porosity, and thickness. Theoretically, the radiative cooling power of a semi-ideal selective emitter with reflectivity and emissivity values of 0.97 and 0.9 was determined. The findings provide

recommendations for creating a thermally insulating barrier for radiative cooling systems that operate continuously. When covered with a PE barrier at night as opposed to the semi-ideal emitter without any covering, it was demonstrated that the emitter recorded a temperature reduction of 15K and a net cooling power of 91 W/m^2. Similar results were obtained during the day, with a maximum temperature reduction of 13 K and 81 W/m^2 of cooling power. They came to the conclusion that mesoporous materials' spectral and weighted transmittance rose when particle size, volume fraction, and film thickness decreased. Because of its superior thermal insulating qualities, relatively high infrared transmission, and solar reflectance, the PE mesoporous film offered the highest performance for radiative.

2.7 Current Geographical Spread of daytime radiative Cooling and Performances

Table 2.3 presents the current status of daytime radiative cooling in terms of geographical spread, performance overview highlighting location, cooling power and sub-ambient temperature of the coolers.

Table 2.3 Geographical Spread of daytime radiative Cooling and Performances

S/N	Source	Year	Location	Latitude	Composition of cooler/ cooler size	Ambient Temperature	Cooler Temperature	Temperature Deviation	Cooling Performance
1	Hossain et al	2015	Australia	25.3ºS	Metal dielectric CMM pillars	NA	NA	9ºC	NA
2	Gao et al	2019	China	39.55ºN	PCSUVA-PET-Ag	27.7ºC	20ºC	7.7ºC	NA
3	Zhao et al	2018	China	32ºN	NA	25ºC	40ºC	15ºC	95W/m^2
4	Zhao et al	2019b	China	32ºN	NA	20ºC	12.5ºC	7.7ºC	75 W/m^2
5	Wang et al	2021	China	32ºN	Hierarchically porous PMMA	28ºC	20ºC	8ºC	85 W/m^2
6	Tso et al	2017	China	32ºN	SiO_2/HfO_2 of 7 layers with Vacuum	30ºC	32ºC	2ºC	38 W/m^2
7	Ross et al	2018	China	32ºN	AEMT enhanced	25ºC	10ºC	15ºC	87 W/m^2
8	Jeong et al	2018	China	32ºN	100m^2 surface area	27ºC	17ºC	10ºC	1600 W/m^2
9	Jeong et al	2020	China	32ºN	PDMS on SiO_2 & Ag	32.2ºC	26ºC	6.6ºC	19.7 W/m^2

10	Jeong et al	2019	China	32ºN	TiO_2/SiO_2 (500:500)	30ºC	12.8ºC	7.2ºC	14.3 W/m^2
11	Zhu et al	2019	China	32ºN	MgF_2/TiO_2/PDMS/ Si/Ag	35ºC	22.4ºC	12.6ºC	106 W/m^2
12	Zhou et al	2021	China	32ºN	10 layers of Ag-SiO_2 nanocomposite	22.5ºC	8ºC	14.5ºC	273.3 W/m^2
13	Li et al	2020	China	32ºN	$CaCO_3$-acrylic paint	15ºC	-17ºC		50 W/m^2
14	Li et al	2019	China	32ºN	T-$AlPO_4$/C-AlPO4	27.5ºC	23.3ºC	4.2ºC	NA
15	Fan et al	2020	China	32ºN	SiO_2/8YSZ coating	27ºC	11.7ºC	10.3ºC	95.1 W/m^2
16	Zhu et al	2021	China	32ºN	PDMS/Ag reflector	22.5ºC	19ºC	3.3ºC	72.7 W/m^2
17	Liu et al	2019	China	32ºN	PTX/SiO_2/$CaMoO_4$	40ºC	53ºC	13ºC	28 W/m^2
18	Bao et al	2017	China	32ºN	NA			5ºC	NA
19	Bhatia et al	2018	CA, USA	32.2ºN	Polished Al/PET/Cu emitter	18ºC	12ºC	6ºC	45W/m^2
20	Zhao et al	2019	Buffalo, USA	40.7ºN	NA	6ºC	-5ºC	11ºC	120W/m^2
21	Raman et al	2014	CA, USA	32.2ºN	7 layers of SiO_2/HfO_2	17.4ºC	12.5ºC	4.9ºC	40W/m^2

22	Kou et al	2017	CA, USA	32.2ºN	Polymer-Silica-Mirror	29ºC	20.8ºC	8.2ºC	127 W/m^2
23	Zhu et a	2015	CA, USA	32.2ºN	Double-sided crystalline silica wafer	NA	NA	13ºC	NA
24	Zhai et al	2017	Colorado, USA	39ºN	Transparent polymer (TPX)/ SiO_2/Ag	33ºC	32ºC	1ºC	93 W/m^2
25	Zhao et al	2019 d	Colorado, USA	39ºN	PDMS metal/ Commercial reflector mirror	28ºC	23ºC	5ºC	NA
26	Chen et al	2016	CA, USA	32.2ºN	Si_3N_4/Si/Al/Si wafer	37.4ºC	-4.8ºC	42ºC	NA
27	Li et al	2017	CA, USA	32.2ºN	Al_2O_3/SiN/TiO_2/SiN	67ºC	61.3ºC	5.7ºC	1000 W/m^2
28	Zhao et al	2019 e	Buffalo, USA	40.7ºN	NA	12ºC	6ºC	6ºC	120 W/m^2
29	Zhao et al	2019 a	Colorado, USA	39ºN	Radicold module ().34m^2)	32.5ºC	23ºC	9.5ºC	607 W/m^2
30	Wang et al	2020	Lafayette, USA	30.22ºN	RC with CPV	NA	NA	(5-36)ºC	146.3 W/m^2

31	Lee et al	2018	Korea	35.9ºN	SiO_2/Si_3N_4/MIM	40ºC	36.1ºC	3.9ºC	NA
32	Lee et al	2019	Dame, USA	41.7ºN	NA	47ºC	37ºC	10ºC	NA
33	Torgerson et al	2019	CA, USA	32.2ºN	ZnO/PE resin	27ºC	17ºC	10ºC	110 W/m^2
34	Bergman et al	2018	Kansas, USA	38.5ºN	Selective surface	27ºC	18.9ºC	8.1ºC	NA
35	Raphaeli et al	2013	CA, USA	32.2ºN	5layers of MgF_2/TiO_2/Ag	27ºC	NA	NA	100 W/m^2
36	Zhao et al	2019	USA	32.2ºN	NA	32.5ºC	22ºC	10.5ºC	76.1 W/m^2
37	Atiganyanun et et al	2018	Mexico USA	39ºN	NA			4ºC	NA
38	Mandal et al	2018	Phonix USA	33.5ºN	NA			6ºC	96W/m^2
39	Han et al	2020	Singapore	1.3ºN	7layers of HfO_2/SiO_2	30ºC	36ºC	6ºC	80.9W/m^2

40	Orel et al	1993	Slovenia	46^{o}N	7layers of HfO_2/SiO_2	15.4^{o}C		10^{o}C	35 W/m^2
41	Kesebas et al	2017	Turkey	38.9^{o}N	7layers of TiO_2/SiO_2	NA	NA	NA	100 W/m^2
42	Suichi et al	2019	NA		NA			3^{o}C	NA
43	Huang et al	2017	NA		NA			6^{o}C	100W/m^2
44	Wu et al	2017	NA		NA				29W/m^2
45	Wu et al	2018	NA		NA				122W/m^2

From table 2.3, the performance overview of the daytime radiative cooling with respect to location showed that geographical location affects the cooling effect obtainable with the same material as seen in the works of Han et al (2020); Orel et al (1993); Kecebas et al (2017), representing differing climatic regions of Australia, China and Turkey respectively. The material of the cooler however remains the leading determiner of the cooling effect alongside the location as shown by the work of Hossain et al (2015). Several coolers with different compositions have been tested in different locations in china of different latitudes likewise USA and varied ranges of sub-ambient temperature were obtained. The results obtained from different locations in China with differing climates show temperature depression that range from 2^{o}C to 15^{o}C with the highest and lowest temperature drops recorded in Hong Kong. Likewise, the cooling powers range from results 14.3W/m^2 to 1600W/m^2. The works done in USA included the ones done in Califonia, Buffalo, Colorado, Dame, Lafayette, Kansas, Mexico and Phonix. The results from these locations indicates a ranging of temperature drop from 1^{o}C to 42^{o}C. The works of Chen et al (2016) in Califonia when costly of Tin Selenide (SnSe) was used as well as that of Wang et al (2020) in Lafayette when a PVC is integrated with the radiative cooler, recorded the highest temperature drops of 42^{o}C and (5^{o}C-36^{o}C) respectively.

The results obtained also depended on the overall surface area of the cooler as seen in Jeong et al 2018 where a net cooling power of 1600W/m^2 was obtained using a cooler surface area of 100m^2 (10x10)m^2. To enhance the cooling power of the cooler, a higher number of layers for the selective emitters must play a vital role as indicated by the results of the works of Raphaeli et al (2013); Han et al (2020); Orel, et al (1993); Kecebas et al (2017); Raman et al (2014) and Zhou et al (2021). The result of the table 2.3 gives an indication of the effect of geographical spread, surface area/size of the cooler on the cooler performance have direct relationship with each other.

2.8 Comparative analysis of the materials for diurnal passive radiative cooling

The analysis of the various radiative cooling materials for daytime radiative cooling showed that metals like silver and aluminum-based substrates are commonly used as a back reflector in the designs of diurnal passive radiative cooling. Despite this advantage of high solar reflectance, for silver and aluminum reflectors, it will be noted that the radiative coolers still have some surface roughness in reality making the silver or aluminum deposited on them not to be smooth as well. Also, this roughness or imperfection in films can result from the use of sputtering or vapor deposition process, and hence, silver and aluminum usually have a reflectance of approximately 0.94-0.95 and 0.94 respectively. Another setback with silver is its instability and ability to easily corrode when exposed to high-level pollution and humidity as well as the difficulty of depositing it on an emitter so as to yield high reflectance (Yang and Zhang, 2020). These setbacks make non-silvered designs like polymers with comparable reflectance to be more preferred for diurnal radiative cooling applications.

By reason of inorganic materials used in nano photonic designs, high durability can be guaranteed for diurnal passive radiative cooling applications. These inorganic materials have wavelength and subwavelength scales with special quality that can tailor spectral properties for selective thermal emittance. Other factors of great significance that promote real-world diurnal radiative cooling apart from durability are cost and scalability. When one-dimensional, two-dimensional, and three-dimensional planar photonic designs are compared, the 2-D and 3-D structures can provide higher emissions within the atmospheric transparency window as a result of their high degree of freedom (Santamouris and Feng, 2018; Liu et al, 2019). However, the high emissivity of the 2-D and 3-D designs, and their general difficulty in fabrication at scale due to high cost, complexity, and stringency limit their application and hence further explorations are needed in photonic radiative cooling systems as they are still limited to laboratory research (Zhao et al, 2019a).

Paints have the unique advantage of coating flexibility as well as high scalability and cost-effectiveness and so can be more applicable for radiative cooling design as these can be made into near-ideal broadband coolers. A recent report by Mandal et al (2020) with BaSO4 or Al_2O_3-based super-white coatings gave a solar reflectance (98% and 94% respectively) that is greater or equal to that of the designs with silver. The durability, as well as the chemical harmful nature of this design by Mandal et al (2020), is still a huge challenge. The effect of dust must be evaluated carefully because of its degrading effect on the cooling performance of porous structures as well as their mechanical stability which is a potential concern also. When wet deposition and melt fabrication methods are used for less expensive nanoparticles-embedded mixtures, large-area applications are easily achieved and hence a radiative cooling. The challenge of this design is in controlling the size and distribution of the particles and must be addressed (Zeyghami et al, 2018). Considering the cost and large-scale fabrication, polymer-based metamaterials are tipped as good materials in the future for radiative cooling as a result of their incredible advantage over nano photonic materials (Santamouris and Feng, 2018). The disadvantage of this design is its inability to last under direct sunlight and quick aging. They are also more liable to damages by UV light after long-term exposure. Table 2.3 gives a summary of the diurnal passive radiative cooling materials.

2.9 Applications of DPRC

The need to apply the technology of passive radiative cooling in a building envelope cannot be over-emphasized as the main objective is to remove heat and achieve a temperature reduction. Several material designs with enticing optical properties have been utilized to achieve this purpose. To be able to realize an effective design of DPRC system, important problems that ranged from the way the system is configured and controlled, the end-user cooling load profiles, to what extent the weather condition affects the system, the cost implication and future gain must be given adequate attention. Passive radiative cooling within the diurnal hours of the day and its application offers great potential

for solving the problem of energy crisis as well as attracting considerable interest in recent times. Areas of application of the concept are discussed in the subsequent section.

2.9.1 Space Cooling

Several materials with spaces (e.g. buildings, vehicles, and containers) have been designed for human use to meet their need and require cooling for thermal comfort. The amount of energy requirement for cooling these spaces, especially using air conditioners and fans is extremely high and accounts for about 10% of the global electricity use (Zhao et al, 2019). Using DPRC under good condition, about 80% of the cooling load of a residential building can be provided (Zeygamiet al, 2018; Algarni et al, 2019). DPRC devices can be configured using two approaches for practical application.

2.9.1.1 Space cooling by direct contact

The first approach involved applying the coating directly on the surface that requires cooling as shown in figure 2.47. This approach has the advantage of direct and efficient heat exchange as well as the simplicity of the system. However, the approach is limited as it cannot be controlled and switched in different climatic conditions (e.g. in the summer period and winter when cooling has to be shut down completely). This approach is more or less a permanent approach as the DPRC coating will still be losing heat to the cold outer space except if covered (Mandal et al 2019). In an application scenario, this approach can be used in building envelopes as well as vehicles, containers, and other surfaces like the oil storage tanks that are directly exposed to the sky. Oil storage has two setbacks, risk of high flammability, side reaction, and degradation of the oil at elevated temperatures and hence needs a controlled temperature-low temperature. Therefore, brushing the surface directly with and laminating it with a thin-film-based coating will be enough to achieve a sub-ambient temperature for the oil tankers. Another application scenario of DPRC that is very straightforward is the building envelope as the technology has a huge capability of achieving a reduced energy consumption and CO_2 emission.

Because of the differences in location and weather, the effectiveness of this approach in the building is dependent on the climate. For example, the tropical regions like Singapore, the Middle East, and most of the countries in Africa like Nigeria, where the temperature is usually high with a relatively infinitesimal drop during certain periods of the year highly demand this approach but it is ideal for cold places like Chicago and Northern Europe. The vehicle is another appealing area of application of DPRC coating with a great potential for the market. The mileage of vehicles is usually greatly reduced by the use of air conditioning to keep the temperature low and hence achieve thermal comfort in the vehicles. Some vehicles self-driving or autonomous and so uses cameras to operate, which are sensitive to temperature. These cameras also require effective shielding and cooling. Likewise, trucks and oil tankers as well as containers particularly require a cool environment (low temperature) for the transportation of the contents such as foods and temperature-sensitive goods. The essence of low temperature for the above makes DPRC coating application an attractive technology for real-life application.

(a) Rooftop

(b) Trucks

(c) Oil tanks

Figure 2.47: Scenarios of direct building application of DPRC (Chen et al, 2020)

2.9.1.2 Space cooling using integrated active systems

The second approach for building configuring of DPRC is the use of a fluid-based heat exchanger to achieve cooling in buildings where the heat is removed from the space. The heat transfer here is by the use of active systems like fans and pumps as well as a dehumidifier. Active systems that integrate

DPRC with other energy systems like photovoltaic-thermal systems (Mu et al, 2017; Miyawaki et al, 2020), Heating and Ventilation Air conditioning systems (Farmahini et al, 2020; Jeong et al, 2018), and thermoelectric [TE] cooling systems include air-based (Chen et al-2021), open and closed-loop water-based systems (Goldstein et al, 2017) and hybrid systems (Zhang et al, 2018; Katramiz et al, 2020). The use of this approach is quite appealing in the future because of its controllability, especially in the winter when the system can be shut down completely. However, this approach has not been widely adopted in recent times for building integration because it is more complicated and efficiency losses can still be inherent in it during the heat exchanging process. To enhance the life of the DPRC surface, it can also be integrated into panels for preservation. Another area of application of this approach is in power generation. The radiative cooling surface can be used for power generation if integrated with heat-to-electricity conversion methods. Using this approach to generate power was demonstrated by Raman et al (2019) where a thermoelectric module was placed between a radiative cooling surface and the ground. They suggested that a power generation of 25mW/m^2 is feasible during the night. This power generation is attractive for an emergency situation as well as a supplement to streetlights that are powered with solar and off-grid applications.

2.9.2 Solar cell cooling

Devices' temperature such as photovoltaic cells increases when they are in operation and this necessitates the need to monitor the temperature rise of the device as the efficiency and the lifetimes of the system are greatly reduced by elevated temperature (Royney, 2004). The efficiency of a solar cell of silicon origin is about 22% and for a 1% temperature increase, and this efficiency decreases by about o.1% as a result of the negative temperature coefficient of the cell which is approximately 0.45% (Skoplaki and Palyvos, 2009). Also, further research has shown that the efficiency of the solar cell is further reduced since a greater part of the solar energy is converted into heat as the actual effective spectral range is very small (0.3-1.1μm). In thermal management of solar cells, non-radiative heat

transfer plays an essential role in dissipating heat for the cell, and hence, suppressing it is of no essence. This is a result of solar cells' operating temperature being higher than the surrounding air temperature. According to Zhu et al. (2014), the emissivity of Si-based solar cells can reach 0.85 due to the significant absorption dip of Si near the wavelength of 9um within the atmospheric transparency window. It is, therefore, necessary to design and apply a special DPRC coating that could strongly radiate heat and effectively reflect the solar radiation in the sub-band-gap and the ultraviolet regimes. The result of the experiment demonstrated by Li et al (2017) showed that a temperature reduction of over 5.7^{o}C is feasible for Si-based solar cells. However, the cost and limitation of the technology of photonic structure make it hard to use selectively reflecting structures on a commercial basis. Also, Wang et al (2020) designed, refined, and fabricated a high-concentration PV system integrated with radiative cooling. In spite of the additional weight, their experiment demonstrated that, depending on the operating conditions, radiative cooling can contribute anywhere from 25% to 62% of the total cooling power of a CPV system with a flat plate heat sink without requiring additional power. As a result, the experiment produced a significant temperature drop of 36 oC and cooling power of 140 W/m2, which translated into an 8% to 27% relative increase in their Gasb PV cell's open-circuit voltage, or roughly 28 to 75MV. The temperature drop also suggested that different kinds of solar cells could have longer lifetimes, which could lead to their application in additional CPV systems.

2.9.3 Water Harvesting

A problem with population growth and industrial development is the lack of fresh water, which can be addressed by using the radiative cooling coating to harvest more water from the atmosphere. This is especially true in the humid and arid regions of the world (Khalil et al., 2016). By using space as the heat sink and dew point collection technology, a surface can be passively cooled below the dew point and water vapor can condense from the atmosphere. There is a lot of water vapor in the atmosphere, which makes the technology very promising for freshwater harvesting. The convective condenser uses

only convection to achieve cooling; in contrast, the radiative condenser used during the day increases the rate of condensation for freshwater harvesting. Even in favorable conditions, the convective condenser's condensation rate is predicted to be nearly twice as high as that of a radiative condenser. Zhou (2021) states that a high condensation rate of 2.5 L/m2h will improve the water-production cycle by raising the vapour pressure gradient within the harvesting system, which is significantly higher than the theoretically reported limit of the one-sun evaporation rate. Several research has been conducted in the field of condenser coating (Benlatta et al, 2017; Guan et al, 2014) and metrological parameter (Dong et al, 2020; Liu et al, 2020) in order to improve the performance of DPRC condenser. In addition, multifunctional coatings can be adopted for harvesting water from the atmosphere since they favour droplet nucleation and water removal. Dai et al. (2018) developed a hydrophilic directional slippery surface for swift nucleation and water removal. They also found that when the DPRC's performance is combined with multifunctional surfaces, better radiative coolers can be created for applications involving dew point harvesting. The schematic for atmospheric water harvesting is shown in Fig 2.48.

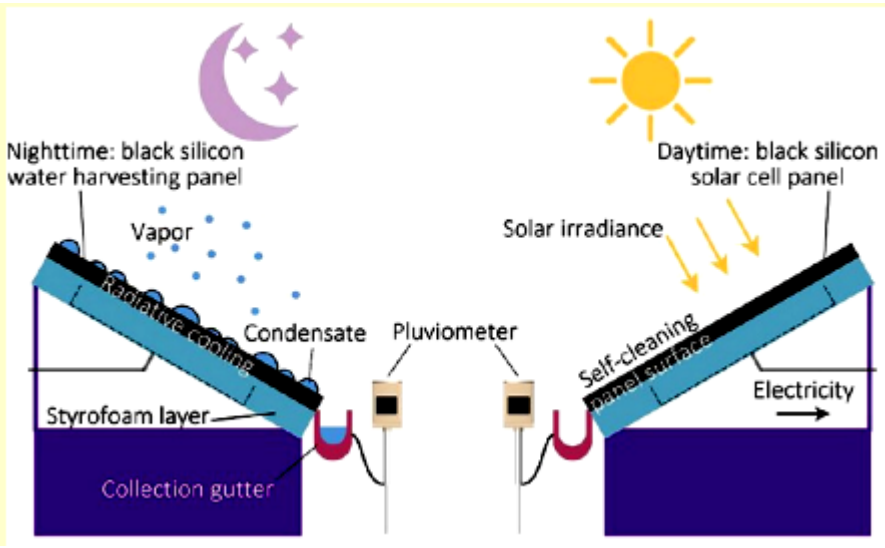

Figure 2.48: Schematic of an atmospheric water harvester for harnessing from the atmosphere (Liu et al, 2022)

2.9.4 Power Generation

Power generation can also be achieved through the ability of the DPRC coating to passively maintain a sub-ambient air temperature for the surface. This is achieved by using a thermoelectric generator to convert the temperature difference into useful electricity, making the thermoelectric generators attract great attention because of their use for recovering power from waste heat and solar heating (Chen et al, 2020; Chen et al,2021). At the night when the photovoltaic systems are not working, the cooling effect in the DPRC can be maximized by connecting it to a TE model to generate electricity. The electricity generation at the night can be widely applied to power sensors and lighting in dark spaces. Therefore, optimizing the emitter of a radiative cooling system can enhance the power density for power generation. In addition, power can be produced during the day when a TE model is coupled with a selective emitter that has strong emittance in the LWIR atmospheric transparency window and high reflectance in the solar spectrum. This combination also keeps the surface of the TE generator cool throughout the day, enabling continuous TE generation. On the other hand, by attaching a broadband emitter with strong emittance in the atmospheric LWIR window and high reflectance in the solar spectrum to the TE device, heating of the broadband will be caused during the day by solar absorption and cooling during the night by thermal radiation through the atmospheric window. This makes the temperature difference gradually reduce to zero from morning to evening of the day and hence the output of the TE generation, which is also being affected by weather changes like the cloud. Therefore, it behooves TE users to cautiously consider the temperature difference generated in the daytime and other factors like sign changes if continuous electricity is to be generated. Mu et al (2019) used Si_3N_4-SiO_2-based structure coated on a silver layer as shown in Fig 2.49 to demonstrate thermoelectric power generation through passive radiative cooling technique.

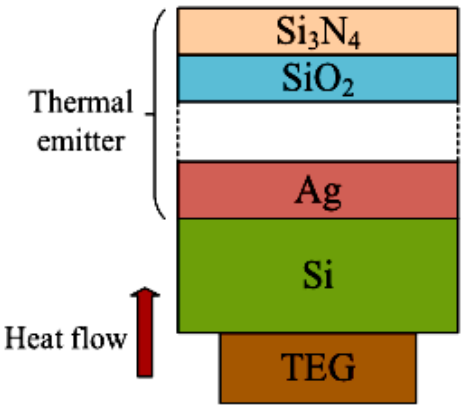

Figure 2.49: Si_3N_4-SiO_2-Ag-based structure for thermoelectric power generation (Mu et al, 2019)

2.10 Other Applications of DPRC

There are yet more DPRC application areas that have been reported in research. Water cooling is one of these application areas. In order to cool water to 10.6oC below ambient at noon under stationary settings, Zhao et al. (2019) developed the Radiative Cooled Cold Collection (RadiCold) module. The utilization of radiative sky cooling was investigated using a scalable metamaterial at a reasonable cost. The study examined how several meteorological factors, such as wind speed, precipitable water, and cloud cover, affected the radiative cooling process. Under 952 W/m2 average solar irradiances, the RadiCold system displayed a maximum cooling power of 1,296 W at night and an average cooling power of 607 W at midday (12–2 p.m.). For continuous daytime and nighttime cooling, a building-integrated RadiCold system is suggested. The cooling of the human body is a further application. According to Zeng et al. (2021), large-scale woven metal textiles with randomly distributed scatterers exhibiting a hierarchical morphological design can achieve high emissivity (94.5%) in the atmospheric window and high reflectivity (92.4%) in the sun spectrum. They proposed that the integration of passive radiative cooling structures into personal thermal management technology could provide people with an effective defense against the intensifying effects of global climate change. It was discovered through research that the metal fabric could reduce body temperature by about 4.8°C when

applied across a human body as opposed to commercial cotton materials. They noted that our metal textiles have the appropriate mechanical strength, waterproofness, and breathability for commercial apparel in addition to their effective radiative cooling capacity. For applications such as passive radiative cooling, smart textiles, and adaptive clothing, the low cost and excellent performance of metal fabrics offer substantial advantages. Hsu et al. (2016) developed nanoporous polyethylene fabric, which transmitted mid-infrared human radiation without producing visible light. He presented a personal temperature management system using fabrics that have metal nanowires inserted in them. The excellent thermal insulation qualities of the nanowires combined with their conductive network offered a means of providing joule heating to complement passive insulation layers. The developed fabrics can improve radiative cooling performance while still having the ability to breathe, absorb water, and resist wear by their mechanical strength as a result of the porous nature of the nanowires.

2.11 Configurations for building integration of diurnal passive radiative cooling

Passive radiative cooling techniques have great potentials to be integrated into the building envelopes to achieve thermal comfort and enhance energy-saving. There are numerous designs that have been used to incorporate passive radiative cooling panels into different building systems; these systems can be classified as hybrid, air-based, or water-based radiative cooling systems (Zhao et al., 2019a). According to Parker (2005) and Parker and Sherwin (2008), there is a distinction between air-based and water-based radiative cooling systems. The former use air as a heat exchange medium, while the latter utilize water. Additionally, hybrid systems incorporate enhanced features aimed at augmenting a building's energy efficiency. Water-based radiative cooling systems are two which are open and closed water systems. Open water systems such as roof water ponds (Ali, 2007) use thermal radiation and evaporation to reject heat from the building to the outer environment. In a closed system, water flows through the closed pipes beneath the radiative cooling system and serves as a heat carrier to provide

cooling, and the cooled water is then circulated around the pipes and the water storage tank thereby achieving energy efficiency in the building. (Meir et al, 2002; Saitoh and Fajino, 2001; Tevar et al, 2015). The radiative cooling system performance can be enhanced when integrated energy supply devices such as air conditioners in buildings. This combination was demonstrated by Goldstein et al (2017) where water was cooled below the ambient using a non-evaporative water-cooling panel. The temperature drop of the water and corresponding net cooling power were 3-5^{o}C and 40-70% respectively and when integrated into an air conditioning system, an improved efficiency was noticed with a drastic drop in energy usage. Figure 2.50 illustrates the schematic of a non-evaporative water cooling panel alone and when it is integrated into a condenser. Also, cooling water to a sub-ambient temperature of 10.6^{o}C can be produced by utilizing a glass-polymer hybrid metamaterial. The cooled water produced at night is stored and used in the daytime since cooling demand in the nighttime is low. Energy savings of 64–82% and 2-45% in the winter and summer, respectively, were achieved in a commercial building by using this operating mode that combines daytime condenser cooling with overnight storage. Wang et al. (2018) evaluated the energy-saving capabilities of a 5000 square meter building using a developed photonic-based radiative cooling system (Figure 2.51), which covered roughly 60% of the rooftop and saved roughly 23% of the building's electricity consumption in comparison to a cool roof-based radiative cooling system. Heidarinejah et al. (2010) used a hybrid system to augment the convectional cooling efficiency, combining a nighttime radiative cooling system with an evaporative cooling system, strengthening the pre-cooling impact. After being stored in the water tank, the cool water produced during the night flows by means of the cooling coil unit, which pre-cools the water by exchanging cooling energy with hot air from the surrounding atmosphere. By incorporating the radiative module into an indirect evaporative cooling system, the shortcomings of a stand-alone evaporative cooling system are therefore overcome and a more energy-efficient cooling effect is obtained (Farmahini- Farahani and Heidarinejad, 2012; Farmahini Farahani et al, 2010). The

schematic of the configuration proposed by Heidarinejad et al (2010) is illustrated in figure 2.52. Since the power generated by the radiative cooling module has a low density, it is possible to combine the phase change material (PCM) for thermal storage with a radiative cooler to provide cooling power continuously. In order to cool the buildings during the day, a nocturnal radiative cooler and a microencapsulated PCM (MPCM) slurry were mixed, as figure 2.53 illustrates (Zhang and Niu, 2012). The cooling power used to achieve this diurnal cooling was transferred to the piped water, which cools the building is from the MPCM slurry storage. The result showed an energy-saving rate of over 77% in dry weather conditions for a low-rise building. Lei et al. (2017) also used a cool-colored coating with MPCM as an external surface to provide the best possible cooling of buildings by combining the cool paints' solar reflection and the MPCM's residual heat absorption. Chung and Park (2016) investigated the usage of cool reefs combined with MPCM to lessen the heating penalty throughout the winter.

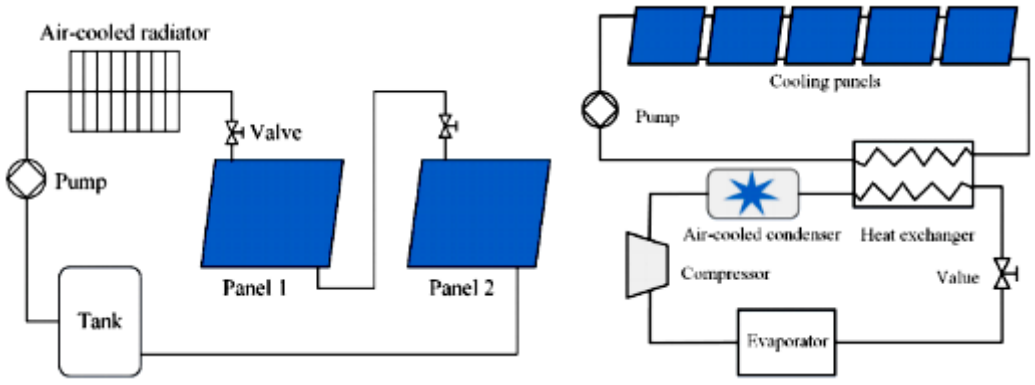

Fig. 2.50: Non-radiative water cooling panel of a configuration of two panels connected in series and radiative cooling connected with a condenser (Goldtein et al, 2017)

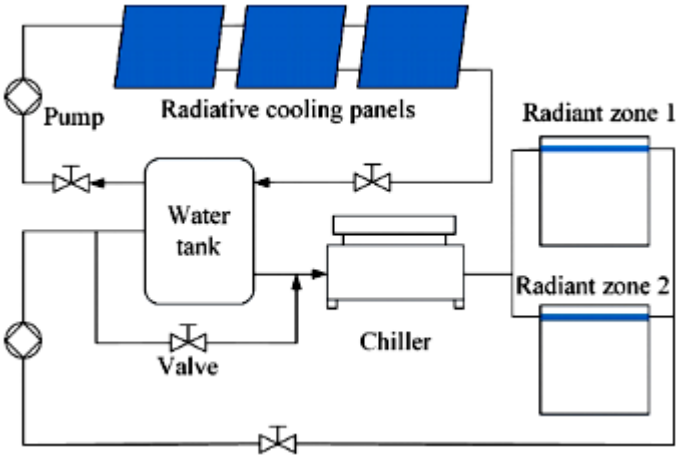

Fig. 2.51: Photonic-based radiative cooling system (Wang et al, 2018)

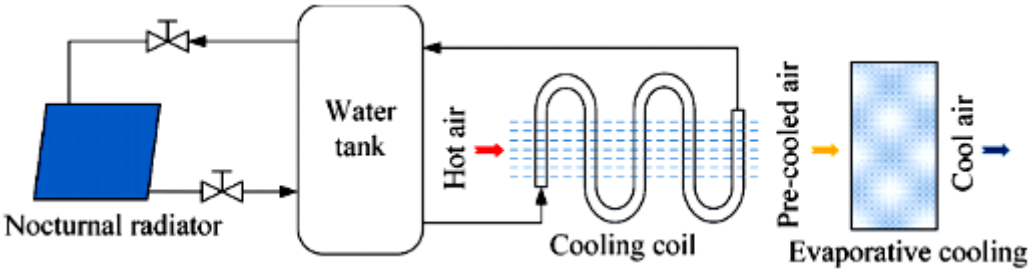

Fig. 2.52: Nocturnal radiator integrated with direct evaporative cooling system (Heidarinejad et al, 2010)

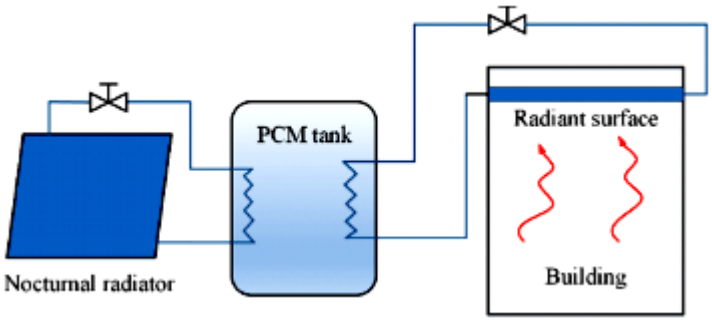

Fig. 2.53: Nocturnal radiative cooling integrated with PCM for thermal storage (Zhang and Niu, 2012)

2.12 Summary of findings from the literature

An extensive review of available literature on nocturnal and diurnal radiative cooling has been conducted. The literature review sets out to ascertain the extent of work done, establish research gap(s), and then devise the most suitable means of filling the identified knowledge gap(s). It was also to explore the modeling and experimental approaches so far adopted in studying diurnal passive radiative cooling systems, and their applications. The available works range from simple dual-layer radiative coolers to complex multilayer photonic coolers. The thickness of the emitters and their thickness ratio as well as the number of alternating layers play a vital role in the enhancement of the emissivity. Although increasing the thickness of the MPEA and $BaSO_4$ far above the chosen thickness will increase the average thermal insulation but infrared transmittance decreases as well as the cost implication. Therefore, achieving higher thermal insulation, high I-R transmittance and cost-effectiveness is the motivation for the choice of dual-layer of MPEA and $BaSO_4$ in this design as increasing a compromise between the increase in cooler thickness and porosity will bring about good enhancement in the average thermal insulation and weighted transmittance of the cooler (Huang et al, 2022).

Both experimental and numerical approaches have been adopted in studying diurnal radiative cooling. However, most theoretical approaches have concentrated on material development and optical characterization of such materials to ascertain the behavior in the solar band and atmospheric window respectively.

Literature shows that achieving daytime radiative cooling is location specific because of varying climatic conditions. As a result, model input parameters vary and hence the system output. Therefore, it is necessary to model and design a system that could be adapted to our local climate to realize daytime radiative cooling. It is worthy of note that all the available work has been conducted under fixed

weather condition of clear sky with low humidity. Therefore, the system behavior in wet and highly humid climates Nigeria needs to be investigated to extend its widespread adoption.

Apart from optical characterization, available works have only limited interest to determination of the cooling power of the radiative cooler without any practical integration with indoor thermal comfort application in buildings both at the experimental and theoretical levels. Full system optimization and hence widespread implementation would entail a holistic system description including possible building integration, mostly from theoretical perspective before consideration of a full practical integration. This is because experimentation has become imperative to fully investigate to what extent the simulated predictions are true, so that the feasibility of real-time application of the concept for indoor cooling purposes will be established.

From the foregoing, there is no study at present that has taken care of field and theoretical investigation of passive daytime radiative cooling techniques under regions of Nigerian wet and humid tropical climatic conditions. This is therefore the motivation for this research.

CHAPTER 3

RESEARCH METHODOLOGY

3.1 Diurnal passive radiative cooling system configuration

The configuration of the diurnal passive radiative cooling system integrated in a building envelope is shown in Fig. 3.1.

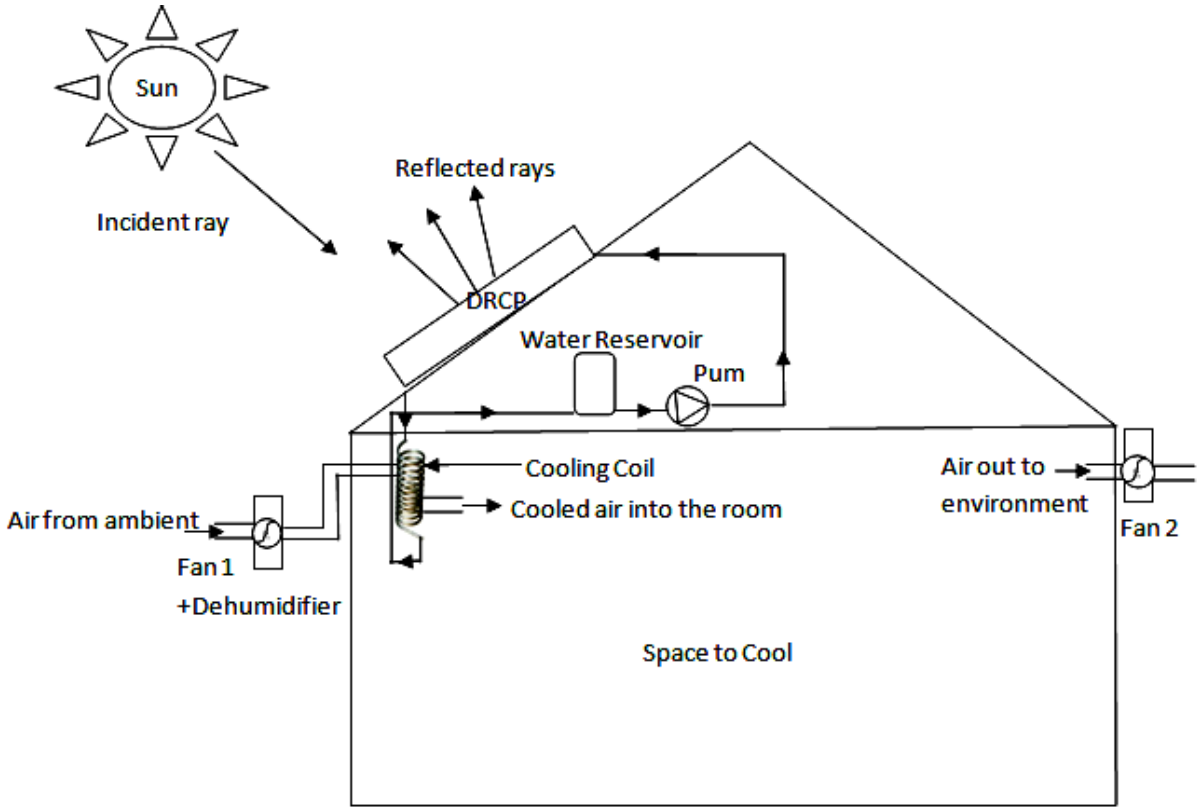

Fig 3.1: Diurnal Passive Radiative Cooling (DPRC) system configuration

The cooling system consists of a mesoporous polyethylene (MPEA) or Barium Sulphate ($BaSO_4$) as structural material for diurnal passive radiative cooling (DPRC); a water reservoir for cold water storage after circulation through the DPRC; a pump (for cold water circulation from the cold water reservoir to the DPRC); two (2) fans for air circulation into and out of the room; a dehumidifier for ambient air pre-cooling; a cooling coil serving as a heat exchanger to further cool the ambient air sucked into the room by Fan1; valves, connectors, and pipe network.

3.1.1 Description of the diurnal passive radiative cooler (DPRC)

The schematics of the diurnal passive radiative coolers are shown in Fig. 3.2. The radiative cooler which is by design the selective surface functions as the heart of the DPRC system. Radiative coolers are characterized by very high reflectivity in the solar band and high emission of thermal radiation in the atmospheric spectrum. It emits heat to the environment as well as reflects greater part of the solar radiation thereby causing the cooling of the space during the day time. The DPRC system consists of two different silver-coated radiative cooling surfaces which are spectrally selective in both the solar radiation and atmospheric window bands. This is because they have very low spectral absorptivity in the solar radiation spectrum (0.2-3μm). The efficiency of the selective surfaces depends on spectral emissivity (which must be very high within the atmospheric window wavelength), and very low heat gain from the surrounding. The design of the selective surfaces was done by sizing the different components of the diurnal passive radiative coolers and two (2) different cooler materials were chosen. The first cooler consists of a mesoporous polyethylene aerogel (MPEA) material as shown in Fig. 3.1a. The MPEA was deposited unto a 200nm thick silver reflector of high solar reflectance. Polyethylene aerogel (PEA) is a low-density, high-porosity, and open-cell porous polyethylene (PE) material characterized by micrometer-sized pores. The porous structure of the PEA sample makes it strongly scattering at shorter wavelengths (0.3-2.5μm), resulting in a high reflectance of solar irradiation (R_{solar} = 0.922). The characteristic strong absorption of polyethylene is due to asymmetric stretching, bending, and wagging of CH_2 molecules (Leroy, 2019). This characteristic porous structure and ultra-low-density (10-50kg/m^3) of PEA give it exceptional optical and thermal properties, which makes it an excellent thermal insulator. This insulating property of the PEA as a result of its low density and microporous structure make its thermal conductivity to be very low compared to that of air (0.03W/mK), which makes it ideal for high-performance sub-ambient radiative cooling, even at large thicknesses, which was not possible with previous materials such as nano-porous polyethylene. The

choice for use of the MPEA for the cooler is because of its high emissivity and absorptivity of 0.97 and 0.90 respectively as well as the best thermal insulation performance. Making the PEA mesoporous brings an improvement in its spectral properties for efficient sub-ambient cooling. Mesoporous materials have a large specific surface area and a wide range of porosity, with pore sizes ranging from 2 to 50 nm (Armandi et al., 2010). The infrared transparent mesoporous materials shown in the schematic of Fig. 3.2a, are optimally designed with high solar reflectance working as selective and insulating films for all-day radiative cooling applications by taking the advantages of optical selectivity and low thermal conductivity of aerogel. Investigating the effects of particle size, porosity, and thickness, the insulating barrier provided by the MPEA provides guidelines for the development of a thermally insulating barrier for all-day radiative cooling devices.

Fig.3.2b shows the second cooler structure with Barium Sulphate ($BaSO_4$) deposited atop the silver reflector. The whitish appearance of the $BaSO_4$ structure makes it transparent and strongly scattering at shorter wavelengths (0.3-2.5μm), which also results in a high reflectance though with lower absorption. The cooling system also incorporates a polyethylene film, referred to as a window screen (Mingke et al., 2015), which serves to reduce wind effects and convection losses from the top of the surface. The polyethylene film is also highly transparent, allowing passage of long wavelength and short wavelength radiation. In order for the selective surfaces to function effectively, both the surface and the windscreen would allow the exchange of radiation within the entire 0.2-25μm wavelength window, covering both the solar radiation spectrum of 0.2-3μm and atmospheric window spectrum of 8-13μm. Thus, the optical properties of the windscreen depend on the period of the day; the windscreen being characterized by high transmission in the wavelength range of 8-13 μm. At present, compounds such as SiO_2, TiO_2, MgO, Lithium Ferride, PTE, BaSO4 and ZnS have been used as radiative cooling surfaces with only MPEA achieving up to 11^oC equilibrium temperature lower than the ambient. Although most inorganic materials achieve equilibrium temperature close to the MPEA and are more stable under

direct sunlight, they are reportedly extremely expensive and complex to fabricate. Leroy et al (2019) reported an optically selective and thermally insulating cooling surface of PEA, with polyethylene (PE) film as a convective cover (or windscreen) to reduce losses due to convection. They found out that PE film has high spectral transmittance in the entire 0.2-2.5µm spectrum while the PEA selective surface has spectral absorptivity of 0.92 within 0.2-3µm wavelength and spectral emissivity of 0.94 within 8-13µm wavelength and 0.55 outside the solar radiation and atmospheric window (i.e., 3-8µm and 13-25µm) spectra, respectively. The coolers were fabricated in the thin film Laboratory of Namiroch Nig. Ltd, Abuja.

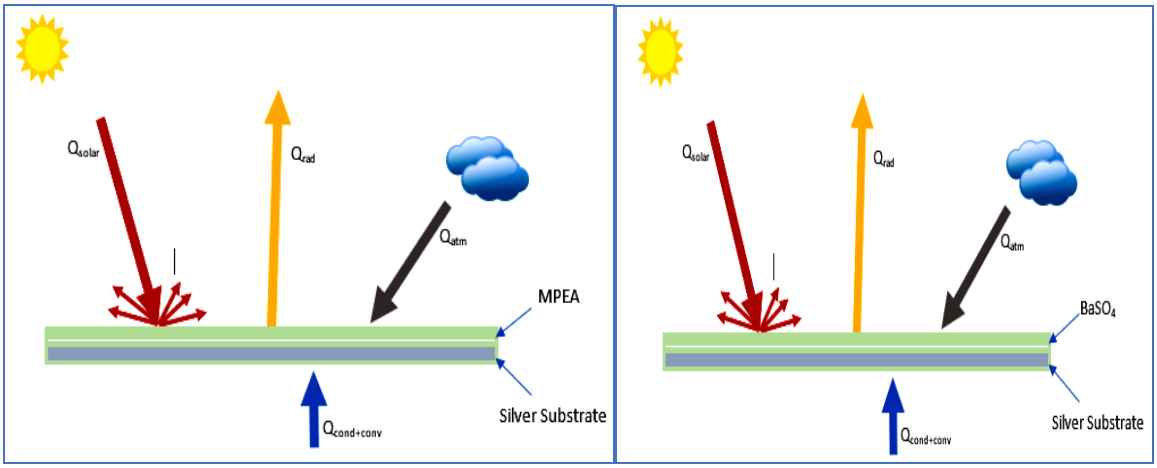

(a) (b)

Fig 3.2: Configuration of the Diurnal Passive Radiative Cooler

3.1.2 Principles of Operation

The MPEA diurnal passive radiative cooling system, which is mounted on a cavity that serves as the building prototype operates for 24 hours of the day, capturing the diurnal characteristics of the radiator with the prevailing climatic conditions. The cavity serves as a support for the structure while also serving the purpose of mitigating against heat gains from the surroundings through conduction and convection on the system. It is made of wood which is a poor conductor of heat but is also covered with sheets of Aluminium foils; a very reflective material in order to protect the cavity from radiation.

During the daytime, most of the solar radiation from the sun reaching the DPRC panel is reflected away from the radiative cooler, which is exposed to the sky under direct sunlight and atmospheric radiation. About 97% of the solar radiation from the sun, which is incident on the surface of the radiative cooler is reflected back to the atmosphere due to the high reflectivity (0.966) of the silver reflector and hence keeps the panel surface facing the indoor space at a sub-ambient temperature. Infrared irradiance coming from the atmosphere strongly interacts with heat gains from the space to be cooled by the mesoporous structure of the polyethylene aerogel and about 93% of this heat is emitted to the atmosphere. This is because the mesoporous polyethylene (MPEA) structure is extremely emissive across the full atmospheric transmission window while remaining transparent to the solar spectrum. The Earth's atmosphere has a highly transparent window in the infrared (IR) wavelength range (8-13μm) known as the atmospheric transparency window.

Ambient air from outside is sucked by Fan1 and passed through the dehumidifier for filtering and pre-cooling. The dehumidification process involves the removal of water molecules from the air thereby pre-cooling the air. As the pre-cooled air flows across the coils of the cooling coil unit, it gives up some heat to the chilled water flowing through the coils. This water that has taken up this energy regains its initial ambient state and flows back to the reservoir or tank so that it can be circulated again by the pump through the DPRC panel. At the same time, the air that has been cooled flows into the indoor space to provide comfort cooling.

Immediately this cooled air flows into the room space it mixes with the already existing air in the room and an air current develops due to buoyancy phenomenon. The cooler air displaces the warmer and flows towards the lower parts of the room while the warmer moves upwards so that it can continue to be cooled as the conditioned air continues to flow into the room. Air is vented out of the room through the second fan designated as Fan2.

The above process continues throughout the day from sunrise to sunset. After sunset, the process still continues well into the nocturnal hours until sunrise the following day. But at this time, it operates on a night-sky mode. The energy exchange process is now between DPRC panel and the sky through the atmospheric transparency window. The water continues to be cooled as it is circulated by the pump through the panel and the air filtration and dehumidification process continue as well as room air conditioning through panel-cooling coil-air-cooling arrangement.

3.2 Design analysis of the radiative cooler

When light rays fall on an object, part of the light rays can be reflected, absorbed, or scattered. Energy rejected and absorbed by a body through radiative cooling is governed by certain principles, and is consistent in each direction to maintain a heat balance within the body. Usually, in heat transfer processes, the flow of heat is from a higher temperature source (i.e., hot surface of the body) to a lower temperature sink (i.e., cold outer space of the universe) (Chen et al, 2016). According to Kirchoff's law, heat is exchanged among bodies at different temperatures through the absorption and emission of electromagnetic waves. The atmosphere having a property of selective emission for the whole electromagnetic radiation spectrum experiences this phenomenon of absorption and emission through the spectrum. It selectively permits certain wavelengths of radiation within a certain range (8-13μm) to pass through it. This wavelength range is where the atmosphere is transparent and allows radiation to completely pass through and reach outer space (Raman et al, 2014).

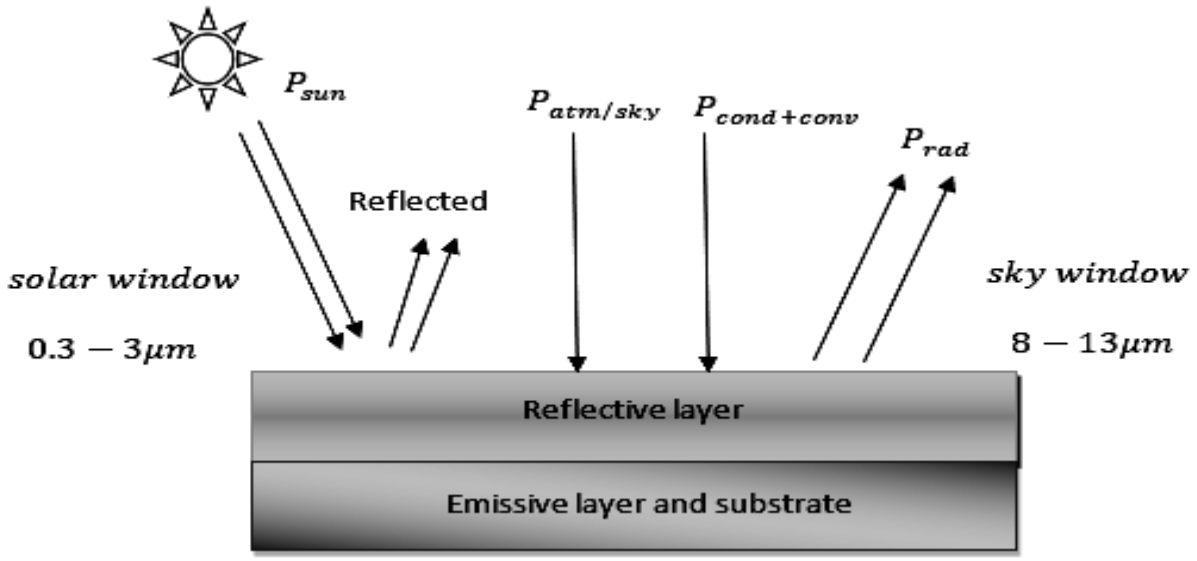

Fig. 3.3: Energy interaction in the DPRC

Energy transformation within the structure shown in Fig. 3.3 (from a source to a sink) takes place in the form of heat transfer by radiation, conduction and convection.

The net radiative cooling power of the system, $\boldsymbol{P_{cool}}$ is calculated using the relation:

$$P_{cool} = P_{rad} - P_{atm} - P_{cond+conv} - P_{sun} \qquad 3.1$$

Where $\boldsymbol{P_{rad}}$ is the energy radiated by the cooler within the atmospheric transparency window, $\boldsymbol{P_{atm}}$ is the radiant energy from the sky or atmosphere, $\boldsymbol{P_{sun}}$ is the solar irradiation, $\boldsymbol{P_{cond+conv}}$ is the heat energy from the surrounding by virtue of conduction and convection.

A positive value of $\boldsymbol{P_{cool}}$ suggests an efficient system which would lead to a drop in temperature of the system, and is possible only if the combined power of the sun, the atmosphere and the losses are less than the energy radiated by the cooling system, i.e., $\boldsymbol{P_{rad} > (P_{sun} + P_{atm} + P_{cond+conv})}$.

To successfully design the system, and hence evaluate the cooling power, several factors such average maximum ambient temperature (T_{amb}), temperature of the cooling structure ($T_c = T_{rad}$), and wind speed (v) for the study location were considered.

3.2.1 Sky Radiation

The atmosphere is heated up by the short-wave infrared from the sun and the heat as long-wave infrared is radiated to the terrestrial environment. Gases such as water vapor (H_2O) and carbon dioxide (CO_2) which are contained in the atmosphere are responsible for about 90% heating of ground level. The infrared from the sun is absorbed by the molecule of these gases in the atmosphere, which re-radiates the absorbed infrared as heat to the terrestrial environment. The sky condition such as clear and cloudy sky influences the amount of the radiation from the atmosphere. For a clear sky condition, the atmosphere is assumed to be a black body i.e. $\varepsilon_{sky} = 1$ and the sky is at the same temperature with ambient i.e.,$T_{sky} = T_{amb}$.

According to Stefan Boltzmann's law, the long-wave radiation from the blackbody is given as:

$$P = \varepsilon_s \sigma {T_{sky}}^4 \qquad 3.2$$

Where T_{sky} is the temperature of the sky (K), and ε_s is the emissivity of the sky.

Therefore, for a clear sky condition,

$$P = \varepsilon_s \sigma T_{amb}^4 \qquad 3.3$$

Where σ is the Steffan-Boltzmann constant given as 5.67037×10^{-8}, ε_s is the sky emissivity and T_{amb} is the ambient temperature.

To calculate the radiation from the sky, the sky emissivity, ε_{sky} has to be determined. Form an experiment conducted by Idso (1981), the sky emissivity within the atmospheric window can be correlated as:

$$\varepsilon_{8-13,0} = 0.24 + (2.98 \times 10^{-8} P_w{}^2 exp^{\frac{3000}{T_{amb}}}) \quad 3.4$$

Where P_w is the partial pressure of water vapor in the atmosphere, and T_{amb} is the ambient temperature.

The partial pressure of water vapour in the atmosphere (P_w) can be evaluated from the relative humidity (RH) correlation given as:

$$RH = 100 \times \frac{P_w}{P_{ws}} \quad 3.5$$

Where P_{ws} is the water vapor saturation pressure defined by Perry, et al (2007) as:

$$P_{ws} = \frac{e^{(77.3450+0.0057\,T-7235/T)}}{T^{8.2}} \quad 3.6$$

Where e is a constant given as 2.718 and T is the dry bulb temperature T_{db}(K).

According to Frank and Chika (2017), the mean daily RH value in Owerri is given as 0.87(dry bulb), and the dry bulb temperature T_{db} is 25.5˚C. Hence, the dry bulb temperature evaluated in Kelvin as:

$T_{db} = 25.5 + 273 = 298.5K$

Substituting for the dry bulb temperature in Eq. (3.6), the vapour pressure at saturation point can be evaluated as:

$$P_{ws} = \frac{2.178^{(77.3450+0.0057\,(298.5)-7235/298.5)}}{298.5^{8.2}}$$

$$P_{ws} = \frac{2.178^{54.818}}{298.5^{8.2}}$$

$$P_{ws} = 3237 P_a$$

From Eq. 3.5, the partial pressure of water vapour can then be evaluated as:

$$0.87 = \frac{P_w}{3237}$$

$$P_w = 2816.19P_a \approx 2.816kP_a \; or \; 28.16mbar$$

Now, substituting for P_w in Eq. 3.4 and noting that the average ambient temperature for the study location is 32°C (305K), we have that:

$$\varepsilon_{8-13,0} = 0.24 + (2.98x10^{-8}x(28.16)^2 exp^{(3000/305)}$$

$$\varepsilon_{8-13,0} = 0.24 + (0.44)$$

$$\varepsilon_{8-13,0} = 0.68$$

Finally, the values for the sky emissivity within the atmospheric window, $\varepsilon_{8-13,0}$ and the ambient temperature, T_{amb} are substituted into Eq. 3.3, having

$$P = 0.68 \times 5.67037 \times 10^{-8} \times 305^4$$

$$\boldsymbol{P = 333.67W/m^2}$$

The total atmospheric radiation of the sky on an inclined surface may be calculated thus,

$$P(\alpha) = P_A(\alpha) + P_G(\alpha) \qquad 3.7$$

Where $P(\alpha)$ is the total long-wave sky radiation as a function of tilt angle α, $P_A(\alpha)$ is the atmospheric radiation, and $P_G(\alpha)$ is the ground component of atmospheric radiation.

The atmospheric radiation $P_A(\alpha)$ and ground component of atmospheric radiation $R_G(\alpha)$ are respectively given as (Duffie and Beckman, 2013).

$$P_A(\alpha) = P_A cos^2\left(\alpha/2\right) + bI_7\sigma T_a^4 \quad 3.8$$

$$P_G(\alpha) = sin^2\left(\alpha/2\right)(\varepsilon_g\sigma T_g^4 + \rho_g P_A) \quad 3.9$$

Where α is the tilt angle, b is a constant ranging from 0.07 to 0.14, I_7 is a function of the tilt angle given as 0.2, T_g =29.1°C is the ground surface temperature, and ε_g = 0.9887 is ground emissivity. The ground reflectivity, ρ_g is given as:

$$\rho_g = 1 - \varepsilon_g \quad 3.10$$

$$\rho_g = 1 - 0.9887$$

$$\rho_g = 0.0113$$

The values used for T_g and ε_g are extracted from the Land Surface Temperature (LST) and Land Surface Emissivity (LSE) Port Harcourt data table. (Nwaerema et al, 2019)

Substituting the values of $b, I_7, R_A, \varepsilon_g, T_a \; and \; \alpha$ into Eqs. 3.8 and 3.9,

$$P_A(\alpha) = 333.672 \times cos^2\left(35/2\right) + 0.009 \times 0.2 \times 5.67033 \times 10^{-8} \times (305)^4$$

$$P_A(\alpha) = 303.5 + 8.8325$$

$$P_A(\alpha) = 312.33 W/m^2$$

$$P_G(\alpha) = sin^2\left(35/2\right) \times (0.009 \times 5.67037 \times 10^{-8}(29.1 + 273) + (0.0113 \times 333.672)$$

$$P_G(\alpha) = 0.0904 \times (466.959 + 3.7705)$$

$$P_G(\alpha) = 42.55 W/m^2$$

Hence, the sky radiation, P_{sky} from the cooler is given as

$$P(\alpha) = P_A(\alpha) + P_G(\alpha)$$

$$P(\alpha) = 354.88 W/m^2$$

The incident solar radiation on a flat surface can be reflected, absorbed, or transmitted as shown in Fig. 3.4. For power conservation to be maintained, then the sum of the reflected, absorbed, and transmitted power must add up to the incident power.

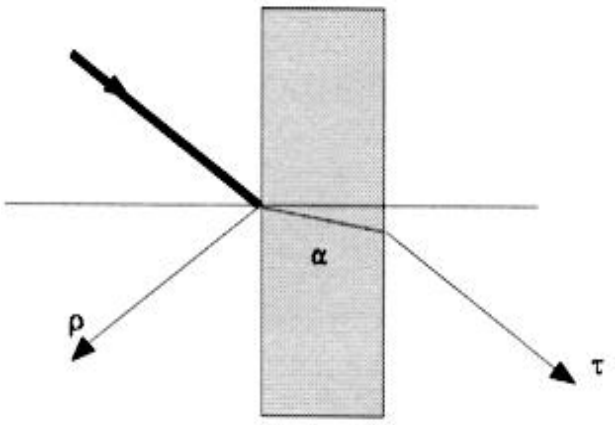

Fig 3.4: Reflection, absorption and transmission of incident radiation on a flat surface

According to Kirchhoff's law, a surface that is perfectly reflecting is said to maintain equilibrium, since all the radiation that goes to it is reflected back (transmittance, τ =0). But if it is not perfectly reflecting, any deficiency in its reflectivity must be made up exactly by emissivity (Wolfe, 1998).

Thus, the conservation of energy requires that the amount of energy that is reflected, absorbed, or scattered is expressed using the relation:

$$\alpha + \rho + \tau = 1 \qquad 3.11$$

where α, ρ, and τ are the absorbed, reflected, and scattered energy, respectively.

Since the transmittance is negligible for a perfectly reflecting surface, then,

$$\varepsilon = 1 - \rho \qquad 3.12$$

Therefore, Kirchhoff's law can be stated very succinctly as absorptivity equals emissivity ($\alpha = \varepsilon$).

Under identical conditions (that the emissivity and absorptivity are measured for a sample at the same temperature and in the same spectral band), the spectral emissivity equals the spectral absorptivity, the

total emissivity equals the total absorptivity, and each polarization component of either spectral or total emissivity equals that of the equivalent absorptivity.

Within the range of the infrared spectrum, the absorptivity of Mesoporous Polyethylene Aerogel, MPEA is 0.90 (Huang et al, 2022). Therefore, the fraction of the sky radiation absorbed by the system is thus given as:

$$\alpha P_{sky} = 354.88 \times 0.90$$

$$\boldsymbol{\alpha P_{sky} = 319.392 W/m^2}$$

3.2.2 Solar Radiation

The incident irradiation from the sun on the cooler surface may be expressed as (Duffie and Beckmann, 2013).

$$P_{sun} = I_b R_b + I_d \left(\frac{1+COS\alpha}{2}\right) + I_{\rho g}\left(\frac{1-cos\alpha}{2}\right) \qquad 3.13$$

Where I_b is the beam radiation, I_d is the diffused radiation, R_b is the beam radiation tilt factor.

According to Kalogirou (2014), the correlation for the beam tilt radiation factor is given by:

$$R_b = \frac{\cos\theta}{\cos(\phi)} = \frac{\sin(L-\alpha)\sin(\delta)+\cos(L-\alpha)\cos(\delta)\cos(h)}{\sin(L)\sin(\delta)+\cos(L)\cos(\delta)\cos(h)} \qquad 3.14$$

Where L is the latitude of the study location, α is the tilt angle which is the angle between the plane of the surface in question and the horizontal, h is the hour angle, and δ is the declination angle, which is the angular position of the solar noon with respect to the plane of the equator. At the maximum solar peak which occurs at noon, h = 0.

The declination angle can be found through the following correlation (Duffie and Beckman, 2013).

$$\delta = \left(\frac{180}{\pi}\right)(0.006918 - 0.399912\cos B + 0.070257\sin C - 0.006758\cos 2B + 0.000907\sin 2B - 0.002697\cos 3B + 0.00148\sin 3B) \quad 3.15$$

And B is defined as:

$$B = (n-1)\frac{360}{365} \quad 3.16$$

And n is the day number which can be obtained from the table of day number for the year. According to Arora (2009), the earth receives 7% more radiation in January than in July. Hence, January is assumed to have maximum solar radiation. Assuming a value $n = 1$. This is substituted into equation (3.16) giving;

$$B = (1-1)\frac{360}{365}$$

$$B = 0\,rad$$

Inputting the value of B into equation (3.15),

$$\delta = \frac{180}{\pi}(-0.407)$$

$$\delta = -23.05^{\circ}$$

From Eq. 3.14, the beam radiation tilt factor is calculated thus:

$$R_b = \frac{\sin(5.485-35)\sin(-23.05)+\cos(5.485-35)\cos(-23.05)\cos(0)}{\sin(5.485)\sin(-23.05)+\cos(5.485)\cos(-23.05)\cos(0)}$$

$$R_b = \frac{1.115}{0.88} = 1.267$$

The radiation scattering and absorption effects of the atmosphere vary with time because of the changing atmospheric conditions and air mass. To solve the beam radiation component of the solar irradiation, the radiation received on a horizontal surface under clear sky conditions is given by:

$$I_{b-horizontal} = \tau_d G_{OH} \quad 3.17$$

where τ_b is the atmospheric transmittance for beam radiation and G_{OH} is the extraterrestrial radiation on a horizontal surface outside the earth atmosphere, expressed as:

$$G_{OH} = G_{on} \cos(\phi) \quad 3.18$$

Where G_{on} is the extraterrestrial normal radiation given as:

$$G_{on} = G_{sc}\left[1 + 0.033 \cos(\frac{360n}{365})\right] \quad 3.19$$

G_{sc} is the Solar Constant which is the energy from the sun per unit time received per unit area of a surface perpendicular to the direction of propagation of the radiation at mean earth-sun distance outside the atmosphere. It is given as 1367W/m^2.

$$\cos(\phi) = \sin(L)\sin(\delta) + \cos(L)\cos(\delta)\cos(h) \quad 3.20$$

From Eq. 3.19,

$$G_{on} = 1367\left[1 + 0.0033 \cos(\frac{7\times360}{365})\right]$$

$$G_{on} = 1367(1.00328)$$

$$G_{on} = 1371.5 W/m^2$$

From Eq. 3.20,

$$\cos(\phi) = \sin(5.485)\sin(-22.912) + \cos(5.485)\cos(-22.912)\cos(0)$$

$$\cos(\phi) = 0.879$$

Then, Eq. 3.18 gives,

$$G_{OH} = 1371.5 \times 0.879$$

$$G_{OH} = 1204.6\, W/m^2$$

The atmospheric transmittance, τ_b for beam radiation through the clear atmospheres is by:

$$\tau_b = a_1\, exp\left(\frac{-K}{\cos\theta_2}\right) + a_0 \qquad 3.21$$

For a clear sky with 23km visibility, the constant $a_0,\ a_1\ and\ K$ in the above correlation are evaluated from $a_0^*, a_1^*\ and\ K^*$ as shown in the relation below for altitudes less than 25km:

$$a_0^* = 0.4237 - 0.00821(6 - A)^2 \qquad 3.22$$

$$a_1^* = 0.5055 + 0.00595(6.5 - A)^2 \qquad 3.23$$

$$K^* = 0.2711 + 0.01858(2.5 - A)^2 \qquad 3.24$$

Where A is the altitude of the observer in km. The correction factor applied to $a_0^*, a_1^*\ and\ K^*$ are, respectively,

$$r_0 = {a_0}/{a_0^*} \qquad 3.25$$

$$r_1 = {a_1}/{a_1^*} \qquad 3.26$$

$$r_K = {K}/{K^*} \qquad 3.27$$

From the altitude map, the altitude of Owerri, A_{owerri} is given as $72.72m\ or\ 0.07272km$. Substituting for A= 0.07272 in Eqs 3.22 to 3.24, $a_0^*, a_1^*\ and\ K^*$ can be evaluated. Depending on the climate under study, the values of $r_0, r_{1,}\ and\ r_k$ can be obtained from table 3.1, and with that, the values of $a_0,\ a_1\ and\ K$ can be estimated from Eqs 3.25 to 3.27.

Table 3.1: Correction Factor for different climates (Hottel, 1976)

Climate Type	r_0	r_1	r_k
Tropical	0.95	0.98	1.02
Mid latitude Summer	0.97	0.99	1.02
Subarctic Summer	0.99	0.99	1.01
Mid latitude Winter	1.03	1.01	1.00

The values obtained for the various parameters from equations 3.22 to 3.27, are tabulated in Table 3.2.

Table 3.2: Constants for transmissivity of the atmosphere

a_0^*	a_0	a_1^*	a_1	K^*	K
0.135	0.128	0.751	0.736	0.380	0.388

Therefore, the atmospheric transmittance (Eq. 3.21) is finally evaluated as:

$$\tau_b = 0.128 + 0.736\ exp\left(\frac{-0.388}{\cos\theta_z}\right)$$

Where $\cos\theta_z$ is the cosine of the zenith angle.

But,

$$\sin(\theta_z) = \cos l \cos h \cos(\delta) + \sin l \sin \delta \qquad 3.28$$

$$\sin(\theta_z) = 0.8796$$

$$\theta_z = Sin^{-1}(\theta_z) \qquad 3.29$$

$$\theta_z = 61.64°$$

And, $\cos\theta_z = \cos(61.64)$

$$\cos\theta_z = 0.475$$

Therefore,

$$\tau_b = 0.128 + 0.736exp\left(\frac{-0.388}{0.475}\right)$$

$$\tau_b = 0.603$$

And,

$I_{b-horizontal} = G_{OH}\, x\, \tau_b = 1201.6 \times 0.603$

$\boldsymbol{I_{b-horizontal} = 724.2\ W/m^2}$

According to Duffie and Beckman (2013), the clear-sky diffused radiation (I_d) on a horizontal surface can be calculated from empirical relationship between the transmission coefficient for beam and diffuse radiation for clear days from:

$$\tau_d = \frac{I_d}{I_o} = 0.271 - 0.294\tau_b \qquad 3.30$$

τ_d is the ratio of the diffused radiation to the extraterrestrial beam radiation on the horizontal plane, $I_o = G_{OH}$, is the extraterrestrial beam radiation in the horizontal plane and is substituted for I_d in equation (3.30). Hence,

$\frac{I_d}{I_o} = 0.271 - 0.294\tau_b$

$\frac{I_d}{I_o} = 0.271 - 0.294(0.603)$

$\frac{I_d}{I_o} = 0.0868$

Putting the value of $I_o = G_{OH}$

$I_d = 0.08686 \times 1201.6$

$\boldsymbol{I_d = 104.23 W/m^2}$

The view factor component between the atmosphere and the radiative cooler is calculated using:

$$F' = {}^1/_2\,(1 + \cos(\alpha)) \qquad 3.31$$

Where $F^{'}$ is the view factor between the atmosphere and the radiative cooler.

$$F^{'} = {}^{1}/_{2}\,(1 + \cos(35))$$

$$F^{'} = 0.91$$

$$G_B = I_d \times F^{'} \qquad 3.32$$

$$\boldsymbol{G_B = 94.8 W/m^2}$$

Similarly**,** for the ground reflection,

$$G_B = F^{''} \qquad 3.33$$

Where $F^{''}$ is the view factor between the ground and the radiative cooling system and is given by:

$$F^{''} = {}^{1}/_{2}\left(\frac{1-\cos(\alpha)}{2}\right) \qquad 3.34$$

$$F^{''} = {}^{1}/_{2}\left(\frac{1-\cos(35)}{2}\right) \qquad 3.35$$

$$F^{''} = {}^{1}/_{2}\left(\frac{1-\cos(35)}{2}\right)$$

$$F^{''} = 0.0904$$

To finally evaluate the ground radiation, the ground reflectivity when the ground is bare and dry, ρ_g is approximated to $\rho_g = 0.2$ (Duffie and Beckman, 1991). Therefore,

$$G_G = (G_D + G_B) \qquad 3.36$$

$$G_G = 104.23 + 726.4$$

$$\boldsymbol{G_G = 831.03 W/m^2}$$

$$G_G = 0.2 \times 0.0904 \times 831.03$$

$$\boldsymbol{G_G = 145.03 W/m^2}$$

$$G_B = R_B \times I_B \quad (3.37)$$

$$G_B = 1.13 \times 726.4$$

$$\boldsymbol{G_B = 920.6 W/m^2}$$

$$G_T = G_B + G_D + G_G \quad (3.38)$$

$$G_T = 920.6 + 95.2 + 15.03$$

$$\boldsymbol{G_T = 1030 W/m^2}$$

According to Cengel (2002), the transmissivity of an opaque surface is zero. But, the sum of the absorptivity (α) and reflectivity (ρ) is unity. Hence, from Eq. 3.11,

$$\alpha = 1 - \rho_{rad} \quad (3.39)$$

According to Huang et al (2022), the reflectivity of a Mesoporous Polyethylene Aerogel is 0.97. Hence, the absorptivity is given as:

$$\alpha = 1 - 0.97$$

$$\alpha = 0.03$$

Given the reflectivity of the proposed cooling coating to be 0.97, the sun's radiation absorbed by the cooling coating is given by:

$$P_{sun} = \alpha G$$

$$P_{sun} = 0.03 \times 1030.5$$

$$\boldsymbol{P_{sun} = 30.915 W/m^2}$$

3.2.3 Radiation from the MPEA Cooler

Radiation from the cooler, which is the energy radiated by the cooler determines the cooling power of the radiative cooler and is calculated using the formula:

$$P_{rad} = A\varepsilon\sigma T^4 \quad 3.40$$

The emissivity of the MPEA coating is 0.90 (Huang et al, 2022), and a drop of 9^o was recorded in the ambient temperature.

$$T_{rad} = T_{amb} - 9$$

$$T_{rad} = 32 - 9$$

$$T_{rad} = (23 + 273)K = 296K$$

$$P_{rad} = 0.90 \times 5.67 \times 10^{-8} \times 302^4$$

$$\boldsymbol{P_{rad} = 424.476 W/m^2}$$

3.2.4 Conduction and Convection

The heat transferred to the cooler (W/m^{2}K) from the environment due to conduction and convection losses is given by:

$$P_{cond+conv} = h_c(T_{amb} - T_{rad}) \quad 3.41$$

Where the heat transfer coefficient, h_c according to Lin et al (2020) is given as:

$$h_c = 2.5 + 2v \quad 3.42$$

$$h_c = 2.5 + 2x3.55$$

$$h_c = 9.6 \text{ W/m}^2$$

$$P_{cond+conv} = 9.6(32 - 23)$$

$$P_{cond+conv} = 9.6 \times 3$$

$$\boldsymbol{P_{cond+conv} = 28.8 W/m^2}$$

From the above calculations of the values of the components of the energy balance equation of the system, the net radiative power of the radiative cooling system is therefore, given as:

$$\boldsymbol{P_{cool} = P_{rad} - P_{atm} - P_{cond+conv} - P_{sun}}$$

$$\boldsymbol{P_{cool} = 424.476 - 319.392 - 28.8 - 30.915}$$

$$\boldsymbol{P_{cool} = 45.369 W/m^2}$$

With the area of the cooler $A_{rad} = 0.16m^2$, the effective power of the cooler in W/m^2 is calculated to be

$$P_{cool} = 7.259W$$

3.3 Determination of the Thicknesses of MPEA/$BaSO_4$ Radiative Cooler

For optimum operation of the radiative cooler, it is necessary to determine the ideal thicknesses of the various layers of the radiative cooler. This is done to ensure optimal performance of the system. The angle of incidence of the sun, θ_i is required to successfully calculate the thickness of the different layers of the radiative cooler.

The angle of incidence of the sun is calculated from the relation (Hottel, 1976):

$$\cos\theta_i = \sin\delta \sin\phi \cos\alpha + \sin\delta \cos\phi \sin\alpha \cos A_{ZS} + \cos\delta \cos\phi \sin\alpha \cos h - \cos\delta \sin\phi \sin\alpha \cos A_{ZS} \cos h - \cos\delta \sin\alpha \sin A_{ZS} \sin h \quad (3.43)$$

Where δ is the declination angle, the angular position of the sun at solar noon with respect to the plane of the equator; α is the tilt angle which is the angle between the plane of the surface in question and the horizontal. ϕ is latitude, the angular location north or south of the equator; h is the Hour angle, the angular displacement of the sun east or west of the local meridian due to rotation of the earth on its axis at 15◦ per hour; A_{ZS} is the Solar altitude angle, the angle between the horizontal and the line to the sun.

The maximum solar peak is at noon. Thus, h = 0. δ is the declination angle, which is the angular position of the solar noon with respect to the plane of the equator.

But $h = 0°, \alpha = 35°, A_{ZS} = 90°, \phi = 5.4, \delta = -22.912°$

Substituting the above values into Eq. 3.43 simplifies it to:

$$\cos\theta_i = \sin\delta \sin\phi \cos\alpha + \sin\delta \cos\phi \sin\alpha \cos A_{ZS} \quad 3.44$$

$$\cos\theta_i = \sin(-22.912)\sin(5.4)\cos(35) + \sin(-22.912)\cos(5.4)\sin(35)\cos(90)$$

$$\cos\theta_i = 0 - 0.2205$$

$$\theta_i = \cos^{-1}(0.2205)$$

$$\theta_i = 91.26°$$

3.3.1 Thickness of MPEA or $BaSO_4$ layer

The thickness, d of the thin film layer of MPEA or $BaSO_4$ can be calculated using the expression (Sun et al, 2023).

$$d = \frac{\pi\lambda_0}{4n\times\theta_i} \quad 3.45$$

Where n is defined as the refractive index of the material, λ_0 is the wavelength of the material with values $n = 3.3255\ at\ 0.3\mu m$ and $n = 2.2477\ at\ 2.5\mu m$.

Therefore, at $\lambda_0 = 0.3\mu m$,

$$d = \frac{\pi\lambda_0}{4n\times\theta_i} = \frac{\pi\times0.3}{4\times3.3255\times1.59279} = 0.044\mu m$$

And at $\lambda_0 = 2.5\mu m$,

$$d = \frac{\pi\lambda_0}{4n\times\theta_i} = \frac{\pi\times2.5}{4\times2.2477\times1.59279} = 0.055\mu m$$

3.4 Fabrication of DPRC prototypes and Description of the Experimental Setup

After the design, the specifications were sent to the thin film Laboratory of Namiroch Nig. Ltd, Abuja, where the prototypes were fabricated. The following section outlines the fabrication processes used in producing the radiative cooler prototypes. The coolers consist of layers of Mesoporous Polyethylene Aerogel (MPEA) and Barium Sulphate ($BaSO_4$) all deposited on a silver reflector.

3.4.1 Fabrication of the MPEA

The thermally induced phase separation (TIPS) method of aerogel formation was adopted in the fabrication of the sample of the MPEA. The MPEA was made by combining an antioxidant and a polymer that were all bought from Sigma-Aldrich [UK] in a solvent. In a sealed beaker maintained at room temperature, the ultrahigh-molecular weight polyethylene polymer [0.5 weight percent (wt%); 429015] was combined with 99.3 weight percent paraffin oil (76235) as a solvent and 0.2 weight percent butylated hydroxytoluene (W218405) as an antioxidant. The solution was then heated to 150°C in a silicone oil bath and stirred with a magnetic stirrer for approximately 30 minutes to achieve a complete dissolution of the polymer in the solvent. The homogenous solution was then poured into a heated circular aluminum mold with a 10 cm diameter and a 6-mm depth. The mold was then inserted in a water bath at 5°C, initiating the TIPS and resulting in a polymer gel.

The paraffin oil and then the hexane were removed using a three-step solvent exchange process, which was required to ensure chemical compatibility with the critical point dryer that was used to dry the gel. The critical point drying method prevented the porous structure from collapsing during the process by replacing the ethanol from the PEA with air. It is important to note that the initial polymer concentration was selected to maximize the gel's structural integrity, infrared transmittance, and solar reflectivity during the fabrication process. The sample thickness was chosen as a compromise between the number of samples required for the experiments to achieve the desired thicknesses and the fabrication time. The above processes are detained schematically as shown in Fig. 3.5

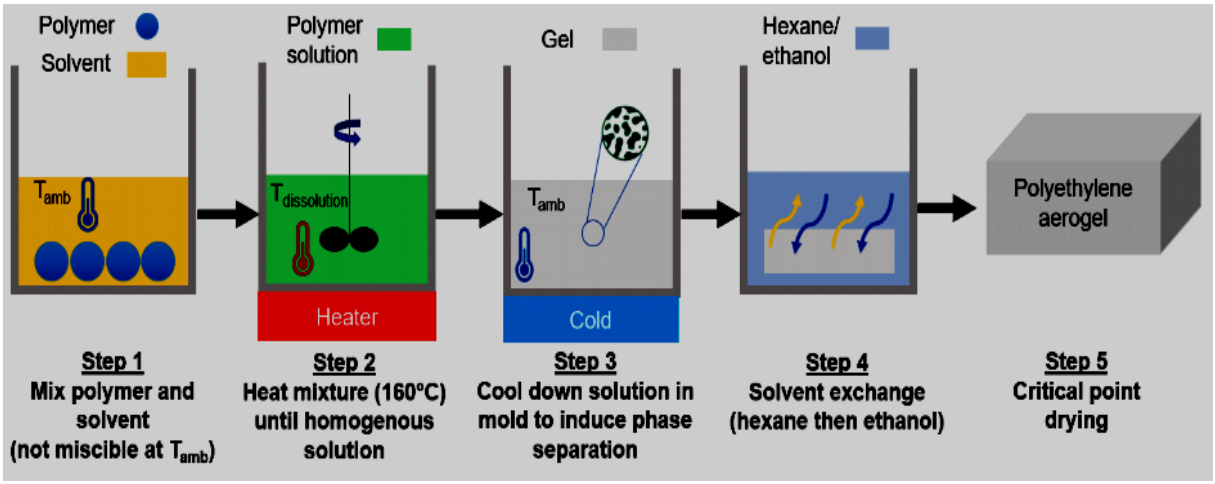

Fig. 3.5: The fabrication process of Mesoporous Polyethylene Aerogels

The major setback associated with the above method for aerogel preparation is that of shrinkage and breakage as shown on the sample in Fig. 3.6.


Fig. 3.6 Schematic of the collapsed MPEA structure

Following the above setback, a novel method was adopted where the Paraffin oil was replaced with Toluene while the hexane was replaced with acetone. Similarly, instead of replacing the ethanol from the PEA with air using the critical point drying method, propanol was washed off using water.

Therefore, other several steps were adopted in the final preparation of the polyethylene aerogel cooler structure. 3.5g of the high-density polyethylene (HDPE), 0.5 weight % (wt %) was dissolved directly in a 100ml of toluene from Sigma Aldrich. The mixture was heated to 170^{o}C and stirred for about 30 minutes on a hot plate stirrer until a homogenous solution is obtained. The solution obtained above is

rapidly quenched by pouring it into the circular aluminum tray, which was subsequently immersed in an ice bath to initiate the thermally induced phase separation (TIPS) process, which results in the formation of a polymer gel. Next, the solvent was gradually removed from the gel by exchanging it multiple times with first Acetone followed by absolute propanol to remove the acetone (all purchased from Sigma Aldrich, UK). Finally, distilled water was used to wash off the propanol before drying. The gel is vacuum filtered and dried on a hot plate at 70^{o}C for 4 hours. The uncracked, which is the final MPEA sample as shown in Fig. 3.7 was cut into a 40mm square flat shape and mounted on the square cavity created on the diurnal radiative cooling test chamber.

Fig. 3.7: Schematic of the final MPEA structure

3.4.2 Preparation of barium sulfate ($BaSO_4$) Nano crystals

The preparation of the barium sulphate involves the use of the following materials such as Barium Chloride (from Kermel), Absolute Ethanol (from Sigma Aldrich), sodium sulphate (from Molychem), acrylic emulsion (from Visa Petroleum Resources Ltd) and distilled water. All chemicals were of analytical grade and were used without further purification. The preparation of the barium sulphate nano crystals involves a precipitation method, which is briefly presented. The precursor solutions were

prepared by dissolving the Barium Chloride (solution A) and Sodium Sulphate salt (solution B) separately to form 0.5M and 0.6 M solutions respectively in de-ionized water in the case of batch 1 and 70% ethanol, in the case of batch 2. Solutions A and B of the respective batches were mixed together with minimum stirring using a magnetic stirrer to create barium sulphate of mixed sizes. The reaction was performed at room temperature. Next, the products (from the two batches) were aged for six hours and subsequently purified by centrifugal action at 4000 RPM, and finally washed with water. The two batches (1&2) were mixed together to form multi-sized Barium sulphate nanocrystals. The washed nano crystals were transferred to a filter paper and dried on a temperature-controlled hot plate at 70^{o}C. The final barium sulphate sample as shown in Fig. 3.8 was cut into a 40mm square flat shape to be mounted on the square cavity created on the diurnal radiative cooling test chamber.

Fig. 3.8: Schematic of the $BaSO_4$ structure

3.4.3 Construction of the diurnal radiative cooling test chamber

The diurnal radiative cooling test chamber is rectangular in shape made of pieces of plywood for the two rectangular sides and the base, each measuring 200*130mm, and two pieces of 130mm x 130mm for the square end sides. The sides are joined with wood adhesive and secured further with 1inch nails. Thereafter, two 10mm thick square cavity of dimension 40mm was created in the polystyrene block

measuring 200 x130 x 20mm for mounting the Mesoporous Polyethylene Aerogel and Barium Sulphate structures, which is deposited on a substrate with silver as reflector on top to serve the purpose of the emitter. The polystyrene block measures 200mm x 150mm in area and 80mm in height and was positioned at about 200mm away from the open end of the chamber. A Low-Density Polyethylene (LDPE) is placed (200mm) above the MPEA and $BaSO_4$ as a windscreen. The LDPE is transparent across all wavelengths and allows both the shortwave and longwave radiations in the solar and atmospheric window spectra. A rectangular hole was bored on the side of the box to make provision for cable passage for the data logger connection. This was sealed off with an adhesive to minimize heat gain and loss by the system. Additionally, the test chamber was sealed with aluminum foil to reflect unwanted incident sunrays. The set-up of the test chamber mimicking the building envelope is as shown in the Fig. 9. The detailed drawing of the test chamber with the various views are presented in Appendix A.

Fig. 3.9: Test chamber before preloading with the selective radiative surfaces

In order to control heat gained by the setup, wood, which is a poor conductor was chosen as the major material for the support. The wood was cut to appropriate sizes according to design specifications. Vertical support was fastened with nails at the end side of the frame whose height gives the desired tilt angle to the diurnal radiative cooling test chamber.

3.5 Instrumentation and Experimentation

3.5.1 Instrumentation

Fig. 3.10: The experimental setup

To explore the performance of the diurnal passive radiative coolers, the experimental set-up was designed as shown in Fig. 3.10. The set-up comprises diurnal passive radiative test chamber loaded with two 40mm by 40mm cavities bearing the silver substrate with Mesoporous Polyethylene Aerogel and Barium Sulphate nanocrystal. The MPEA passive radiative cooler was fabricated using the thermally induced phase separation method (TIPS) of aerogel formation while the Barium Sulphate nanocrystal ($BaSO_4$) was prepared using a precipitation method (PM). It also has a LDPE windscreen at the top, placed 200mm above the MPEA and $BaSO_4$ surfaces. It is highly transparent and was employed to ensure high transmission of solar radiation, while blocking out convective heat transfer from the coolers. It also limits air draft (air coming into and going out of the chamber) and prevents

debris from entering the test chamber. The cavities bearing the MPEA and $BaSO_4$ nanocrystal samples were placed at the center of the test chamber on a thick polystyrene foam to reduce heat conduction between the specimen and the chamber. Provisions were made through the chamber to connect self-adhesive DHT11 (K-type) thermocouple temperature sensors to the MPEA and $BaSO_4$ nanocrystal structures and another DHT11 sensor was appropriately positioned to measure the ambient temperature. The DTH11 sensors were connected to the HOBO Onset data logger interfaced with a personal computer for real time temperature monitoring and recording. All thermocouples were calibrated using a precision immersion-style resistance temperature detector (RTD) sensor before use. Other instruments that made up the test bed include solarimeter, wind vane and humidity sensors for measuring solar irradiation, wind speed and relative humidity during the test period. The test set-up is a mobile structure that makes it easily moveable to other locations for evaluation.

3.5.2 Experimentation

Field tests were conducted using the set-up in three different study locations, namely Owerri, Imo State, Abuja, and Afikpo, Ebonyi State, Nigeria at different periods or seasons of the year. The choice of Abuja was to carry out a preliminary trial to ascertain the functionality of the system since it is the fabrication center. Afikpo was chosen because it mimicked a coastal area while Owerri is the actual study center. The first set of field trials was carried out in the open field in the building of Namiroch Nigeria Ltd Laboratory, Abuja on the 18th to 22nd of May, 2023. The test spanned a period of 7am to 6:00pm on the 18th of May, while it ran for four consecutive days from 7:00am on the 19^{th} to 11:00pm on the 22nd of May, 2023. After calibrating the sensors, the data logger was first configured and launched with the ON/OFF button before logging started. The temperatures of the two DPRC samples, namely MPEA and $BaSO_4$ were recorded and stored in the data acquisition device (HOBO Onset data logger) at every one-minute interval for the specified days of the tests. The incident solar radiation was

measured with solar intensity meter (secondary standard pyranometer). A humidity sensor was used to measure the humidity while silicon heat mat was used the heating power.

Radiative cooling experiments were repeated at the Department of Mechanical Engineering Building, Federal University of Technology, Owerri, Imo State from [July 12] to [July15] 2023; and open field of Deeper Life Bible Church, Afikpo, Ebonyi State, from [July 09] to [July 11] 2023 which ran for three consecutive days for a 24 hours cycle starting from 6:00am each day. DHT11 temperature sensors were also used to pick the temperature of the cooler and the ambient temperature. The data logger was employed to record the samples of the MPEA and $BaSO_4$ and ambient temperatures every 5 minutes and the meteorological data including wind speed, humidity, and solar irradiation were collected with high-precision devices every 30 minutes interval.

The data obtained from the above tests are presented in Appendices B, and C respectively, and results are analysed, presented and discussed accordingly in chapter four.

3.6 Formulation of Model Equations

Numerical study provides a detailed insight into the complex heat transfer phenomena occurring in the diurnal passive radiative cooling system, and helps in quantifying the cooling performance of the system. The temperature history and cooling power of the DPRC can be predicted in virtually all climates including the ones where the field tests have been conducted, using a generic model. The modelled DPRC is shown in Fig. 3.11. Fig. 3.11 is the section view of Fig. 3.9 showing MPEA or $BaSO_4$ nanocrystal deposited on the silver reflector substrate. The whole structure is sitting on a polystyrene foam embedded in the wooden frame as shown. The transparent LDPE windscreen is clearly shown positioned at a distance from the DPRC.

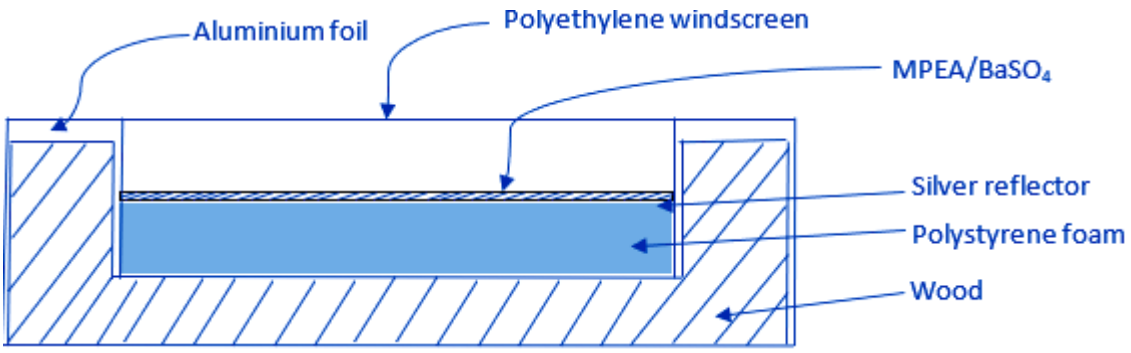

Fig. 3.11: Configuration of the modelled DPR cooler

Formulating the model equation for the DPRC system involves the development of the mathematical model for the transient analysis and optimization of the system. The model development comprises two major sections, namely, diurnal radiative cooling occurring from 0:6-16:00 hours and nocturnal radiative cooling occurring from 22:00-06:00 hours. The differential equations for the spectral selective emitter are developed for the two operating periods. The physics of solar radiation and basic principles of heat transfer are employed in the formulation and modelling of the system. The heat fluxes and temperature differentials are detailed to predict the temperature of the system and hence, serve as a useful tool to allow any user to predict its performance in a given location and orientation. The DPRC section of Fig.3.11 with the energy interchange with the surroundings is shown in Fig.3.12.

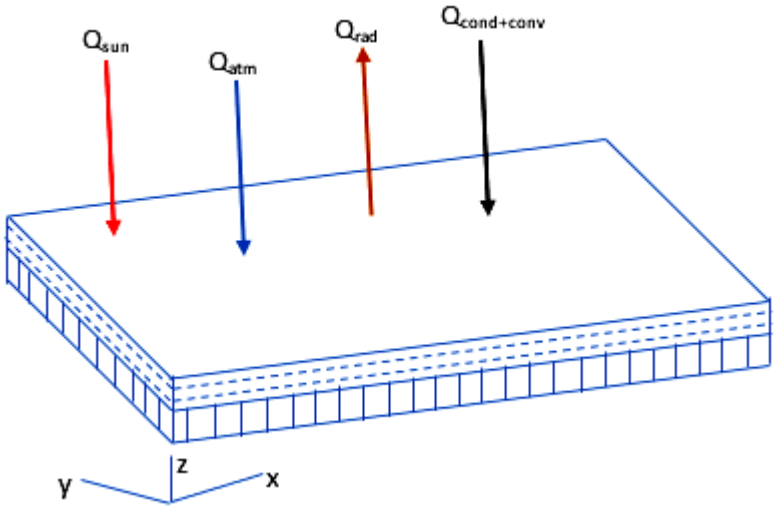

Fig.3.12. DPRC and energy interchange with the surroundings

3.6.1 Simplifying Assumptions

In formulating the governing equations for the energy interaction between the passive radiative cooler (PRC) and the environment, the following assumptions were made.

a. The radiative cooler is considered a single control volume with a negligible thermal capacitance.
b. The heat transfer within the selective surface is treated as a three-dimensional heat exchange. This is so because the radiative panel of thickness of about 4mm is reasonable for heat flow across the thickness. Hence, heat flow in the plate is by conduction along the length, width and height (thickness).
c. The optical properties are dependent on the optical characteristics of the material of the emitter.
d. The material of the cooler is homogeneous and the thermo-physical properties do not vary with temperature. This is so because though there is a variation of these properties with temperature but this variation is insignificant to reasonably alter their performance in the system and temperature range under study.
e. There is no internal heat generation in the selective emitter. This is because there is no inherent auto-energy generation in the cooler structures.
f. Only the top heat losses are accounted for. It is assumed that the edge and bottom of the RC system are sufficiently insulated and thus edge and bottom heat losses are considered negligible.
g. Heat losses to the ambient from the emitter are by radiation and convection, considering eddy effects.

3.6.2 Energy Balance Equations

The control volume approach is adopted in the development of the governing equations. The control volume of the DPRC systems is as shown in Fig. 3.13.

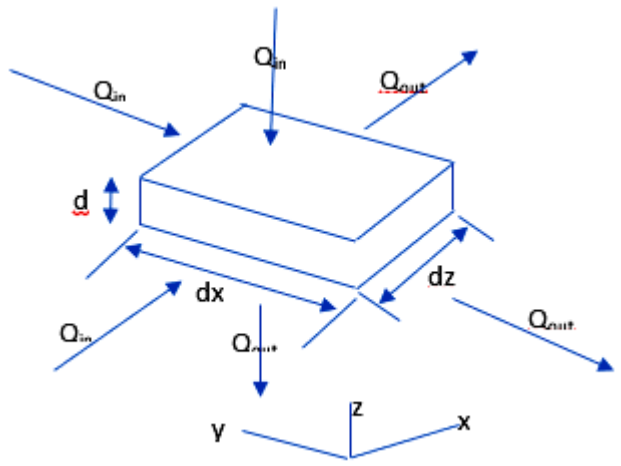

Fig. 3.13: Schematic illustration of the Control Volume

From the law of conservation of energy, the general energy balance for a control volume can be expressed as:

$$\begin{aligned} &The\ net\ energy\ flux\ of\ the\ control\ volume\ + \\ &Internal\ Heat\ generation\ in\ the\ control\ volume\ = \\ &Rate\ of\ increase\ in\ internal\ Energy\ of\ the\ control\ volume \end{aligned} \qquad 3.46$$

This implies in mathematical terms that:

$$Q_{in} - Q_{out} + Q_{i.gen} = Q_{int} \qquad 3.47$$

Alternatively,

$$Q_{in} + Q_{i.gen} = Q_{out} + Q_{int} \qquad 3.47$$

From the control volume of Fig 3.13, the heat flow into the control volume, Q_{in} is given by:

$$Q_{in} = Q_x + Q_y + Q_z + Q_{solar} + Q_{atm} \qquad 3.48$$

Where Q_x is the heat flow into the control volume in the x-direction, Q_y is the heat flow into the control volume in the y-direction, Q_z is the heat flow into the control volume in the z-direction; Q_{solar} is the incident solar radiation and Q_{atm} is the absorbed atmospheric downward radiation.

The heat into the control volume along y-z plane (x-direction), is given by Fourier relation as [Nwaji, 2019]:

$$Q_{in-x} = -k_x A \frac{\partial T}{\partial x} \quad 3.49$$

Where A is the cross-sectional area of the control volume in the x-direction and k_x is the thermal conductivity of the material of the cooler.

From Fig. 3.13, $A = dydz$. Thus equation 3.49 becomes:

$$Q_{in-x} = -k_x dydz \frac{\partial T}{\partial x} \quad 3.50$$

Similarly, the heat flux into the control volume in the y-direction is given as:

$$Q_{in-y} = -k_y \frac{\partial T}{\partial z} dxdz \quad 3.51$$

Also, the heat flux into the control volume in the z-direction is given as:

$$Q_{in-z} = -k_z \frac{\partial T}{\partial z} dxdy \quad 3.52$$

Thus, the total heat flux into the control volume is obtained by substituting Equations 3.50, 3.51 and 3.52 into Eq. 3.48, yielding:

$$Q_{in} = -\left(k_x \frac{\partial T}{\partial x}\right) dydz + \left(-k_y \frac{\partial T}{\partial y} dxdz\right) + \left(-k_z \frac{\partial T}{\partial z}\right) dxdy + Q_{solar} dxdz + Q_{atm} dxdz \quad 3.53$$

Also, from Fig. 3.13, the heat flux out of the control volume, Q_{out} is mathematically written as follows:

$$Q_{out} = Q_{x+dx} + Q_{y+dy} + Q_{z+dz} + Q_{rad} + Q_{losses} \quad 3.54$$

Where Q_{x+dx} is the heat conducted out of the control volume in the x-direction; Q_{y+dy} is the heat conducted out of the control volume in the y-direction; Q_{z+dz} is the heat conducted out of the control volume in the z-direction; Q_{rad} is the heat thermally radiated by the radiative cooler within the atmospheric transparency window, and Q_{losses} is the total heat losses due to conduction and convection.

The heat flux out of the control volume in the x-direction, Q_{x+dx} expanded using the Taylor series expansion is given as:

$$Q_{x+dx} = Q_x + \frac{\partial Q_x}{\partial x} dx \quad 3.55$$

Substituting for Q_x in Eq.3.55 results in:

$$Q_{x+dx} = -k_x \frac{\partial T}{\partial x} dydz + \frac{\partial}{\partial x}(-k_x dydz \frac{\partial T}{\partial x} dx)$$

Which simplifies to:

$$Q_{x+dx} = \left[-k_x\left(\frac{\partial T}{\partial x}\right) + \frac{\partial}{\partial x}\left(-k_x\frac{\partial T}{\partial x}\right)dx\right]dydz \quad 3.56$$

Similarly, in the y-direction and z-direction, the heat flux out of the control volume is given as:

$$Q_{y+dy} = \left[-k_y\left(\frac{\partial T}{\partial y}\right) + \frac{\partial}{\partial y}\left(-k_y\frac{\partial T}{\partial y}\right)dy\right]dxdz \quad 3.57$$

$$Q_{z+dz} = \left[-k_z\left(\frac{\partial T}{\partial z}\right) + \frac{\partial}{\partial z}\left(-k_z\frac{\partial T}{\partial z}\right)dz\right]dxdy \quad 3.58$$

In summary, the total heat flux out of the control volume is obtained by substituting Eqs 3.56 and 3.57, and 3.58 into Eq 3. 54, resulting into:

$$Q_{out} = \left[-k_x\left(\frac{\partial T}{\partial x}\right) + \frac{\partial}{\partial x}\left(-k_x\frac{\partial T}{\partial x}\right)dx\right]dydz + \left[-k_y\left(\frac{\partial T}{\partial y}\right) + \frac{\partial}{\partial y}\left(-k_y\frac{\partial T}{\partial y}\right)dy\right]dxdz + \left[-k_z\left(\frac{\partial T}{\partial z}\right) + \frac{\partial}{\partial z}\left(-k_z\frac{\partial T}{\partial z}\right)dz\right]dxdy + Q_{rad}dxdz + Q_{losses}dxdz \quad 3.59$$

The net heat flux into the control volume and the absorbed solar energy result in increase in the thermal energy of the control volume. This is given by the rate of change of the heat capacity of the control volume with respect to time and is expressed as:

$$Q_{int.} = \rho_e c_{p-e}\frac{\partial T}{\partial t}dxdydz \quad 3.60$$

Where ρ_e = density of the radiative cooling material (emitter) and

c_{p-e} = specific heat capacity of the radiative cooling material (emitter)

Therefore, the energy balance of the control volume is obtained by substituting Eqs 3.53, 3.59 and 3.60 into equation 3.47. This gives,

$$-\left(K_x\frac{\partial T}{\partial x}\right)dydz + \left(-K_y\frac{\partial T}{\partial y}dxdz\right) + \left(-K_z\frac{\partial T}{\partial z}\right)dxdy + Q_{solar}dxdz + Q_{atm}dxdz + Q_{i.gen}dxdydz = \left[-K_x\left(\frac{\partial T}{\partial x}\right)dydz + \frac{\partial}{\partial x}\left(-K_x\frac{\partial T}{\partial x}\right)dx\right]dydz + \left[-K_y\left(\frac{\partial T}{\partial y}\right) + \frac{\partial}{\partial y}\left(-K_y\frac{\partial T}{\partial y}\right)dy\right]dxdz + \left[-K_z\left(\frac{\partial T}{\partial z}\right)dxdy + \frac{\partial}{\partial z}\left(-K_z\frac{\partial T}{\partial z}\right)dz\right]dxdy + Q_{rad}dxdz + Q_{losses}dxdz + \rho_e c_{p-e}\frac{\partial T}{\partial t}dxdydz. \quad 3.61$$

Expanding equation 3.61 and simplifying gives

$$-K_x\left(\frac{\partial T}{\partial x}\right)dydz\ -\ K_y\left(\frac{\partial T}{\partial y}\right)dxdz - K_z\left(\frac{\partial T}{\partial z}\right)dxdy + Q_{solar}dxdz +\ Q_{atm}dxdz + Q_{i.gen}dxdydz =$$
$$-K_x\left(\frac{\partial T}{\partial x}\right)dydz - \frac{\partial}{\partial x}\left(K_x\frac{\partial T}{\partial x}\right)dxdydz - K_y\left(\frac{\partial T}{\partial y}\right)dxdz - \frac{\partial}{\partial y}\left(K_y\frac{\partial T}{\partial y}\right)dxdydz - K_z\left(\frac{\partial T}{\partial z}\right)dxdy -$$
$$\frac{\partial}{\partial z}\left(K_z\frac{\partial T}{\partial z}\right)dxdydz + Q_{rad}dxdz +\ Q_{losses}dxdz +\ \rho_e c_{p-e}\frac{\partial T}{\partial t}dxdydz$$

3.62

Rearranging by collecting similar terms together, equation 3.62 becomes:

$$-K_x\left(\frac{\partial T}{\partial x}\right)dydz + K_x\left(\frac{\partial T}{\partial x}\right)dydz\ - K_y\left(\frac{\partial T}{\partial y}\right)dydz + K_y\left(\frac{\partial T}{\partial y}\right)dydz\ - K_z\left(\frac{\partial T}{\partial z}\right)dxdy +$$
$$K_z\left(\frac{\partial T}{\partial z}\right)dxdy + \frac{\partial}{\partial x}\left(K_x\frac{\partial T}{\partial x}\right)dxdydz\ + \frac{\partial}{\partial y}\left(K_y\frac{\partial T}{\partial y}\right)dxdydz\ + \frac{\partial}{\partial z}\left(K_z\frac{\partial T}{\partial z}\right)dxdydz + Q_{solar}dxdz +$$
$$Q_{atm}dxdz + Q_{i.gen}dxdydz - Q_{rad}dxdz\ -\ Q_{losses}dxdz = \rho_e c_{p-e}\frac{\partial T}{\partial t}dxdydz$$

3.63

Therefore, the energy balance of the control volume is expressed as:

$$\frac{\partial}{\partial x}\left(K_x\frac{\partial T}{\partial x}\right)dxdydz\ + \frac{\partial}{\partial y}\left(K_y\frac{\partial T}{\partial y}\right)dxdydz\ + \frac{\partial}{\partial z}\left(K_z\frac{\partial T}{\partial z}\right)dxdydz + Q_{solar}dxdz +\ Q_{atm}dxdz +$$
$$Q_{i.gen}dxdydz - Q_{rad}dxdz -\ Q_{losses}dxdz = \rho_e c_{p-e}\frac{\partial T}{\partial t}dxdydz$$

3.64

Taking assumption 3 into cognizance, where the internal heat generation, $Q_{i.gen}$ = 0, then Equation 3.64 then becomes:

$$\frac{\partial}{\partial x}\left(k_x\frac{\partial T}{\partial x}\right)dxdydz\ + \frac{\partial}{\partial y}\left(k_y\frac{\partial T}{\partial y}\right)dxdydz\ + \frac{\partial}{\partial z}\left(k_z\frac{\partial T}{\partial z}\right)dxdydz + Q_{solar}dxdz +\ Q_{atm}dxdz -$$
$$Q_{rad}dxdz -\ Q_{losses}dxdz = \rho_e c_{p-e}\frac{\partial T}{\partial t}dxdydz$$

3.65

We know that equation 3.65 is of the form:

$$dQ = \nabla(K\nabla T)dxdydz \qquad 3.66$$

Where $dQ = Q_{int-energy} =\ \rho_e c_e\frac{\partial T}{\partial t}dxdydz$

$$\therefore \rho_e c_e\frac{\partial T}{\partial x}dxdydz =\ \nabla(K\nabla T)dxdydz \qquad 3.67$$

$$\rho_e c_e\frac{\partial T}{\partial x}dxdydz = (K\nabla^2 T)dxdydz \qquad 3.68$$

The Laplacian operator for a Cartesian coordinate system is given as $\nabla^2 = \frac{\partial^2}{\partial x^2} + \frac{\partial^2}{\partial z^2}$.

Therefore, Eq. 3.68 becomes:

$$\left[K_x\left(\frac{\partial^2 T}{\partial x^2}\right)dxdydz + K_y\left(\frac{\partial^2 T}{\partial y^2}\right)dxdydz + K_z\left(\frac{\partial^2 T}{\partial z^2}\right)dxdydz\right] + Q_{solar}dxdz + Q_{atm}dxdz - Q_{rad}dxdz - Q_{losses}dxdz = \rho_e c_{p-e}\frac{\partial T}{\partial t}dxdydz \quad 3.69$$

$$\left[K_x\left(\frac{\partial^2 T}{\partial x^2}\right) + K_y\left(\frac{\partial^2 T}{\partial y^2}\right) + K_z\left(\frac{\partial^2 T}{\partial z^2}\right)\right]dxdydz + [Q_{solar} + Q_{atm} - Q_{rad} - Q_{losses}]dxdz = \rho_e c_{p-e}\frac{\partial T}{\partial x}dxdydz \quad 3.70$$

Rearranging and simplifying, and considering homogeneity of material properties,

$$\rho_e c_{p-e}\frac{\partial T}{\partial t}dy = \left[\left(\frac{\partial^2 T}{\partial x^2}\right) + \left(\frac{\partial^2 T}{\partial y^2}\right) + \left(\frac{\partial^2 T}{\partial z^2}\right)\right]kdy + Q_{solar} + Q_{atm} - Q_{rad} - Q_{losses} \quad 3.71$$

3.6.3 Evaluation of model input parameters

The incident solar radiation, Q_{solar} comprises direct (or beam) radiation and diffuse radiation. Flat-plate spectrally selective surfaces are known to collect both beam and diffuse components of incident solar radiation (Nwaji, 2019). The diurnal passive radiative surface has different properties such as transmittance, absorptance and reflectance when solar radiation is incident on it. The diffuse component of the incident radiation, which is dependent on the proportion of the sky viewed by the surface decreases with the sky clearness while the beam radiation increases with the clearness of the sky (Amos, 2009). The short wavelength of radiation reaching any horizontal surface on the earth may be direct or diffuse. Emitters are not usually installed horizontally but given an inclination that is dependent on the latitude of the location of installation.

The DPRC flat surface on a horizontal and inclined surfaces are as shown in Figs 3.14a and b.

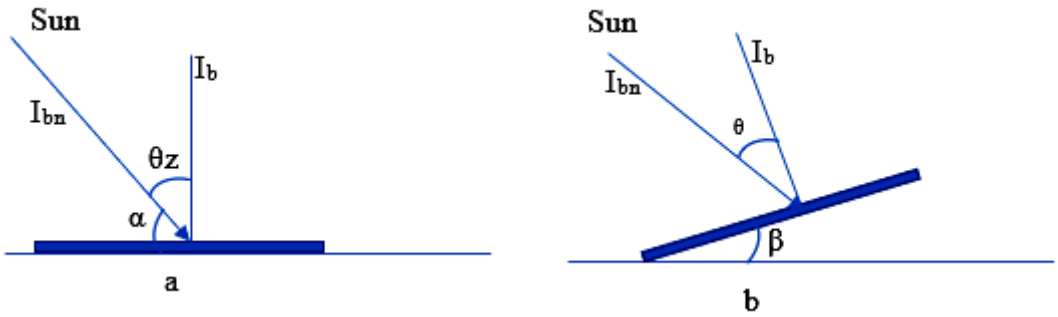

Fig. 3.14: Beam radiation on horizontal and inclined surfaces

The total amount of radiation from the sun, Q_{solar} on a tilted surface (solar radiation power) is given as the sum of set of radiation streams, comprising the beam radiation, the three components of diffuse radiation and the ground reflected radiation. Mathematically, it is given as Eq. 3.72.

$$Q_{solar} = I_{b,t} + I_{d,t} + I_{g,t} \qquad 3.72$$

Where, $I_{t,T}$ is the incident beam radiation on the tilted surface; $I_{d,t}$ is the incident diffused radiation on the tilted surface and $I_{g,t}$is the incident reflected radiation on the tilted surface.

When the tilt factor of the tilted surface is taken into consideration, the expression of the solar power can be given as Eq. 3.13:

$$Q_{solar} = I_b R_b + I_d \left(\frac{1+COS\alpha}{2}\right) + I_{\rho g} \left(\frac{1-cos\alpha}{2}\right)$$

Where, I_b is the beam radiation, I_d is the diffused radiation, $I_{\rho g}$ is the ground reflected radiation, and R_b is the beam radiation tilt factor.

According to Kalogirou (2014), the correlation for the beam radiation tilt factor, R_b is given by Eq. 3.14:

$$R_b = \frac{\cos\theta}{\cos(\phi)} = \frac{\sin(L-\alpha)\sin(\delta)+\cos(L-\alpha)\cos(\delta)\cos(h)}{\sin(L)\sin(\delta)+\cos(L)\cos(\delta)\cos(h)}$$

Where L is the latitude which is the angular location north of the equator and has a value of 5.4˚ for FUTO, α is the tilt angle which is the angle between the plane of the surface in question and the horizontal, δ is the declination angle, which is the angular position of the solar noon with respect to the plane of the equator, and h is the hour angle, which is zero at noon when the maximum solar peak occurs.

The declination angle can be correlated using Eq. 3.15.

$$\delta = \left(\frac{180}{\pi}\right)(0.006918 - 0.399912\cos B + 0.070257\sin B - 0.006758\cos 2B + 0.000907\sin 2B - 0.002697\cos 3B + 0.00148\sin 3B)$$

Where B is defined as Eq. 3.16.

$$B = (n-1)\frac{360}{365}$$

And n is the day number which is the nth day of the year in the range $1 \leq n \leq 365$. According to Arora (2009), the earth receives 7% more radiation in January than in July. Hence, January is assumed to have maximum solar radiation, with $n = 1$ on the first day.

The solar irradiation received on a horizontal surface under clear sky conditions is given by combining Eqs 3.17-3.20, yielding:

$$I_{b-hor} = \tau_d G_{sc}\left[1 + 0.033\cos(\frac{360n}{365})\right]\sin(L)\sin(\delta) + \cos(L)\cos(\delta)\cos(h) \qquad 3.73$$

$G_{sc}$is the energy from the sun per unit time received per unit area of a surface perpendicular to the direction of propagation of the radiation at mean earth-sun distance outside the atmosphere.

To successfully calculate τ_d, the atmospheric transmittance, τ_b for beam radiation through the clear atmospheres is necessary and is given by Eq. 3.21.

$$\tau_b = a_1 \, exp\left(\frac{-K}{\cos\theta_2}\right) + a_0$$

The constants $a_0,\ a_1\ and\ K$ from the above correlation for a clear sky are evaluated from Eqs 3.22-3.27, and table 3.1 as outlined before.

$$a_0^* = 0.4237 - 0.00821(6 - A)^2 \qquad 3.22$$

$$a_1^* = 0.5055 + 0.00595(6.5 - A)^2 \qquad 3.23$$

$$K^* = 0.2711 + 0.01858(2.5 - A)^2 \qquad 3.24$$

$$r_0 = {a_0}/{a_0^*} \qquad 3.25$$

$$r_1 = {a_1}/{a_1^*} \qquad 3.26$$

$$r_K = {K}/{K^*} \qquad 3.27$$

The clear-sky diffused radiation (I_d) on a horizontal surface is modelled from the empirical relationship between the transmission coefficient for beam and diffuse radiation for clear days, given as:

$$\tau_d = 0.271 - 0.294\tau_b \qquad 3.74$$

Noting also that τ_d is the ratio of the diffused radiation, I_d to the extraterrestrial beam radiation on the horizontal plane, I_o given as:

$$\tau_d = \frac{I_d}{I_o} \qquad 3.75$$

Since $I_o = G_{OH}$,

$$I_d = \tau_d G_{OH} \qquad 3.76$$

Therefore,

$$I_d = 0.271 - 0.294\tau_b * G_{sc}\left[1 + 0.033\cos(\frac{360n}{365})\right]\sin(L)\sin(\delta) + \cos(L)\cos(\delta)\cos(h) \quad 3.77$$

The above equations are substituted into Eq. 3.13 to make up the final expression for the solar irradiation incident on the cooler surface.

Noting that the model equations for Q_{atm}, Q_{rad}, $Q_{cond+conv}$ are the same as P_{sky}, P_{rad} and $P_{cond+conv}$, respectively, there are modelled as Eqs 3.2, 3.40 and 3.41 accordingly.

Therefore, the final model equation of energy interaction in the PRC is derived by substituting the expressions for Q_{solar}, Q_{atm}, Q_{rad} and $Q_{cond+conv}$ into Eq. 3.71, resulting in:

$$\rho_e c_{p-e} dy \frac{\partial T}{\partial t} = kdy\left[\left(\frac{\partial^2 T}{\partial x^2}\right) + \left(\frac{\partial^2 T}{\partial y^2}\right) + \left(\frac{\partial^2 T}{\partial z^2}\right)\right] kdy + I_b R_b + I_d\left(\frac{1+COS\alpha}{2}\right) + I_{\rho g}\left(\frac{1-cos\alpha}{2}\right) + \mathcal{E}_{sky}\,\sigma {T^4}_{sky} - A_c \varepsilon \sigma {T_s}^4 - h_c(T_{amb} - T_{rad}) \quad 3.78$$

3.6.4 Numerical solution methodology

To generate solution for the model equation (3.78), numerical discretization was done using the finite element numerical scheme. FlexPDE version 7.21/W64 3D was used to develop a code for the numerical solution of Eq. 3.78. The model was parameterized using the climatic data of the test locations for validation purposes. Thereafter, extensive sensitive analyses were done for the optimization of the cooling system. The results of the simulation are also presented and discussed in chapter four, while the numerical data from the simulation are presented in Appendices D, E, and F.

CHAPTER FOUR

RESULTS AND DISCUSSION

4.1 Results

The results obtained from the study are presented in figs 4.1-4.80. Figs 4.1-4.12 illustrate the experimental temperatures for $BaSO_4$ and MPEA with that of the ambient in the three experimental test locations of Abuja, Afikpo, and Owerri. The results of comparative studies for the performances of the coolers was presented in figs 4.1.13-4.1.18 whereas Figs 4.19-4.36 show the effect of climatic conditions such as relative humidity, wind and daily solar radiation on the performance of the radiative coolers in the test locations. Figs 4.37-4.45 presents the numerical results for $BaSO_4$ and MPEA in selected states of the geopolitical regions of Nigeria, which includes the three experimental test locations. Figs 4.46-4.54 illustrates the cooling powers of $BaSO_4$ together with MPEA for Afikpo and selected states in the six geopolitical zones of Nigeria. The results of the validation studies were presented in Figs 4.55-4.57 while Figs 4.58-4.71 show the thermal distribution on the $BaSO_4$ and MPEA coolers. Finally, the parametric studies were presented in Figs 4.72-4.80

4.1.1 Experimental Investigation

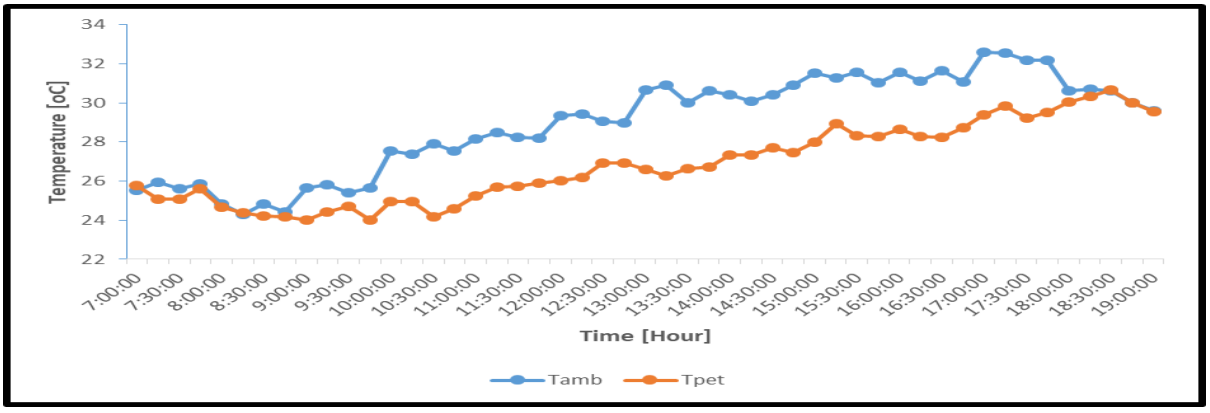

Fig. 4.1: Experimental cooler temperatures of MPEA, and Ambient on May 18, 2023 in Abuja, Nigeria

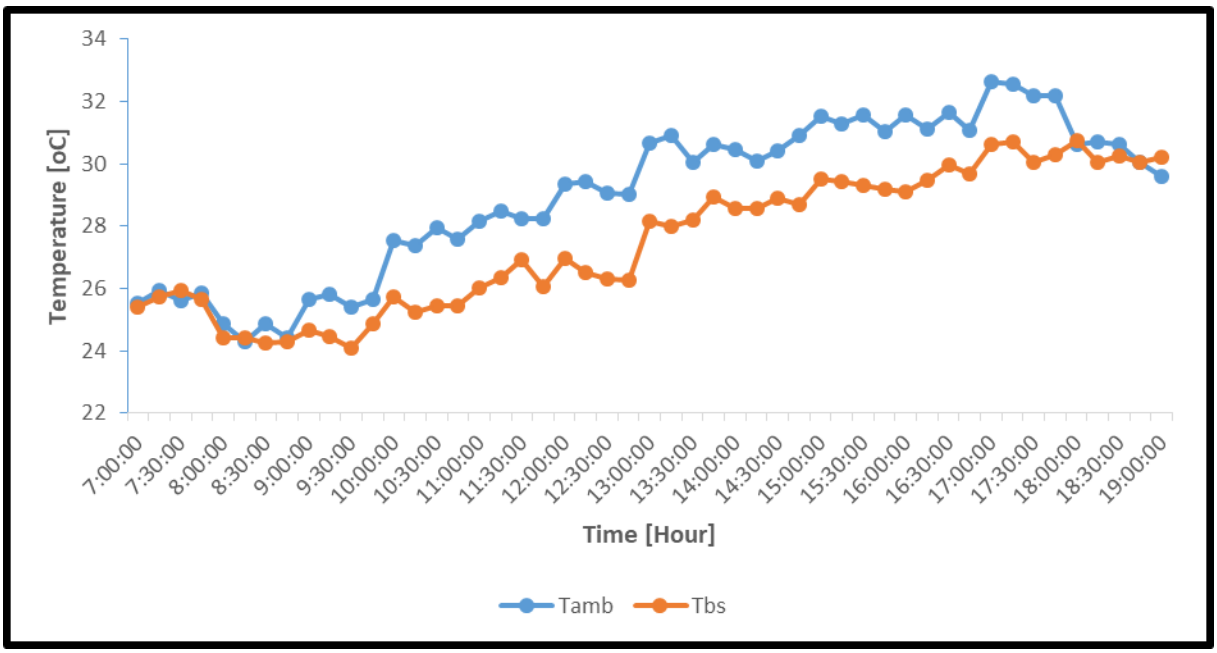

Fig. 4.2: Experimental cooler temperatures of $BaSO_4$, and Ambient on May 18, 2023 in Abuja, Nigeria

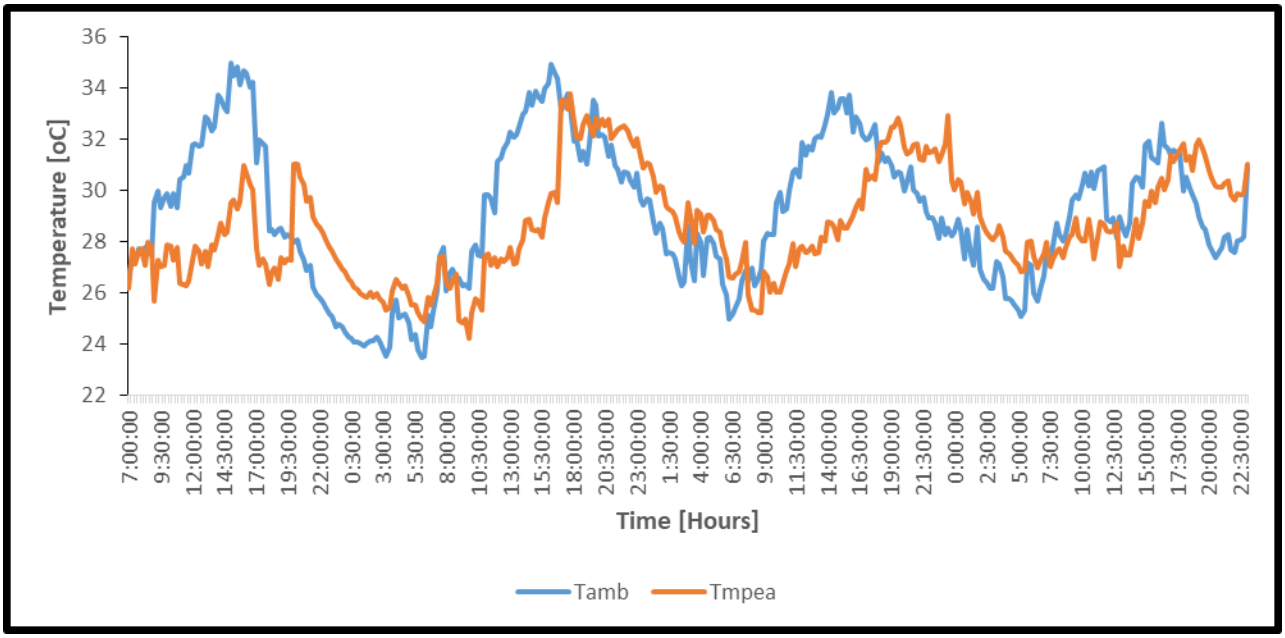

Fig. 4.3: Experimental cooler temperatures of MPEA, and Ambient during May 19-22, 2023 in Abuja, Nigeria

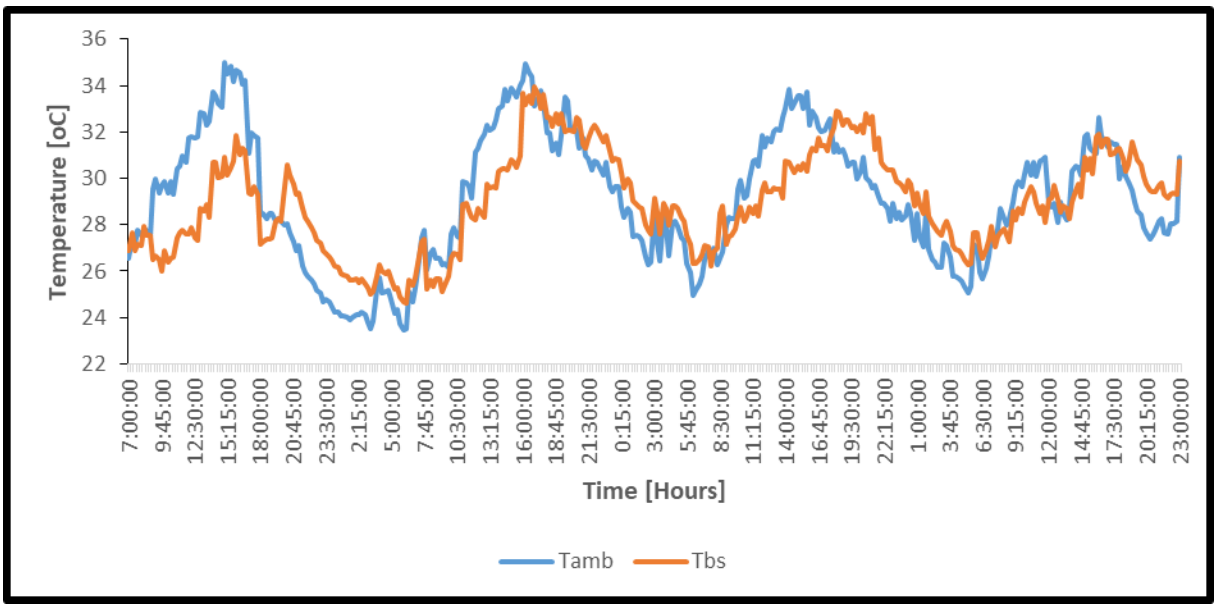

Fig. 4.4: Experimental cooler temperatures of $BaSO_4$, and Ambient during May 19-22, 2023 in Abuja, Nigeria

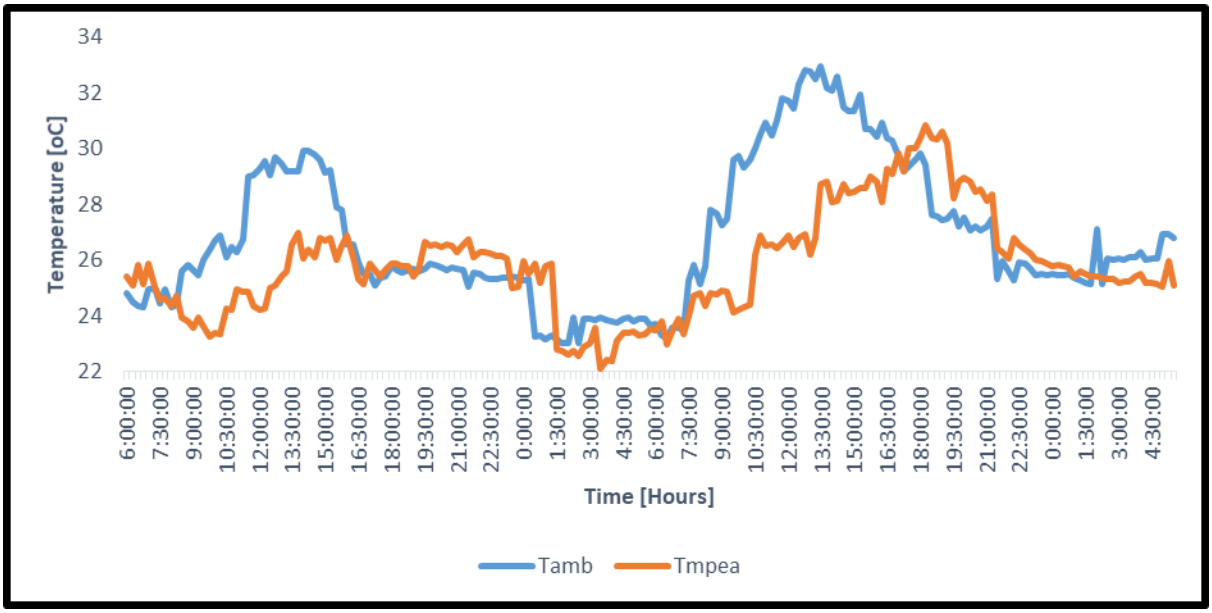

Fig. 4.5: Experimental cooler temperatures of MPEA, and Ambient during July 16-17, 2023 in Afikpo, Nigeria

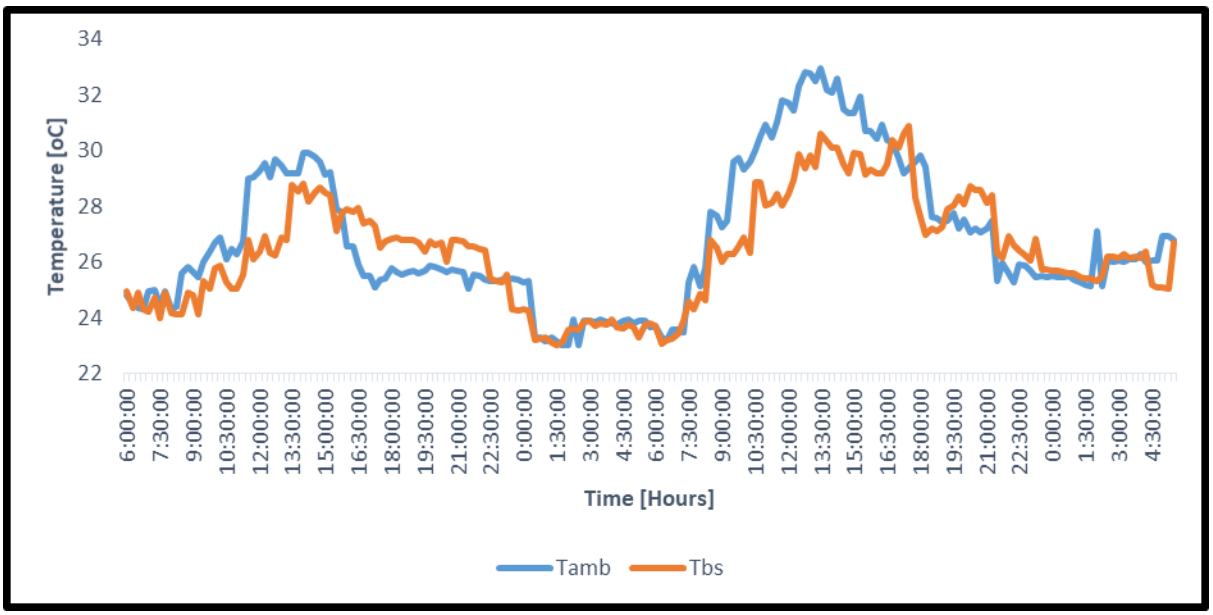

Fig. 4.6: Experimental cooler temperatures of $BaSO_4$, and Ambient during July 16-17, 2023 in Afikpo, Nigeria

Fig. 4.7: Experimental cooler temperatures of MPEA, and Ambient during August 10-13, 2023 in Afikpo, Nigeria

Fig. 4.8: Experimental cooler temperatures of $BaSO_4$, and Ambient during August 10-13, 2023 in Afikpo, Nigeria

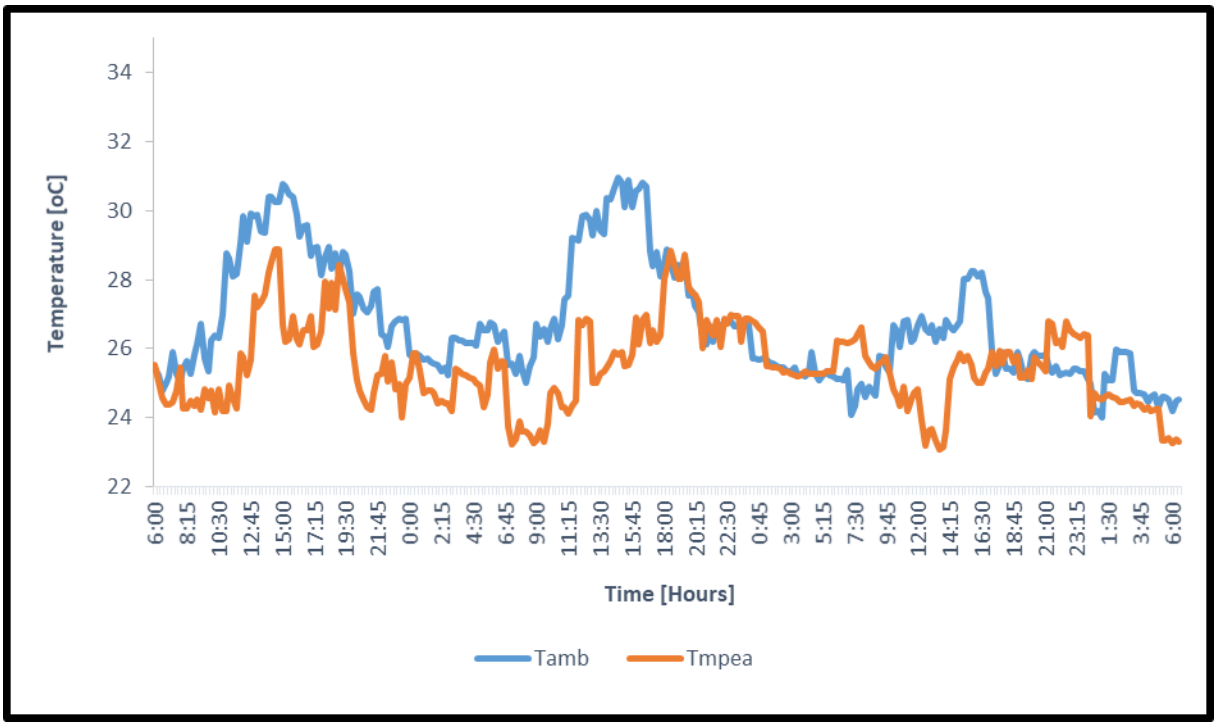

Fig. 4.9: Experimental cooler temperatures of MPEA, and Ambient during July 12-15, 2023 in Owerri, Nigeria

Fig. 4.10: Experimental cooler temperatures of $BaSO_4$, and Ambient during July 12-15, 2023 in Owerri, Nigeria

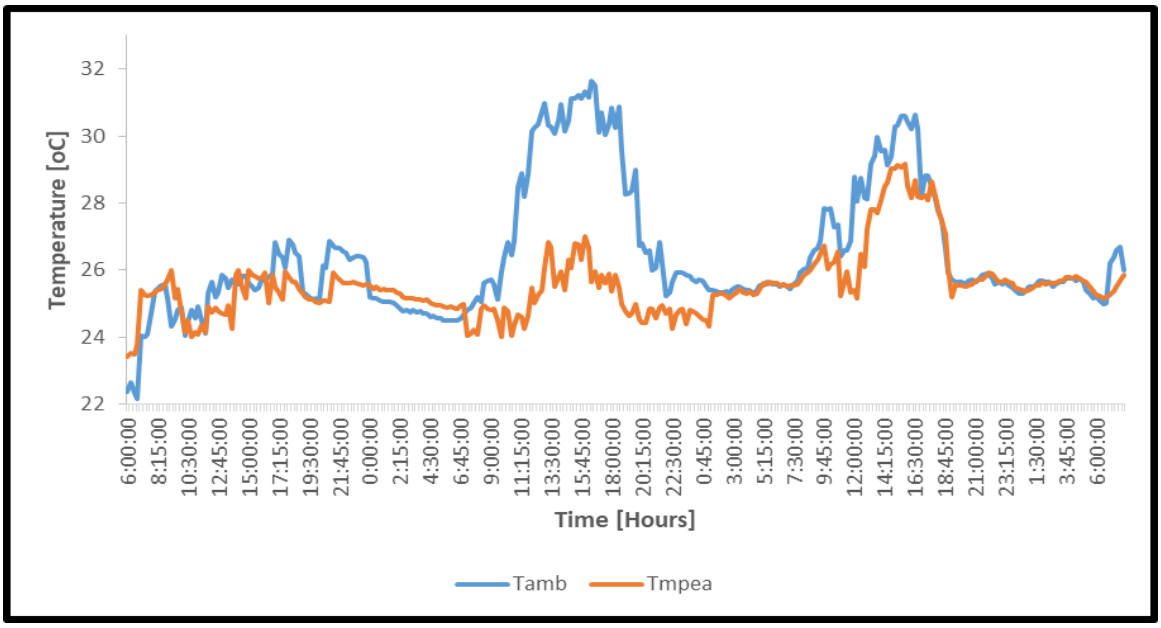

Fig. 4.11: Experimental cooler temperatures of MPEA, and Ambient during August 14-17, 2023 in Owerri, Nigeria

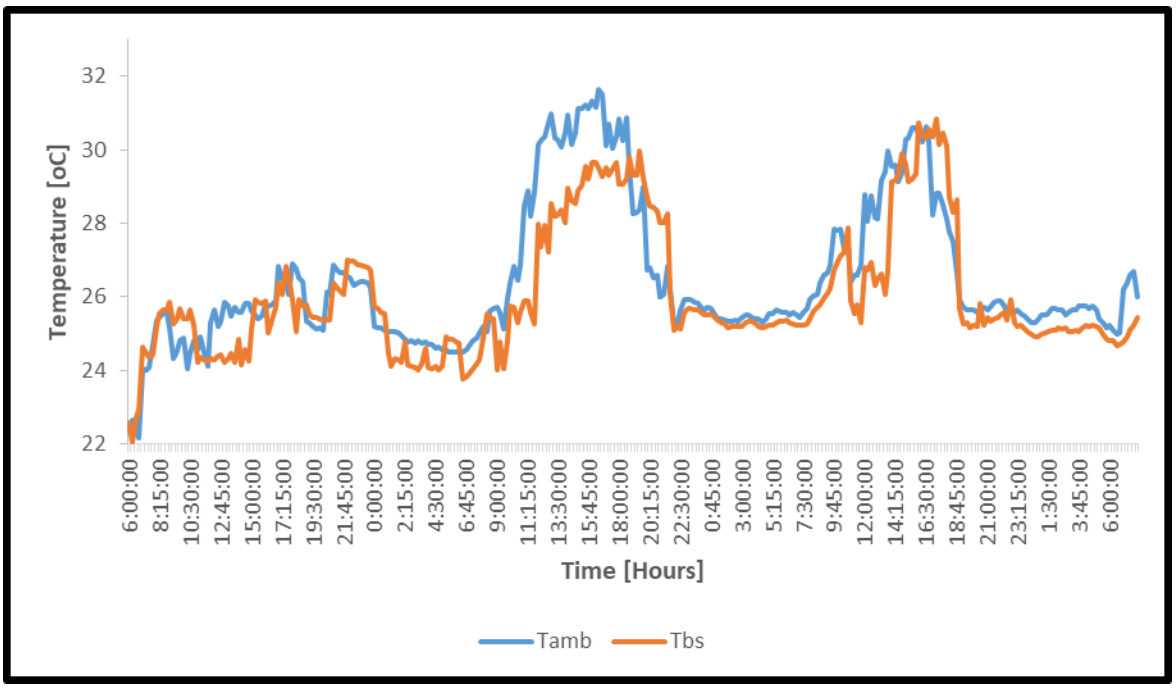

Fig. 4.12: Experimental cooler temperatures of $BaSO_4$, and Ambient during August 14-17, 2023 in Owerri, Nigeria

4.1.2 Comparative Studies

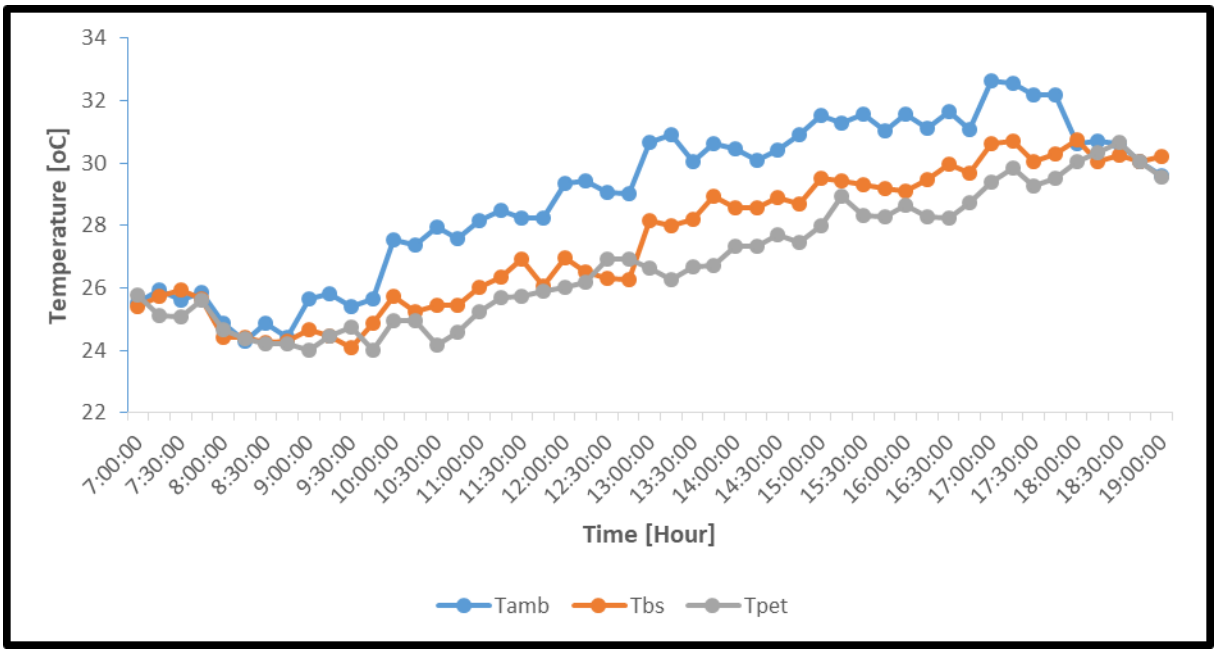

Fig. 4.13: Experimental cooler temperatures of $BaSO_4$, MPEA, and Ambient on May 18, 2023 in Abuja, Nigeria

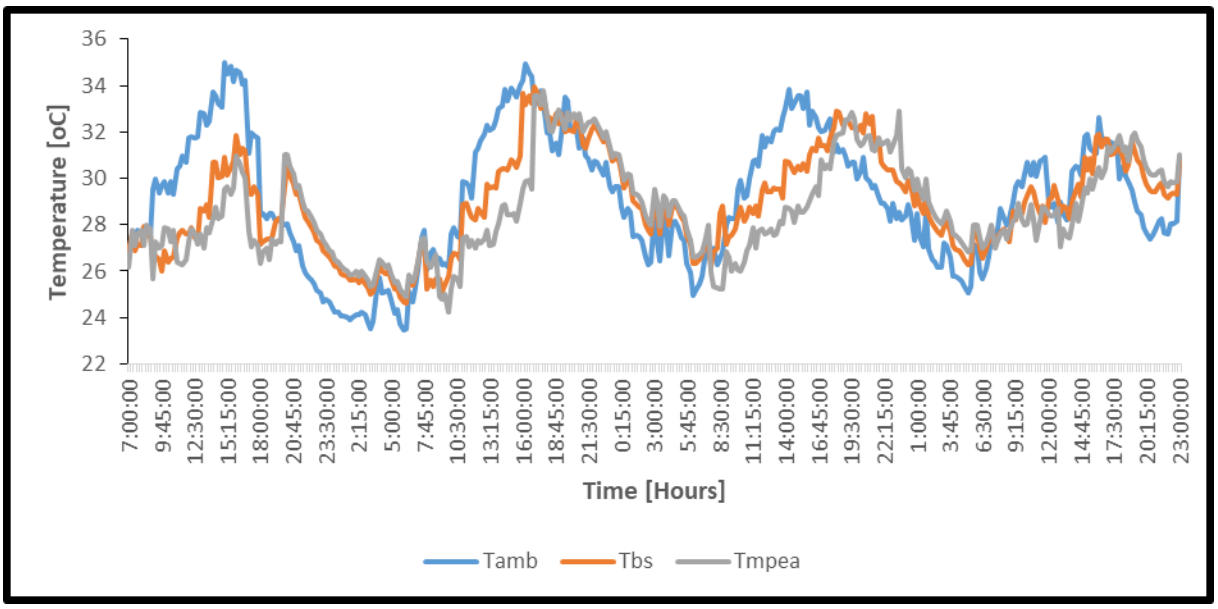

Fig. 4.14: Experimental cooler temperatures of $BaSO_4$, MPEA, and Ambient during May 19-22, 2023 in Abuja, Nigeria

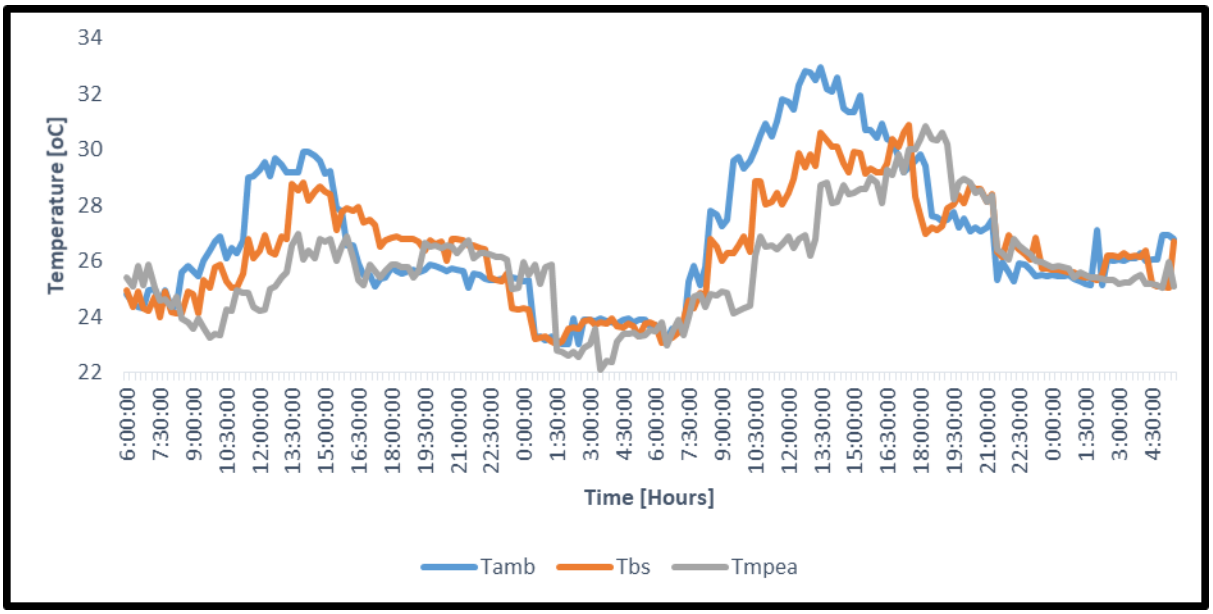

Fig. 4.15: Experimental cooler temperatures of $BaSO_4$, MPEA, and Ambient during July 16-17, 2023 in Afikpo, Nigeria

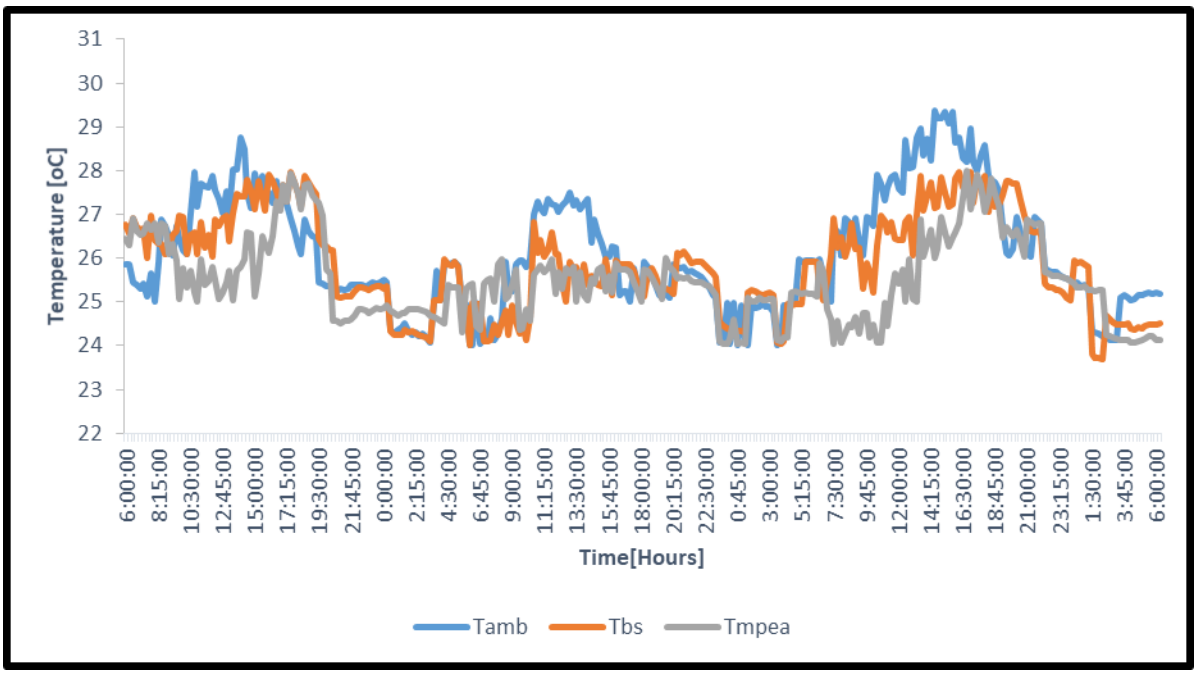

Fig. 4.16: Experimental cooler temperatures of $BaSO_4$, MPEA, and Ambient during August 10-13, 2023 in Afikpo, Nigeria

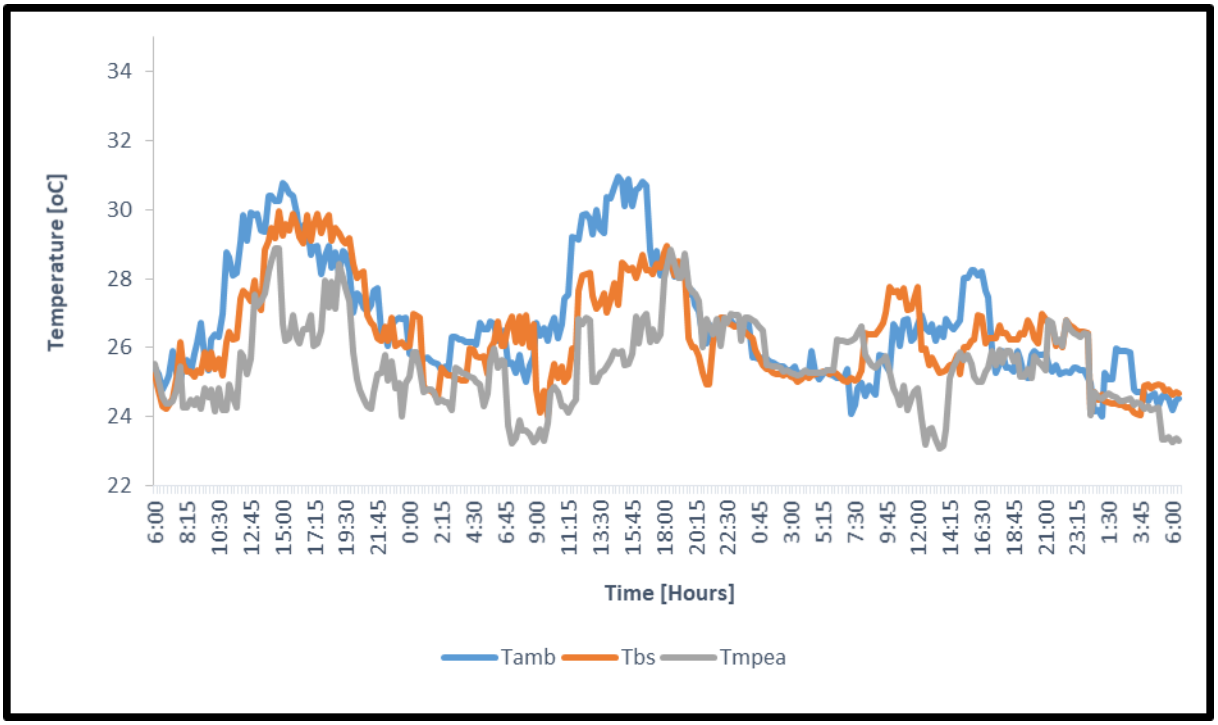

Fig. 4.17: Experimental cooler temperatures of $BaSO_4$, MPEA, and Ambient during July 12-15, 2023 in Owerri, Nigeria

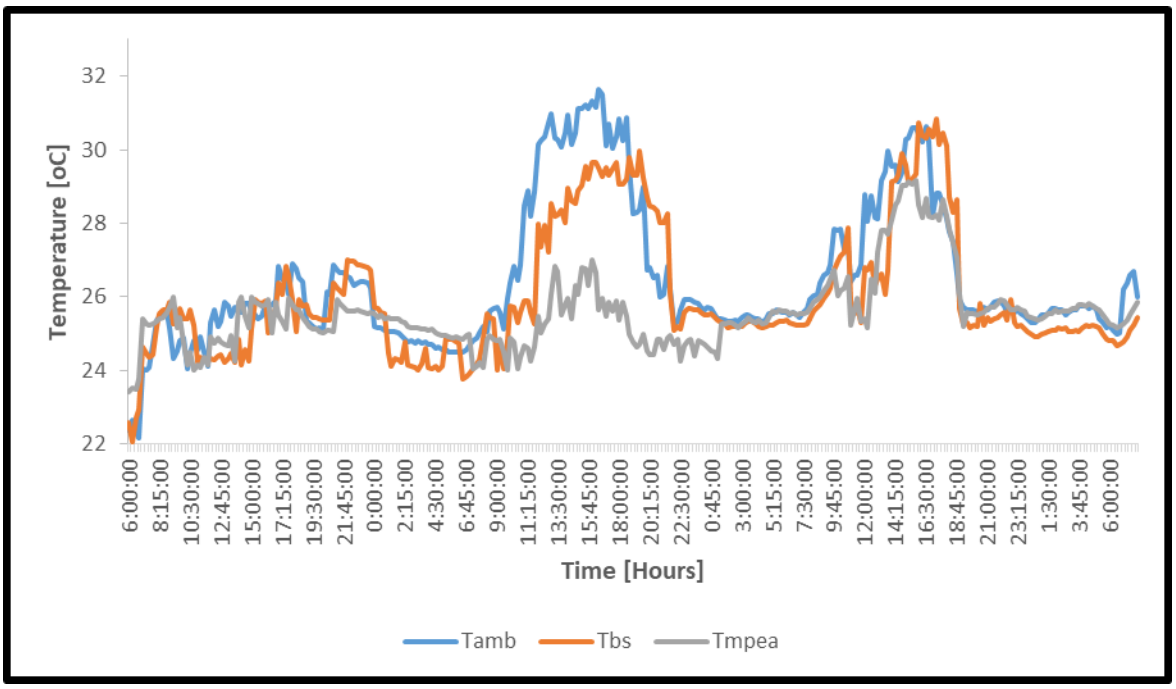

Fig. 4.18: Experimental cooler temperatures of $BaSO_4$, MPEA, and Ambient during August 14-17, 2023 in Owerri, Nigeria

4.1.3 Effect of Climatic Conditions on the performance of the radiative coolers

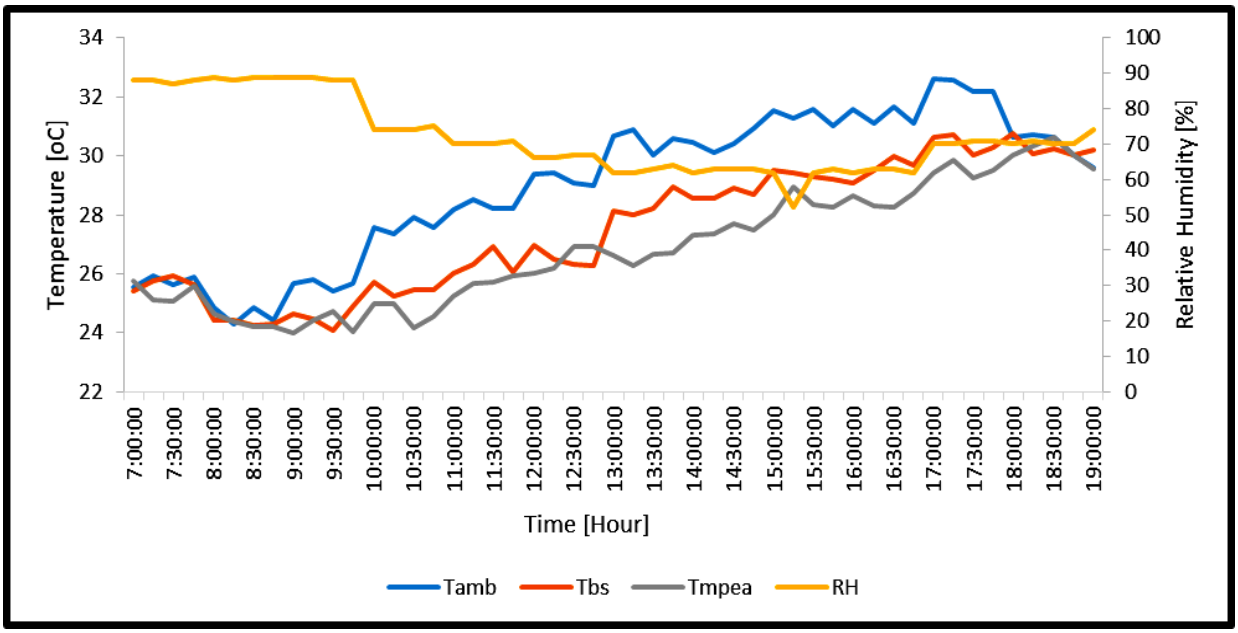

Fig. 4.7: Effect of Humidity on the coolers performance on May 18, 2023 in Abuja, Nigeria

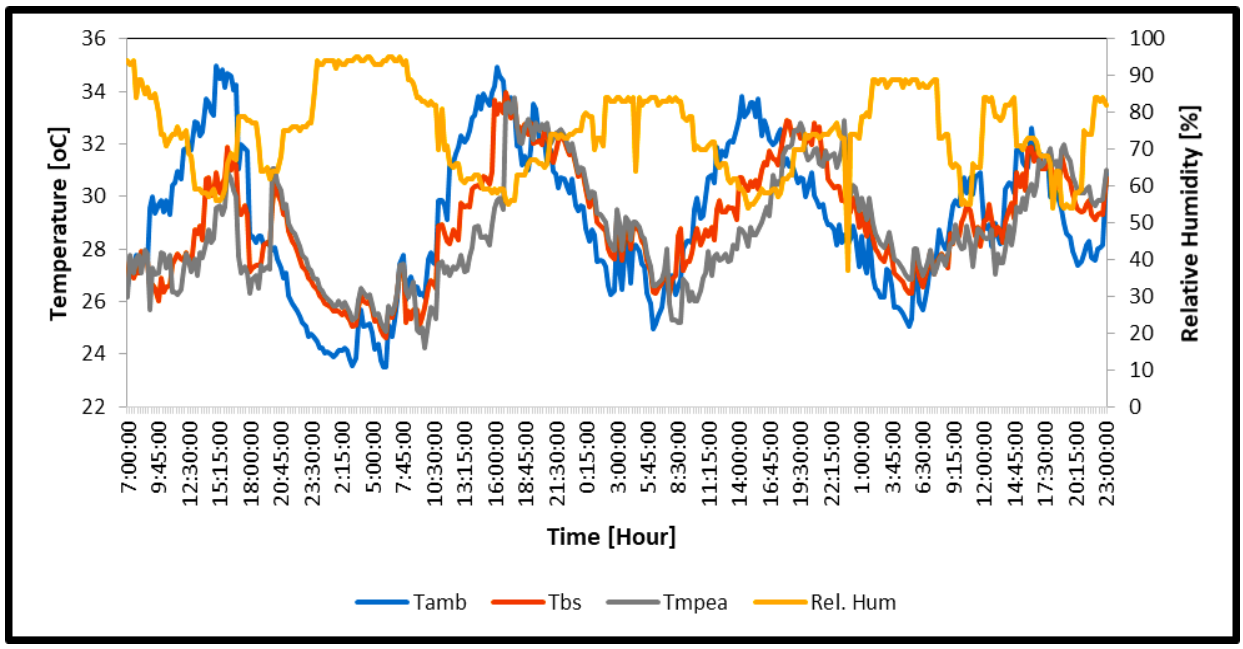

Fig. 4.8: Effect of Humidity on the coolers performance during May 19-22, 2023 in Abuja, Nigeria

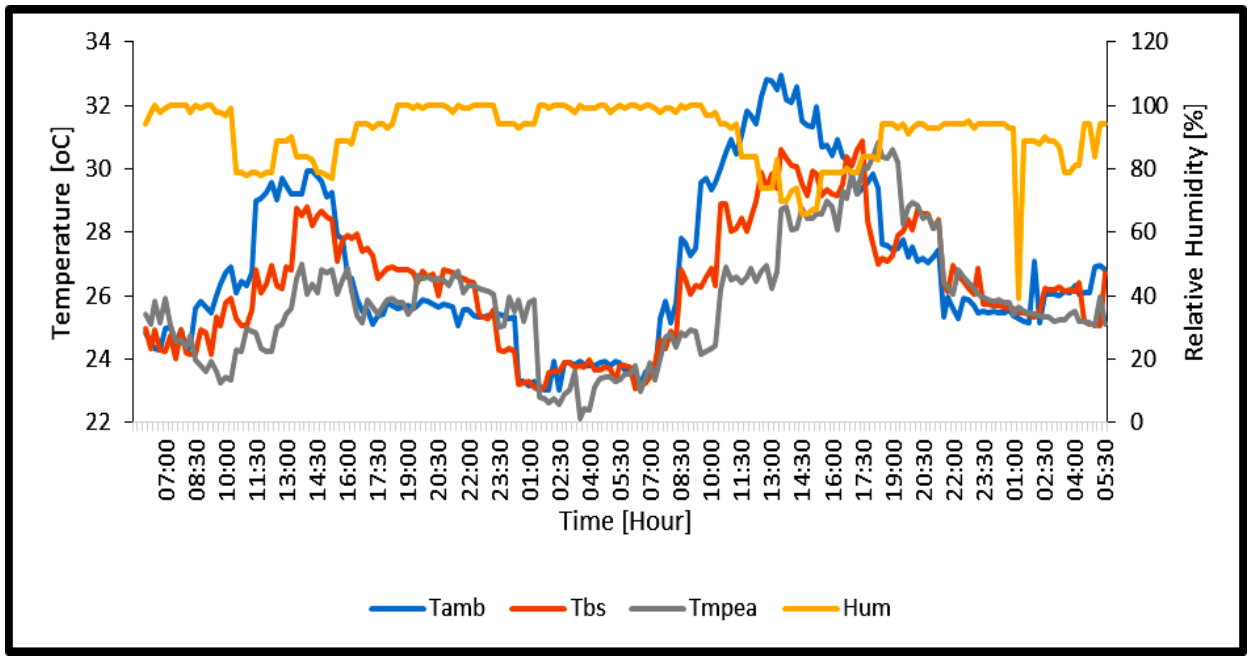

Fig. 4.9: Effect of Humidity on the coolers performance during July 16-17, 2023 in Afikpo, Nigeria

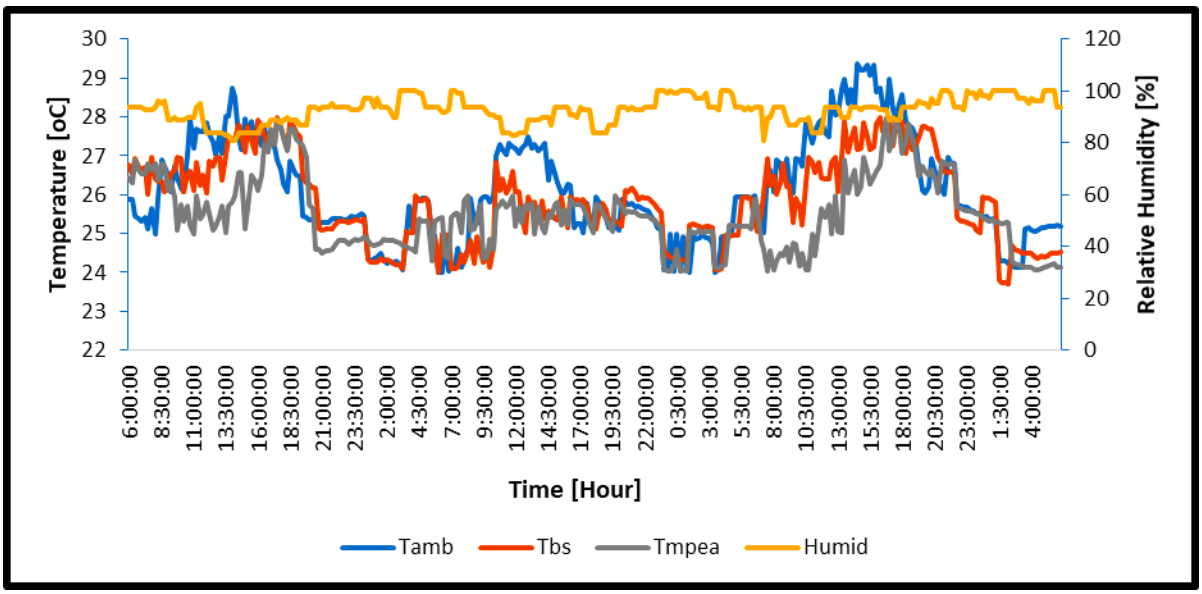

Fig. 4.10: Effect of Humidity on the coolers performance during August 10-13, 2023 in Afikpo, Nigeria

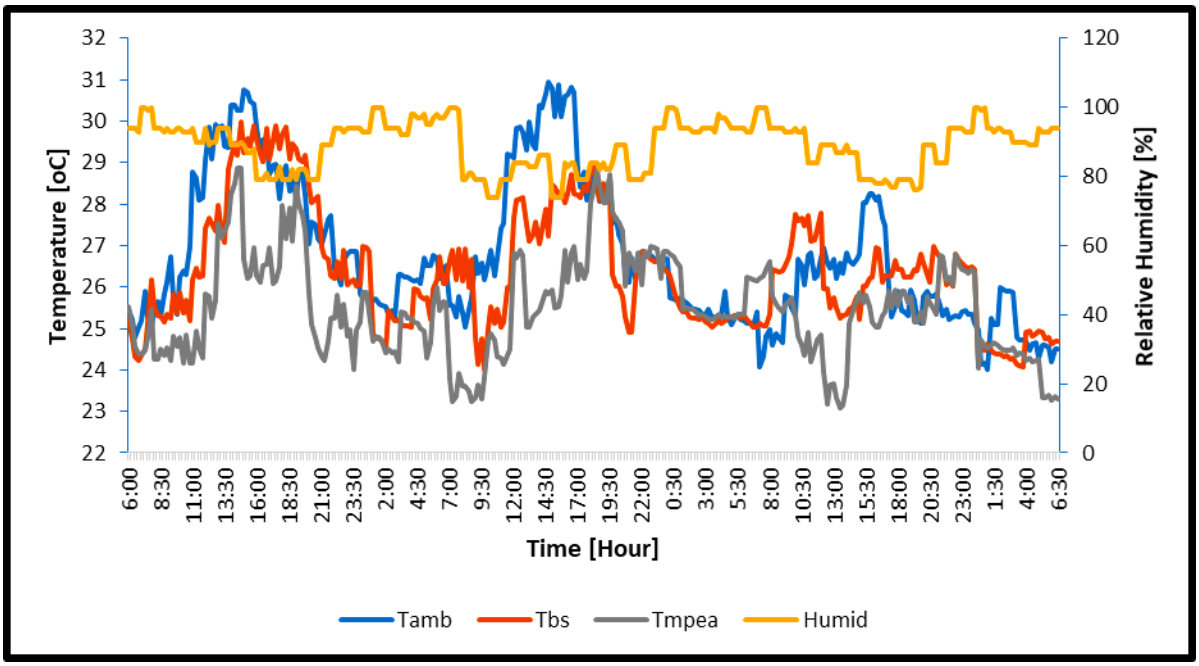

Fig. 4.11: Effect of Humidity on the coolers performance during July 12-15, 2023 in Owerri, Nigeria

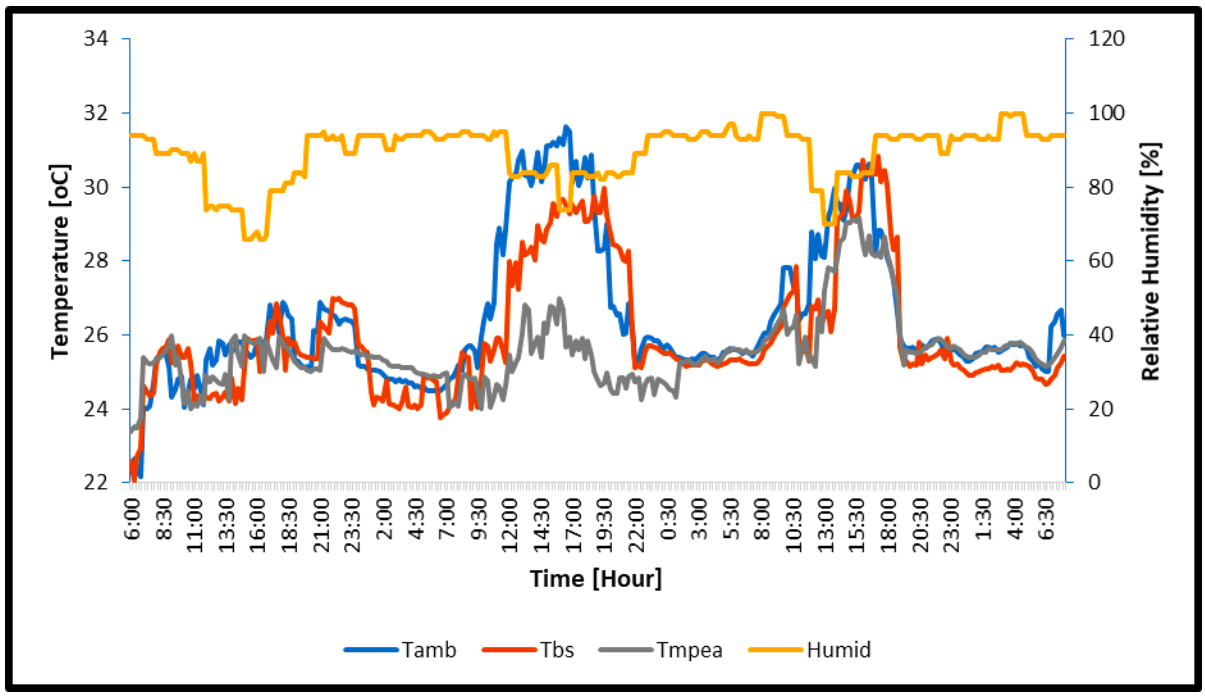

Fig. 4.12: Effect of Humidity on the coolers performance during August 14-17, 2023 in Owerri, Nigeria

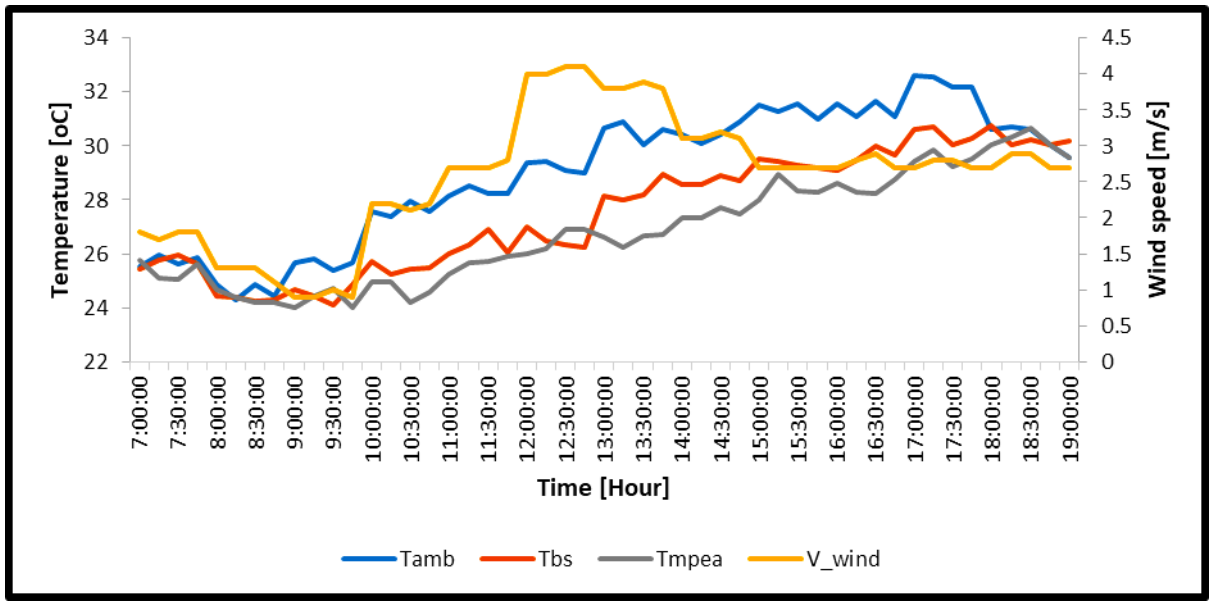

Fig. 4.13: Effect of wind speed on the coolers performance during May 18, 2023 in Abuja, Nigeria

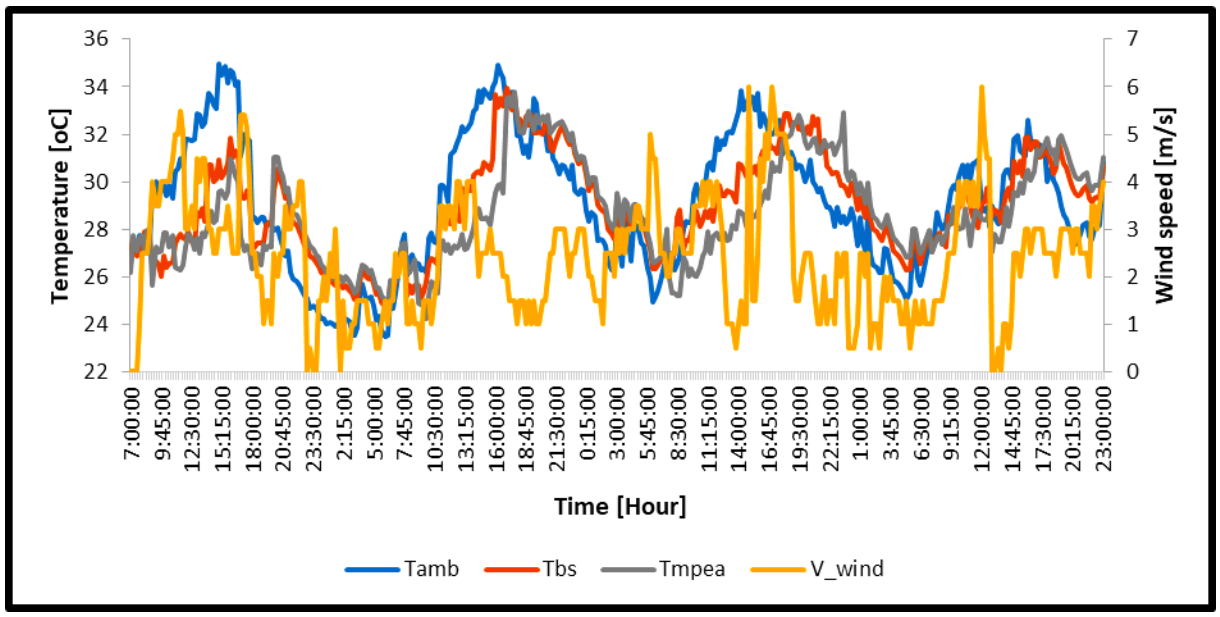

Fig. 4.14: Effect of wind speed on the coolers performance during May 19-22, 2023 in Abuja, Nigeria

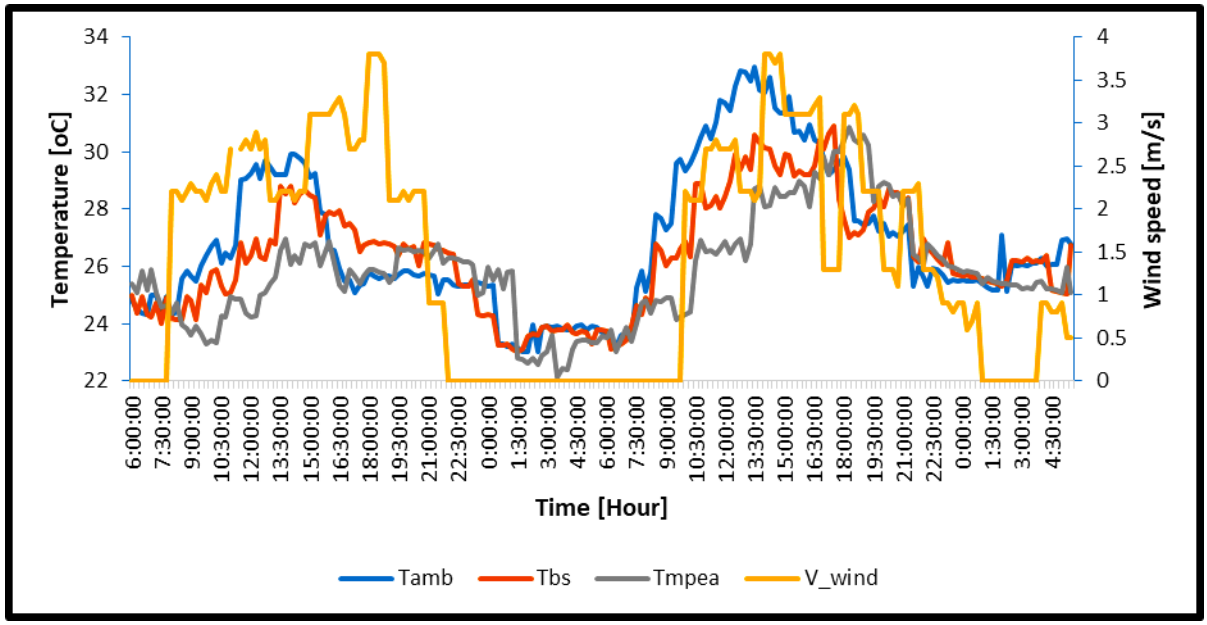

Fig. 4.15: Effect of wind speed on the coolers performance during July 16-17, 2023 in Afikpo, Nigeria

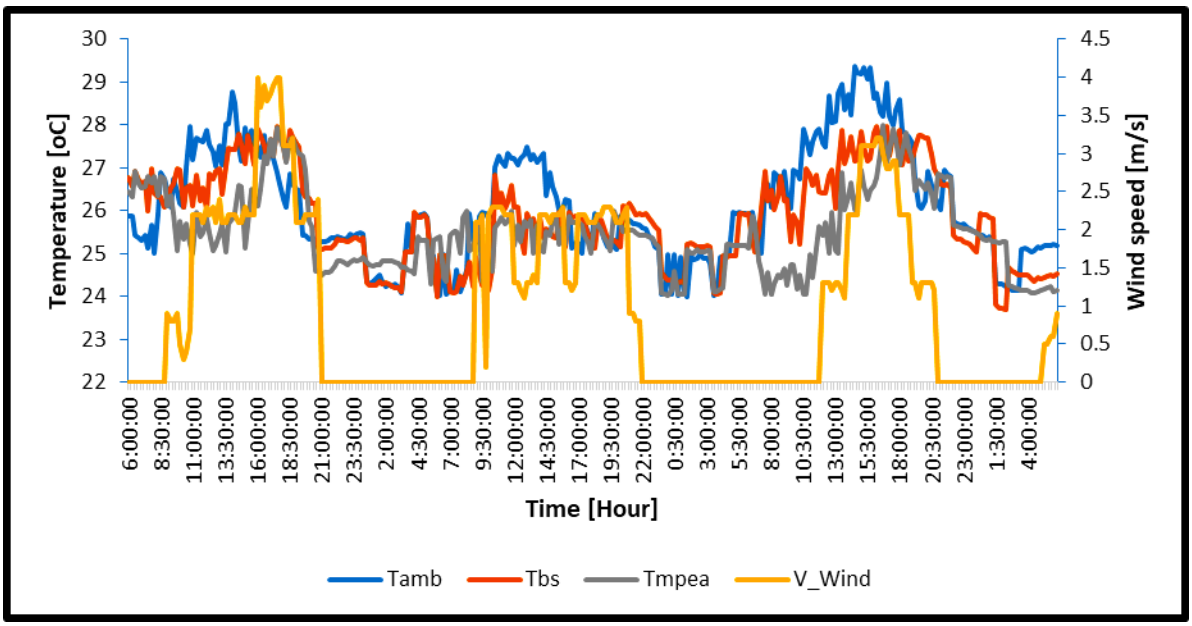

Fig. 4.16: Effect of wind speed on the coolers performance during August 10-13, 2023 in Afikpo, Nigeria

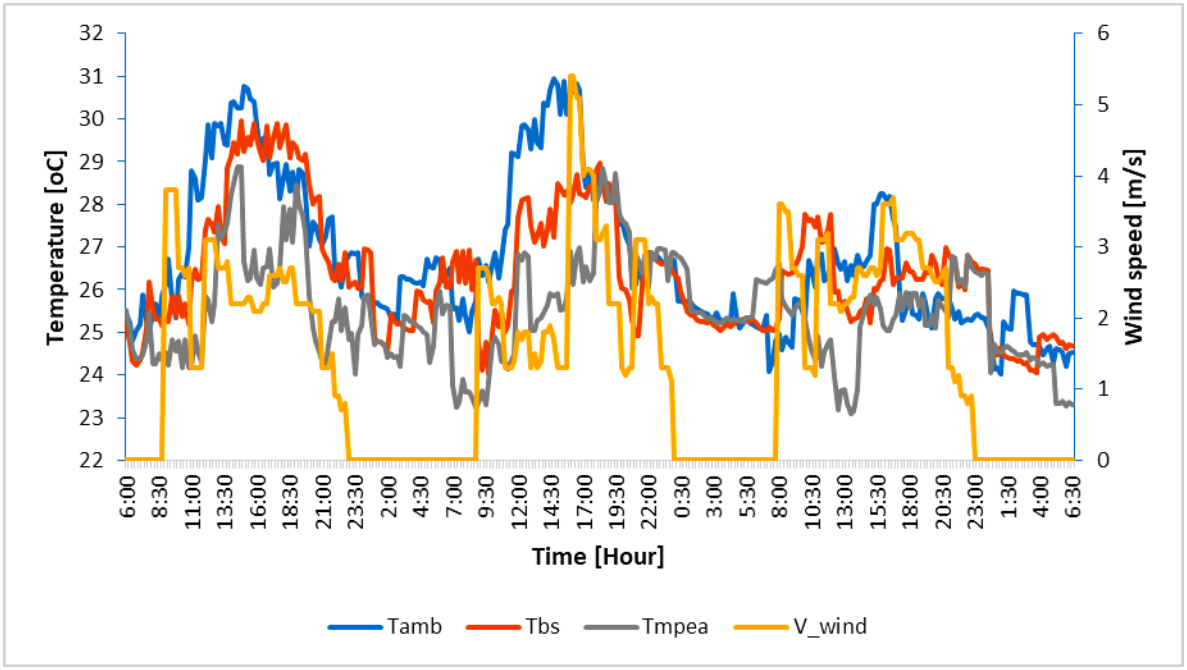

Fig. 4.17: Effect of wind speed on the coolers performance during July 12-15, 2023 in Owerri, Nigeria

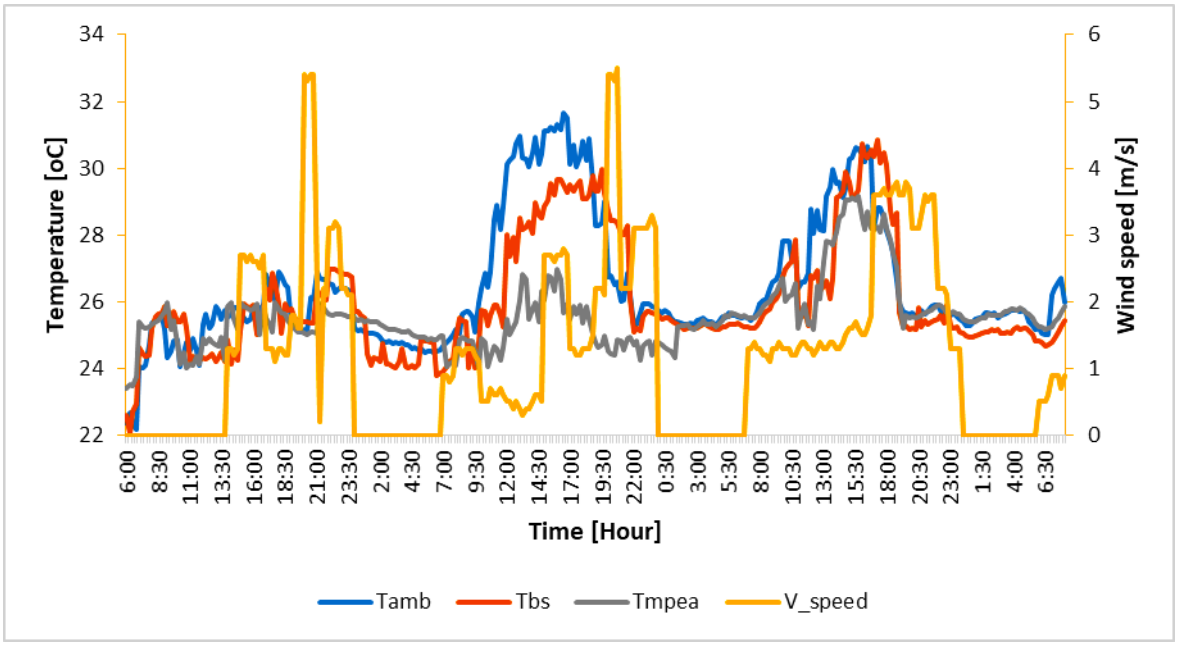

Fig. 4.18: Effect of wind speed on the coolers performance during August 14-17, 2023 in Owerri, Nigeria

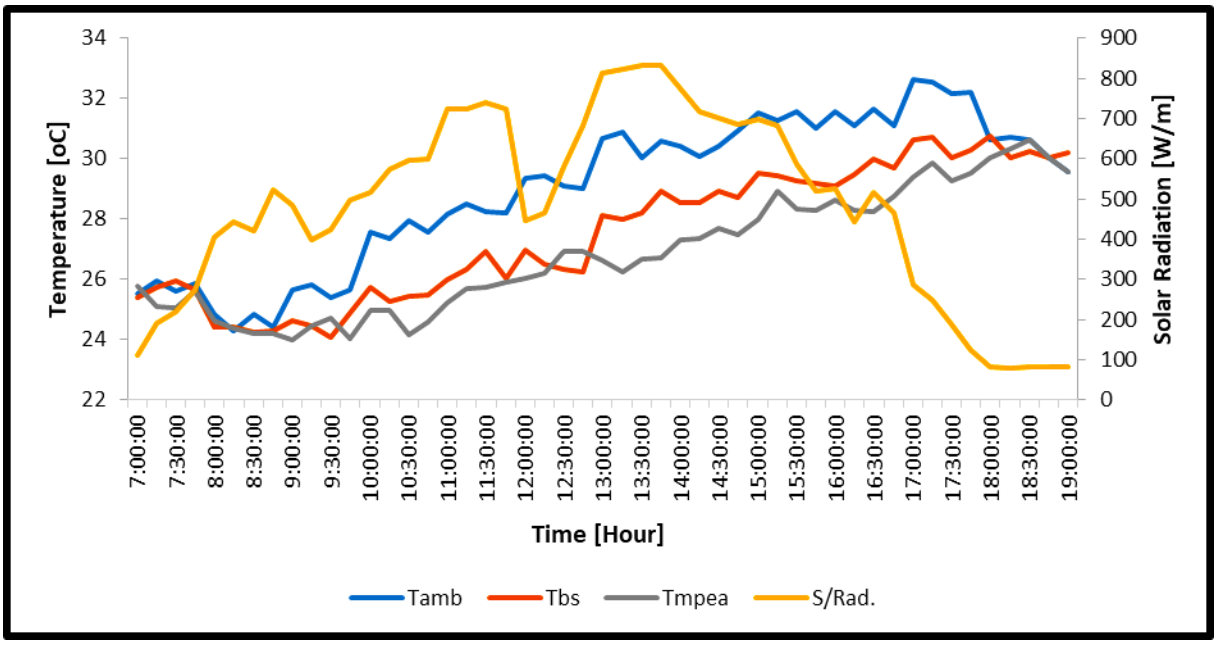

Fig. 4.19: Effect of solar radiation on the coolers performance during May 18, 2023 in Abuja, Nigeria

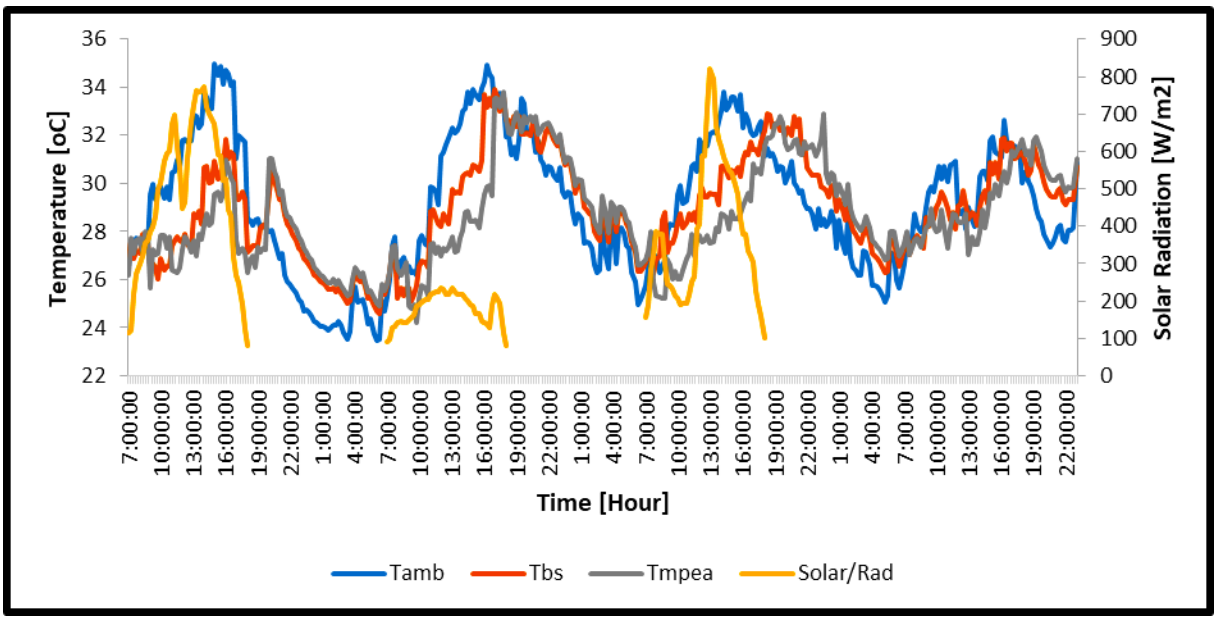

Fig. 4.20: Effect of solar radiation on the coolers performance during May 19-22, 2023 in Abuja, Nigeria

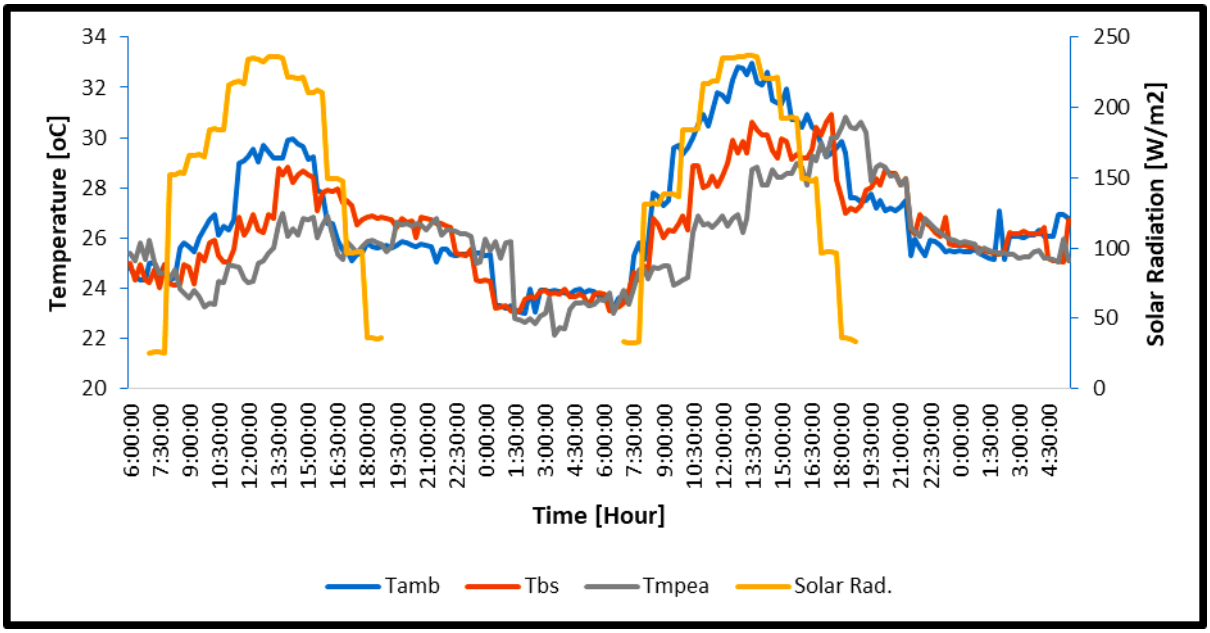

Fig. 4.21: Effect of Solar Radiation on the coolers performance during July 16-17, 2023 in Afikpo, Nigeria

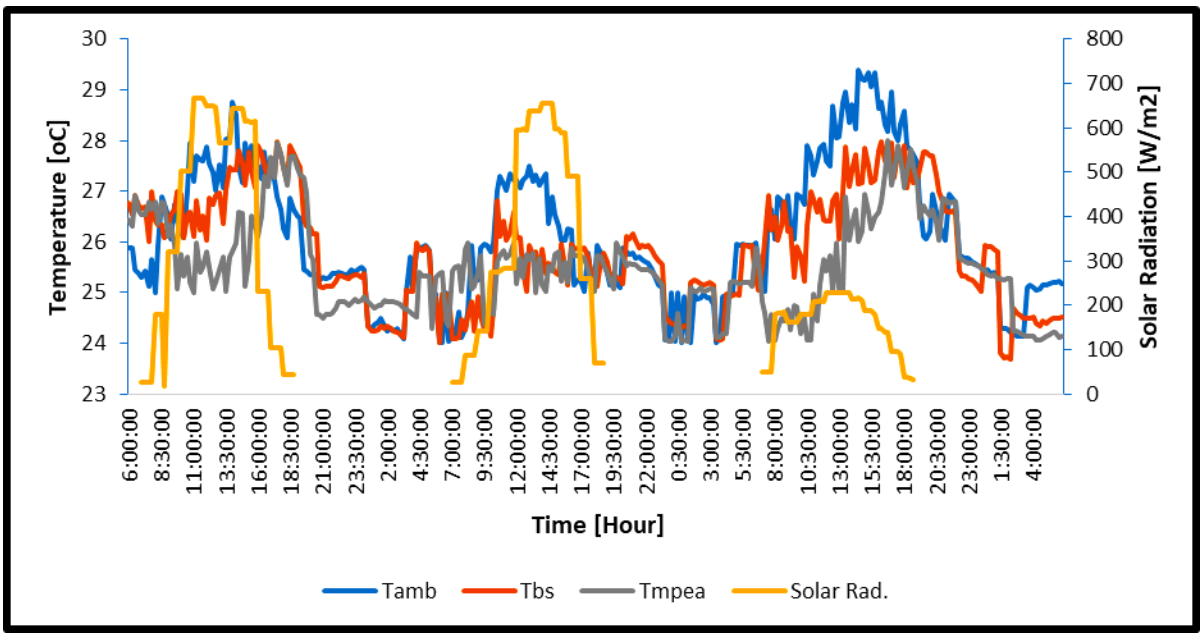

Fig. 4.22: Effect of solar radiation on the coolers performance during August 10-13, 2023 in Afikpo, Nigeria

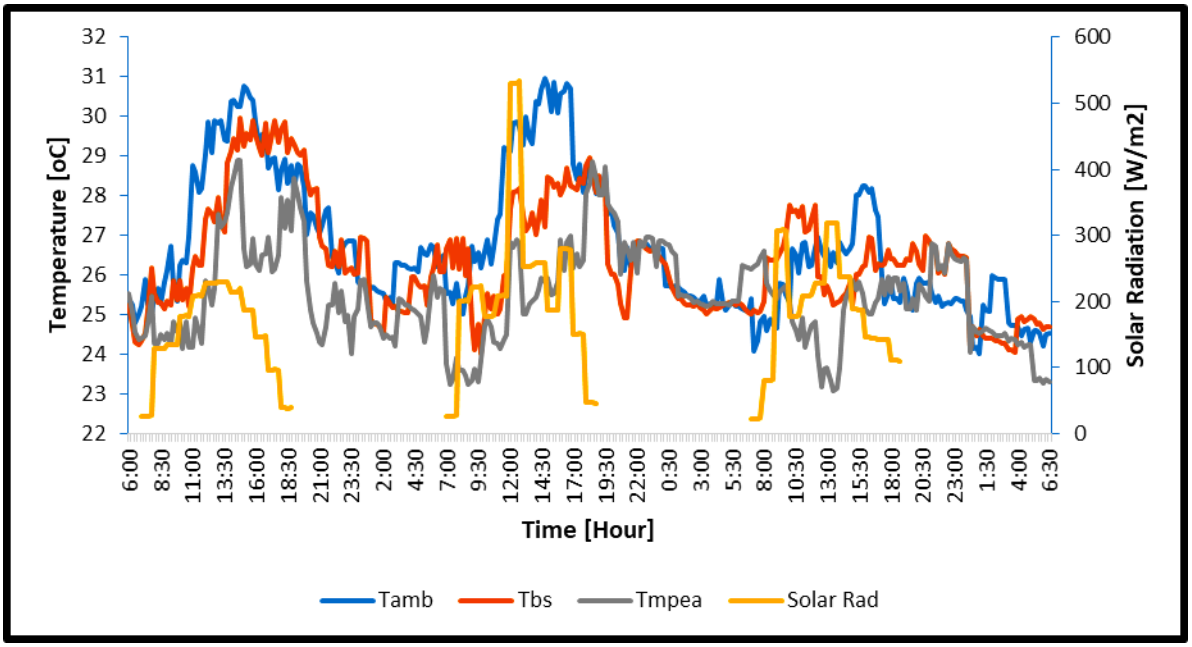

Fig. 4.23: Effect of Solar Radiation on the coolers performance during July 12-15, 2023 in Owerri, Nigeria

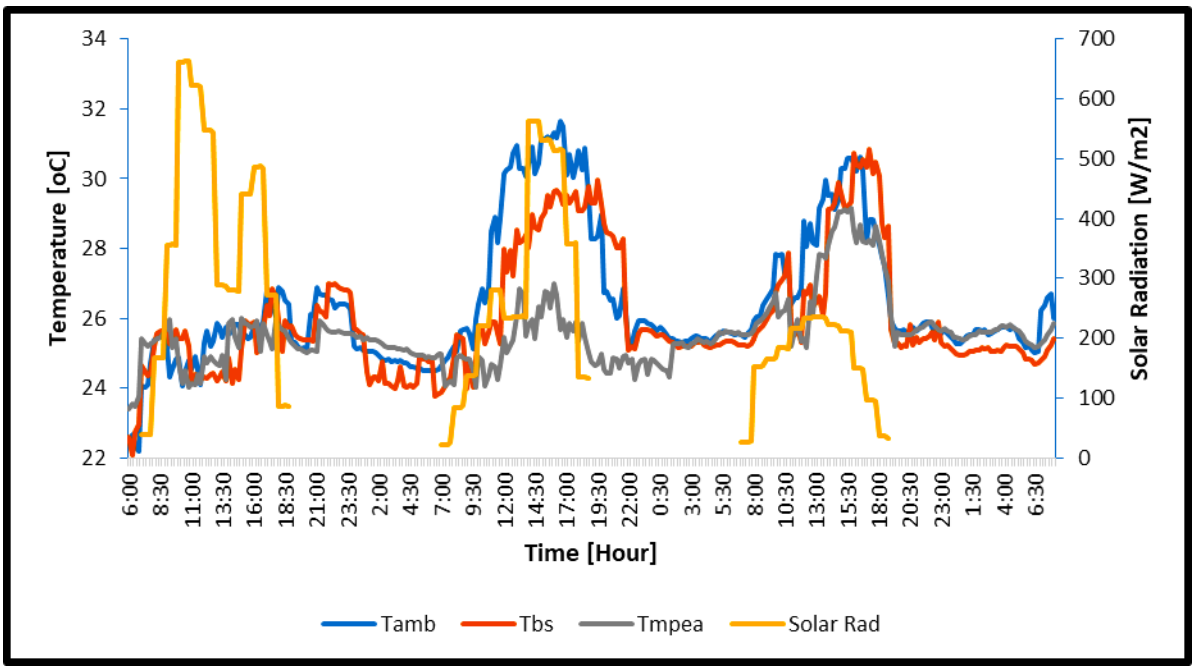

Fig. 4.24: Effect of Solar Radiation on the coolers performance during August 14-17, 2023 in Owerri, Nigeria

4.1.4 Numerical Investigation

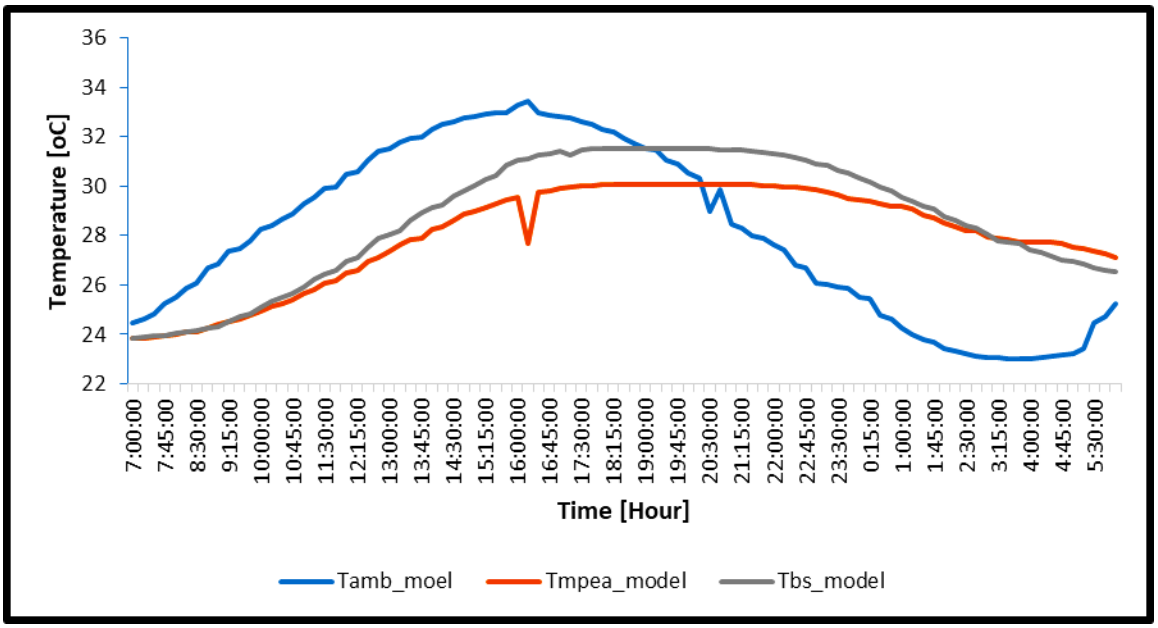

Fig. 4.25: Predicted cooler temperatures for Abuja, Nigeria

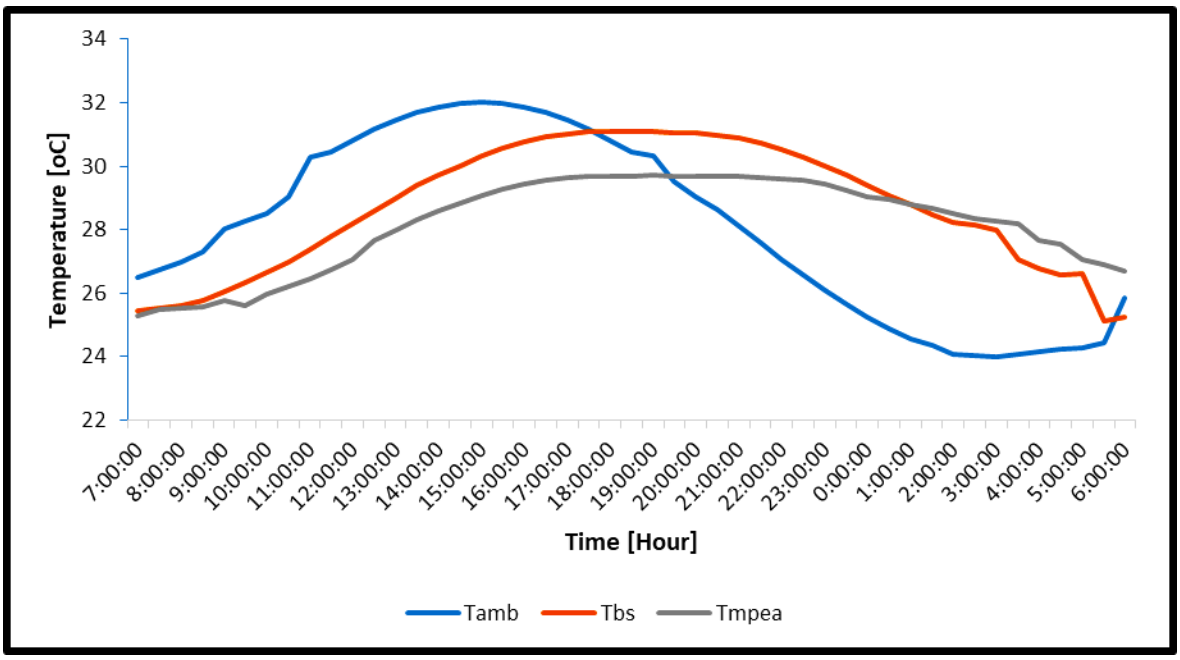

Fig. 4.26: Predicted cooler temperatures for Adamawa, Nigeria

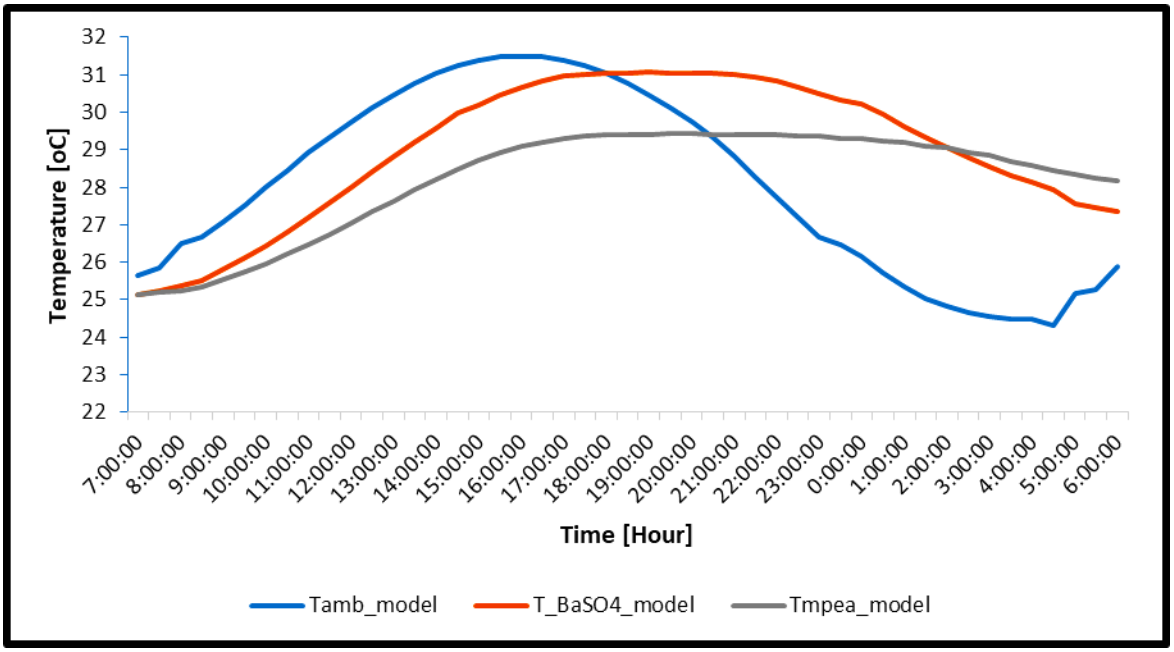

Fig. 4.27: Predicted cooler temperatures for Afikpo, Nigeria

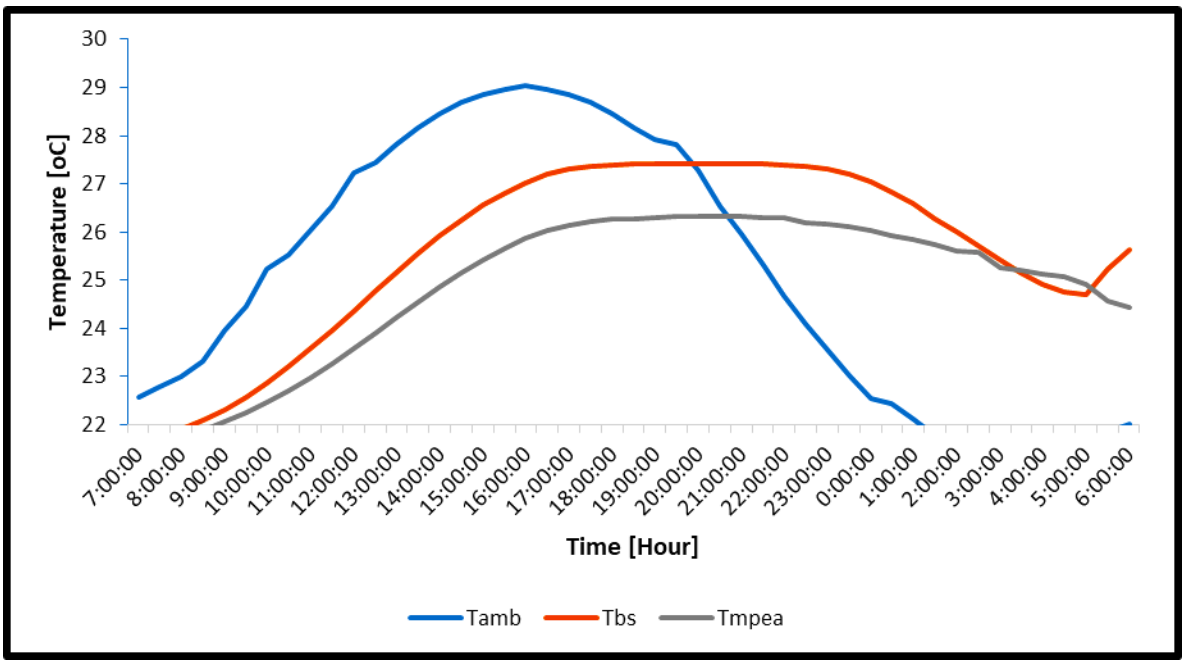

Fig. 4.28: Predicted cooler temperatures for Ekiti, Nigeria

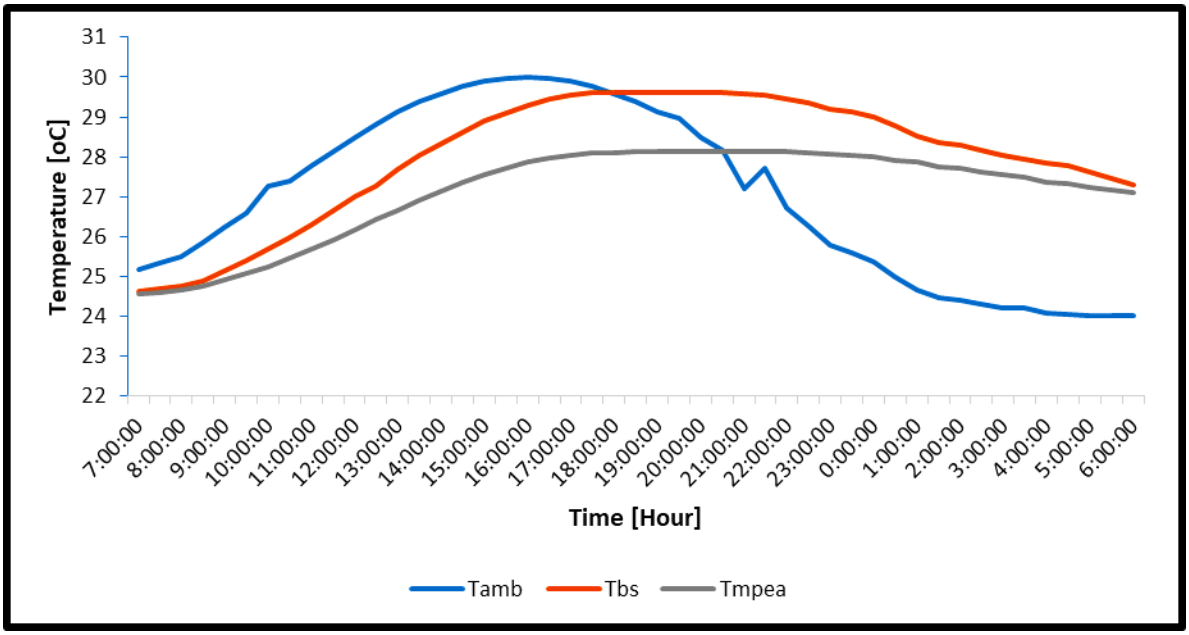

Fig. 4.29: Predicted cooler temperatures for Kaduna, Nigeria

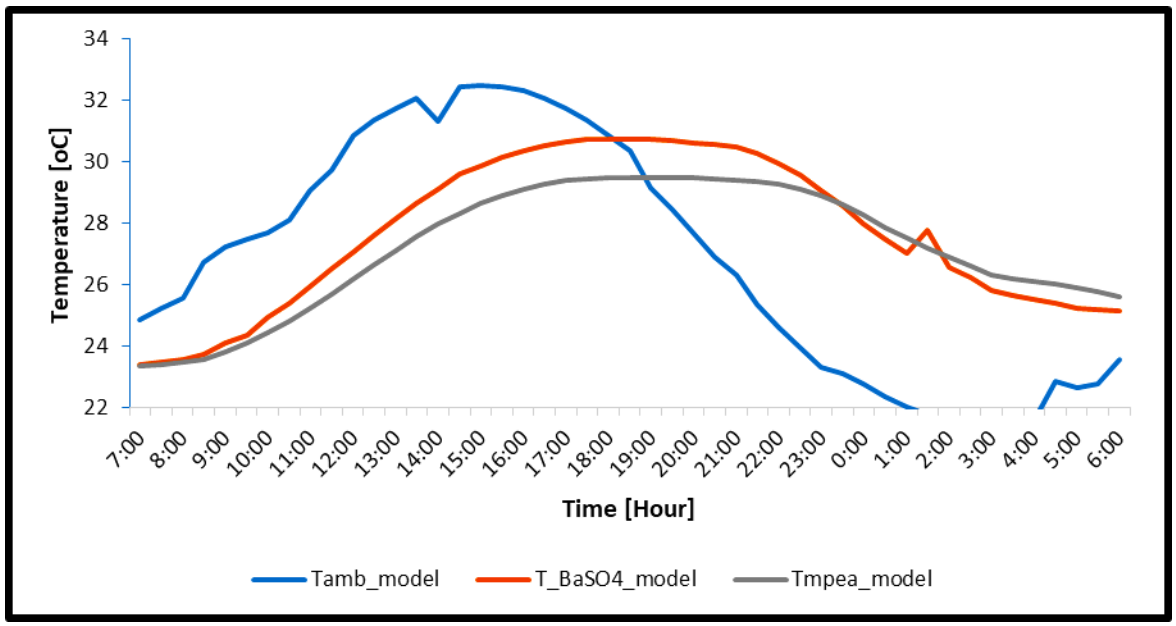

Fig. 4.30: Predicted cooler temperatures for Owerri, Nigeria

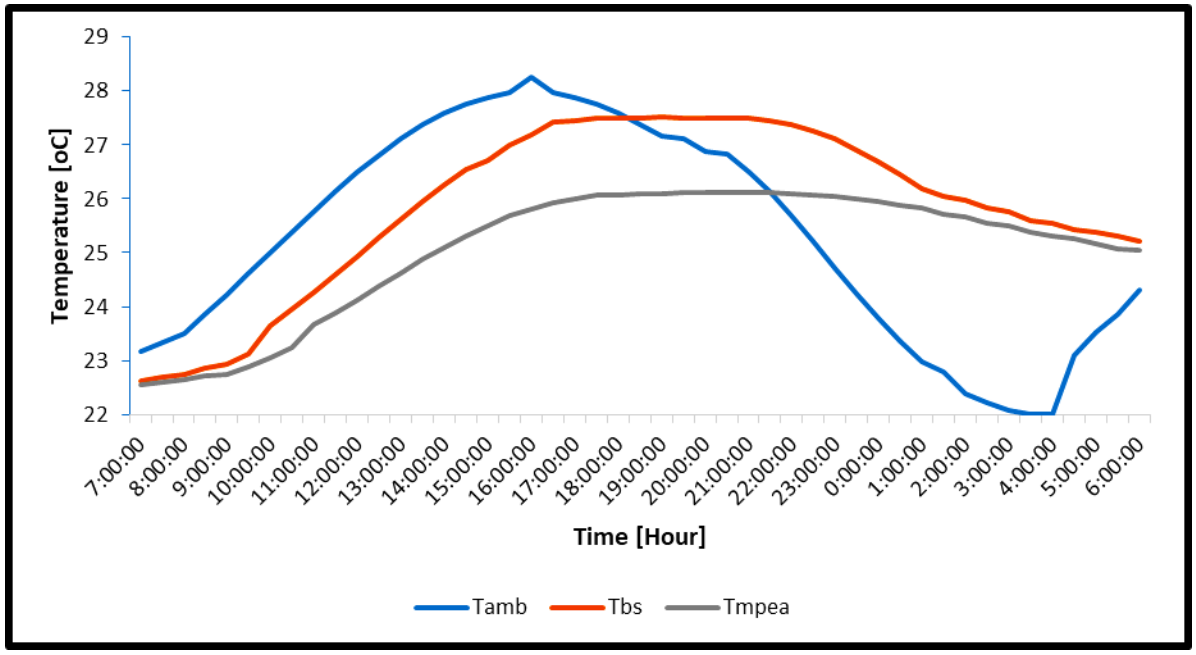

Fig. 4.31 Predicted cooler temperatures for Warri, Nigeria

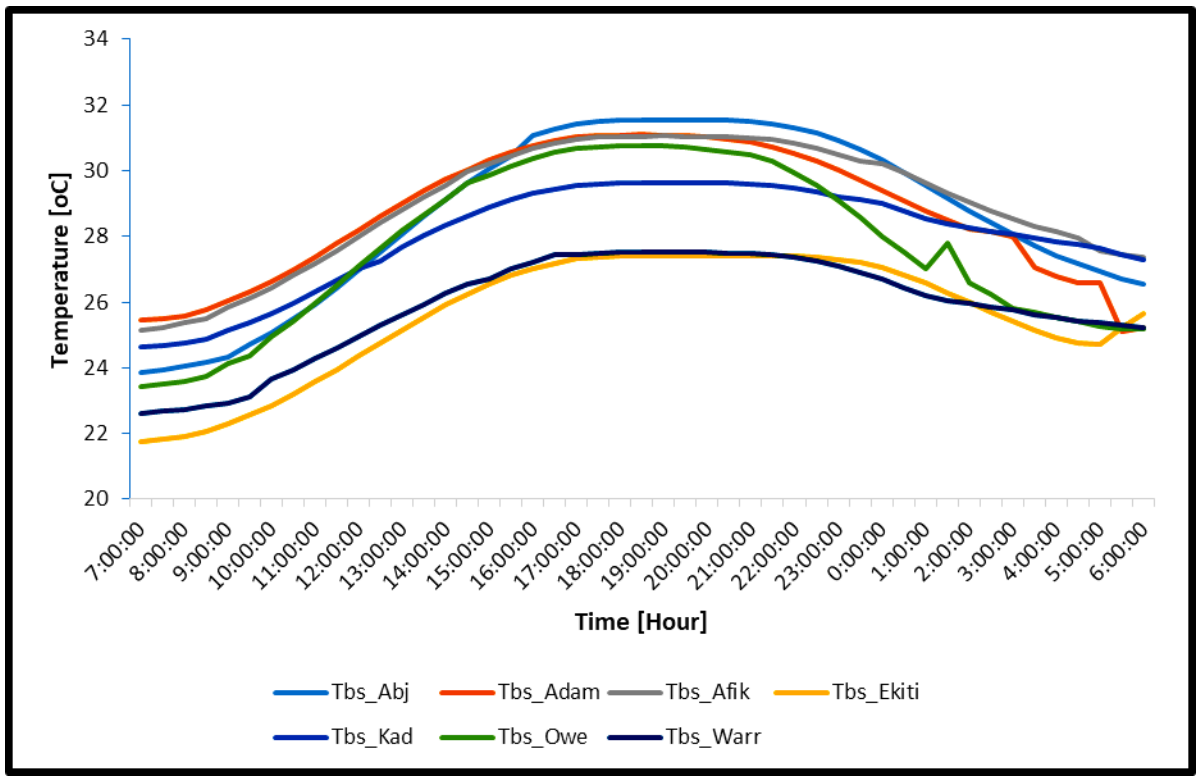

Fig 4.32: Predicted Temperatures of $BaSO_4$ for all the seven test states in Nigeria

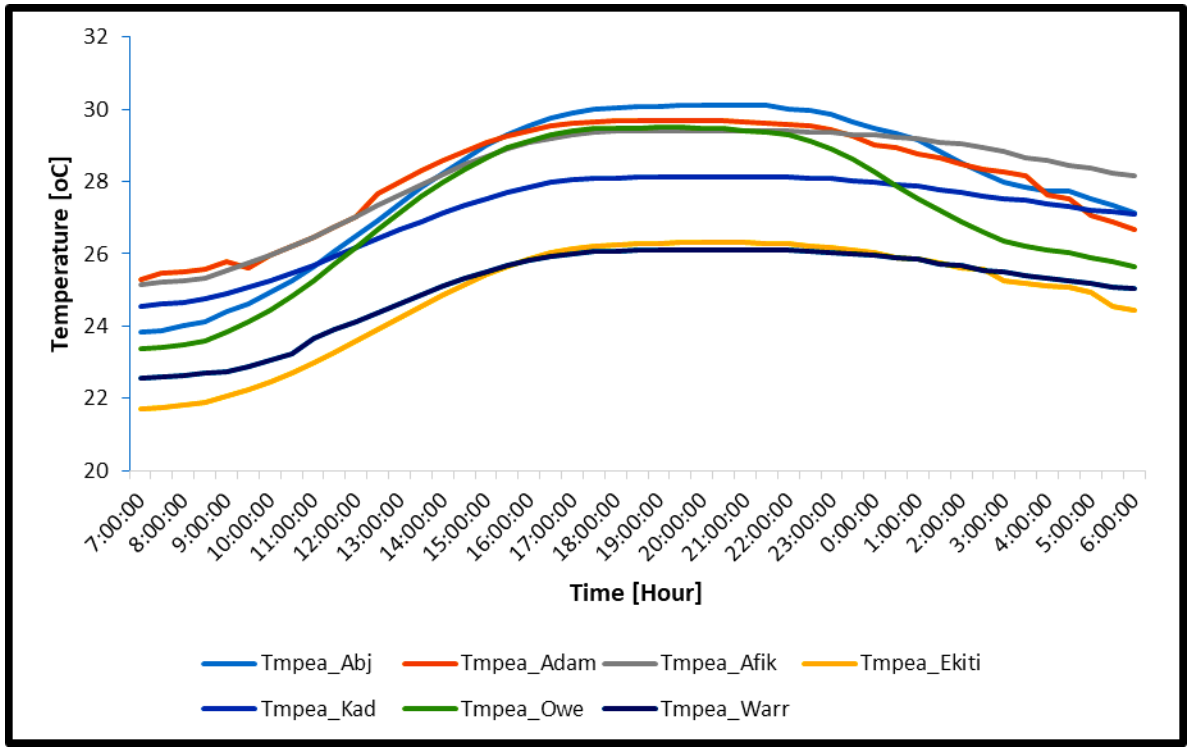

Fig 4.33: Predicted Temperatures of MPEA for all the seven test states in Nigeria

4.1.5 Prediction of Cooling Power

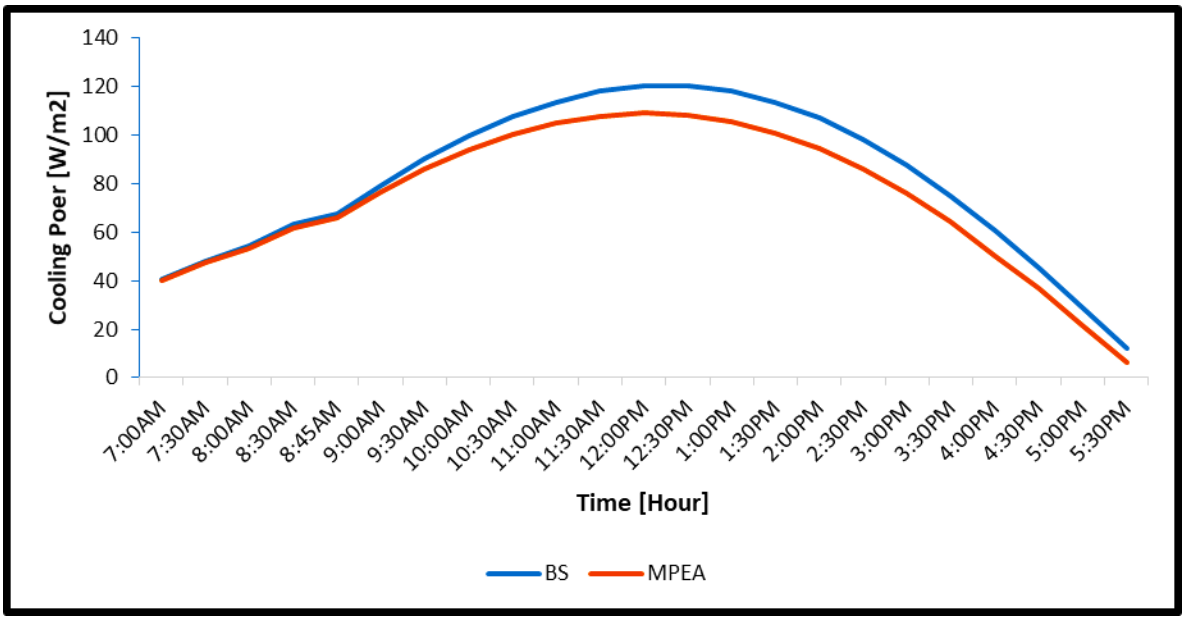

Fig 4.34: Predicted Cooling power plot for Abuja

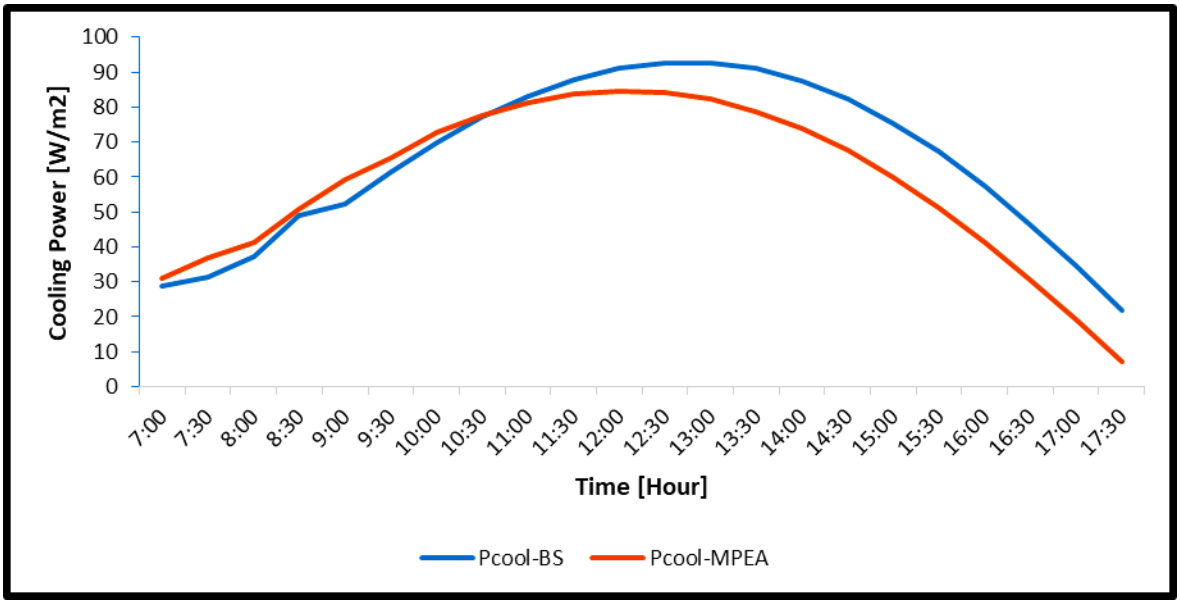

Fig 4.35: Predicted Cooling power plot for Adamawa

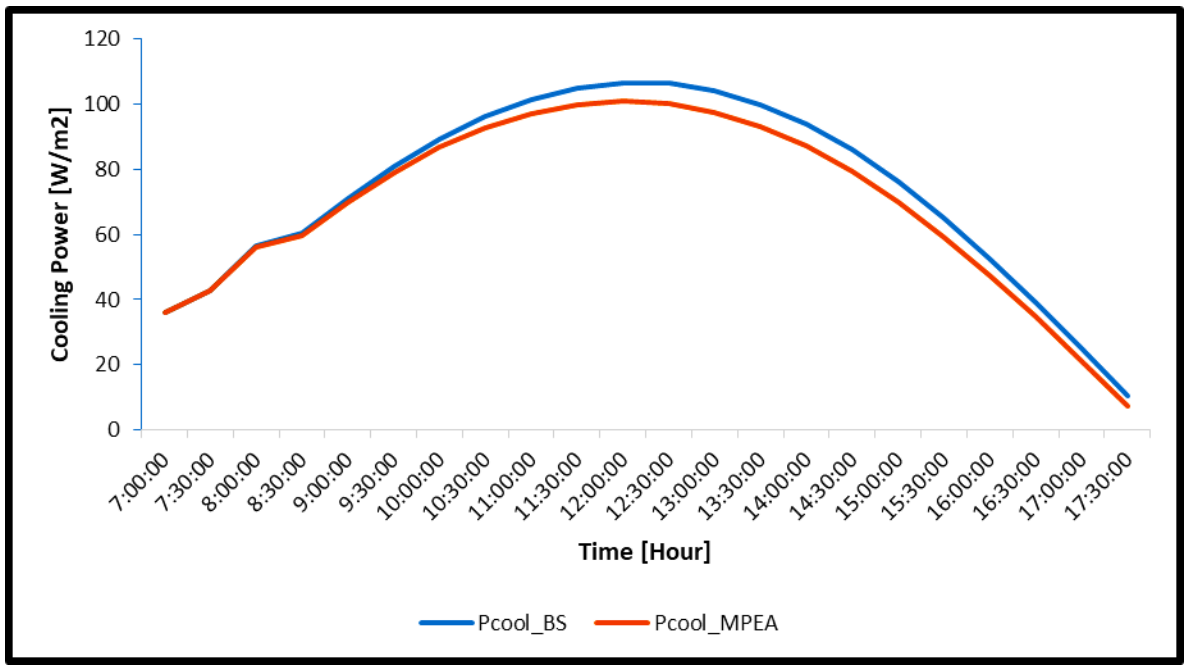

Fig 4.36: Predicted Cooling power plot for Afikpo

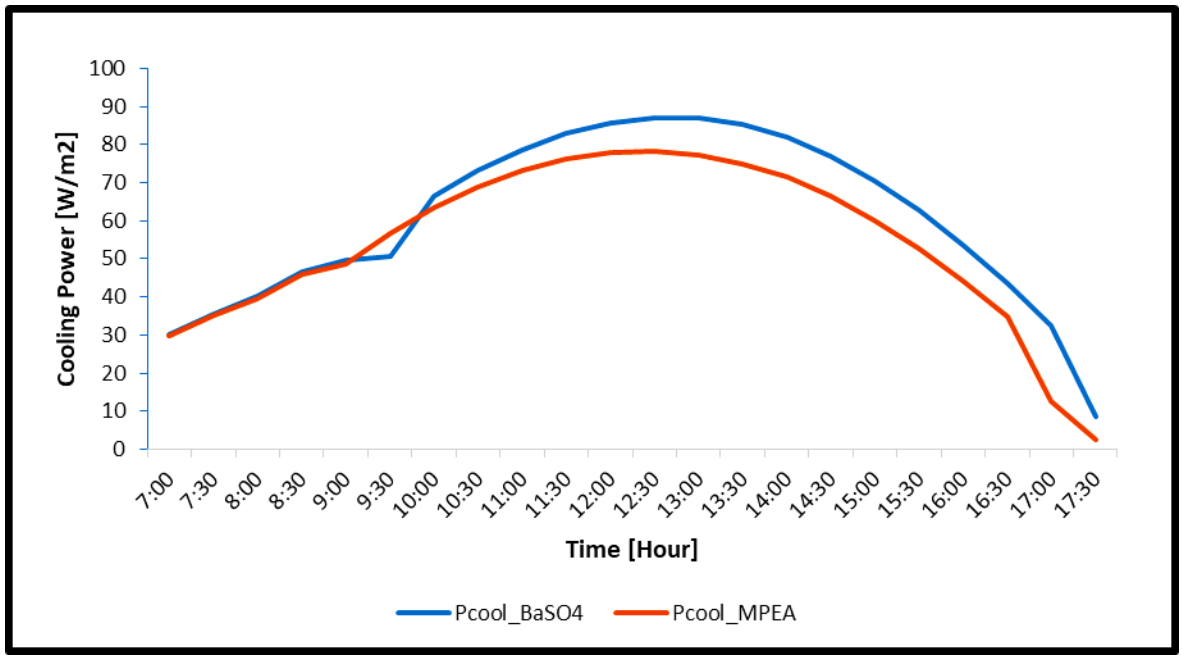

Fig 4.37: Predicted Cooling power plot for Ekiti

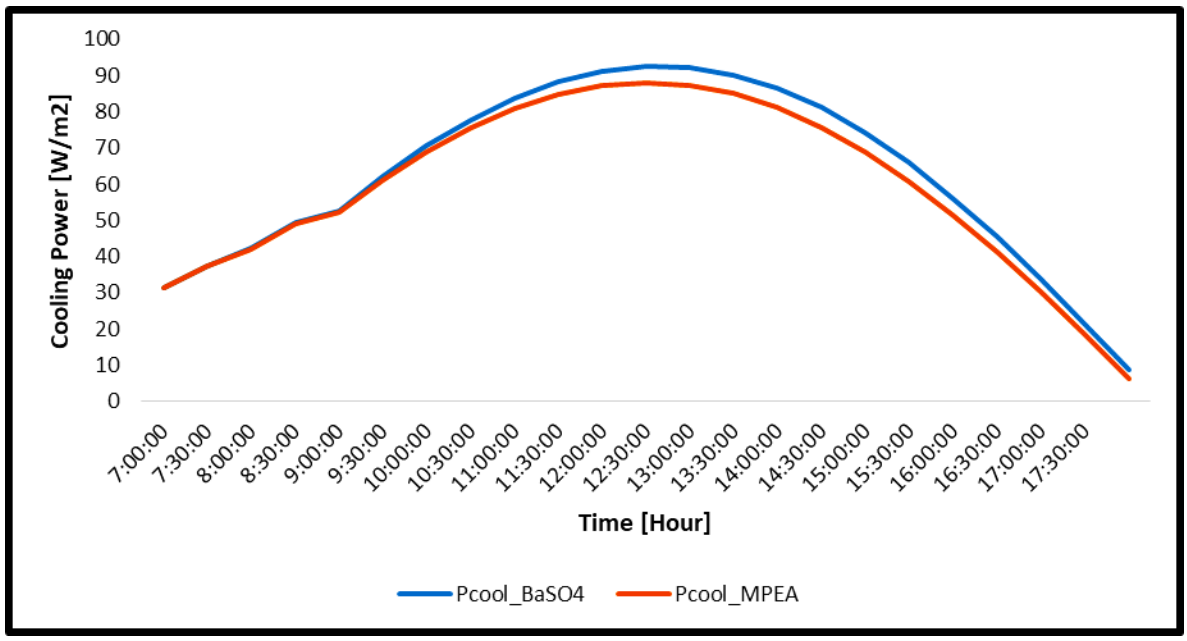

Fig 4.38: Predicted Cooling power plot for Kaduna

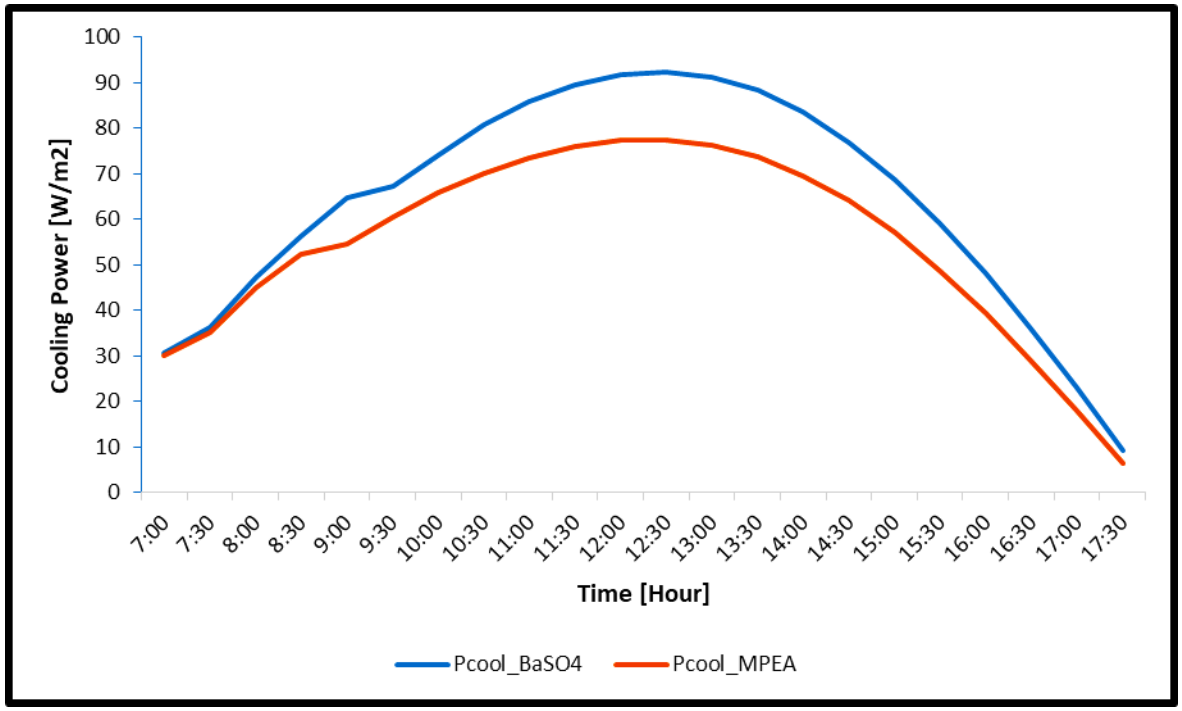

Fig 4.39: Predicted Cooling power plot for Owerri

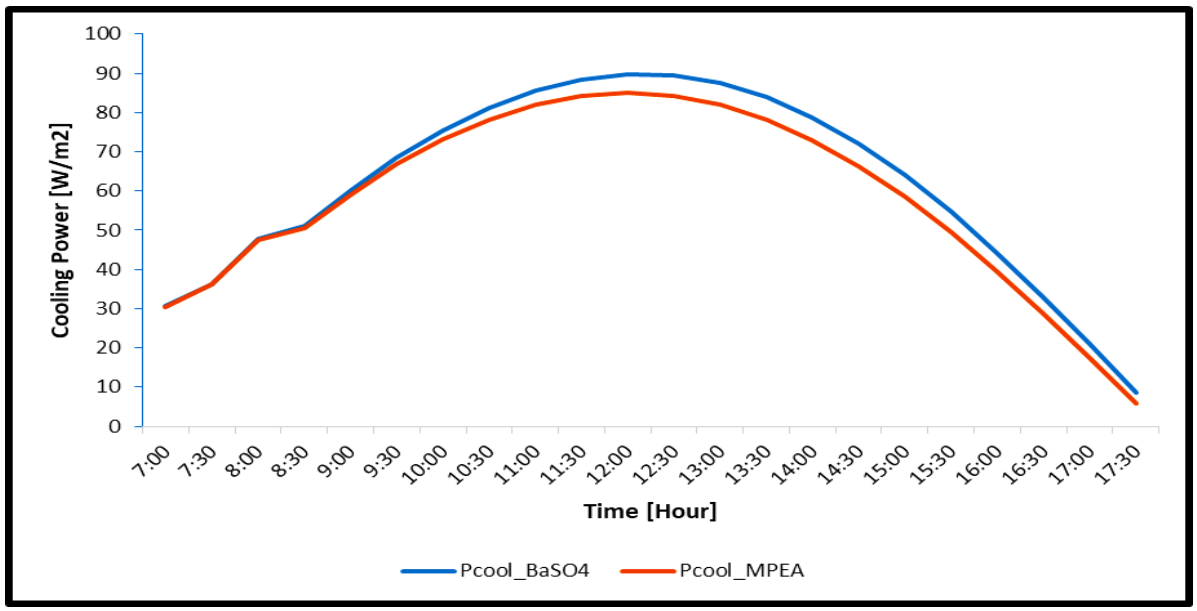

Fig 4.40: Predicted Cooling power plot for Warri

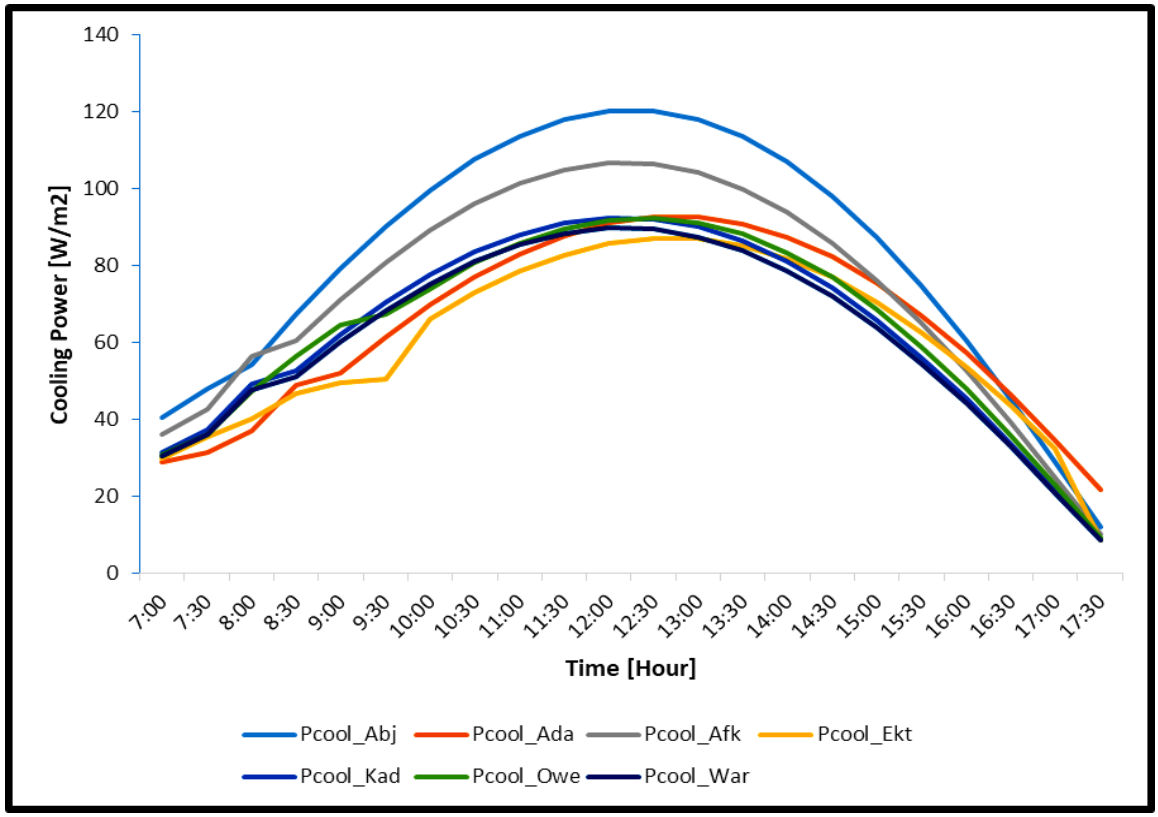

Fig 4.41: Predicted Cooling power plot of $BaSO_4$ for all the test locations in Nigeria

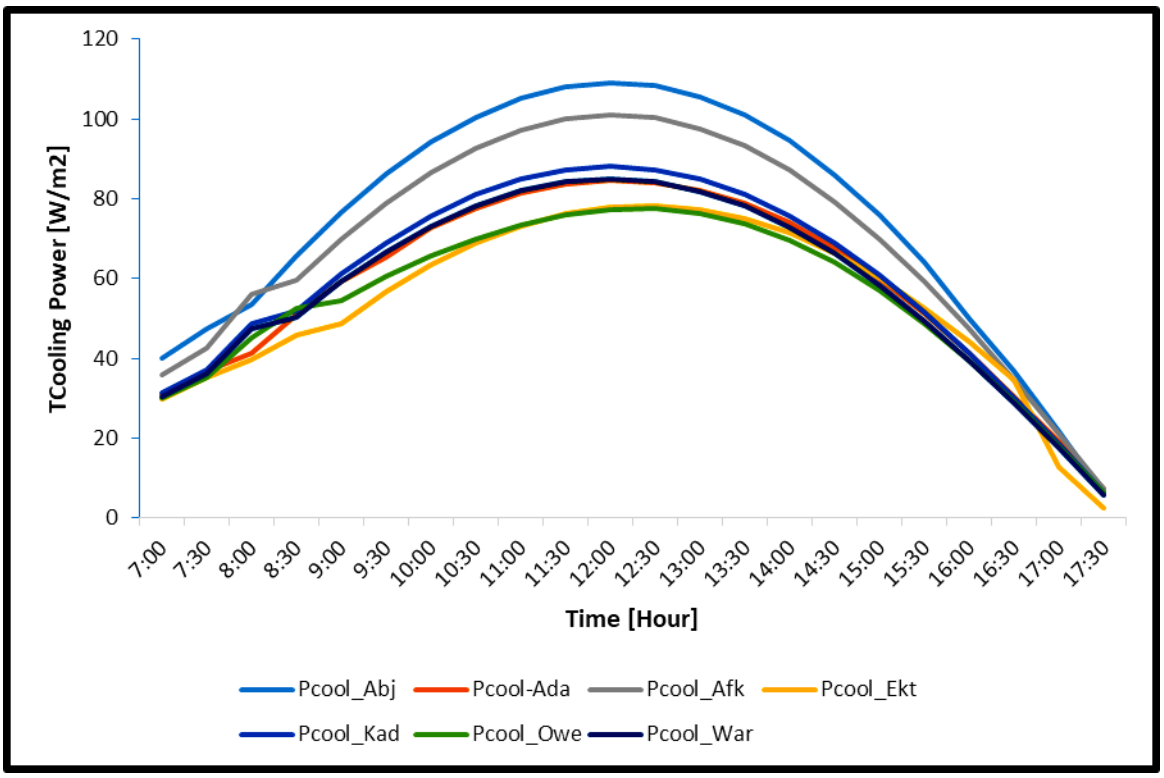

Fig 4.42: Predicted Cooling power plot of MPEA for all the test locations in Nigeria

4.1.6 Validation Studies

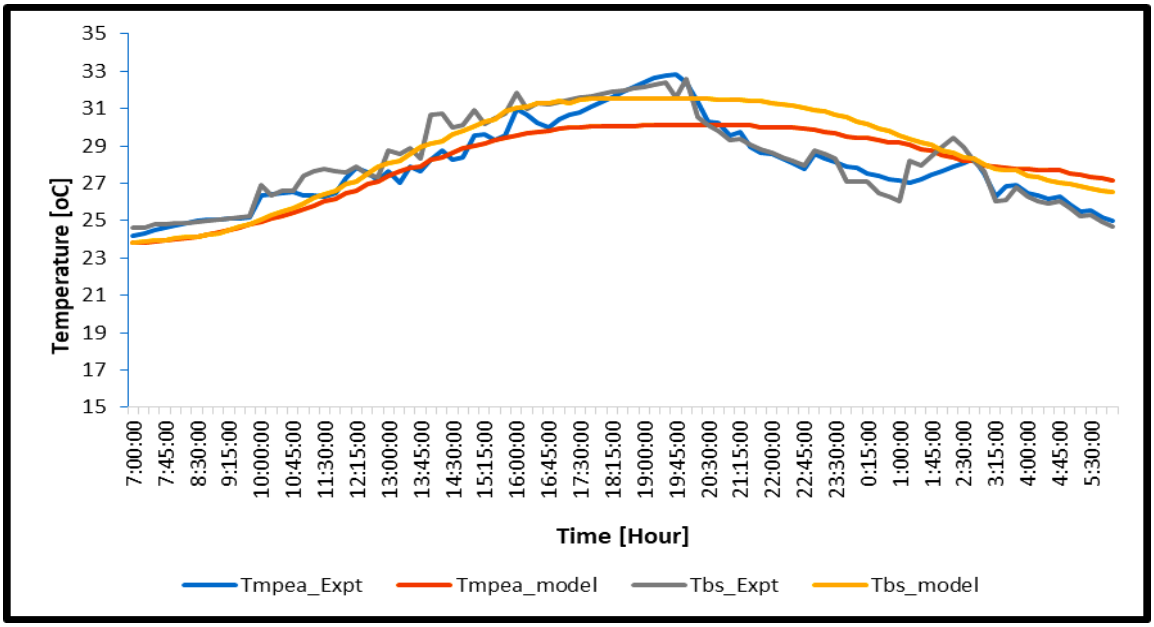

Fig. 4.43 Comparison of model and experimental temperature data of the coolers

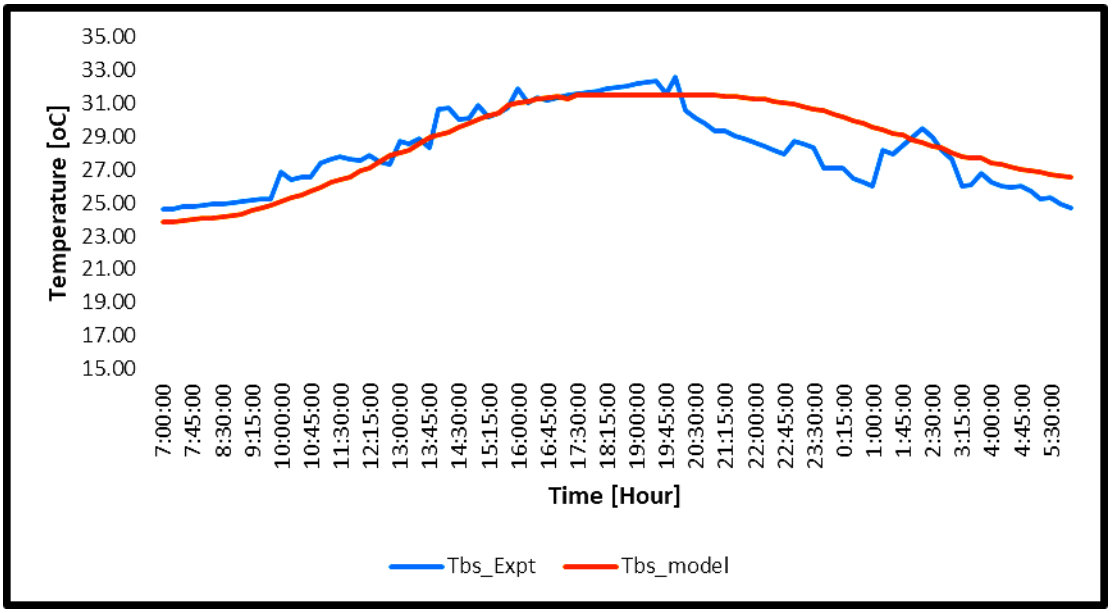

Fig. 4.44 Comparison of model and experimental temperature data of $BaSO_4$

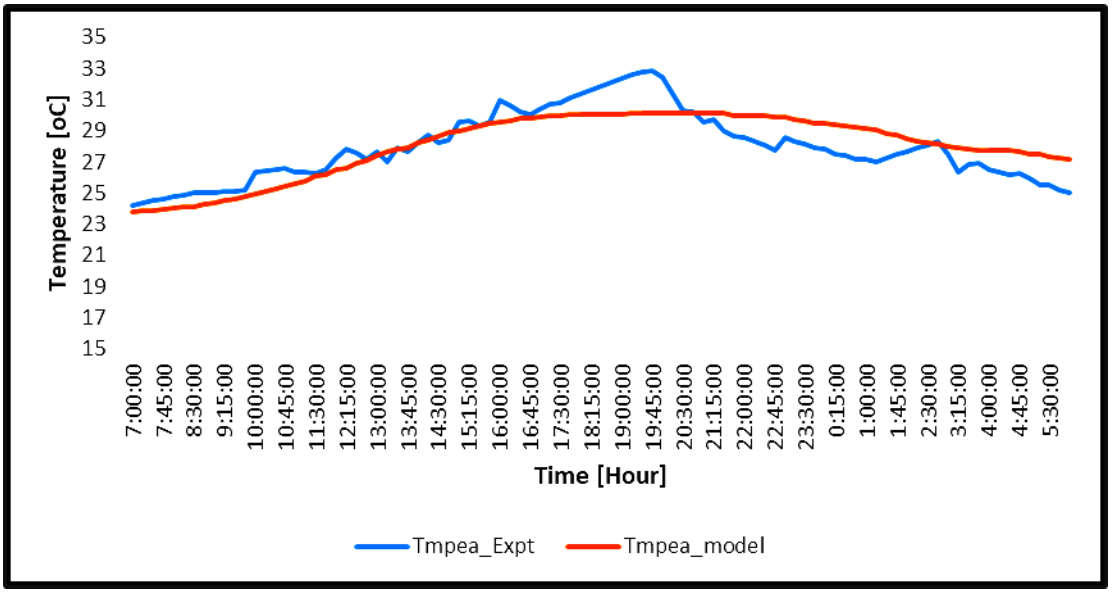

Fig. 4.45 Comparison of model and experimental temperature data of MPEA

4.1.7 Thermal Distribution on the Radiative coolers

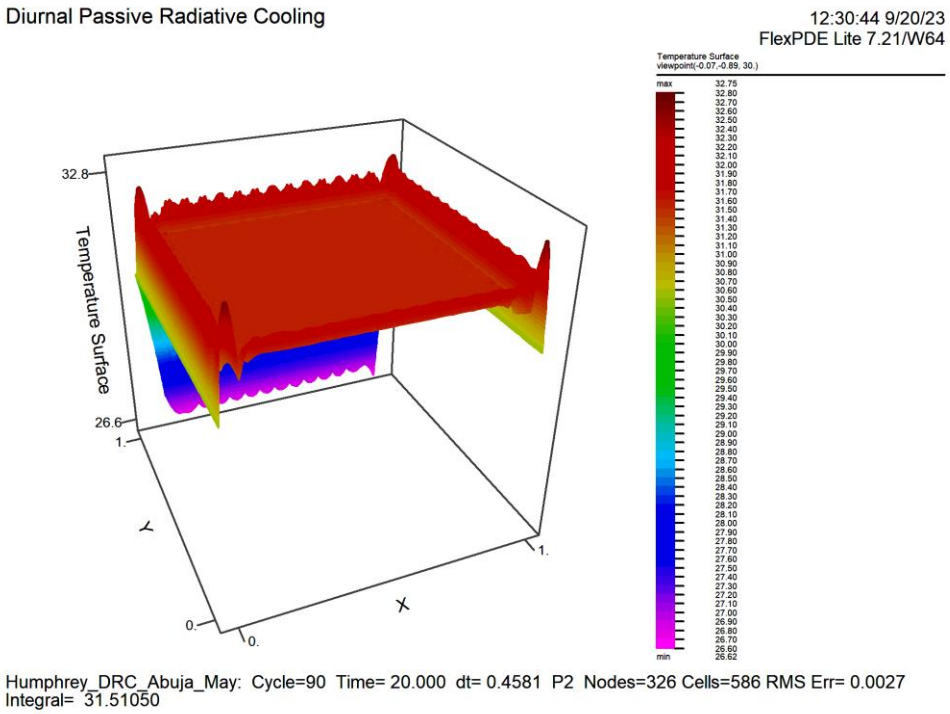

Fig 4.46: $BaSO_4$ surface temperature plot for Abuja, Nigeria

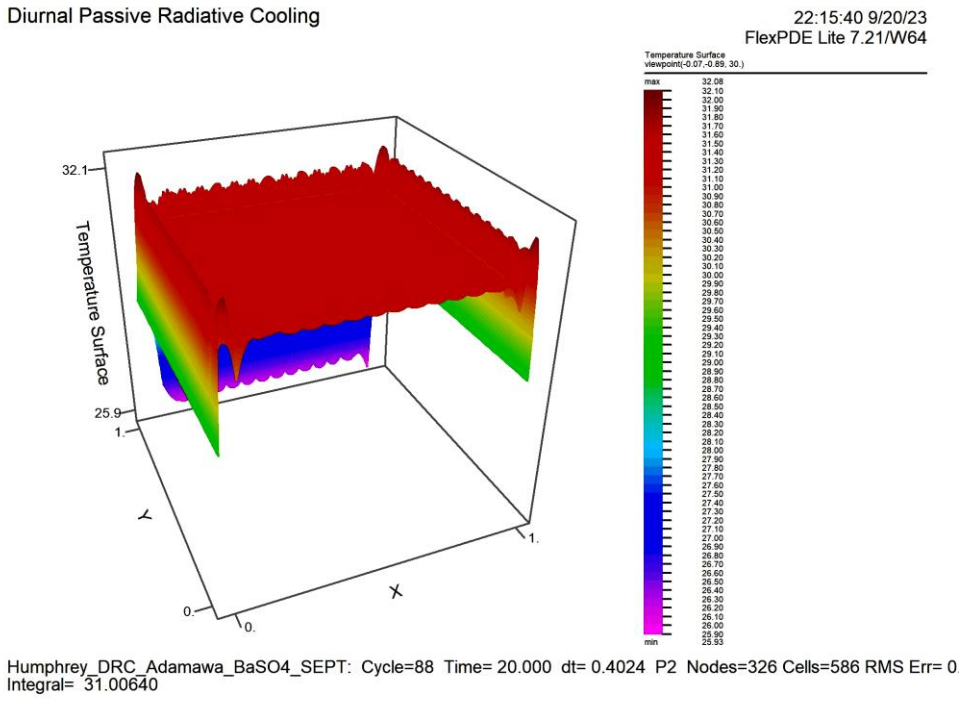

Fig 4.47: $BaSO_4$ surface temperature plot for Adamawa, Nigeria

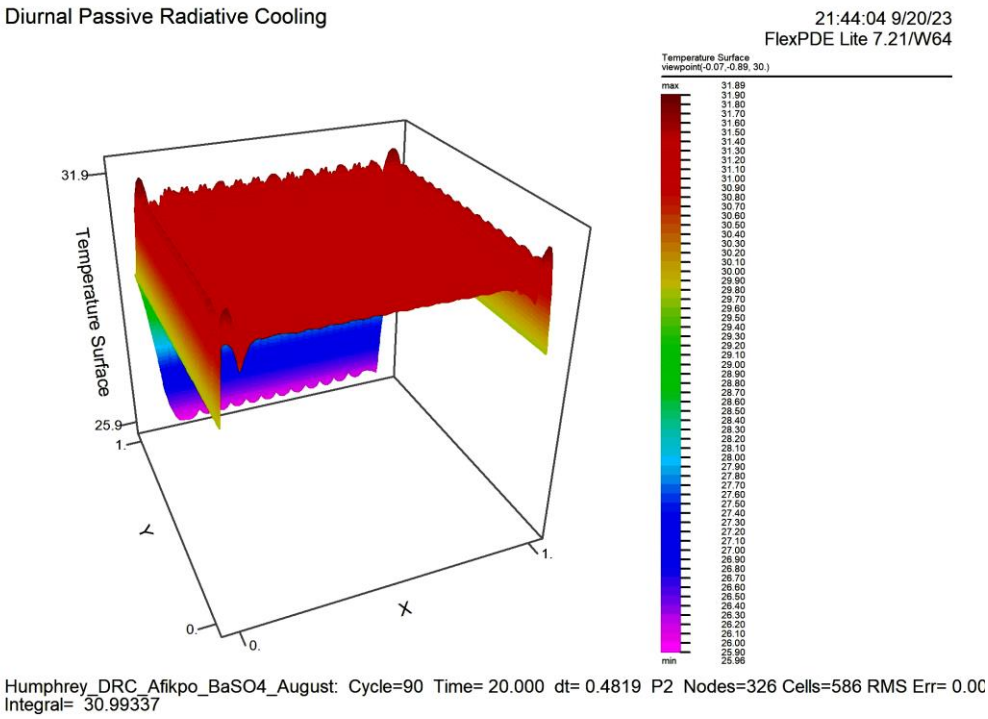

Fig 4.48: $BaSO_4$ surface temperature plot for Afikpo, Nigeria

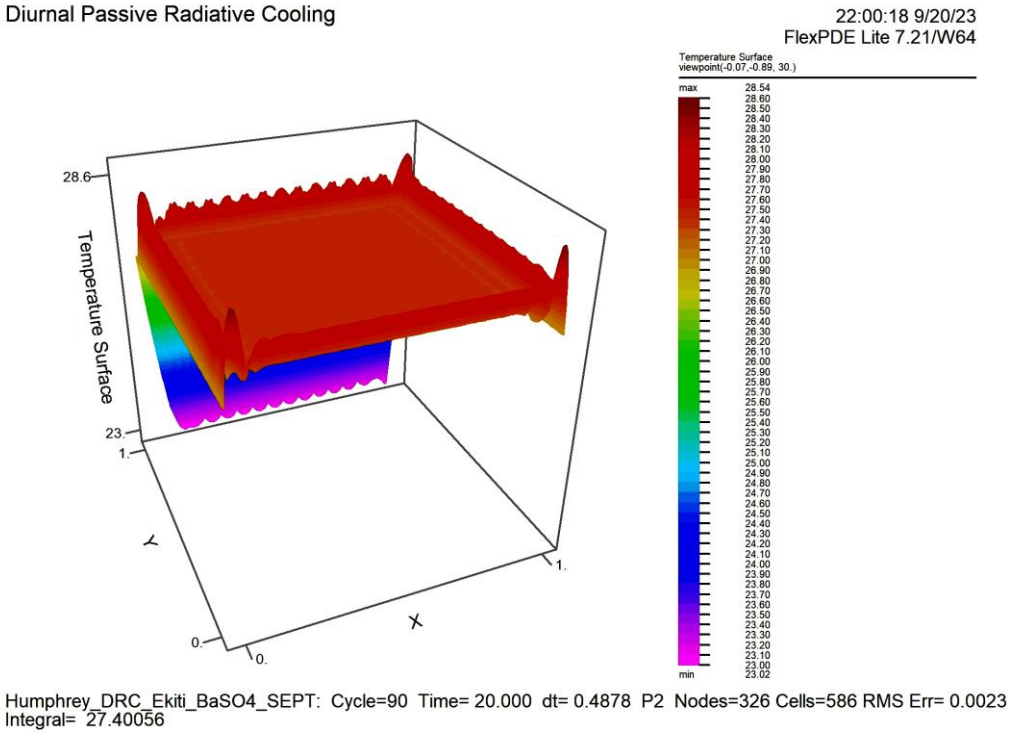

Fig 4.49: $BaSO_4$ surface temperature plot for Ekiti, Nigeria

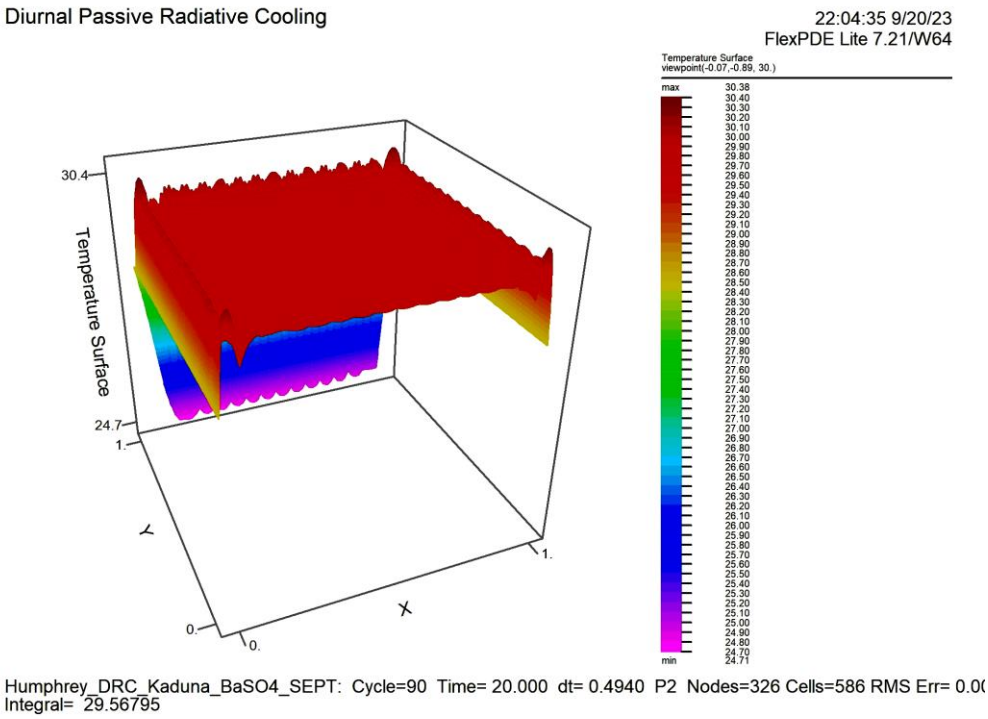

Fig 4.50: $BaSO_4$ surface temperature plot for Kaduna, Nigeria

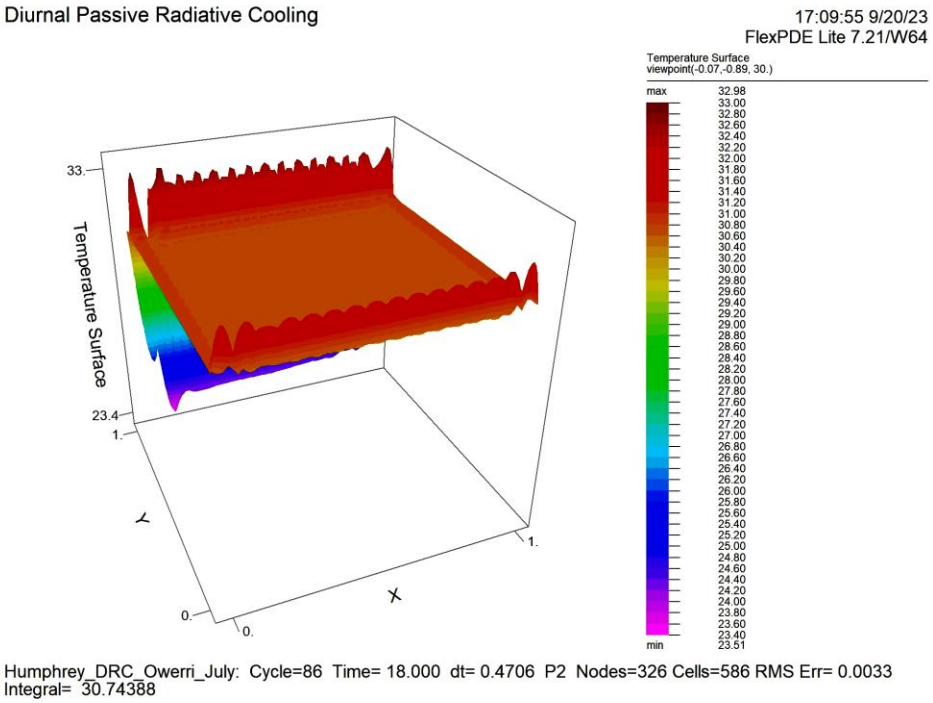

Fig 4.51: $BaSO_4$ surface temperature plot for Owerri, Nigeria

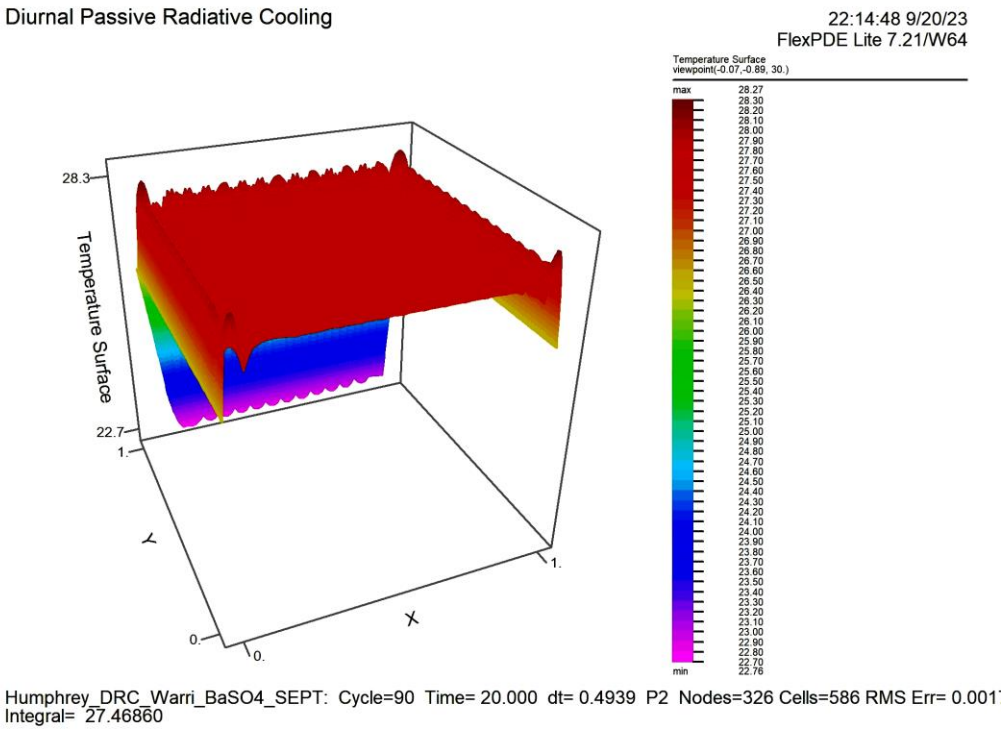

Fig 4.52: $BaSO_4$ surface temperature plot for Warri, Nigeria

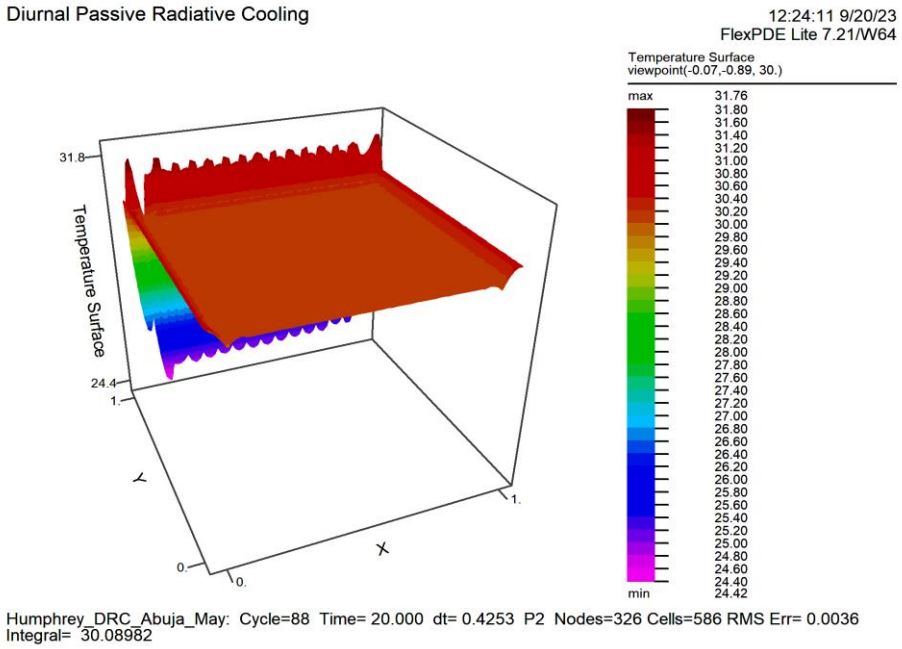

Fig 4.53: MPEA surface temperature plot for Abuja, Nigeria

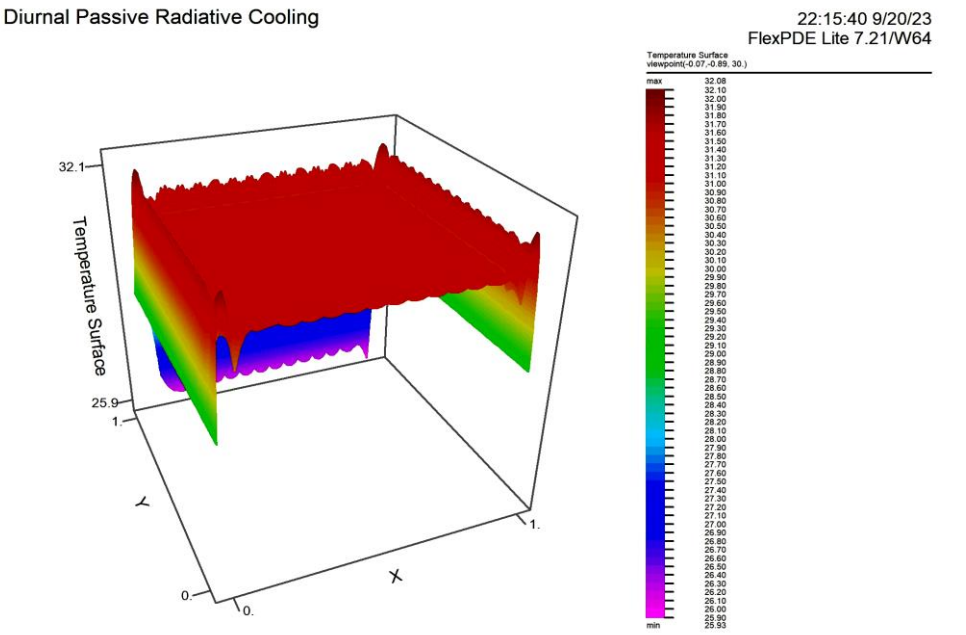

Fig 4.54: MPEA surface temperature plot for Adamawa, Nigeria

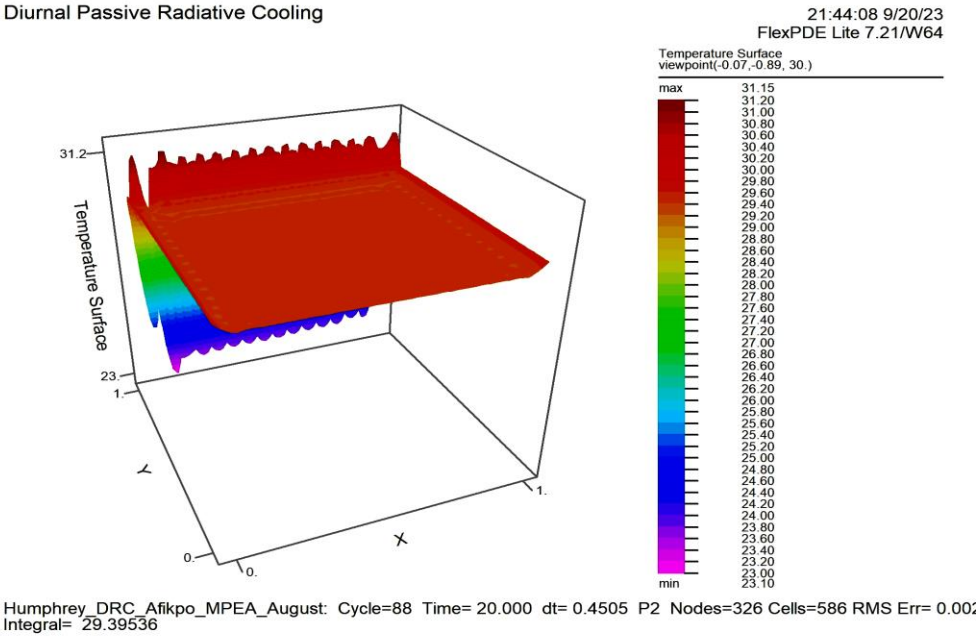

Fig 4.55: MPEA surface temperature plot for Afikpo, Nigeria

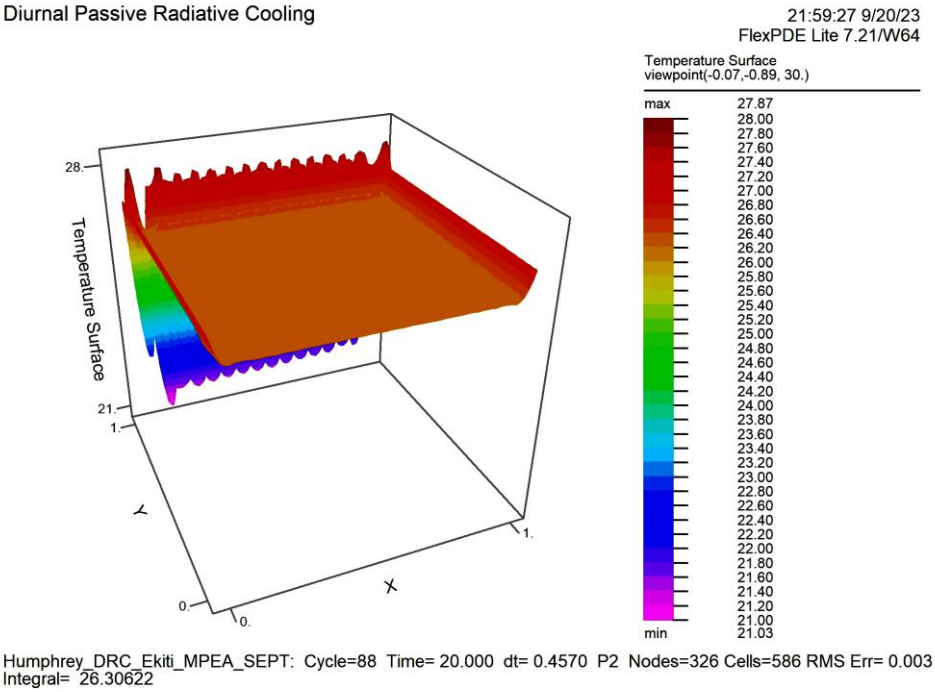

Fig 4.56: MPEA surface temperature plot for Ekiti, Nigeria

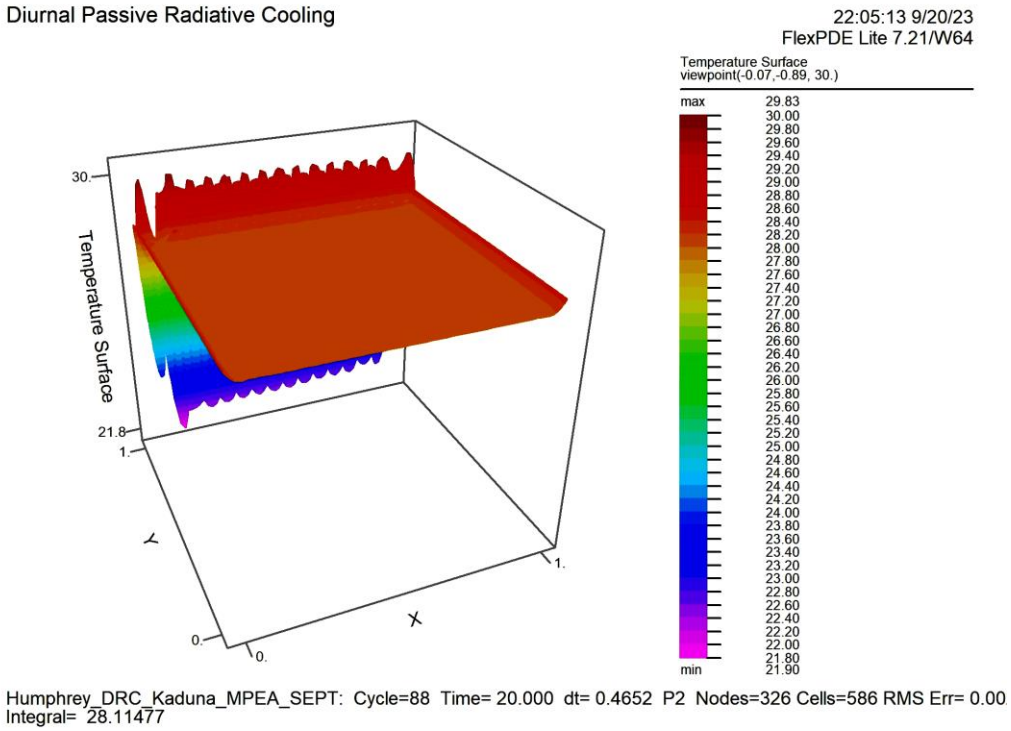

Fig 4.57: MPEA surface temperature plot for Kaduna, Nigeria

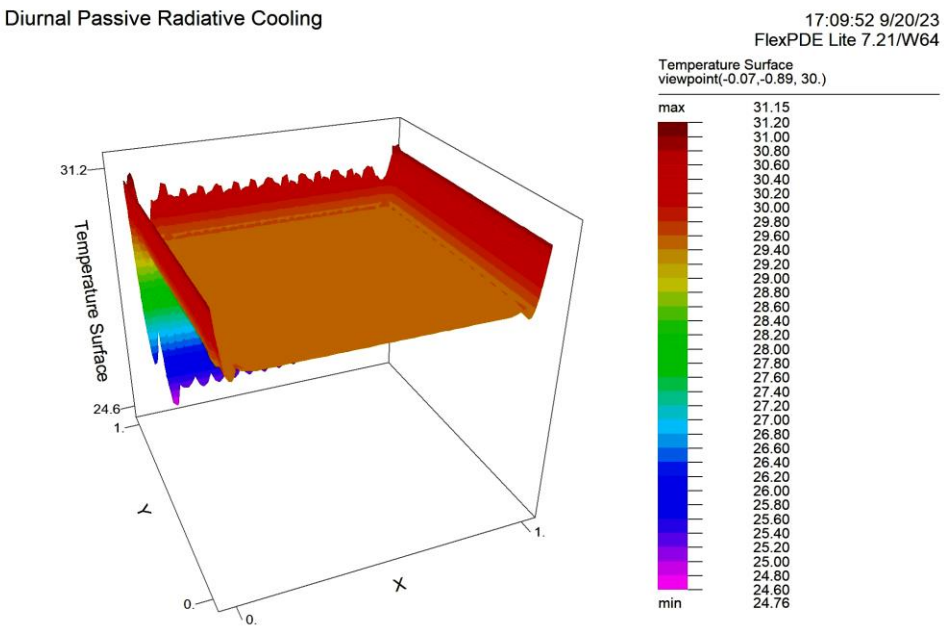

Fig 4.58: MPEA surface temperature plot for Owerri, Nigeria

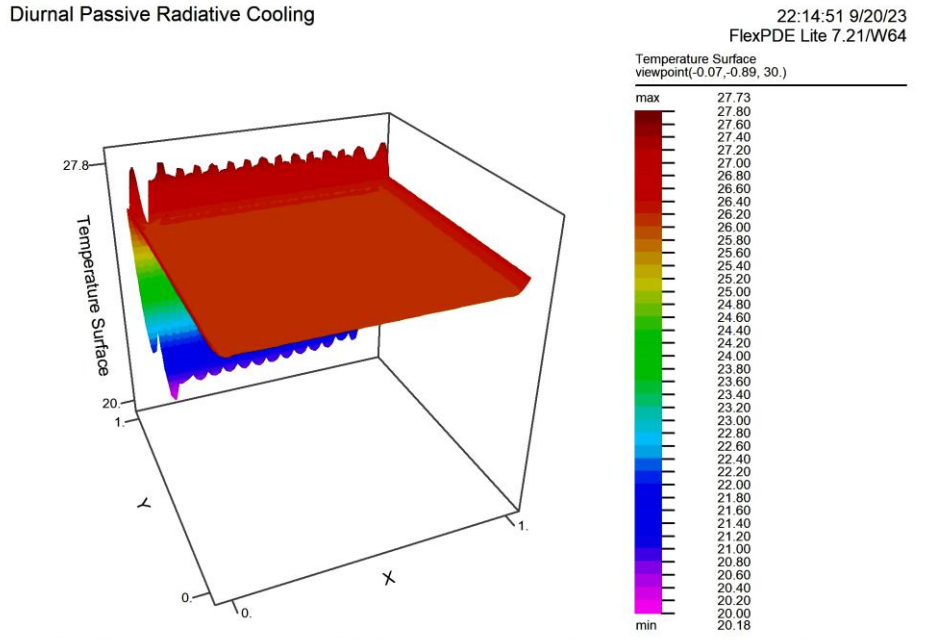

Fig 4.59: MPEA surface temperature plot for Warri, Nigeria

4.1.8 Parametric Analyses

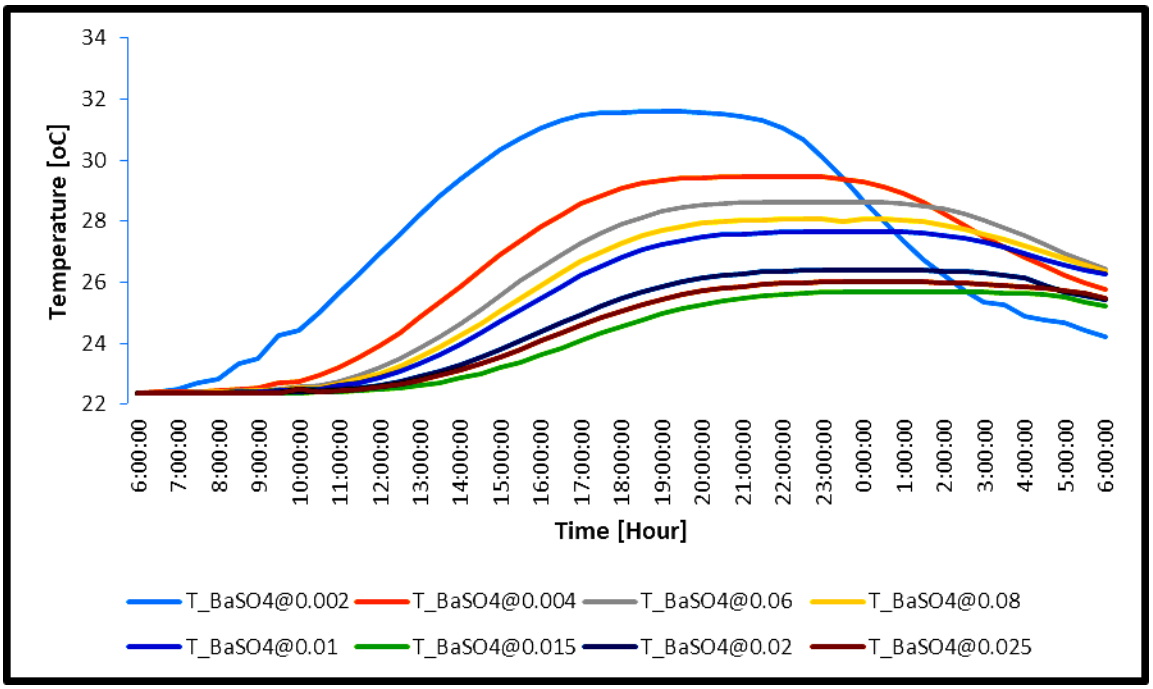

Fig 4.60: $BaSO_4$ temperature profile at varying thicknesses

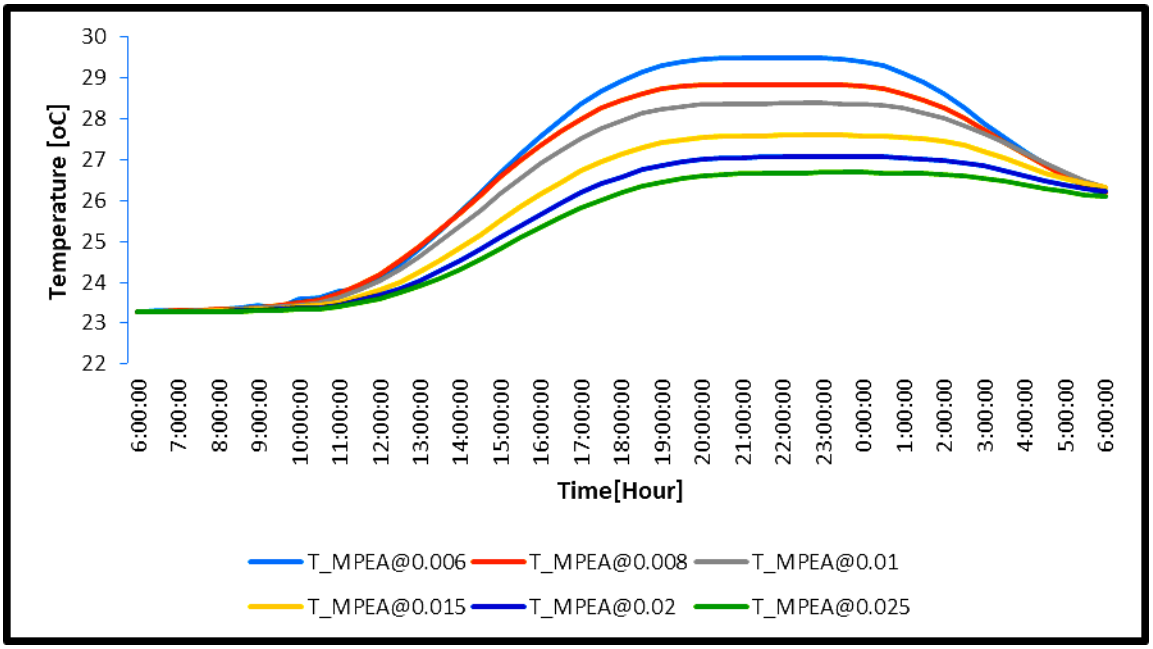

Fig 4.61: MPEA temperature profile at varying thicknesses

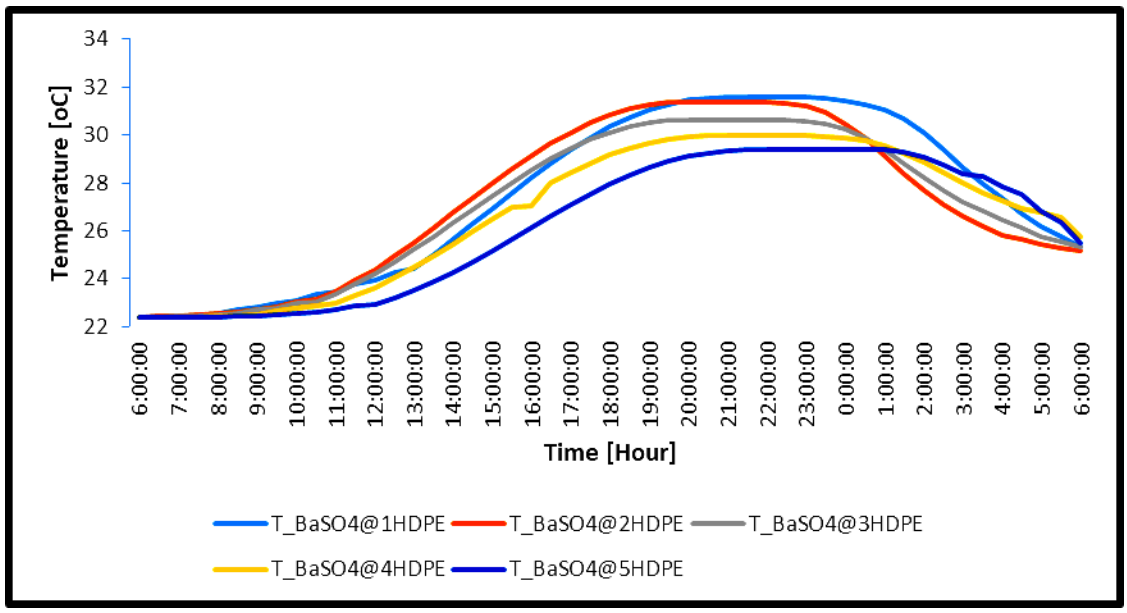

Fig 4.62: $BaSO_4$ temperature profile at varying number of Wind Screens

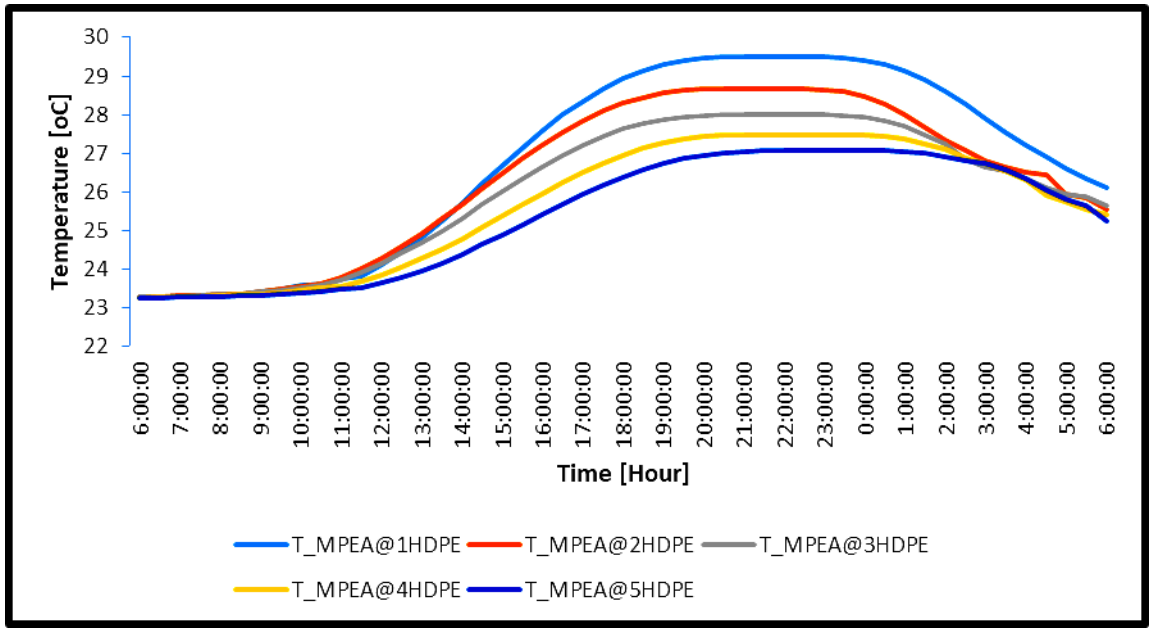

Fig 4.63: MPEA temperature profile at varying number of Windscreens

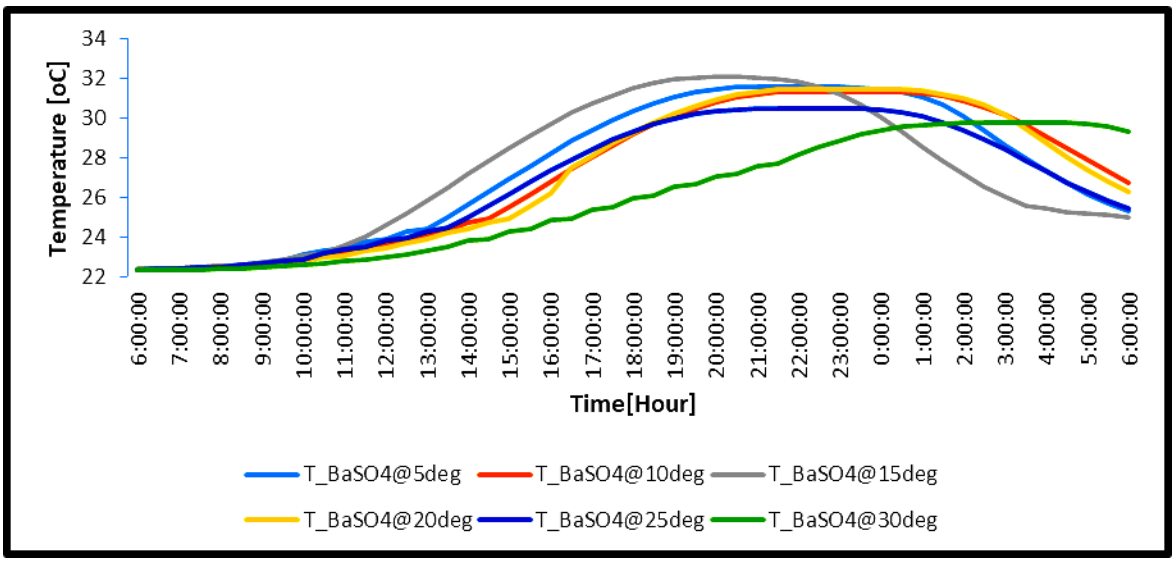

Fig 4.64: $BaSO_4$ temperature profile at varying orientations

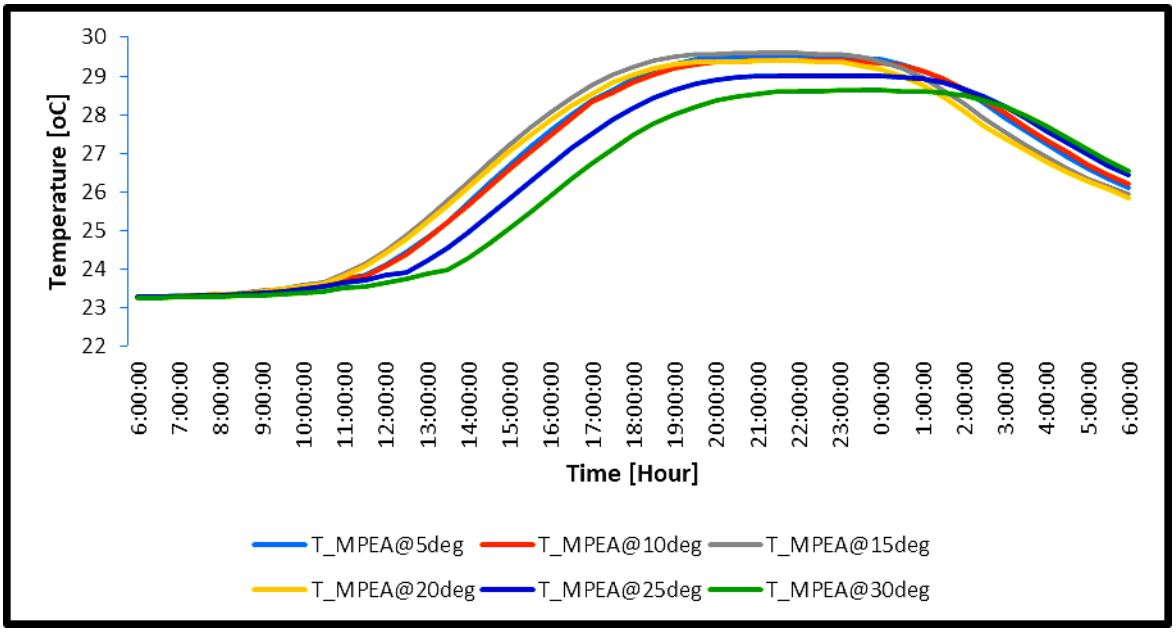

Fig 4.65: MPEA temperature profile at varying orientations

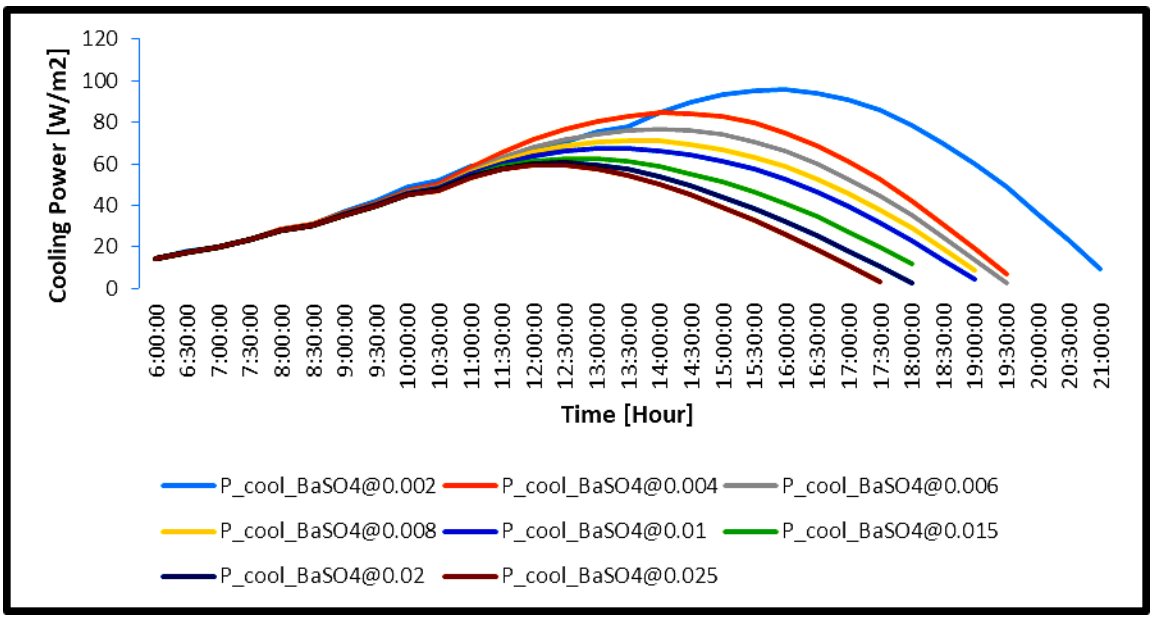

Fig 4.66: $BaSO_4$ Cooling Power profile at varying thicknesses

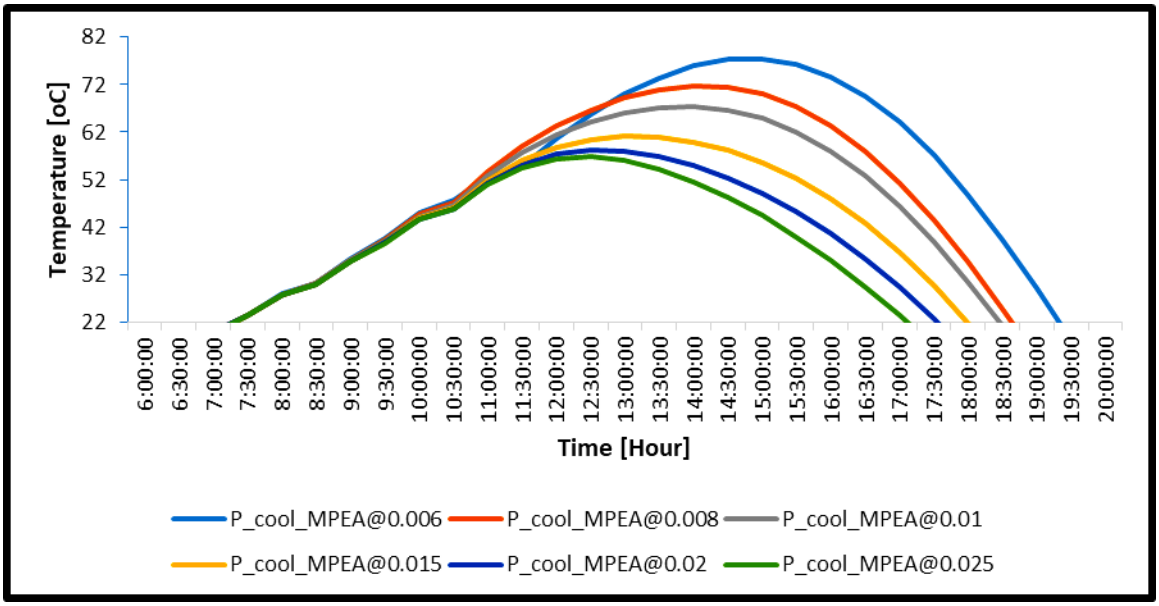

Fig 4.67: MPEA Cooling Power profile at varying thicknesses

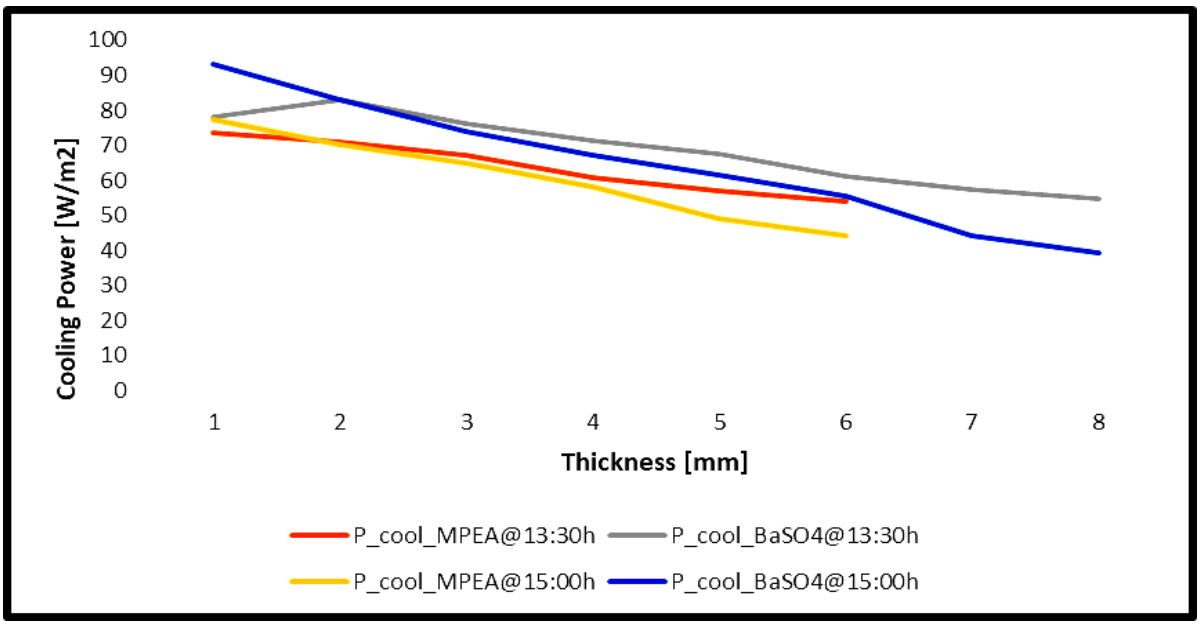

Fig 4.68: $BaSO_4$ and MPEA Cooling Power at maximum solar irradiation

4.2 DISCUSSION

The results obtained from the study as presented in figs 4.1-4.80 are discussed in this section. Section 4.2.1 discusses the results of figs 4.1-4.12 that illustrate the experimental temperatures for $BaSO_4$ and MPEA with that of the ambient in the three experimental test locations of Abuja, Afikpo, and Owerri. Figs 4.13-4.18 presents the discussion of the Comparative studies for the coolers as presented in section 4.2.2. Figs 4.19-4.36 that show the effect of climatic conditions such as relative humidity, wind and daily solar radiation on the performance of the radiative coolers in the test locations are discussed in section 4.2.3. The discussion of the results of Figs 4.37-4.45 that presents the numerical temperatures for $BaSO_4$ and MPEA with that of the ambient in the six geopolitical locations of Nigeria and Afikpo are presented in section 4.2.4. Figs 4.46-4.54 that illustrates the cooling powers of $BaSO_4$ together with MPEA for Afikpo and the six geopolitical zones of Nigeria are discussed in section 4.2.5. Section 4.2.6 that presents the validation studies are discussed in Figs 4.55-4.57. Figs 4.58-4.71 that show the show

the thermal distribution on the $BaSO_4$ and MPEA coolers are discussed in section 4.2.7 while Figs 4.72-4.80 discusses the results of the parametric analysis in section 4.2.8 to determine the effect of thermophysical and material properties of the system.

4.2.1 EXPERIMENTAL PERFORMANCE EVALUATION OF THE SYSTEM

Figures 4.1-4.12 show the results obtained from experimental investigation to ascertain the diurnal and nocturnal sub-ambient cooling temperature of the coolers in Abuja, Afikpo, and Owerri. The experimental plot of Fig 4.1 on May 18 in Abuja shows that there was no noticeable variation in temperatures between the MPEA and the ambient temperature at about 7:00 AM, and beyond this time to 7:45 AM, slight cooling was noticed. At about 8:30 AM, the cooler presented increasing sub-ambient cooling temperatures, reaching a maximum of 4^oC at about 1:15 PM until about 6:00 PM when there was no observable change in temperature. This remarkable drop in temperature between the hours of 8:30 AM and 6:00 PM shows that cooling was achieved within the diurnal hours of the day.

The experimental plot of Fig 4.2 on May 18 in Abuja shows that the $BaSO_4$ radiative cooler presented no noticeable variation in temperatures with the ambient temperature at about 7:00 AM. The $BaSO_4$ temperature remained the same with the ambient beyond this time until 7:45 AM. At about 8:30 AM, increase in the sub-ambient cooling temperatures was observed, reaching a maximum of 2^oC for $BaSO_4$ at about 1:15 PM and this persisted until about 6:00 PM when there was no observable change in temperature.

Fig 4.3 presents a temperature plot of MPEA, which is similar to that of Fig 4.1 but for four (4) consecutive days (May 19-22) trial in Abuja. In the early hours of May 19, from 7:00 AM to 8:30 AM, the plot indicates that the cooler temperature was the same as the ambient. There was a sharp drop in temperatures of the coolers as the ambient temperature increased resulting in a sub-ambient cooling temperature of 5^oC between 9:00 AM and 4:15 PM the same day. From 4:30 PM to 7:30 PM, there was

a decrease in the sub-ambient temperature to 1.5^{o}C. Slight heating commenced at about 8:00 PMM until 7:30 AM the next day, May 20 when slight cooling started. At about 9:45 AM, the cooler showed a marked cooling, which continued appreciably until 5:30 PM with a maximum sub-ambient temperature of 5^{o}C at about 1:30 PM-4:30 PM. Heating effect resumed from 5:00 PM and continued until 6:45 AM the next day, May 21, which could be because the coolers exchange all the heat with the outer space. From 8:00 AM on |May 21, reasonable cooling has already started, which increased, reaching a maximum sub-ambient temperature of 5^{o}C at about 2:45 PM. Once again, the heating of the system commenced at about 6:00 PM until 8:00 AM the next day, May 22. From 8:30 Am on May 22, cooling occurred until about 6:15 PM with a maximum cooling temperature of 3^{o}C at about 11:45 AM. Finally, the last heating phase started from 5:30 PM until 10:45 PM when the trial was stopped. The maximum temperature drops as recorded from the experiment is consistent with the reports on diurnal passive radiative cooling by Raman et al (2014), which presented a sub-ambient temperature of 4.9^{o}C.

Fig 4.4 presents the same temperature plot of $BaSO_4$ as that of Fig 4.2 for four (4) consecutive days (May 19-22) trial in Abuja. From 7:00 AM to 8:30 AM, the plot indicates that the temperatures were the same as the ambient in the early hours of May 19. The cooler recorded a sharp drop in temperature resulting in a sub-ambient cooling temperature of 2^{o}C for $BaSO_4$ between 9:00 AM and 4:15 PM the same day. From 4:30 PM to 7:30 PM, a decrease in the sub-ambient temperature to about 0.5^{o}C was noticed. At about 8:00 PM, slight heating commenced until 7:30 AM the next day, May 20 when slight cooling started. Heating resumed from 5:00 PM and continued until 6:45 AM the next day, May 21, and then from 8:00 AM, reasonable cooling commenced, reaching a maximum sub-ambient temperature of 3^{o}C at about 2:45 PM. There was heating commenced at about 6:00 PM until 8:00 AM on May 22 and from 8:30 the same day, cooling occurred until about 6:15 PM with a maximum cooling temperature of 2^{o}C at about 11:45 AM. The final phase of heating commenced from 5:30 PM until 10:45 PM when the trial was stopped.

The experimental result of the investigation done in Afikpo on July 16-17 for the MPEA cooler is presented in Fig 4.5. The result showed a heating effect between 6:00 AM when the trial started and 7:30 AM but from this time, there was no noticeable change in temperatures with the ambient untill 8:30 AM when cooling started and increased remarkably, reaching a maximum of 5^{o}C on July 16. At about 4:15 PM, the cooler started heating, which continued until 1:45 AM the next day, July 17 when the MPEA suddenly started cooling and persisted until about 6:00 AM-7:30 AM when there was no noticeable change in temperature. From 8:00 AM, remarkable cooling resumed, reaching a maximum of 6^{o}C for MPEA, which is in agreement with the temperature drops of 2-6^{o}C reported by Chen et al (2022) and Zhao et al (2019). The heating effect started and continued until 2:30 AM the next day, July 18 when cooler resumed cooling again.

Fig 4.6 presents the experimental result of the investigation done in Afikpo on July 16-17 for $BaSO_4$. The result showed the trial started at about 6:00 AM but there was no noticeable variation in temperatures of the cooler and the ambient between 7:30 AM and 8:30 AM, after which cooling started and increased remarkably, reaching a maximum temperature drop of 3^{o}C below the ambient temperature on July 16. There was heating effect as from 4:00 PM until 11:30 PM when the cooler suddenly started cooling. The cooling effect continued until about 6:00 AM-7:30 AM when there was no more noticeable variation in temperature with the ambient. A significant cooling resumed at about 8:00 AM, reaching a maximum of 3^{o}C. Alternation of heating and cooling effect started at 4:45 PM and continued until 4:00 AM on July 18, when continuous cooling resumed again.

Fig 4.7 shows the result of the experimental investigation conducted in Afikpo on August 10-13 for the MPEA radiative cooler. The plot showed that cooling occurred from 6:00 AM until 9:30 AM on August 10, increased progressively, and reaching a maximum of 1^{o}C. At about 2:15 PM heating

commenced and continued until 8:30 PM when the cooler showed a significant cooling effect, resumed heating again at 1:00 AM until 3:30 AM the next day, August 11, and then nocturnal cooling from 4:00 AM until 5:30 AM. Again, the cooler experienced heating from 5:30 AM until 8:30 AM when diurnal cooling started. Diurnal cooling started from 8:30 AM on August 11 and reaching a maximum of 2^{o}C at 12:30 PM. The cooling effect decreased until 4:30 PM when heating commenced and alternated with cooling until 5:00 AM on August 12 when diurnal cooling recommenced. A maximum sub-ambient temperature of 2^{o}C was reached at about 10:30 AM. Again, diurnal heating commenced at about 6:45 PM until about 3:30 AM on August 13 when cooling resumed. However, from 10:30 PM-12:00 AM and 1:30 AM-2:45 AM, cooling effect was recorded.

The experimental investigation conducted in Afikpo on August 10-13 for $BaSO_4$ is presented in Fig 4.8. Cooling occurred between 6:00 AM and 9:30 AM on August 10 and increased progressively, reaching a maximum of 1^{o}C at 2:15 PM. Heating commenced at about 7:15 PM continued until 8:30 PM when a significant cooling effect was observed. The system resumed heating again at 1:00 AM until 3:30 AM the next day, August 11, when nocturnal cooling and lasted until 5:30 AM. Diurnal cooling started from 8:30 AM on August 11, 2023 and reached a maximum of 2^{o}C at 12:30 PM. The cooling and heating effects alternated after 12:30 PM until 5:00 AM on August 12 when diurnal cooling recommenced. Finally, diurnal heating commenced at about 6:45 PM and continued until about 3:30 AM on August 13 when cooling resumed.

Fig 4.9 presents the result of the field trial that was done in Owerri on July 12-15 for MPEA radiative cooler. The figure shows that diurnal cooling started immediately after the trial started at 6:00 AM on July 12. The cooling reached a maximum of 3^{o}C at about 11:00 AM, and was maintained until the next day, July 13 with heating at 5:00 PM-9:00 PM, 11:45 PM-12:45 AM, and 6:15 AM-8:15 AM on the same day. Maximum diurnal cooling temperature of 3.5^{o}C at 3:30 PM, which is consistent with the temperature drops (2-6^{o}C) recorded by Joseph et al (2023), Huang et al (2022), Huang and Ruan

(2017). On July 14 heating commenced from 6:30 PM until 12:30 PM with a maximum diurnal cooling temperature of 1^{o}C at about 1:30 PM. At about 5:00 PM, heating of both coolers commenced until about 1:00 AM on July 15 when nocturnal cooling started and lasted until 4:30 AM.

The result of the field trial in Owerri on July 12-15 is presents in Fig 4.10 with cooling starting almost immediately after the trial started at 6:00 AM on July 12. A maximum cooling temperature of 3^{o}C was recorded at about 11:00 AM with heating at 5:00 PM-9:00 PM, 11:45 PM-12:45 AM, and 6:15 AM-8:15 AM on July 13. On 13th July, a maximum diurnal cooling temperature of 3.5^{o}C was recorded at about 3:30 PM. The heating of the cooler on July 14 commenced from 6:30 PM until 12:30 PM and showed a maximum diurnal cooling temperature of 1^{o}C at about 1:30 PM. Also, heating of the cooler commenced at about 5:00 PM until about 1:00 AM on July 15 when nocturnal cooling started.

The result of the experimental investigation MPEA in Owerri on August 14-17 is presented in fig 4.11 with heating from 6:00 AM until about 11:30 AM-12:45 PM when a very minimal diurnal cooling occurred. At about 2:00 PM, cooler recorded a maximum sub-ambient diurnal cooling temperature of 6^{o}C. On the second day, August 15, 2023, maximum diurnal cooling temperature of 2^{o}C occurred at about 4:30 PM and the cooler maintained this cooling effect until 2:30 AM when there was no more observable variation in temperature with the ambient. From 7:00 PM, the cooler got heated until 10:15 PM when the temperature differential remained constant until the next day. Sensible diurnal sub-ambient cooling resumed at 10:45 AM on August 16 and reached a maximum of 3.5^{o}C at 12:15 PM. From 5:00 PM, the cooler got heated until 7:00 PM when it resumed cooling again.

Fig 4.12 shows the result of the experimental investigation for $BaSO_4$ in Owerri on August 14-17 with diurnal cooling at about 11:30 AM-12:45 PM and at about 2:00 PM the coolers recorded a maximum sub-ambient diurnal cooling temperature of 1^{o}C. During the trial on August 15, diurnal cooling resumed at about 6:30 AM for $BaSO_4$, and reached a maximum of 2^{o}C at about 4:30 PM. There was

heating of the cooler from 7:00 PM until 10:45 PM when the temperature differential remained unchanged. Diurnal sub-ambient cooling occurred at about 10:45 AM on August 16 and reached a maximum of 2.5^{o}C for $BaSO_4$ at 1:00 PM. The cooler got heated between 5:00 PM and 7:00 PM when it resumed cooling.

4.2.2 COMPARATIVE STUDIES

Figures 4.13-4.18 show the results obtained from experimental investigation of the coolers performance in Abuja, Afikpo, and Owerri. The experimental plot of Fig 4.13 on May 18 in Abuja compares the performance of the MPEA and $BaSO_4$ coolers, and it is shown that there was no noticeable variation in temperatures between the MPEA and the ambient temperature at about 7:00 AM. Beyond this time to 7:45 AM, slight cooling was noticed with the MPEA while the $BaSO_4$ temperature remained the same with the ambient. At about 8:30 AM, both coolers presented increasing sub-ambient cooling temperatures, reaching a maximum of 4^{o}C for MPEA and 2oC for $BaSO_4$ at about 1:15 PM until about 6:00 PM when there was no observable change in temperature. This remarkable drop in temperature between the hours of 8:30 AM and 6:00 PM shows that cooling was achieved within the diurnal hours of the day.

Fig 4.14 presents a temperature plot of the MPEA and $BaSO_4$ radiative coolers for four (4) consecutive days (May 19-22) trial in Abuja. In the early hours of May 19, from 7:00 AM to 8:30 AM, the plot indicates that there was no variation of temperature between the MPEA, $BaSO_4$ and ambient. There was a sharp drop in temperatures of the coolers resulting in a sub-ambient cooling temperature of 5^{o}C for the MPEA and 2^{o}C for $BaSO_4$ between 9:00 AM and 4:15 PM the same day. From 4:30 PM to 7:30 PM, the sub-ambient temperature decreased to 1.5^{o}C for MPEA and about 0.5^{o}C for $BaSO_4$. At about 8:00 AM, the $BaSO_4$ showed a marked cooling than the MPEA, which trend was quickly overtaken by the MPEA at 9:45 AM where the drop in temperature was obvious. Heating resumed from 5:00 PM and

continued until 6:45 AM the next day, May 21. From 8:00 AM on |May 21, reasonable cooling has started especially with the MPEA cooler, which increased, reaching a maximum sub-ambient temperature of 5^{o}C for MPEA and 3^{o}C for $BaSO_4$ at about 2:45 PM. Furthermore, the heating of the system commenced at about 6:00 PM until 8:00 AM the next day, May 22 and then from 8:30 AM, cooling occurred until about 6:15 PM with a maximum cooling temperature of 3^{o}C for MPEA and 2^{o}C for $BaSO_4$ at about 11:45 AM. Finally, the last heating phase started from 5:30 PM until 10:45 PM when the trial was stopped.

The result of the experimental investigation in Afikpo on July 16-17 for both coolers is presented in Fig 4.15. The result showed that there was slight heating effect between 6:00 AM when the trial started and 7:30 AM and from 8:30 AM cooling started, reaching a maximum of 5^{o}C for MPEA and 3^{o}C for $BaSO_4$ on July 16. The $BaSO_4$ started heating first at about 4:00 PM, while MPEA followed accordingly 15 minutes later. The heating of the $BaSO_4$ and MPEA continued until 11:30 PM, and 1:45 AM the next day, July 17 when cooling started. The cooling of both coolers continued until about 6:00 AM-7:30 AM when there was no noticeable change in temperature with the ambient. A maximum sub-ambient cooling temperature of 6^{o}C for MPEA and 3^{o}C for $BaSO_4$ were obtained on this day. At about 4:45 PM, the $BaSO_4$ started heating effect, which was followed by the MPEA 15 minutes later. The heating continued for MPEA until 2:30 AM the next day, July 18, 2023 while the $BaSO_4$ showed a slight cooling from 6:30 PM until 7:00 PM.

In Fig 4.16, the result of the experimental investigation in Afikpo on August 10-13 is presented. Cooling occurred in both coolers between 6:00 AM and 9:30 AM on August 10 and reached a maximum of 3^{o}C for MPEA and 1^{o}C for $BaSO_4$ at 2:15 PM until 7:15 PM after which heating commenced. The heating continued until 8:30 PM when the MPEA showed a significant cooling effect. Nocturnal cooling occurred between 4:00 AM and 5:30 AM on July 11, 2023 and between 5:30 AM and 8:30 AM, the coolers experienced heating. The maximum sub-ambient cooling temperature of 2^{o}C

for MPEA at 2:00 PM and for $BaSO_4$was recorded at 12:30 PM during this day. The cooling effect alternated with heating effect until 5:00 AM on August 12 when cooling recommenced. A maximum sub-ambient temperature of 3.5^oC for MPEA and 2^oC for $BaSO_4$ was reached at about 10:30 AM on August 12, 2023. Diurnal heating occurred between 6:45 PM and 3:30 AM on August 13 when cooling resumed while cooling effect occurred between 10:30 PM and 12:00 AM and 1:30 AM and 2:45 AM for the $BaSO_4$ cooler.

Fig 4.17 presents the result of the field trial in Owerri on July 12-15 where diurnal cooling started at about 6:00 AM on July 12 and progressed, reaching a maximum of 4.5^oC for MPEA and 3^oC for $BaSO_4$ at about 11:00 AM. This cooling effect was maintained until the next day, July 13 for MPEA while the $BaSO_4$ recorded heating at 5:00 PM-9:00 PM, 11:45 PM-12:45 AM, and 6:15 AM-8:15 AM on July 13. Maximum sub-ambient cooling temperature of 5^oC for MPEA and 3.5^oC for $BaSO_4$ was reached for both coolers at 3:30 PM. On July 14, 2023, the heating of the coolers commenced from 6:30 PM until 10:00 AM for MPEA and 12:30 PM for $BaSO_4$ and also showed a maximum diurnal cooling temperature of 3.5^oC for MPEA and 1^oC for $BaSO_4$ at about 1:30 PM.

The result of the experimental investigation in Owerri on August 14-17 is presented in fig 4.18 with initial heating at the early hours of the day but at about 12:00 PM-1:45 PM, the MPEA showed a minimal diurnal cooling while the diurnal cooling of the $BaSO_4$ occurred at about 11:30 AM-12:45 PM. On August 15, diurnal cooling resumed at about 6:30 AM, reaching a maximum of 6^oC for MPEA and 2^oC for $BaSO_4$ at about 4:30 PM. The MPEA maintained the cooling effect until 2:30 AM when there was no more observable change in temperature with the ambient while the $BaSO_4$ heated from 7:00 PM until 10:45 PM. On August 16, 2023, sensible diurnal sub-ambient cooling resumed at 10:15 AM and reached a maximum of 3.5^oC for MPEA at 12:15 PM and 2.5^oC for $BaSO_4$ at 1:00 PM. The MPEA maintained a noticeable change in temperature with the ambient between 5:00 PM and 7:00 PM, while the $BaSO_4$ got heated.

4.2.3 EFFECT OF CLIMATIC CONDITIONS ON THE PERFORMANCE OF THE SYSTEMS

The result of the experimental investigation to study the effect of climatic conditions such as relative humidity, wind speed, and solar radiation on the performance of the diurnal passive radiative cooling (DPRC) systems in Abuja, Afikpo, and Owerri are shown in Fig 4.19-4.36.

Fig 4.19 shows the effect of relative humidity on the MPEA and $BaSO_4$ performances on May 18. Between the hours of 7:00 AM and 9:45 AM at a relative humidity of 88%, the sub-ambient cooling temperature obtained was lower compared with the times of the day with lower relative humidity (74%-62%). The sub-ambient temperature for both coolers was highest when the humidity was lowest (about 62%). The same trend was observed in Fig 4.20 for the effect of relative humidity on the performance of the systems on May 19-22. At the times of high relative humidity of 94% at 7:00 AM on May 19, 93% at12:00AM-8:00 AM on May 20, 79%-83% at 12:30 AM-8:45 AM on May 21, and 88% at 2:30 AM-7:15 AM on May 22, there were no significant cooling instead heating was noticed around these times. At lower relative humidities of 56% (3:00 PM) and 62% (7:45 AM) on May 19, 56% (5:30 AM) on May 20, 55% (3:00 PM) on May 21, as well as 55% (10:30 AM and 7:15 PM) on May 22, there was remarkable sub-ambient cooling of 2-5^{o}C for MPEA, which was not feasible at higher relative humidities. The cooling same effect was also noticed for $BaSO_4$ with a sub-ambient cooling temperature of about 1-3^{o}C.

In the experimental investigation of Afikpo on July 16-17 shown in Fig 4.21, reasonable sub-ambient cooling was observed when the relative humidity dropped to 78% (10:45 AM-3:15 AM), 67% (3:00APM), and 78% (3:45 AM) on July 16, 17, and 18 respectively. The sub-ambient cooling at these relative humidity points for MPEA was 5-6^{o}C and 2-3^{o}C for $BaSO_4$. However, at a higher relative humidity of 98-100% for the test days, heating was observed for both coolers. This result is in

agreement with the report of Jeong et al (2020) that the cooler performance deteriorated at high humid weather. The inclement weather with high humidity is as a result of unfavourable sky condition of low atmospheric transparency.

Fig 4.22 shows a sub-ambient cooling temperature of about 5oC when the relative humidity dropped to 81-89% across the three test days (August 10-13) in Afikpo. At higher relative humidity of 100%, mostly observed in the night, heating occurred and, in some cases, a very minimal cooling. The relatively high relative humidity of this climate not only affected the cooler temperatures but also the ambient.

Fig 4.23 presents how the sub-ambient cooling of MPEA and $BaSO_4$ was affected by the relative humidity of Owerri across the trial days on July 12-15. In the early hours of the day at about 6:00 AM, slight heating was observed but cooling immediately resumed as the relative humidity dropped from 100% to 74%. At the lowest relative humidity, sub-ambient cooling was 3-5^{o}C in each of the days. In the night-times, both coolers especially the MPEA were able to show some level of cooling at some high relative humidity.

For the experimental trials of August 14-17 in Owerri, the result presented in Fig 4.24 shows a similar trend of the sub-ambient cooling as those in other test locations. Usually, times of lower relative humidities of 74-66% presented higher sub-ambient cooling whereas other times with increased relative humidity up to 100% showed minimal cooling, and in some cases, heating. Similarly, it was noticed that the relative humidity, in most cases, occurred at night and during rainfall as observed on August 14.

Fig 4.25 shows a plot of wind speed with cooler temperatures to ascertain how wind speed affects the performance of the coolers. The investigation was conducted on May 18 in Abuja, and the result revealed that at a wind speed of 1.8m/s around 7:30 AM, MPEA showed a slight cooling while the

$BaSO_4$ showed no significant cooling. From 9:00 AM-9:45 AM, both coolers showed a slight cooling when the wind speed was 0.9m/s. As the wind speed increased from 2.2m/s at about 10:00 AM to 4m/s at about 12:00PM, sub-ambient cooling was significant, reaching a maximum value of 5^{o}C. As the wind speed drops, the cooling effect also reduces and becomes insignificant at 6:15 PM with wind speed reaching up to 2.9m/s.

Fig 4.26 presents the same result on how the wind speed affected the sub-ambient cooling for a continuous trial in Abuja on May 19-22. There was no noticeable change in the ambient temperature and that of the coolers around 7:00 AM when the wind speed was zero until around 9:00 AM-11:30 AM, 5:00 PM when the wind speed increased to 4m/s, and 5:00 PM when the wind speed was 5.5m/s. There was a continuous sharp decrease and increase in wind speed from 7:45 PM-9:00 AM where heating occurred in the system. On May 20, the wind speed increased to 4m/s around 12:45 PM where significant diurnal sub-ambient cooling occurred. Similarly, as the wind speed dropped sharply to 1m/s at about 7:45 PM, there was cooling but heating commenced until 8:00 AM when the wind speed started rising, reaching a maximum value of 6m/s at about 3:00 PM on the third test day where the maximum sub-ambient diurnal cooling temperature of 5^{o}C occurred. The same trend of sharp decrease in wind speed resulted in a heating effect that occurred from 7:15 PM-7:00 AM because of a sharp increase of the wind speed up to 6m/s. This rise in wind speed resulted in a drop in the cooler temperature below the ambient.

Fig 4.27 presents a plot of how the wind speed affects the diurnal sub-ambient cooling for the coolers. Before 7:30 AM on the first day when the wind speed was 0m/s, there was significant cooling but from 9:00 AM when the wind speed increased to 2.2m/s and above, remarkable diurnal sub-ambient cooling occurred and decreased as the wind speed decreased. A similar trend occurred on the second day of the test as the diurnal sub-ambient cooling increased with an increase in wind speed. The wind speed and cooling plot pattern for August 10-13 in Afikpo shown in Fig 4.28 followed the same pattern as that of

Fig 4.27. The diurnal cooling was more significant at times the wind speed rose from 0m/s to 2.1m/s on the first day, 2.2m/s on the second day, and 1.2m/s on the third day. As usual, heating and occasionally non-appreciable cooling was witnessed as the wind speed decreased.

Fig 4.17 shows how the sub-ambient cooling was impacted by the wind speed pattern for the investigation in Owerri on July 12-15. Before, sunrise, the wind speed rose to 3.8m/s and fluctuated between that speed and 2.7m/s, within which time the cooling effect was remarkable before sunset. The drop in wind speed resulted in insignificant sub-ambient cooling. A similar trend was observed for the remaining two days of the test as the cooling effect was observed to be high at elevated wind speeds. Similarly, the test in Owerri on August 14-17 as shown in Fig 4.30 presents a similar observation to what Fig 4.29 presented. Sub-ambient cooling was significantly increased at times of elevated wind speeds across the entire three days of the test whereas heating or insignificant cooling occurred at low wind speeds.

Fig 4.31 shows the experimental solar radiation plot for Abuja on May 18. This plot shows the effect of solar radiation on the ambient and cooler temperatures. The figure shows that the cooler temperatures as well as the ambient temperature increased as the solar radiation increased. However, the sub-ambient cooling increased at times when the solar radiation dropped. The figure also revealed that while the ambient temperature increased appreciably with an increase in solar radiation, the increase in temperature of the coolers dragged as a result of their high reflectivity (0.97 for MPEA and 0.98 for $BaSO_4$).

Fig. 4.32 shows the experimental result of the plot for solar radiation for Abuja on May 19-22 to ascertain the effect of solar radiation on the performance of the radiative coolers. It is shown that solar radiation was highest ($772W/m^2$) around 2:00 PM, which resulted in an increase in the ambient and cooler temperatures. The coolers maintained a diurnal cooling effect as the sub-ambient cooling

increased with a decrease in the solar radiation and reached a maximum at about 12:00PM (about 5^{o}C for MPEA and 3^{o}C for B/S) when the solar radiation dropped to 446W/m2 during the daytime. On May 20 when the lowest solar radiation was recorded, the highest and lowest solar radiation reached 234W/m^2 at 12:00PM and 130W/m^2 at 4:30 PM respectively. Sub-ambient cooling was highest at the time of lowest solar radiation as stated above as against the time of highest solar radiation. Similarly, the solar radiation for May 21 reached the highest value of 822W/m^2 at 1:00 PM and lowest value of 192W/m2 at 10:45 AM and at this time of lowest solar radiation, the sub-ambient cooling reached a maximum value of 5-6^{o}C for the MPEA and 2-3^{o}C for the B/S.

Fig. 4.33 shows the experimental result of the plot for solar radiation for Afikpo on July 16-17 to ascertain the effect of solar radiation on the performance of the radiative coolers. It is shown that solar radiation was highest (236W/m^2) around 1:30 PM, which resulted in an increase in the ambient and cooler temperatures. The coolers maintained a diurnal cooling effect as the sub-ambient cooling increased with a decrease in the solar radiation and reached a maximum at about 11:45 AM (about 5-6^{o}C for MPEA and 3-4^{o}C for B/S) when the solar radiation dropped to 217W/m^2 during the daytime. On July 17, the highest solar radiation reached 236W/m^2 at 1:345PM. Sub-ambient cooling was highest at the time the solar radiation decreased to 131W/m^2 as against the time of highest solar radiation.

Fig. 4.34 presents a plot of the experimental result for Afikpo on August 10-13 to investigate the effect of solar radiation on the sub-ambient cooling of the coolers. The plot shows a remarkable corresponding increase in temperatures of the coolers and ambient as the solar radiation increased. The solar radiation reached a maximum of 668W/m^2 and at 11:30 AM on July 10, but when the solar radiation decreased to 567W/m^2 at 1:30 PM, the sub-ambient cooling temperature reached 5^{o}C. The solar radiation reached a maximum value of 655W/m^2 at 2:30 PM on July 11. When the solar radiation decreased to 283W/m^2, the sub-ambient cooling temperature reached a maximum value of 2^{o}C for MPEA and 1^{o}C for B/S. A similar trend was observed for July 12 as the diurnal cooling was highest at

a suppressed solar radiation, even though the solar radiation was lowest on this day for the three days of the investigation.

Fig. 4.35 shows the plot of the effect of solar radiation on the sub-ambient cooling of the coolers for Owerri on July 12-15. The first day of the investigation recorded the lowest solar radiation while the second day recorded the highest. The highest solar radiation for the first day was 229W/m^2 at 1:00 PM and the lowest was 178W/m^2. The sub-ambient cooling temperature reached 5^{o}C when the solar radiation decreased to 178W/m^2. On the second day, the solar radiation reached a maximum value of 533W/m^2 at 12:45 PM but when it decreased to 186W/m^2 at 3:45 PM, the coolers achieved a sub-ambient diurnal cooling temperature of 6^{o}C and finally, on the third day, the highest solar radiation of 319W/m^2 was reached at 1:45 PM. With a decrease in the solar radiation of 237W/m^2 at 2:30 PM towards evening time, both coolers achieved a sub-ambient diurnal cooling temperature of 4^{o}C for the MPEA and 2^{o}C for the.

Fig. 4.36 presents the plot of the effect of solar radiation on the sub-ambient cooling of the coolers for Owerri on July 14-17. The first day of the investigation recorded the highest solar radiation while the second day recorded the lowest. The highest solar radiation for the first day was 663W/m^2 at 10:30 PM and the lowest was 280W/m^2 at 2:45 PM. The sub-ambient cooling temperature on the first day was very low at about 1^{o}C when the solar radiation decreased to 280W/m^2. On the second day, the solar radiation reached a maximum value of 562W/m^2 at 2:30 PM but when it decreased to 235W/m^2 at 1:45 PM, the coolers achieved a sub-ambient diurnal cooling temperature of 6^{o}C for MPEA and about 2^{o}C for $BaSO_4$. Finally, on the third day where the lowest solar radiation was recorded of the test days, the highest solar radiation of 236W/m^2 was reached at 1:00 PM. With a decrease in the solar radiation to 149W/m^2 at 2:30 PM towards evening time, both coolers achieved sub-ambient diurnal cooling temperatures of 4^{o}C for the MPEA and 2^{o}C for the $BaSO_4$.

4.2.4 THEORETICAL PERFORMANCE EVALUATION OF THE SYSTEM

The performance evaluation of the present cooling system is presented in Figures 4.37-4.45. Fig 4.37 presents the performance of the $BaSO_4$ and MPEA in May in Abuja, Nigeria. It shows that the two coolers achieved a diurnal radiative cooling in the test location with the MPEA showing a better performance with a sub-ambient cooling temperature of about 6^oC whereas the sub-ambient cooling temperature of $BaSO_4$ was just about 2^oC. Both coolers experienced a heating effect at sunset, after 7:30 PM for $BaSO_4$, and 8:30 PM for MPEA all through the nocturnal periods of the day.

Fig 4.38 presents the performance of the $BaSO_4$ and MPEA in September in Adamawa, Nigeria. The plot shows that the two coolers achieved a diurnal radiative cooling in the test location with the MPEA showing a better performance with a sub-ambient cooling temperature of about 3^oC whereas the sub-ambient cooling temperature of $BaSO_4$ was just about 0.7^oC. Both coolers experienced a heating effect at sunset, after 5:30 PM for BaSo4 and 7:30 PM for MPEA all through the nocturnal periods of the day.

Fig 4.39 presents the performance of the $BaSO_4$ and MPEA in August in Afikpo, Nigeria. It shows that the two coolers achieved a diurnal radiative cooling in the test location with the MPEA showing a better performance with a sub-ambient cooling temperature of about 2.5^oC whereas the sub-ambient cooling temperature of $BaSO_4$ was just about 1^oC. Both coolers experienced a heating effect at sunset, after 6:00 PM for BaSo4 and 8:30 PM for MPEA all through the nocturnal periods of the day.

The same trend of diurnal cooling performance was maintained by both coolers as shown in Fig 4.40, fig 4.41, Fig 4.42, and Fig 4.43 for Ekiti (2^oC for $BaSO_4$ and 3^oC for MPEA), Kaduna (1^oC for $BaSO_4$ and 3^oC for MPEA), Owerri (2^oC for $BaSO_4$ and 4^oC for MPEA), and Warri (1^oC for $BaSO_4$ and 3^oC for MPEA) respectively. Similarly, both coolers experienced a heating effect at sunset, after 8:30 PM and 9:00 PM for $BaSO_4$ and MPEA respectively in Ekiti; 6:00 PM and 8:30 PM for $BaSO_4$ and MPEA

respectively in Kaduna; 6:30 PM and 7:00 PM for $BaSO_4$ and MPEA respectively in Owerri, and 6:30 PM and 9:30 PM for $BaSO_4$ and MPEA respectively in Warri all through the nocturnal periods of the test days.

Fig 4.44 shows the plot of temperatures of $BaSO_4$ for all seven test locations, which represents the six geopolitical regions in Nigeria. The plot indicates that $BaSO_4$'s cooler performance in Ekiti and Warri was the best (about 27.5^oC). The cooler also performed fairly well in Kaduna with the highest temperature of 29.6^oC but its performance was equally better than the performance in Owerri with the highest temperature of 30.7^oC. Similarly, the cooler performance in Afikpo and Adamawa with the same highest cooling temperature of about 31^oC was below the performances of the cooler in Ekiti, Warri, Owerri, and Kaduna. The cooler had the least performance in Abuja where the highest temperature of about 31.5^oC was recorded.

Fig 4.45 shows the plot of temperatures of MPEA for all seven test locations, which represents the six geopolitical regions in Nigeria. The plot indicates that MPEA cooler performance in Warri was the best (about 26^oC), followed by that of Ekiti with the highest temperature of 26.3^oC. The cooler also performed fairly well in Kaduna with the highest temperature of 28.1^oC, in which its performance was equally better than the performance in Owerri and Afikpo with the highest temperature of 29.5^oC. Similarly, the cooler performance of the cooler in Adamawa with the same highest temperature of about 29.7^oC was below the performance of the cooler in Ekiti, Warri, Owerri, Kaduna, and Afikpo. The cooler had the least performance in Abuja where the highest temperature of about 30.1^oC was recorded.

4.2.5 COOLING POWER OF THE RADIATIVE COOLERS IN THE DIFFERENT TEST LOCATIONS

Figures 4.46-4.54 present the results of the cooling power for investigation carried out in the seven test locations, which represent the six geopolitical zones of Nigeria. Fig 4.46 shows the cooling power of the investigation that was done in Abuja. The cooling powers of the $BaSO_4$ and MPEA were observed to rise uniformly from sunrise at about 7:30 AM with a cooling power of 47.44W/m^2 until about 9:30 AM when the cooling power of $BaSO_4$ showed a significant difference from that of MPEA. The $BaSO_4$ reached a maximum cooling power of 120.29W/m^2 at about 12:30 PM while the MPEA cooling power reached a maximum of 108.84W/m^2 at about the same time. The $BaSO_4$ maintained a higher cooling power than the MPEA even during the drop at sunset.

Fig 4.47 shows the cooling power of the trial that was done in Adamawa. The MPEA showed a slightly higher cooling power than that of the $BaSO_4$ (28.85W/m^2) from sunrise at about 7:30 AM until about 11:00 AM when both coolers maintained the same cooling power of 81.32W/m^2 after which time the $BaSO_4$ rose above that of the MPEA. The $BaSO_4$ reached a maximum cooling power of 92.77W/m^2 at 1:30 PM while the MPEA reached its maximum cooling power of 84.64W/m^2 at 12:00 PM. Afterwards, both coolers showed a similar trend in a drop in cooling power with the $BaSO_4$ maintaining a higher cooling power than that of the MPEA until sunset.

Fig 4.48 shows the cooling power of the investigation that was done in Afikpo. The cooling powers of the $BaSO_4$ and MPEA were observed to rise uniformly from sunrise at about 7:00 AM with a cooling power of 36W/m^2 until about 9:00 AM when the $BaSO_4$ started showing a slightly higher cooling power than that of MPEA. The $BaSO_4$ reached a maximum cooling power of 106.74W/m^2 at about 12:00 PM while MPEA cooling power reached a maximum of 101.06W/m^2 at about the same time.

Both coolers showed the same trend but $BaSO_4$ maintained a slightly higher cooling power than the MPEA during the drop in cooling power towards sunset.

Fig 4.49 shows the cooling power of the investigation that was done in Ekiti. The cooling powers of the $BaSO_4$ and MPEA were observed to rise uniformly from sunrise at about 7:00 AM with a cooling power of 29.74W/m^2 until about 9:30 AM when the MPEA started showing a slightly higher cooling power than that of $BaSO_4$. However, the cooling power of $BaSO_4$ overtook that of MPEA at about 10:00 AM, and at about 12:30 PM, both coolers reached a maximum cooling power of 87.16W/m^2 (for $BaSO_4$) and 78.31W/m^2. Both coolers showed the same trend but $BaSO_4$ maintained a slightly higher cooling power than the MPEA during the drop in cooling power towards sunset.

Fig 4.50 shows the cooling power of the investigation that was done in Kaduna. The cooling powers of the $BaSO_4$ and MPEA were observed to rise uniformly from sunrise at about 7:00 AM with a cooling power of 31.37W/m^2 until about 10:00 AM when the $BaSO_4$ started showing a slightly higher cooling power than that of MPEA with a cooling power of 69W/m^2. The $BaSO_4$ reached a maximum cooling power of 92.49W/m^2 at about 12:30 PM while MPEA cooling power reached a maximum of 88.09W/m^2 at about the same time. Both coolers showed the same trend but $BaSO_4$ maintained a slightly higher cooling power than the MPEA during the drop in cooling power towards sunset.

Fig 4.51 shows the cooling power of the investigation that was done in Owerri. The cooling powers of the $BaSO_4$ and MPEA were observed to rise uniformly from sunrise at about 7:00 AM with a cooling power of 30.18W/m^2 until about 8:00 AM when the $BaSO_4$ started showing a slightly higher cooling power than that of MPEA with a cooling power of 45.05W/m^2. The $BaSO_4$ reached a maximum cooling power of 92.45W/m^2 at about 12:30 PM while MPEA cooling power reached a maximum of 77.53W/m^2 at about the same time. Both coolers showed the same trend but $BaSO_4$ maintained a slightly higher cooling power than the MPEA during the drop in cooling power towards sunset.

Fig 4.52 shows the cooling power of the investigation that was done in Warri. The cooling powers of the $BaSO_4$ and MPEA were observed to rise uniformly from sunrise at about 7:30 AM with a cooling power of 36.1W/m^2 until about 9:00 AM when the $BaSO_4$ started showing a slightly higher cooling power than that of MPEA. At about 12:00 PM, both coolers reached a maximum cooling power of 89.81W/m^2 (for $BaSO_4$) and 84.99W/m^2. Both coolers showed the same trend but $BaSO_4$ maintained a slightly higher cooling power than the MPEA during the drop in cooling power towards sunset.

Fig 4.53 shows the cooling powers of $BaSO_4$ for the investigation that was done in the seven test locations, which were observed to rise accordingly from sunrise. Abuja recorded the highest cooling powers for $BaSO_4$ in all the test locations with a maximum value of 120.09W/m^2 at about 12:00 PM and was followed by the cooling power of 106.74W/m^2, which was recorded in Afikpo at about 12:00 PM. Next to the cooling power of Afikpo are Adamawa and Owerri with a maximum of 92.77W/m^2 and 92.45W/m^2 respectively at 12:00 PM and 12:30 PM. The remaining three locations of Kaduna, Warri, and Ekiti accordingly recorded maximum cooling powers of 91.88W/m^2 at 12:00 PM, 89.81W/m^2 at 12:00 PM, and 87.16W/m^2 at 12:30 PM respectively.

Fig 4.54 shows the cooling powers of MPEA for the investigation that was done in the seven test locations and were observed to show a similar trend to that of fig 4.41. In this plot, Abuja recorded the highest cooling powers for MPEA in all the test locations with a maximum value of 109.09W/m^2 at about 12:00 PM and was followed by the cooling power of 101.06W/m^2, which was recorded in Afikpo at about the same time. Next to the cooling power of Afikpo was Kaduna with a maximum cooling power of 88.09W/m^2 at 12:00 PM. Both Adamawa and Warri shared the same maximum cooling power of 84.99W/m^2 at about 12:00 PM. Similarly, the remaining locations of Ekiti and Owerri recorded a slightly lower maximum cooling power of 77.34W/m^2 at 1:00 PM.

Generally, the cooling powers recorded in Abuja and Afikpo remained higher than in other locations for both BaSO4 and MPEA. Ekiti and Warri recorded the lowest cooling power for BaSO4 while Ekiti and Owerri recorded the lowest cooling power for MPEA.

4.2.6 VALIDATION STUDIES

The theoretical model development in this work has been validated using results from a comprehensive experimental study carried out in Owerri's location from 6:00 a.m. on July 12 to 06:00 am July 13, 2023. The validation studies was limited to Owerri's location since other test locations presented similar trend. The model was parameterized using the prevailing weather conditions under which the experiment was conducted. Fig 4.55 shows experimental and numerical temperature profiles for the coolers in Owerri, Nigeria. It can be seen from the figure that the model data closely matches the experimental data, as the two temperature profiles follow the same trend for both the $BaSO_4$ and MPEA radiative coolers. During the early hours of the day, the model temperature data were relatively close to the experimental data until around 7:45 p.m., covering the entire diurnal operation of the system. However, during the nocturnal performance period, both coolers follow the same trend, both experimentally and numerically, as seen in the widened difference in the experimental and model data. During this period of widened difference in both data (around 20:00PM), the system acts as a thermal shield that will not permit the surface to exchange heat with the environment. This continued throughout the night but was predominant during the nocturnal thermal cooling. The model correctly predicted the daily performances of the coolers as it captured the time-variant behaviour of the systems during the period. Figs 4.56 and 4.57 show the validation studies for the two coolers separately in order to enable us to provide a statistical correlation between the experimental and model data. The cooler's size, optical characteristics, and material properties were used to set the model's parameters. It is

evident that there is a similar pattern between the experimental and expected findings. There is a variation of ±2.73^{o}C in the model and experimental temperatures of the MPEA cooler, and a variation of ±1.81^{o}C in the model and experimental temperatures of the $BaSO_4$. For the MPEA, the model uncertainty for the experimental temperature is 2.23^{o}C while it is 2.02^{o}C for the model temperature. Likewise, for the $BaSO_4$, the model uncertainty (standard deviation) for the experimental temperatures is 2.37^{o}C whereas 2.55^{o}C for the model temperature. The ratio of the experimental and model temperatures to the total standard uncertainties of the experiment and model is 0.64. It is indicated as the difference between the two sets of temperatures for the MPEA. Similarly, 0.37 is the ratio of the experimental and model temperatures to the total standard uncertainties of the experiment and model, which also gives the difference between the two sets of temperatures for the $BaSO_4$. As a necessary condition for model accuracy, the ratio of the uncertainty of the combined uncertainties of theory and experiment must be less than 1.0 (Nwaji et al, 2020).

The present experimental result was validated by comparing it with the results of other works from the literature. The maximum sub-ambient cooling temperatures obtained from the present experimental result of Fig 4.1 and Fig 4.2 for Abuja, Fig 4.3 and Fig 4.4 for Afikpo as well as fig 4.5 and Fig 4.6 for Owerri were compared with that of the result from the works of Raman et al (2014) in California, USA. A close look at the figure shows that both results maintained the same trend with a very close range of maximum temperature below the ambient. The sub-ambient temperature of the work of Raman et al (2014) is 4.9^{o}C while that of the present work was also in the range of 4-6^{o}C. Their result of the cooling power from their work was lower than the cooling power recorded in the present work, which also indicates that it under-predicted that of the present cooling power. The experimental results were also compared with works of Leroy et al (2019), Zhu et al (2021), Huang et al (2022), Bhatia et al (2018), Zhao et al (2019), and Zhou et al (2021). The results of temperature reduction below ambient reported by Leroy et al (2019) around midday showed a much higher sub-ambient temperature of about 11^{o}C,

indicating an over-prediction of the experimental result. However, the cooling power of 96W/m^2 from their work was consistent with that of the experiments, which ranged from 77-120W/m^2 in all the locations of investigation. In the works of Huang et al (2022), Chen et al (2022), Wang et al (2021), and Zhao et al (2019), respectively recorded sub-ambient temperatures of 2^{o}C, 4^{o}C, 6-8.9^{o}C, 12.6^{o}C, both the sub-ambient temperatures and cooling powers showed a consistent trend with that of the experiments. The cooling power of 45W/m^2 in the work of Bhatia et al (2018) under-predicted that of the experiments while the sub-ambient cooling temperature was consistent with the experimental results. In the works of Zhou et al (2021), both the sub-ambient cooling temperatures (12^{o}C) and cooling powers (273.3/m^2) over-predicted those of the experiments as they all showed a value higher than that of the experiment. A similar observation of over-prediction of the sub-ambient temperature was made in the work of Zhu et al (2021), where a temperature drop of 12.6^{o}C below ambient was obtained. When the work of Tso et al (2017) is compared with the experimental results, it was observed that no sub-ambient cooling under direct solar irradiance was recorded for their work whereas the experimental results of the present work showed a significant sub-ambient cooling under direct sunlight. However, the work of Tso et al (2017) presented a significant cooling effect in the night, even though it over-predicted the experimental sub-ambient cooling temperature in the night.

4.2.7 THERMAL DISTRIBUTION ON THE COOLERS

Figures 4.58-4.71 present the results of the thermal distribution on the radiative coolers for the investigation carried out in the three test locations of Abuja, Afikpo, and Owerri. Fig 4.58 shows a 3D topographic display of temperature along the xy-global coordinate of $BaSO_4$ for Abuja, Nigeria, indicating a uniform temperature in the xy-direction but a variation from high to low in the z-direction. There is a cooling effect across the z-direction because of the emissive ability of the surface and as the temperature drops below the ambient temperature. The upper surface of the cooler is at a higher temperature of 32.8^{o}C while the bottom part of the cooler is at a lower temperature of 26.6^{o}C. A similar

trend was observed for the same plot of 3D display of temperature for Adamawa (shown in Fig 4.59), as a cooling effect is observed across the z-direction as a result of the temperature reduction from 32.1^{o}C to 26.9^{o}C. As has been the case in Fig 4.58, there is a uniform temperature distribution in the xy-direction. The surface temperature plot of the $BaSO_4$ cooler for Afikpo is shown in Fig 4.60. The figure indicates a similar surface temperature profile where the variation in temperature was only observed in the z-direction but uniform in the xy-direction. The temperature differential on the surface from top to bottom is 5.2^{o}C. Fig 4.61 shows the surface temperature plot for Ekiti. The plot presents an upper and lower temperature of 28.6^{o}C and 23^{o}Cm, which resulted in a cooling effect across the z-direction of the cooler. Likewise, the surface temperature distribution of the BaSO4 cooler for Kaduna is shown in Fig 4.62 while the plot for the same surface temperature for Owerri is shown in Fig 4.63. Both figures show the same trend as the previous figures discussed above with temperature reduction of 5.7^{o}C and 9.6^{o}C for Kaduna and Owerri respectively. Finally, the temperature distribution of the cooler surface for Warri is presented in Fig 4.64. The result shows that the temperature reduction from the top of the cooler to the bottom is 5.8^{o}C, in the z-direction whereas there is a uniform temperature distribution in the xy-direction.

The 3D topographic display of temperature along the xy-global coordinate of MPEA is shown in Fig 4.65 for Abuja, Nigeria. The plot indicates a uniform temperature distribution in the xy-direction but a variation from high to low in the z-direction, which results in a drop in the temperature of the MPEA below that of the ambient. There is a cooling effect across the z-direction because of the emissive ability of the surface, which results in a temperature drop below the ambient temperature. The surface temperature difference of the cooler across the surface in the z-direction, which results in the cooling effect was 7.4^{o}C. A similar trend was observed for the same MPEA plot of a 3D display of temperature for Adamawa as shown in Fig 4.66. The surface temperatures of the upper and lower part of the cooler were respectively 32.1^{o}C and 25.9^{o}C. The flow of the temperature was observed to be uniform in the

xy-direction while the variation was only seen in the z-direction. Fig 4.67 shows the surface temperature profile of the MPEA cooler in Afikpo and a similar flow pattern of temperature as in the previous plots was observed. The plot shows that the upper and lower surface temperatures of the cooler were respectively 31.2^{o}C and 23^{o}C. The temperature reduction observed across the surface of the cooler is due to the ability of the surface to release most of its heat to the universe. For Ekiti, the surface temperature profile is shown in Fig 4.68 with a temperature reduction of 7^{o}C. The temperature flow pattern for Kaduna, Owerri, and Warri are shown in Figs 4.69, fig 4.70, and fig 4.71. The surface temperature differentials for the cooler in the figures for Kaduna, Owerri, and Warri are respectively 8.8^{o}C, 6.6^{o}C, and 7.8^{o}C. The same temperature distribution pattern as the previously discussed figures was maintained.

4.2.8 PARAMETRIC STUDIES

Figs 4.72-4.77 present the effects of cooler thicknesses, number of windscreens, and angles of inclination on the performance of the radiative coolers with respect to sub-ambient temperature. The effect of thickness on the cooling power of the radiative coolers was presented in Figs 4.78-4.79 while the cooling powers of the BaSO4 and MPEA at a particular time around the period of peak solar radiation are presented in Figs 4.80. The thicknesses of the coolers were varied to ascertain the best thickness for optimum performance of the system.

The temperatures of the $BaSO_4$ radiative cooler at varying thicknesses of 2, 4, 6, 8, 10, 15, 20, and 25mm are presented in Fig 4.72. The figure shows that there is a marked variation of the cooler temperature with the thickness. A remarkable decrease in the cooler temperature can be observed when the thickness increases from 2 to 25mm. Better cooler performance occurs at much higher thicknesses, as the cooler with a thickness of 2mm recorded a maximum temperature of 32^{o}C while the cooler with

a thickness of 25mm recorded 26^{o}C. It was also shown from the plot that the cooler with 2mm thickness showed a sharp reduction in temperature, and resulting in a better performance during night-time. It is therefore clear that the cooling performance of the radiative cooler had a direct relationship with its thickness. At 15mm, the cooler temperature dropped to the minimum, and thereafter increasing the thickness further experienced a corresponding increase in the cooler temperature. The sudden drop in cooler temperature at 25mm thickness suggests that there is a maximum thickness beyond which a radiative material yields no significant diurnal cooling effect. This is in agreement with the report of Huang et al (2022) that a thermally insulating radiative cooling material has no significant cooling when the cooler thickness is increased beyond 20mm.

Fig 4.73 presents the temperatures of the MPEA radiative cooler with time at varying thicknesses of 6, 8, 10, 15, 20, and 25mm. The figure shows that the cooler temperature at the various thicknesses did not present any significant variation in temperature at the hours of the day before 10:00 h. The variation in the cooler temperature became obvious after 12:30 h and increased until around 18:00 h when it became obvious. There is a remarkable cooling performance when the thickness increases from 6mm to 25mm. This result shows that the cooler performed well at higher thicknesses. The cooler with a thickness of 6mm recorded a maximum temperature of 29.49^{o}C at about 20:00h while the cooler with a thickness of 25mm recorded 26.69^{o}C at about 00:00 h. It was also shown from the plot that the cooler with 6mm thickness showed a better nocturnal cooling performance. It is therefore clear that there is a direct relationship between the cooling performance of the radiative cooler and its thickness.

Fig 4.74 shows the variation of temperature of the $BaSO_4$ radiative cooler with time at varying numbers of high-density polyethylene (HDPE) windscreens. The figure shows that the cooler temperature decreased as the number of windscreens increased. During the early hours of the day, no remarkable difference can be observed in the number of windscreens, and this continued until about 10 a.m. From 10:00-11:00 am, the cooler performance still remained best at 1 HDPE windscreen. As the day

progresses, the higher the number of windscreens the better the performance of the cooler as reflected in the case of 5 HDPE recording the lowest cooler temperature almost throughout the daytime and extending to about 1:00 am. Thereafter, the whole process immediately reversed thereby taking the outlook of the behaviour at the early hours of the day. It can be seen, for instance, during peak insolation, that at 1HDPE, the cooler temperature is 29^{o}C; at 2HDPE, the cooler temperature is 28.01^{o}C; at 3HDPE, the cooler temperature is 28^{o}C; at 4HDPE, the cooler temperature 27^{o}C while at 5HDPE, the cooler temperature is 25.25^{o}C. Hence, for the significant part of the diurnal and nocturnal operations, it can be inferred that $BaSO_4$ radiative cooler performs optimally at higher number of windscreens.

Fig 4.75 shows the variation of temperatures of the MPEA radiative cooler at varying number of high-density polyethylene (HDPE) windscreens. The figure shows that the cooler temperature decreased as the number of windscreens increased. There was no remarkable difference observed with the number of windscreens during the early hours of the day, which continued until about 10 am. As the day progresses, the cooler presented a better performance as the higher the number of windscreens increases, which is reflected in the case of 5 HDPE recording the lowest cooler temperature almost throughout the daytime and extending to about 1:00 am. Thereafter, the whole process immediately reversed thereby taking the outlook of the behaviour at the early hours of the day. For instance, during peak insolation, it can be seen that at 1HDPE, the cooler temperature is 30^{o}C; at 2HDPE, the cooler temperature is 29^{o}C; at 3HDPE, the cooler temperature is 28^{o}C; at 4HDPE, the cooler temperature 27.5^{o}C while at 5HDPE, the cooler temperature is 27^{o}C. Hence, for the significant part of the diurnal and nocturnal operations, it can be inferred that MPEA radiative cooler performs optimally at higher number of windscreens.

Fig 4.76 presents the temperatures of the $BaSO_4$ radiative cooler at different angles of inclination of the cooler. The figure shows that exposing the radiative cooler to the sky at an angle of inclination of five

(5), ten (10), fifteen (15), and twenty (20) degrees, there was no significant variation in the temperatures at the early hours of the day but at about 11:00 h, the cooler showed a variation in temperature when inclined at angle of 15 and 30 degrees whereas at angles of inclination of 5, 10, 20 and 25 degrees, the variation in temperature was recorded at about13:30 h even though it was minimal. Although the pattern of behaviour of the cooler with respect to the angle of inclination of 5,10,15,20, and 25 degrees was not clear, the performance was optimal when the angle of inclination is 30 degrees. The cooler performance, which was best at the angle of inclination of 30 degrees indicates that it is sensitive to the orientation of the system. At late hours of the nocturnal periods, the coolers' performance with respect to its orientation did not show any clear pattern as the performance of the cooler at best and worst angles of inclination reversed after 23:00 h. This is true as nocturnal radiative cooling is best at zero inclination.

Fig 4.77 presents the temperatures of the MPEA radiative cooler at different angles of inclination of the cooler. From the figure, it is shown that there was no significant variation in temperature with different angles of inclination, especially at the early hours of the day before 11:00h. There was a noticeable variation in temperature as the angle of inclination increased to 25 and 30 degrees whereas the variation was not significant at angles of inclination of 5, 10, 15, and 20 degrees. The performance of the cooler, which was best at higher angle of inclination of 30 degrees and better at 25 degrees reversed at mid-night at about 2:00 h, making the its performance better at lower angle of inclination. This suggests that at the periods of low or no irradiance and high relative humidity, orientation (inclination) of the cooler counts less for nocturnal radiative cooling.

The cooling power of the $BaSO_4$ radiative cooler at varying thicknesses is presented in Fig 4.78. The cooling power of the cooler at thicknesses of 2, 4, 6, 8, 10, 15, 20, and 25mm did not show any significant variation in temperature before 10:00 h but beyond 12:00 h, the cooler showed a significant variation in cooling power. It can be ascertained that the performance of the radiative cooler is

thickness dependent. The result from the figure shows that at the lowest thickness, the cooler presented a better cooling performance than when the thickness is higher as its cooling power was consistently higher.

Fig 4.79 presents the cooling power of the MPEA radiative cooler at varying thicknesses. The cooling power of the cooler at thicknesses of 6, 8, 10, 15, 20, and 25mm did not show any significant variation in temperature before 11:30 h but beyond 12:00 h, the cooler showed a significant variation in cooling power. It can be ascertained from the figure that the performance of the radiative cooler is thickness dependent and the cooler at lower thickness presented a better cooling performance as its cooling power was consistently higher than when the thickness is lower.

Fig 4.80 shows a line plot of the cooling power of the $BaSO_4$ radiative cooler with varying thicknesses at the point of peak solar irradiation and peak temperature. The cooling powers of $BaSO_4$ and MPEA radiative coolers were seen to decrease progressively as the thickness of the coolers increased. The result from the plot shows that the $BaSO_4$ radiative cooler at a particular thickness performed better than the thermally insulating MPEA cooler. At peak solar irradiation (at about 13:30 h) and a maximum thickness of 25mm, the cooling power of $BaSO_4$ and MPEA were 55.41W/m^2 and 44.35W/m^2 respectively while at a lower thickness of 4mm, their cooling powers were 93.36W/m^2 and 77.52 W/m^2 respectively. The cooling power at peak temperature follow the same trend just as it was observed in the plot during peak solar irradiation. The cooling powers of the coolers at a maximum thickness of 25mm were 83.16W/m^2 for $BaSO_4$ and 70.93W/m^2 for MPEA while it was 61.22W/m^2 and 54.11W/m^2 respectively for $BaSO_4$ and MPEA at a lower thickness of 6mm. It can be seen that the performance of the $BaSO_4$ at both peak solar irradiation and peak temperatures was consistently higher than that of the MPEA.

CHAPTER FIVE

CONCLUSION AND RECOMMENDATION

5.1 Conclusion

Thermal comfort through sub-ambient cooling is vital in everyday life, especially in tropical regions like Nigeria. To achieve this using existing technology, which utilizes fossil fuel, and natural gas is quite expensive and impacts the environment negatively due to harmful emissions. These conventional methods of cooling are responsible for significant CO_2 emissions and are also expensive for developing regions with lower income. Sub-ambient passive cooling technology has the potential to address the problems of thermal comfort with fossil fuel and natural gas while promoting human well-being, and driving sustainable economic growth around the world. In this thesis, the current challenges in space cooling around the world and technical background on passive radiative cooling were presented as well as a review of previous literature work in these areas.

Two diurnal passive radiative coolers composed of a mesoporous polyethylene aerogel (MPEA) and ultra-white Barium Sulphate ($BaSO_4$) have been developed and fabricated and assembled to experimentally investigate the sub-ambient cooling application in building in tropical climates. The optical selectivity, and thermal insulation of MPEA as well as the ultra-white properties of these coolers make good candidates for passive radiative cooling application as they can achieve sub-ambient temperatures and higher cooling powers throughout the day. The fabrication processes for the coolers were also described in this work.

The experimental demonstration of the system to investigate its performance in our climate was done in three locations in Nigeria. The performance of the radiative coolers was evaluated through a three days continuous trials in the three locations of Abuja, Afikpo, and Owerri in the months of May, July and August. The investigation also included the effect of climatic conditions such as relative humidity, wind speed and solar radiation on the performance of the system. The results obtained from the

experiment shows that the radiative cooler presented a sub-ambient cooling temperature of 3-6^{o}C for the MPEA radiative cooler and 2-5^{o}C for the $BaSO_4$ in the daytime under direct sunlight and 1-3^{o}C for both coolers during the nocturnal periods. The cooling power recorded for both coolers was 77-120W/m^2.

Also, a theoretical model to predict the performance of the system in different climatic conditions was developed. The numerical investigations were done in four other states, in addition to the locations for the experimental investigation, to cover the six geopolitical zones of the country. The study was validated by comparing the experimental results with the numerical results and results of works from literature. The experimental and numerical results of the trials performed in Abuja, Afikpo, and Owerri were in agreement with similar sub-ambient temperatures and cooling powers. Again, the experimental results and those from literature showed good agreement. For instance, the experimental result for sub-ambient cooling temperature was 4-6^{o}C while the work of Raman et al (2014) in California, USA showed a sub-ambient cooling temperature of 4.9^{o}C under solar irradiation. The results of the cooling power from the experiment were also validated with the result from Ong et al (2022), which gave a cooling power of 128.75W/m^2. Further validations were carried out by comparing the results of the experimental work with the results from the works of Leroy et al (2019) with a sub-ambient temperature of 7^{o}C; Huang et al (2022) with a sub-ambient temperature of 2^{o}C; Chen et al (2022) with a sub-ambient temperature of 4^{o}C; Wang et al (2021) with a sub-ambient temperature of 6-8^{o}C; Zhou et al (2021) with a sub-ambient temperature of 12^{o}C; Jeong et al (2020) with a sub-ambient temperature of 6.2^{o}C and Zhu et al (2019) with a sub-ambient temperature of 12.6^{o}C. These sub-ambient temperatures are all in agreement with the experimental results with few over predictions as in the Case with the works of Zhou et al (2021) and Zhu et al (2019). Other works from literature that show good agreement with the experimental results are the results from the works of Dobson et al (2005) in Namibia and Meir et al (2003) in Norway with a sub-ambient temperature of 5^{o}C. From Nwaji et al

(2019) in Nigeria, the room space was kept fairly at 5.7^{o}C below the ambient during the day for the day comfort cooling. The results of the sub-ambient temperatures from literature showed good agreement with the experimental results.

The models were also used to carry out sensitivity analyses to determine the effects of the thermophysical and material properties, and climatic conditions to ascertain the optimum performance characteristics of the system. The atmospheric conditions such as high humidity affects the performance of the system as a result of inclement weather, which resulted to over prediction and under prediction of the system performance.

From the foregoing, it is clear that the experimental and numerical results predicted significantly well the performance of the DPRC system in Nigerian tropical climates.

Finally, to ensure practical application and building integration of the concept, the use of the exposure box as a building prototype showed how this cooling architecture could be used in buildings to reduce space cooling energy consumption.

5.2 Recommendation

The cooling performance and the potential benefits of passive radiative cooling architectures have demonstrated. Yet, the long-term performance of the system was not studied as our experimental demonstrations was just a prototype and remained at lab scale.

In this thesis, optically selective, and thermally insulating MPEA and ultra-white BaSO4 coolers, which are limited to lab-scale 4-cm x 4-cm square samples have been used to demonstrate the potential for passive radiative cooling. For deployment of systems for space cooling in commercial and residential buildings, more work will be needed to scale up our current experimental design to larger cooling structures. However, it is discovered that low-density PEAs can be quite soft and prone to

damage, as well as expensive and time-consuming to fabricate due to the challenge of solvent exchanges and the critical point drying steps. Scaling up our lab-scale design will require cheap materials for the selective emitter (or solar reflector), and the insulation layers that can easily be manufactured at scale.

It is recommended that potential future researchers in this area should carry out economic optimization studies as well as effect of the energy system on the reduction of carbon IV oxide (CO_2) emission to the atmosphere, which is believed to be the primary cause of global warming and climatic change. This would be a good and interesting research area since it is obvious that there will be less emission of CO_2 into the atmosphere by the amount of fossil fuel used for space cooling, which would be eliminated by the proposed system.

Future material development and advances in aerogel manufacturing that can address cost, robustness and scalability are thus required if this type of insulation is to be used in harsh climates over long periods of time. Methods of PEA attachment to an emitter and to the frame will also have to be devised. However, it will also be interesting to explore other materials.

5.3 Contribution to Knowledge

(i) There is nowhere at present under Nigerian wet and humid climatic conditions where the study of DPRC that takes care of the field and theoretical investigation of the concept has been done but this has been achieved in this work. Therefore, a system that could be adopted in our climate has been modelled and designed to realize daytime radiative cooling. This is because achieving daytime radiative cooling is location specific because of varying climatic conditions.

(ii) Thermal insulation has been achieved through the use of a mesoporous polyethylene aerogel because of the good thermal insulation properties of aerogels. This solution that could enable

simpler and high-performance radiative cooling addresses the problems of both solar absorption and parasitic heat gain. To suppress solar absorption and parasitic heat gain, the aerogel properties was further designed by finding a compromise between the porosity and thickness of the aerogel.

(iii) This work has shown that diurnal cooling can be realized without a high-temperature radiative shield. This is considered a useful contribution to knowledge because it leads to overall simplicity of design and cost reduction.

References

Alberghini, M., Morciano, M., Fasano, M., Bertiglia, F., Fernicola, V., Asinari, P., and Chiavazzo, E. (2020). Multsageand passive cooling process driven by salinity difference, Science Advance, 6, eaax5015.

Andretta, A., Bartoli, B., Coluzzi, B. et al. (1981). Selective Surfaces for Natural Cooling Devices. Journal of Physics. Colloques, 42(C1): C1-423-C1-430.

Ali, A.H.H. (2007). Passive cooling of water at night in uninsulated open tank in hot arid areas. Energy Conversions Management, 48, 93–100.

Aili, A.; Yin, X.; Tan, G.; Yang, R. (2019). Roof-integrated radiative air-cooling system to achieve cooler attic for building energy saving, Energy Building, 203, 109453.

Al-Obaidi, K.M., Ismail, M., and Rahman, A.M.A., (2014). Passive Cooling Techniques through Reflective and Radiative Roofs in Tropical Houses in Southeast Asia: A Literature Review," Frontiers of Architectural Research, 3(3), pp. 283-297.

Ao, X.; Hu, M.; Zhao, B.; Chen, N.; Pei, G.; Zou, C. (2019). Preliminary experimental study of a specular and a diuse surface for daytime radiative cooling, Solar Energy Materials Solar Cells, 191, 290–296.

Argiriou, A. (2013). Radiative Cooling, Passive Cooling of Buildings, M. Santamouris, and D. Asimakopoulos, eds., Earthscan New York, pp. 424-454

Atiganyanun, S., Plumley, J.B., Han, S.J., et al., (2018). Effective radiative cooling by paint-format microsphere-based photonic random media. ACS Photonics 5 (4), 1181–1187.

Banik, U., Sasaki, K., Reininghaus, N., Gehrke, K., Vehse, M., Sznajder, M., Sproewitz, T., and Agert, C. (2020). Enhancing passive radiative cooling properties of flexible CIGS solar cells for space applications using single layer silicon oxycarbonitride films, Solar Energy Materials and Solar Cells, 209, 220456.

Berdahl, P. (1984). Radiative cooling with MgO and/or LiF layers. Appl. Opt. 23 (3),370–372.

Bergman, T.L. (2018). Active daytime radiative cooling using spectrally selective surfaces for air conditioning and refrigeration systems, Solar Energy, 174, 16–23.

Benlattar, M., Oualim, E.M., Harmouchi, M., et al., (2005). Radiative properties of cadmium telluride thin film as radiative cooling materials. Opt. Commun. 256 (1), 10–15.

Bezerra, P., Silva F., Cruz T., Mistry, M., Vasquez-Arroyo, E., Magalar, L., Cian, E. D., Lucena, A.F.P., Schaeffer R. (2021). Impacts of a warmer world on space cooling demand in Brazilian Households. Energy & Buildings, 234, 110696

Bhatia, B., Leroy, A., Shen, T., Zhao, L., Gianello, M., Li, D., Gu, T., Hu, J., Soljacic, M., and Wang, E.N. (2018). Passive directional sub-ambient daytime radiative cooling, Nature Communications, USA.

Bao, H., Yan, C., Wang, B., et al., (2017). Double-layer nanoparticle-based coatings for efficient terrestrial radiative cooling. Sol. Energy Mater. Sol. Cells 168, 78–84.

Carlosena, L., Andueza, A., Torres, L., Irulegi, O., Hernandez-Minguill, R. J., Sevilla, J. Santamouris, M. (2021). Experimental development and testing of low-cost scalable radiative cooling materials for building applications, Solar Energy Materials & Solar Cells 230, 111209

Chen, Z., Zhu, L., Raman, A., and Fan, S. (2016). Radiative cooling to deep sub-freezing temperatures through a 24-h day-night cycle, Nature Communications, 7, 13729, USA.

Chen, M., Pang, D., Chen, X., Yan, H., Yang Y. (2021). Passive daytime radiative cooling: Fundamentals, material designs, and applications. EcoMat-Wiley, Volume 4, (1).

Chen, M., Pang, D., and Yan, H. (2022). Sustainable and self-cleaning bilayer coatings for high-efficiency daytime radiative cooling. Journal of Materials Chemistry C, 10, 8329–8338.

Chaabane, M., Mhiri, H., Le Palec, G., and Bournot, P (2010). Numerical Study of An Integrated Collector Storage Solar Water Heater, 2nd International Conference on Engineering Optimization September 6 - 9, 2010, Lisbon, Portugal.

Cotton, W. R.; Pielke, R. A. (2007). Human impacts on weather and climate. Cambridge: Cambridge University Press. P. 180. ISBN 978-0-521-84086-6. OCLC 466742997.

Czapla, B., Srinivasan, A., Yin, Q. et al., (2017). Potential for Passive Radiative Cooling by PDMS Selective Emitters, ASME 2017 Heat Transfer Summer Conference.

Delmastro, C., Dulac, J., Abergel, T. (2019). Cooling. Available online: http://iea.org (accessed on 22 December 2019). www.energypedia.info/wiki/Nigeria_Energy_Situation.

Dai, X., Sun, N., Nielsen, S.O., Stogin, B.B., Wang, J., Yang, S., Wong T. (2018). Hydrophilic directional slippery rough surfaces for water harvesting. Science Advances; 4. DOI: 10.1126/sci. adv. aaq0919

Diatezua, D.M., Thiry, P.A., Dereux, A. (1996). Silicon oxynitride multilayers as spectrally selective material for passive radiative cooling applications. Sol. Energy Mater. Sol. Cells 40 (3), 253–259.

Dobson, K.D., Hodes, G., Mastai, Y., (2003). Thin semiconductor films for radiative cooling applications. Sol. Energy Mater. Sol. Cells 80 (3), 283–296.

Dong, M.; Chen, N.; Zhao, X.; Fan, S.; (2019). Chen, Z. Nighttime radiative cooling in hot and humid climates, Optics, Express, 27, 31587.Family, R., Menguc, M.P. (2017) Materials for radiative cooling: A review, Procedia Environmental Science, 38, 752-759.

Eriksson, T.S., Lushiku, E.M., Granqvist, C.G., (1984). Materials for radiative cooling to low temperature. Solar Energy Materials 11 (3), 149–161.

Eriksson, T.S., Jiang, S.J., Granqvist, C.G., (1985). Surface coatings for radiative cooling applications: silicon dioxide and silicon nitride made by reactive rf-sputtering. Solar Energy Materials 12 (5), 319–325.

Family, R., Mengue, M.P. (2017). Materials for radiative cooling: A review, Procedia Environmental Science, 38, 752-759.

Fan, J., Fu, C. & Fu, T. (2020). Yttria-stabilized zirconia coating for passive daytime radiative cooling in humid environment. Applied Thermal. Engineering, 165, 114585.

Feng, J., Gao, K., Santamouris, M., Shah, K., Ranzi, G. (2020). Dynamic impact of climate on the performance of daytime radiative cooling materials, Solar Energy Materials & Solar Cells 208, 110426, Australia

Gao, M., Han, X., Chen, F., Zhou, W., Liu, P., Shan, Y., Chen, Y., Li, J., Zhang, R., Wang, S. (2019). Approach to fabricating high-performance cooler with near-ideal emissive spectrum for above-ambient air temperature radiative cooling. Solar Energy Materials Solar Cells, 200, 110013.

Geetha, N.B., Velraj, R., (2012). Passive Cooling Methods for Energy Efficient Buildings with and without Thermal Energy Storage – A Review, Energy Education Science and Technology Part A: Energy Science and Research, 29(2), pp. 913-946.

Gentle, A.R., Smith, G.B., (2010). Radiative Heat Pumping from the Earth Using Surface Phonon Resonant Nanoparticles. Nano Lett. 10 (2), 373–379.

Goldstein, E.A., Raman, A.P., Fan, S., (2017). Sub-ambient non-evaporative fluid cooling with the sky. Nat. Energy 2 (9).

Guan, H., Sebben, M., Bennett, J. (2014). Radiative- and artificial-cooling enhanced dew collection in a coastal area of South Australia. Urban Water J. 11(3):175-184. doi:10.1080/1573062X. 2013.765494

Granqvist C. G and Hjortsberg A. (1981). Radiative cooling to low temperatures: general considerations and application to selectively emitting SiO films. Journal of Applied Physics 52: 6: 4205-4220.

Granqvist, C.G., Hjortsberg, A., Eriksson, T.S., (1982). Radiative cooling to low temperatures with selectivity IR-emitting surfaces. Thin Solid Films 90 (2), 187–190.

Grenier, P. (1979). R´efrig´eration radiative. Effet de serre inverse. Rev. Phys. Appl. (Paris) 14 (1), 87–90.

Han, D.; Ng, B.F.; Wan, M.P. (2020). Preliminary study of passive radiative cooling under Singapore's tropical climate. Solar Energy Materials Solar Cells, 206, 110270.

Han, D., & Feng, N. B. (2022). *Investigation of passive radiative cooling in tropical climates*. Nanyang Technological University.

Harrison, A.W., Walton, M.R., (1978). Radiative cooling of TiO_2 white paint. Solar Energy 20 (2), 185–188.

Heidarinejad, G., Farmahini-Farahani, M., Delfani, S. (2010). Investigation of a hybrid system of nocturnal radiative cooling and direct evaporative cooling. Build. Environ. 45 (6), 1521–1528.

Hollick, J. (2012). Nocturnal radiation cooling tests, Energy Procedia, 30, 930–936.

Hossain, M. M. and Gu, Min (2016). Radiative Cooling: Principles, Progress, and Potentials Adv. Sci. 2016, 3, 1500360

Hossain, M. M., Jia, B., Gu, M. (2015). A Metamaterial Emitter for Highly Efficient Radiative Cooling," Adv. Opt. Mater. 3(8), 1047–1051.

Hong Kong observatory (2022). What is cooling? [www] Hong Kong observatory Available from https://hko.gov.hk [Accessed May 2022].

Hosseinzadeh, E., Taherian, H. (2012). An experimental and analytical study of a radiative cooling system with unglazed flat plate collectors. Int. J. Green Energy, 9, 766–779.

Hsu, P., Liu, X., Liu, C., Xie, X., Lee, R. H., Welch, A. J., Zhao, T., Cu, Y. (2016). Personal Thermal Management by Metallic Nanowire-Coated Textile. Nano Letters, ACS Publications. doi.org/10.1021/nl5036572.

Hu, M., Pei, G., Wang, Q., et al., (2016). Field test and preliminary analysis of a combined diurnal solar heating and nocturnal radiative cooling system. Appl. Energy 179, 899–908.

Hu, T., Kwan, T.H., Pei, G. (2022). An all-day cooling system that combines solar absorption chiller and radiative cooling, Renewable Energy (2022), doi: https://doi.org/10.1016/ j. renene.2022.01.058.

Huang, Z.; Ruan, X. (2017) Nanoparticle embedded double-layer coating for daytime radiative cooling. Int. J. Heat Mass Transfer, 104, 890–896.

Huang, Y., Pu, M., Zhao, Z., Li, X., Ma, X., Luo, X. (2018). Broadband metamaterial as an "invisible" radiative cooling coat**.** Opt. Communication, 407, 204–207.

Huang, M., Yu, X., Wan, J., Du, Mu., Wang, X., Sun, Q., Tang, G.H. (2022a). All-day effective radiative cooling by optically selective and thermally insulating mesoporous materials. Solar Energy 235 (170–179).

Huang, X., Mandal, J., Raman, A. P. (2022b). Do-it-yourself radiative cooler as a radiative cooling standard and cooling component for device design. Journal of Photonics for Energy, Volume 12, id. 012112

International Energy Agency (2018). The future of cooling [www] International Energy Agency Available from http://www.iea.org [Accessed 18/04/2020].

Jeong, S.Y., Tso, C.Y., Zouagui, M., Wong, Y.M. Chao, C.Y.H. (2018) A numerical study of daytime passive radiative coolers for space cooling in buildings, Building Simulation, 11, 1011–1028.

Jeong, S. Y., Tso, C. Y., Zouagui, M., Wong, Y. M., Chao, C. Y.H. (2018b). A numerical study of daytime passive radiative coolers for space cooling in buildings. Building Simulation 11 (5), 1011–1028. https://doi.org/10.1007/s12273-018-0474-4

Jeong, S. Y., Tso, C. Y., Wong, Y. M., Chao, C. Y., Huang, B. (2020a). Daytime passive radiative cooling by ultra emissive bio-inspired polymeric surface, Sol. Energy Mater. Sol. Cells 206, 110296.

Jeong, S.Y., Tso, C.Y., Ha, J., Wong, Y.M., Christopher, Y.H., Chao, B.H., and Qiu, H. (2020b). Field investigation of a photonic multi-layered TiO_2 passive radiative cooler in sub-tropical climate, Renewable Energy, 146, 44-55.

Katramiz, E., Ghaddar, N., Ghali, K. (2020). Daytime radiative cooling: To what extent it enhances cooling system performance in comparison to night cooling in semi-arid climate? J. Building Engineering, 28, 101020.

Kecebas, M. A., Menguc, M. P., Kosar, A., Sendur, K. (2017). Passive radiative cooling design with broadband optical thin-film filters, J. Quant. Spectrosc. Radiat. Transfer 198, 179–186.

Kou, J., Jurado, Z., Chen, Z., Fan, S., and Minnich, A.J. (2017). Daytime radiative cooling using near-black infrared emitters, American Chemical Society Photonics, 4, 626-630.

Khalil B., Adamowski J., Shabbir A., et al. (2016). A review: dew water collection from radiative passive collectors to recent developments of active collectors. Sustain Water Resour Manag. 2(1):71-86. doi:10.1007/s40899-015-0038-z

Khedari, J., Waewsak, J., Thepa, S., Hirunlabh, J. (2000). Field investigation of night radiation cooling under tropical climate, Renewable Energy, 20, 183–193.

Lee, G.J., Kim, Y.J., Kim, H.M., Yoo, Y.J., Song, Y.M. (2018). Colored, Daytime Radiative Coolers with Thin-Film Resonators for Aesthetic Purposes, Advanced. Opt. Materials, 6, 1–8.

Lee, E., and Luo, T. (2019) Black body-like radiative cooling for flexible thin-film solar cells, Solar Energy Materials and Solar Cells, 194, 222-228.

Leroy, A., Bhatia, B., Kelsall, C.C., et al., (2019). High-performance sub-ambient radiative cooling enabled by optically selective and thermally insulating polyethylene aerogel. Science Advance 5 (10), eaat9480.

Li, W., Shi, Y., Chen, K., Zhu, L., and Fan, S. (2017). A comprehensive photonic approach for solar cell cooling, American Chemical Society Photonics, 4, 774-782.

Li, W., Shi, Y., Chen, Z., et al., (2018). Photonic thermal management of coloured objects. Nat. Commun. 9 (1), 4240.

Li, N., Wang, J., Liu, D., Huang, X., Xu, Z., Zhang, C., Zhang, Z., Zhong, M. (2019). Selective spectral optical properties and structure of aluminum phosphate for daytime passive radiative cooling application. Solar Energy Materials Solar Cells, 194, 103–110.

Li, Z., Chen, Q., Song, Y., Zhu, B., Zhu, J. (2020). Fundamentals, Materials, and Applications for Daytime Radiative Cooling. Advanced Material Technology, 1901007

Lim, X.Z. (2020). The supercool materials that send heat to space, Nature, vol 577.

Lin, K., Chao, L., Chung T. (2021). Insight for promoting revolutionary research in radiative cooling materials and sustainability developments in buildings. Energy & Buildings, 252 di,111400 11

Liu, Y., Bai, A., Fang, Z., Ni, Y., Lu, C., Xu, Z. (2019). A pragmatic bi-layer selective emitter for efficient radiative cooling under direct sunlight. Materials, 12, 1208.

Liu, C., Ay, C., Tsai, C., Lee, M. (2019a). The application of passive radiative cooling in greenhouses, Sustainability, 11, 6703.

Liu, J., Hsu, Z., Zhang, D., Jiao, S., Zhang, J., Gao, F., Ling, J., Feng, W., Zuo, J. (2019b). Research on the performance of radiative cooling and solar heating coupling module to direct control indoor temperature. Energy Conversion Management, 205, 112395.

Liu, J., Zhang, D., Jiao S., Zhou, Z., Zhang, Z., Gao, F., Key, T. (2020). Daytime radiative cooling with clear epoxy resin. Solar Energy Materials and Solar Cells 207 (2020) 110368

Liu, J., Tang, H., Zhang, J., Zhang, D., Jiao, S., & Zhou, Z. (2021). Boosting Daytime Radiative Cooling Performance with Nanoporous Polyethylene Film. *Energy and Built Environment*. https://doi.org/10.1016/j.enbenv.2021.10.001

Liu, X., Beysens, D., Bourouina, T. (2022). Water Harvesting from Air: Current Passive Approaches and Outlook. ACS Materials Lett. 2022, 4, 5, 1003–1024. https://doi.org/10.1021/acsmaterialslett.1c00850

Mandal, J., Fu, Y., Overvig, A., Jia, M., Sun, K., Shi, N., Zhou, H., Xiao, X., Yu, N., Yang, Y. (2018). Hierarchically porous polymer coatings for highly efficient passive daytime radiative cooling, Science 362(6412), 315–319.

Mandal, J., Jia, M., Overvig, A., et al., (2019). Porous Polymers with Switchable Optical Transmittance for Optical and Thermal Regulation. Joule 3 (12), 3088–3099.

Mandal, J., Yang, Y., Yu, N., et al., (2020). Paints as a Scalable and Effective Radiative Cooling Technology for Buildings. Joule 4 (7), 1350–1356.

Meir, M.G., Rekstad, J.B., and Lovvik, M., (2002). A Study of a Polymer-based Radiative Cooling System, Solar Energy, 73(6), pp. 403-417.

Michell, D., Biggs, K.L., (1979). Radiation cooling of buildings at night. Appl. Energy 5 (4), 263–275.

Mihalakakou, G., Ferrante, A., and Lewis, J.O., (1998). The Cooling Potential of a Metallic Nocturnal Radiator, Energy and Buildings, 28(3), pp. 251-256.

Miyawaki, R., Satake, A., Mitani, Y., Ushifusa, Y. (2020). Consideration of reducing purchasing power using photovoltaic excess power by thermal radiative cooling/heating system. Energy Rep. 2020; 6:814-821. doi: 10.1016/j.egyr.11.127.

Mu, E., Wu, Z., Wu, Z., Chen, X., Liu, Y., Fu, X., Hu, Z. (2019). A novel self-powering ultrathin TEG device based on micro/nano emitter for radiative cooling. Nano Energy 55, 494–500.

Muselli, M., Beysens, D., Marcillat, J., et al., (2002). Dew water collector for potable water in Ajaccio (Corsica Island, France). Atmos. Res. 64 (1), 297–312. Nibir, K.D., Ravi Dat and Ashok K.S. (2013). Advance in infrared detector array technology. DOI: 10.5772/51665

Naghshine, B.B., Saboonchi, A. (2018). Optimized thin film coatings for passive radiative cooling applications**,** Opt. Communication, 410, 416–423.

Nilsson, T.M.J., Niklasson, G.A. (1995). Radiative cooling during the day: simulations and experiments on pigmented polyethylene cover foils. Sol. Energy Mater. Sol. Cells 37 (1), 93–118.

Noro, M., Mancin, S., & Riehl, R. (2021). Energy and Economic Sustainability of a Trigeneration Solar System Using Radiative Cooling in Mediterranean Climate. *Sustainability*, *13*, 11446. https://doi.org/10.3390/su132011446

Nwaji, G.N., Okoronkwo, C.A., Ogueke, N.V., Anyanwu, E.E. (2020). Investigation of a hybrid solar collector/nocturnal radiator for water heating/cooling in selected Nigerian cities. Renewable Energy 145, 2561e2574

Nwigwe K.N., Okoronkwo C.A., Ogueke N.V., Ugwuokeand, P.E and Anyanwu E.E. (2012). Transient Analysis of a Nocturnal Radiative Cooling of a Building in Owerri, Nigeria, Research Journal of Applied Sciences, Engineering and Technology 4(15): 2496-2506, 2012, ISSN: 2040-7467, © Maxwell Scientific Organization, 2012.

Ogueke, N. V., Anyanwu, E. E., and Ekechukwu, O.V., (2009). A review of solar water heating systems, Journal of Renewable and Sustainable Energy **1**, 043106.

Ogueke, N. V., Onwuachu, C. C. and Anyanwu, E. E. (2011). Experimental Study of Long-Wave Night Sky Radiation in Owerri, Nigeria for Passive Cooling Application, World Renewable Energy Congress, Linkoping, Sweden, 8-13.

Okoronkwo C.A (2011). Experimental study of passive cooling of a building using long-wave night sky radiation in Owerri, Nigeria, PhD thesis Mechanical Engineering Department, Federal University of Technology, Owerri, Imo State, Nigeria.

Olanrewaju, S. D., Adegun, O. B. (2021). Household energy consumption within a low income neighbourhood in Akure, Nigeria. IOP Conf. Ser.: Materials Science Engineering, 1036, 012025. doi:10.1088/1757-899X/1036/1/012025

Orel, B., Gunde, M.K., Krainer, A., (1993). Radiative cooling efficiency of white pigmented paints. Sol. Energy 50 (6), 477–482.

Palik, E.D. (1998). Handbook of optical constants of solids. Academic press, p. 3.

Parker, D.S. (2005). Theoretical evaluation of the night cool nocturnal radiation cooling concept. Submitted to: US Department of Energy. FSEC-CR-1502-05

Parker, D.S., Sherwin, J.R. (2008). Evaluation of the Night Cool Nocturnal Radiation Cooling Concept: Annual Performance Assessment in Scale Test Buildings Stage Gate 1B. Florida Solar Energy Center, Cocoa, FL (United States).

Raman A.P., Anoma, M. A., Zhu, L., Rephaeli, E., Fan, S. (2014). Passive radiative cooling below ambient air temperature under direct sunlight, Nature 515(7528), 540–544.

Raman, A.P., Li, W., Fan, S., (2019). Generating Light from Darkness. Joule 3 (11), 2679–2686.

Raphaeli E, Raman A and, Fan S. (2013) Ultrabroadband Photonic Structures to Achieve High-Performance Daytime Radiative Cooling. J. Nano Letters 13: 1457-1461.

Raeissi, S., and Taheri, M., (2000) Skytherm: An Approach to Year-round Thermal Energy Sufficient Houses, Renewable Energy, 19(4), pp.527-543.

Royne A, Dey C.J, Mills D.R. (2004). Cooling of photovoltaic cells under concentrated illumination: a critical review. Sol Energy Mater Sol Cells. 2005;86(4):451-483. doi: 10.1016/j.solmat. 09.003

Saitoh, T.S., Fujino, T., (2001). Advanced energy-efficient house (HARBEMAN house) with solar thermal, photovoltaic, and sky radiation energies (experimental results). Sol. Energy 70 (1), 63–77.

Santamouris, M.; Feng, J. (2018). Recent progress in daytime radiative cooling: Is it the air conditioner of the future, Buildings, 8, 168.

Skoplaki, E., Palyvos, J.A. (2009). On the temperature dependence of photovoltaic module electrical performance: a review of efficiency/power correlations. Sol Energy. 2009;83(5):614-624. doi: 10.1016/j.solener. 10.008

Son, S., Jeon, S., Chae, D., Yeop L.S., Liu, Y., Lim, H., Ju-Oh, S., Lee, H. (2020). Colored emitters with silica-embedded perovskite nanocrystals for efficient daytime radiative cooling, Nano Energy, 79, 105461.

Suhendri, S., Hu, M., Su, Y., Darkwa J., Riffat, S. (2020). Implementation of Passive Radiative Cooling Technology in Buildings: A Review. Buildings 10, 215.

Sumathy, K., Ruchi S., Phillip E., Jiawei G. (2013). Recent advances in the solar water heating systems: A review, Renewable and Sustainable Energy Reviews 19 173–190.

Sun, K., Riedel, C.A., Wang, Y., et al., (2018). Metasurface Optical Solar Reflectors Using AZO Transparent Conducting Oxides for Radiative Cooling of Spacecraft. ACS Photonics 5 (2), 495–501.

Sun, J., Wang, J., Guo, T., Bao, H., Bai, S. (2022). Daytime passive radiative cooling materials based on disordered media: A review. Solar Energy Materials and Solar Cells. Volume 236, 111492

Synnefa, A., Santamouris, M., Akbari, H. (2007). Estimating the effect of using cool coatings on energy loads and thermal comfort in residential buildings in various climatic conditions. Energy Build. 39 (11), 1167–1174.

Theordore, L. G. (2018). Active daytime radiative cooling using spectrally selective surfaces for air conditioning and refrigeration systems, Solar Energy, 174, 16-23.

Tevar J., Castaño, S., Marijuan, A.G., Heras, M.R., Pistono, J. (2015). Modelling and experimental analysis of three radio convective panels for night cooling. Energy Buildings. 2015; 107:37-48. doi: 10.1016/j.enbuild. 07.027

Torgerson, E., Hellhake, J. (2019). Polymer solar filter for enabling direct daytime radiative cooling. Solar Energy Materials Solar Cells, 206, 110319.

Trombe, F., (1967). Perspectives sur l'utilisation des rayonnements solaires et terrestres dans certaines r´egions du monde. Rev. Gen. Therm. 6 (70), 1285–1314. University of Wyoming. Upper air data soundings. Available from: http://weather.uwyo.edu/upperair/sounding.html.

Tso, C.Y., Chan K.C., Christopher Y.H., Chao, (2017). A field investigation of passive radiative cooling under Hong Kong's climate, Renewable Energy, 106,52-61.

Vall, S., Castell, A. (2017). Radiative cooling as low-grade energy source: A literature review, Renewable and Sustainable Energy Reviews, 77, 803-820.

Waite, M., Cohen, E., Torbey, H., Piccirilli, M., Tian, Y., Modi, V. (2017). Global Trends in Urban Electricity Demands for Cooling and Heating Energy **2**, 127, 786–802.

Wang, W., Fernandez, N., Katipamula, S., Alvine, K. (2018). Performance assessment of a photonic radiative cooling system for office buildings. Renew. Energy, 118, 265–277.

Wang, Z., Kortge, D., Zhu, J., Zhou, Z., Torsina, H., Lee, C., and Bermel, P. (2020). Lightweight, passive radiative cooling to enhance concentrating photovoltaics, Joule,4, 1-16.

Wang, T., Wu, Y., Shi, L., Hu, X., Chen, M., and Wu, L. (2021). A structural polymer for highly efficient all-day passive radiative cooling. Nature Communications, |12:365| https://doi.org/10.1038/s41467-020-20646-7

Wong, R.Y.M., Tso, C.Y., Chao, Y.H., Huang, B., Wan, M.P. (2018). Ultra-broadband asymmetric transmission metallic gratings for subtropical passive daytime radiative cooling, Solar Energy Materials and Solar Cells, 186, 330-339.

Xia, Z., Fang, Z., Zhang, Z., Shi, K., Meng, Z.(2020). Easy Way to Achieve Self-Adaptive Cooling of Passive Radiative Materials. ACS Applied Materials & Interfaces 12 (24). DOI: 10.1021/acsami.0c05803

Yalçın, A., Blandre, E., Joulain, K., Drevillon, J. (2020). Daytime radiative cooling with silica fiber network , Solar Energy Materials and Solar Cells 206, 110320. France

Cui, Y., Luo, X., Zhang, F., Sun, L., Jin, N., Yang, W. (2022). Progress of passive daytime radiative cooling technologies towards commercial applications. Particuology 67, 57–67

Yang, Y., Zhang, Y. (2020). Passive daytime radiative cooling: principle, application and economic analysis, MRS Energy and Sustainability, vol 7.

Yang, N., Fu, Y., Xue, X., Lei, D., & Dai, J. (2022). Geopolymer-based sub-ambient daytime radiative cooling coating. *EcoMat*. https://doi.org/10.1002/eom2.12284

Young, S., Yan, C., Ha, J., & Ming, Y. (2020). Field investigation of a photonic multi-layered TiO 2 passive radiative cooler in sub-tropical climate. *Renewable Energy*, *146*, 44–55. https://doi.org/10.1016/j.renene.2019.06.119

Zaite, A., Naoual, B., Abid, C., KAISS, A., & KANSO, H. (2022). Integrate of night radiative cooling technology using a photovoltaic thermal collector under three different climates. *International Journal of Thermofluids*, *16*, 100252. https://doi.org/10.1016/j.ijft.2022.100252

Zeng S., Pian S., Su M., Liu X., Wu M., Chen M. (2021). Hierarchical morphology metafabric for scalable passive daytime radiative cooling. Science. 373(6555):692-696.

Zeyghami, M., Goswami, D.Y., Stefanakos, E. (2018). A review of clear-sky radiative cooling developments and applications in renewable power systems and passive building cooling. Sol Energy Mater Sol Cells. 178(178):115-128. doi: 10.1016/j.solmat.2018.01.015.

Zhai, Y., Ma, Y., David, S.N., Zhao, D., Lou, R., Tan, G., Yang, R., and Yin, X. (2017). Scalable-manufactured randomized glass-polymer hybrid metamaterial for daytime radiative cooling," Science, doi: 10.1126/science. aai7899.

Zhang, S., Niu, J. (2012). Cooling performance of nocturnal radiative cooling combined with microencapsulated phase change material (MPCM) slurry storage. Energy and Buildings, 54, 122-130.

Zhao, B., Hu, M., Ao, X., Pei, G. (2017). Conceptual development of a building-integrated photovoltaic–radiative cooling system and preliminary performance analysis in Eastern China, Applied Energy, 205, 626–634.

Zhao, B., Hu, M., Ao, X., Xuan, Q., Pei, G. (2018) Comprehensive photonic approach for diurnal photovoltaic and nocturnal radiative cooling, Solar Energy Materials Solar Cells, 178, 266–272.

Zhao, B., Hu, M., Ao, X., and Pei, G. (2018b). Performance analysis of enhanced radiative cooling of solar cells based on a commercial silicon photovoltaic module, Solar Energy, 176, 248-255.

Zhao, D., Aili, A., Zhai, Y., Lu, J., Kidd, D., Tan, G., Yin, X. (2019). Sub-ambient cooling of water: Toward real-world applications of daytime radiative cooling, Joule, 3, 1-13.

Zhao, B., Hu, M., Ao, X., Chen, N., Pei, G. (2019b). Radiative cooling: A review of fundamentals, materials, applications, and prospects. Applied Energy, 236, 489–513.

Zhao, D., Aili, A., Zhai, Y., Xu, S., Tan, G., Yin, X., Yang, R. (2019c). Radiative sky cooling: Fundamental principles, materials, and applications, Appl. Phys. Rev. 6(2), 021306.

Zhao, B., Ao, X., Chen, N., Xuan, Q., Hu, M., Pei, G. (2019d) General strategy of passive sub-ambient daytime radiative cooling, Solar Energy Materials Solar Cells, 199, 108–113.

Zhao, B., Hu, M., Ao, X., Chen, N., Xuan, Q., Jiao, D., Pei, G. (2019e). Performance analysis of a hybrid system combining photovoltaic and nighttime radiative cooling, Applied Energy, 252, 113432.

Zhao, B., Hu, M., Ao, X., Chen, N., Xuan, Q., Su, Y., Pei, G. (2019f). A novel strategy for a building-integrated diurnal photovoltaic and all-day radiative cooling system, Energy, 183, 892–900.

Zhao, D., Yin, X., Xu, J., Tan, G., Yang, R. (2020). Radiative sky cooling-assisted thermoelectric cooling system for building applications. Energy, 190, 116322.

Zhou, L., song, H., Zhang, N., Rada, J., Singer, M., Zhang, Haufan., Ooi, B.S., Yu, Z., and Gan Q. (2021). Hybrid concentrated radiative cooling and solar heating in a single system, Cell Report Physical Science, 2, 100338.

Zhu, L., Raman, A., Fan, S. (2013). Color-preserving daytime radiative cooling. J Appl. Phys. Letters 103: 223902.

Zhu, L., Raman, A., Wang, K.X., Anoma, M.A., Fan, S. (2014). Radiative cooling of solar cells. Optica. 1(1):32. doi:10.1364/optica.1.000032

Zhu L., Raman, A. P., Fan, S. (2015). Radiative cooling of solar absorbers using a visibly transparent photonic crystal thermal blackbody, Proc. Natl. Acad. Sci. U. S. A. 112(40), 12282–12287.

Zhu, Y., Wang, D., Fan, C., He, P., and Ye, Y. (2019a). A multilayer emitter close to ideal solar reflectance for efficient daytime radiative cooling, Polymers, 11, 1203, China.

Zhu, L., Song, H., Liang, J., Singer, M., Zhou, M., Stegenburgs, E., Zhang, N., Xu,C.,Ng, T., Yu, Z., Ooi, B. (2019b). A polydimethylsiloxane-coated metal structure for all-day radiative cooling, Nature Sustainability, Vol 2, 718-724.

Zhu, Y., Ye, Y., Wang, D., and Cao, Y. (2021). Simple Dual-layer Emitter for Daytime Radiative Cooling. OSA Continuum, OSA Continuum.

Zou, C., Ren, G., Hossain, M.M., et al., (2017). Metal-Loaded Dielectric Resonator Metasurfaces for Radiative Cooling. Adv. Opt. Mater. 5 (20), 1700460.

Appendix A Drawing of the test chamber with the various views

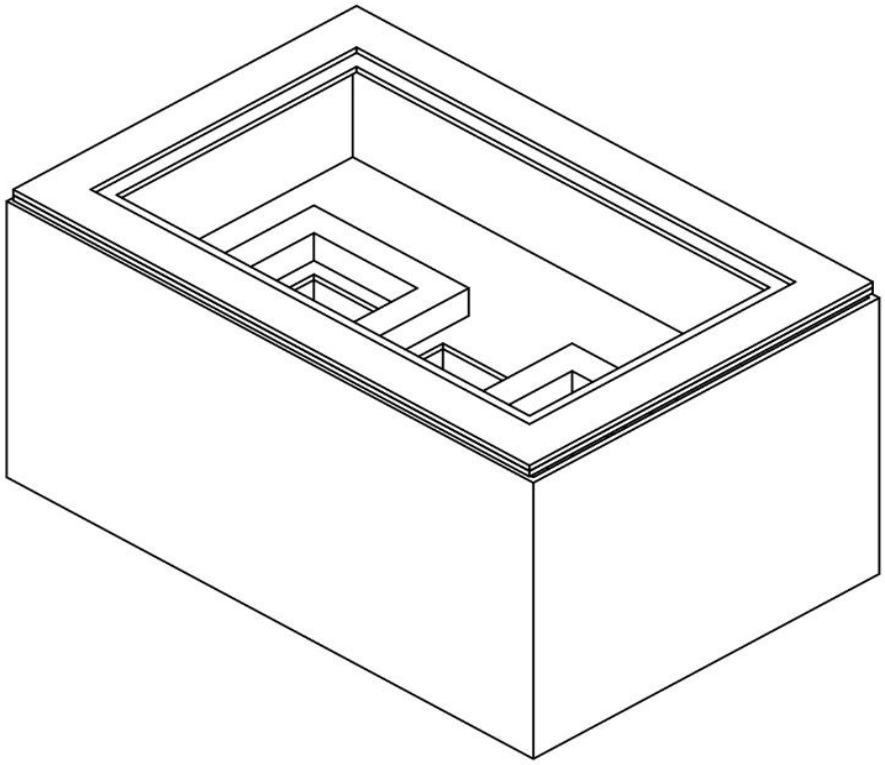

Iso view Complete solar exposure box

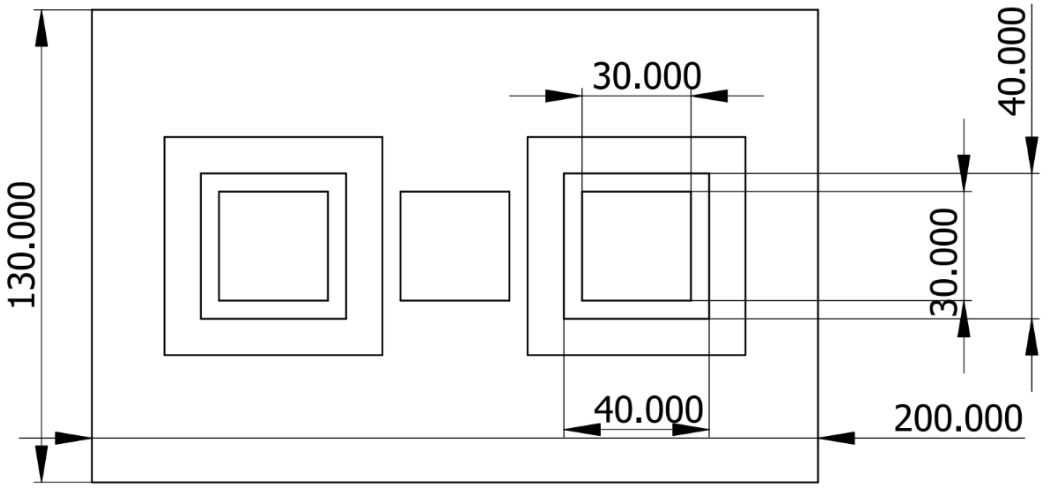

Top view exposure box

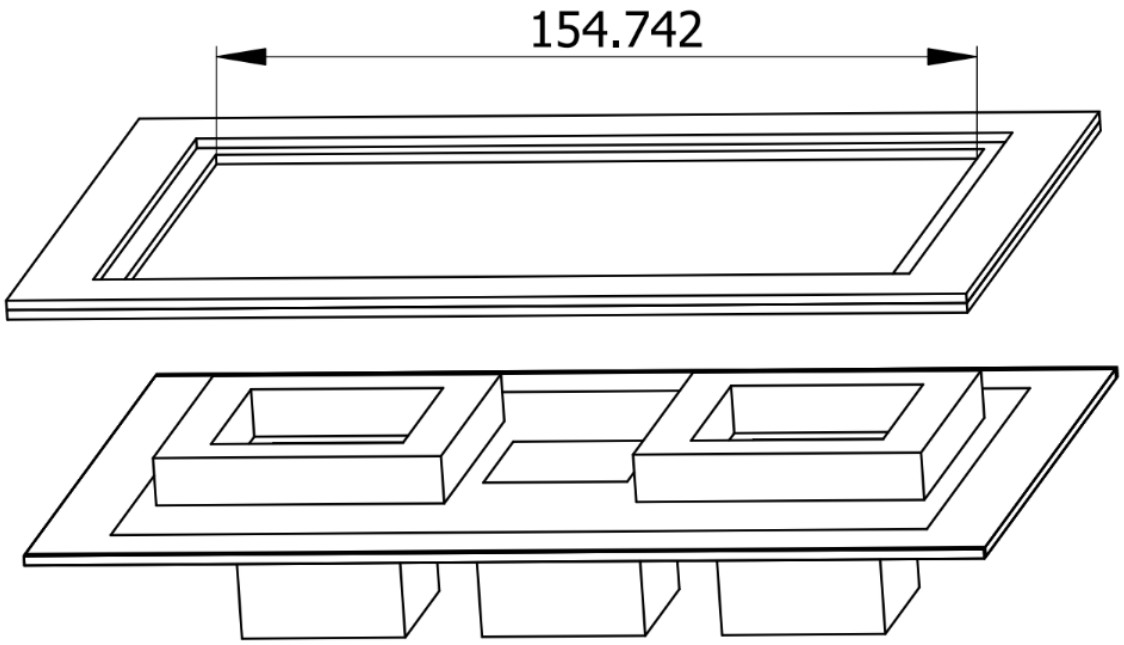

sample well + window layer

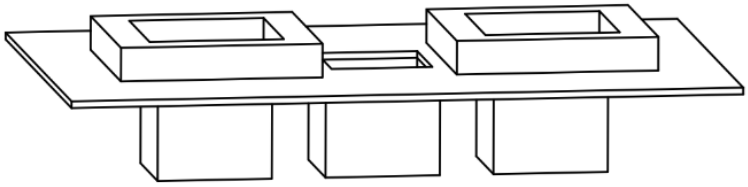

Iso view sample well

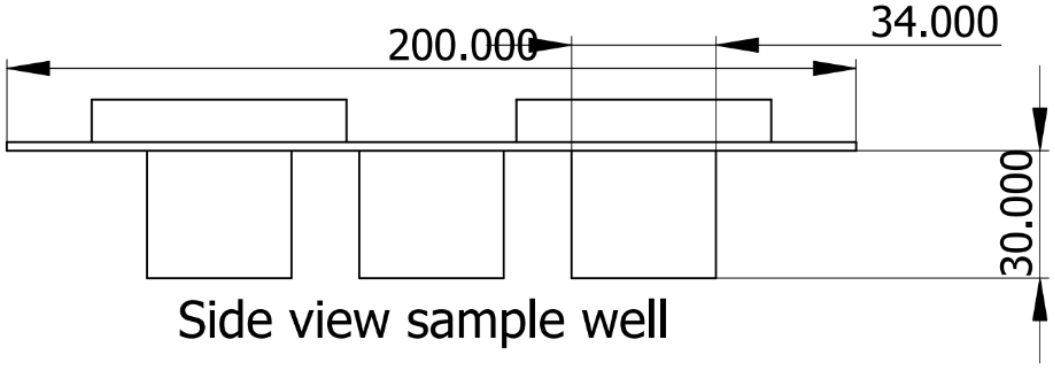

Side view sample well

Appendix B Experimental Temperatures for $BaSO_4$ and MPEA

B1 Experimental Temperatures for $BaSO_4$ and MPEA in Abuja on 18/05/22022

Time	Tamb	Tbs	Tpet
07:00:00	25.53	25.41	25.76
07:15:00	25.95	25.74	25.1
07:30:00	25.61	25.93	25.06
07:45:00	25.87	25.63	25.6
08:00:00	24.85	24.43	24.65
08:15:00	24.28	24.4	24.37
08:30:00	24.85	24.25	24.2
08:45:00	24.42	24.27	24.19
09:00:00	25.65	24.65	24
09:15:00	25.82	24.45	24.44
09:30:00	25.4	24.08	24.73
09:45:00	25.65	24.88	24.02
10:00:00	27.55	25.73	24.96
10:15:00	27.37	25.25	24.96
10:30:00	27.93	25.44	24.18
10:45:00	27.56	25.46	24.57
11:00:00	28.16	26.01	25.23
11:15:00	28.5	26.33	25.68
11:30:00	28.23	26.91	25.72
11:45:00	28.22	26.05	25.91
12:00:00	29.36	26.98	26.02
12:15:00	29.44	26.5	26.2
12:30:00	29.08	26.32	26.91
12:45:00	29	26.26	26.91
13:00:00	30.68	28.14	26.62
13:15:00	30.9	28.01	26.26
13:30:00	30.03	28.21	26.66
13:45:00	30.61	28.94	26.72
14:00:00	30.44	28.56	27.32
14:15:00	30.1	28.55	27.35
14:30:00	30.43	28.91	27.71
14:45:00	30.92	28.7	27.47
15:00:00	31.53	29.53	28
15:15:00	31.28	29.44	28.93
15:30:00	31.56	29.29	28.34
15:45:00	31.02	29.19	28.28
16:00:00	31.59	29.1	28.64
16:15:00	31.1	29.49	28.29
16:30:00	31.67	29.98	28.25
16:45:00	31.09	29.68	28.74
17:00:00	32.62	30.62	29.41
17:15:00	32.56	30.72	29.86
17:30:00	32.17	30.04	29.25
17:45:00	32.2	30.29	29.52
18:00:00	30.64	30.76	30.04
18:15:00	30.71	30.05	30.33
18:30:00	30.64	30.26	30.65
18:45:00	30.03	30.03	30.03
19:00:00	29.58	30.21	29.57

B2 Experimental Temperatures for $BaSO_4$ and MPEA in Abuja on 19-22/05/22022

Time	Tamb_Expt	Tbs_Expt	Tmpea_Expt	Tamb_moel	Tmpea_model	Tbs_model
07:00:00	26.54	26.9	26.19	24.46	23.82	23.85
07:15:00	27.48	27.64	27.74	24.62	23.85	23.88
07:30:00	27.17	26.87	27.11	24.83	23.88	23.94
07:45:00	27.74	27.18	27.62	25.24	23.94	23.97
08:00:00	27.53	27.11	27.74	25.5	24.02	24.07
08:15:00	27.79	27.91	27.09	25.88	24.1	24.11
08:30:00	27.78	27.56	27.98	26.08	24.12	24.16
08:45:00	27.48	27.54	27.83	26.7	24.25	24.26
09:00:00	29.55	26.49	25.66	26.83	24.39	24.31
09:15:00	29.98	26.64	27.27	27.35	24.5	24.52
09:30:00	29.35	26.51	27.02	27.48	24.63	24.71
09:45:00	29.72	26.02	27.09	27.78	24.78	24.84
10:00:00	29.86	26.88	27.86	28.24	24.93	25.07
10:15:00	29.39	26.38	27.83	28.43	25.14	25.33
10:30:00	29.86	26.57	27.28	28.65	25.26	25.48
10:45:00	29.32	26.58	27.76	28.89	25.42	25.68
11:00:00	30.43	27.43	26.38	29.29	25.64	25.94
11:15:00	30.53	27.63	26.34	29.54	25.79	26.21
11:30:00	30.98	27.79	26.27	29.91	26.06	26.44
11:45:00	30.68	27.62	26.48	29.98	26.19	26.58
12:00:00	31.76	27.58	27.25	30.5	26.49	26.96

12:15:00	31.81	27.88	27.81	30.61	26.6	27.12
12:30:00	31.73	27.46	27.6	31.04	26.94	27.51
12:45:00	31.8	27.32	27.14	31.43	27.09	27.88
13:00:00	32.87	28.73	27.62	31.53	27.39	28.06
13:15:00	32.81	28.57	27.01	31.77	27.64	28.18
13:30:00	32.32	28.87	27.87	31.97	27.86	28.6
13:45:00	32.48	28.34	27.66	32.01	27.91	28.92
14:00:00	33.74	30.69	28.26	32.33	28.25	29.12
14:15:00	33.57	30.72	28.74	32.49	28.37	29.23
14:30:00	33.24	30.02	28.26	32.62	28.64	29.61
14:45:00	33.09	30.1	28.37	32.75	28.87	29.79
15:00:00	34.99	30.91	29.55	32.82	29	30.04
15:15:00	34.49	30.16	29.64	32.91	29.15	30.3
15:30:00	34.85	30.46	29.29	32.96	29.31	30.44
15:45:00	34.15	30.74	29.58	33	29.44	30.86
16:00:00	34.69	31.86	30.97	33.29	29.56	31.06
16:15:00	34.58	31.01	30.66	33.45	27.67	31.11
16:30:00	34.06	31.32	30.24	32.96	29.77	31.27
16:45:00	34.23	31.21	30.01	32.88	29.83	31.32
17:00:00	31.06	29.37	27.7	32.82	29.91	31.42
17:15:00	31.98	29.32	27.07	32.79	29.98	31.28
17:30:00	31.84	29.63	27.32	32.61	30	31.5
17:45:00	31.73	29.31	27.11	32.51	30.03	31.52
18:00:00	28.42	27.14	26.31	32.33	30.05	31.53
18:15:00	28.49	27.27	26.82	32.2	30.06	31.53

18:30:00	28.27	27.39	26.99	31.97	30.08	31.54
18:45:00	28.5	27.4	26.51	31.76	30.08	31.54
19:00:00	28.51	27.46	27.38	31.53	30.09	31.54
19:15:00	28.17	28.17	27.16	31.47	30.1	31.54
19:30:00	28.26	28.26	27.32	31.04	30.1	31.54
19:45:00	28.16	28.16	27.25	30.92	30.1	31.54
20:00:00	27.98	29.65	31.04	30.53	30.1	31.54
20:15:00	28.06	30.57	31.04	30.32	30.1	31.54
20:30:00	27.63	30.12	30.51	29	30.1	31.54
20:45:00	27.27	29.78	30.22	29.86	30.1	31.5
21:00:00	26.89	29.33	29.57	28.49	30.1	31.49
21:15:00	27.08	29.35	29.72	28.31	30.1	31.46
21:30:00	26.2	28.68	28.97	28.02	30.1	31.42
21:45:00	25.92	28.3	28.66	27.87	30	31.39
22:00:00	25.8	28.15	28.58	27.62	30	31.31
22:15:00	25.63	27.89	28.33	27.4	29.99	31.25
22:30:00	25.43	27.64	28.08	26.81	29.98	31.15
22:45:00	25.18	27.31	27.78	26.72	29.91	31.06
23:00:00	25.07	27.19	27.6	26.08	29.87	30.93
23:15:00	24.67	26.88	27.3	26	29.76	30.85
23:30:00	24.76	26.78	27.16	25.94	29.67	30.65
23:45:00	24.65	26.61	26.91	25.88	29.5	30.55
00:00:00	24.46	26.45	26.82	25.51	29.46	30.32
00:15:00	24.25	26.2	26.5	25.47	29.41	30.2
00:30:00	24.23	26.14	26.41	24.79	29.32	29.96

00:45:00	24.04	25.9	26.2	24.6	29.21	29.81
01:00:00	24.06	25.86	26.13	24.25	29.17	29.55
01:15:00	24	25.76	25.99	24.01	29.07	29.4
01:30:00	23.89	25.61	25.85	23.78	28.84	29.17
01:45:00	24	25.61	25.84	23.66	28.73	29.09
02:00:00	24.13	25.65	26.02	23.45	28.52	28.78
02:15:00	24.13	25.51	25.8	23.34	28.36	28.63
02:30:00	24.25	25.65	25.99	23.22	28.23	28.41
02:45:00	24.11	25.44	25.77	23.12	28.18	28.33
03:00:00	23.77	25.29	25.6	23.08	27.97	28.05
03:15:00	23.53	25.03	25.31	23.05	27.87	27.8
03:30:00	23.86	25.1	25.4	23.01	27.84	27.72
03:45:00	25.22	25.8	26.05	23	27.76	27.69
04:00:00	25.7	26.28	26.5	23.01	27.75	27.42
04:15:00	25.04	26.02	26.37	23.08	27.74	27.34
04:30:00	25.1	25.9	26.15	23.1	27.73	27.16
04:45:00	25.17	26.02	26.28	23.17	27.69	27.01
05:00:00	24.79	25.68	25.89	23.22	27.52	26.94
05:15:00	24.16	25.25	25.5	23.45	27.47	26.87
05:30:00	24.36	25.3	25.53	24.46	27.35	26.72
05:45:00	23.74	24.92	25.2	24.73	27.25	26.6
06:00:00	23.48	24.69	24.99	25.24	27.13	26.56

B3 Experimental Temperatures for $BaSO_4$ and MPEA in Afikpo on 15-17/07/22022

Time	T_amb	T_BaSO4	T_mpea	Rel. Hum	V_wind	Solar Rad.
06:00:00	24.83	24.98	25.41	100	0	
06:15:00	24.5	24.34	25.1	100	0	
06:30:00	24.34	24.93	25.83	97	0	
06:45:00	24.31	24.3	25.15	98	0	
07:00:00	24.97	24.23	25.9	100	0	25
07:15:00	25.01	24.73	25.06	99	0	26
07:30:00	24.46	24	24.57	99	0	26
07:45:00	24.94	24.92	24.62	100	0	25
08:00:00	24.31	24.18	24.36	100	2.2	152
08:15:00	24.4	24.13	24.73	99	2.2	152
08:30:00	25.59	24.15	23.95	99	2.1	154
08:45:00	25.82	24.93	23.81	99	2.2	153
09:00:00	25.66	24.81	23.6	100	2.3	166
09:15:00	25.47	24.15	23.93	97	2.2	166
09:30:00	26.02	25.34	23.63	97	2.2	167
09:45:00	26.37	25.07	23.27	84	2.1	165
10:00:00	26.71	25.78	23.41	79	2.3	184
10:15:00	26.91	25.9	23.33	79	2.4	185
10:30:00	26.11	25.3	24.27	78	2.2	184
10:45:00	26.46	25.04	24.24	77	2.2	184
11:00:00	26.3	25.06	24.95	79	2.7	216
11:15:00	26.74	25.54	24.87	77		218
11:30:00	29	26.82	24.85	74	2.7	219
11:45:00	29.06	26.1	24.35	74	2.8	217
12:00:00	29.26	26.38	24.22	89	2.7	234
12:15:00	29.56	26.95	24.26	89	2.9	235
12:30:00	29.05	26.33	25	90	2.7	234
12:45:00	29.71	26.24	25.1	90	2.8	233
13:00:00	29.46	26.91	25.41	84	2.1	236
13:15:00	29.19	26.8	25.6	83	2.1	236
13:30:00	29.19	28.78	26.56	83	2.2	236
13:45:00	29.19	28.54	26.98	84	2.2	235
14:00:00	29.92	28.81	26.05	84	2.2	222
14:15:00	29.94	28.2	26.37	84	2.1	222
14:30:00	29.77	28.51	26.1	83	2.2	221
14:45:00	29.62	28.67	26.8	83	2.2	222
15:00:00	29.13	28.5	26.71	79	3.1	211
15:15:00	29.25	28.41	26.82	79	3.1	211
15:30:00	27.9	27.1	26.03	78	3.1	212
15:45:00	27.8	27.78	26.5	77	3.1	211
16:00:00	26.58	27.89	26.87	79	3.1	149
16:15:00	26.56	27.83	26.13	77	3.2	149
16:30:00	25.93	27.96	25.35	79	3.3	149
16:45:00	25.49	27.39	25.13	79	3.1	148
17:00:00	25.53	27.48	25.87	94	2.7	96
17:15:00	25.09	27.29	25.66	94	2.7	96
17:30:00	25.36	26.53	25.41	94	2.8	97
17:45:00	25.41	26.73	25.67	89	2.8	97
18:00:00	25.79	26.84	25.88	100	3.8	36
18:15:00	25.67	26.89	25.9	100	3.8	36
18:30:00	25.58	26.8	25.78	100	3.8	35
18:45:00	25.64	26.81	25.77	100	3.7	36
19:00:00	25.68	26.8	25.43	100	2.1	
19:15:00	25.59	26.71	25.64	100	2.1	
19:30:00	25.7	26.4	26.64	100	2.1	
19:45:00	25.86	26.77	26.54	100	2.2	
20:00:00	25.83	26.6	26.59	100	2.1	
20:15:00	25.72	26.7	26.49	100	2.2	
20:30:00	25.66	26	26.55	100	2.2	
20:45:00	25.73	26.82	26.5	100	2.2	
21:00:00	25.71	26.78	26.3	100	0.9	
21:15:00	25.64	26.74	26.57	100	0.9	
21:30:00	25.05	26.59	26.77	100	0.9	
21:45:00	25.54	26.55	26.1	100	0.9	
22:00:00	25.53	26.47	26.31	100	0	
22:15:00	25.36	26.43	26.31	100	0	
22:30:00	25.31	25.4	26.25	100	0	
22:45:00	25.34	25.32	26.17	100	0	
23:00:00	25.36	25.3	26.14	100	0	
23:15:00	25.39	25.54	26.06	100	0	
23:30:00	25.42	24.3	25.01	100	0	
23:45:00	25.39	24.26	25.06	100	0	
00:00:00	25.29	24.32	25.98	94	0	
00:15:00	25.34	24.25	25.52	94	0	
00:30:00	23.28	23.22	25.88	94	0	
00:45:00	23.29	23.24	25.2	93	0	
01:00:00	23.18	23.3	25.8	94	0	
01:15:00	23.3	23.11	25.86	93	0	
01:30:00	23.16	23.02	22.78	90	0	
01:45:00	23.03	23.1	22.74	90	0	
02:00:00	23.01	23.56	22.63	100	0	
02:15:00	23.94	23.63	22.77	100	0	
02:30:00	23.02	23.59	22.56	100	0	
02:45:00	23.89	23.87	22.87	100	0	
03:00:00	23.9	23.9	23.01	100	0	
03:15:00	23.85	23.74	23.6	100	0	
03:30:00	23.93	23.79	22.1	100	0	
03:45:00	23.84	23.76	22.44	100	0	
04:00:00	23.8	23.95	22.37	100	0	
04:15:00	23.78	23.67	23.12	100	0	
04:30:00	23.9	23.64	23.38	100	0	
04:45:00	23.94	23.75	23.41	100	0	
05:00:00	23.79	23.68	23.43	100	0	
05:15:00	23.92	23.3	23.31	100	0	
05:30:00	23.88	23.77	23.34	100	0	
05:45:00	23.67	23.8	23.54	100	0	
06:00:00	23.7	23.74	23.51	100	0	

06:00:00	23.7	23.74	23.51	100	0	
06:15:00	23.31	23.09	23.8	100	0	
06:30:00	23.21	23.21	23	100	0	
06:45:00	23.6	23.27	23.45	100	0	
07:00:00	23.57	23.42	23.89	100	0	33
07:15:00	23.48	23.9	23.36	100	0	32
07:30:00	25.27	24.61	24	100	0	32
07:45:00	25.82	24.33	24.71	100	0	33
08:00:00	25.14	24.89	24.8	100	0	131
08:15:00	25.8	24.64	24.37	100	0	131
08:30:00	27.79	26.8	24.81	100	0	132
08:45:00	27.67	26.54	24.76	100	0	131
09:00:00	27.27	26.03	24.9	94	0	138
09:15:00	27.51	26.31	24.89	95	0	138
09:30:00	29.59	26.28	24.13	95	0	138
09:45:00	29.72	26.59	24.23	94	0	137
10:00:00	29.34	26.87	24.33	84	2.2	184
10:15:00	29.59	26.34	24.42	90	2.1	184
10:30:00	30	28.88	26.19	90	2.1	184
10:45:00	30.51	28.89	26.9	87	2.1	185
11:00:00	30.92	28.02	26.52	74	2.7	217
11:15:00	30.47	28.12	26.57	74	2.7	217
11:30:00	31.05	28.46	26.43	74	2.8	219
11:45:00	31.81	28.05	26.6	75	2.7	219
12:00:00	31.7	28.45	26.87	70	2.7	235
12:15:00	31.43	28.97	26.47	72	2.7	235
12:30:00	32.3	29.9	26.79	70	2.8	235
12:45:00	32.82	29.39	26.95	70	2.2	236
13:00:00	32.78	29.85	26.22	66	2.2	236
13:15:00	32.49	29.4	26.78	67	2.2	237
13:30:00	32.95	30.6	28.72	67	2.1	237
13:45:00	32.18	30.32	28.82	65	2.2	236
14:00:00	32.09	30.13	28.1	66	3.8	222
14:15:00	32.61	30.09	28.11	66	3.8	221
14:30:00	31.51	29.51	28.74	66	3.7	221
14:45:00	31.36	29.18	28.43	67	3.8	222
15:00:00	31.34	29.93	28.44	79	3.1	192
15:15:00	31.95	29.86	28.58	79	3.1	192
15:30:00	30.7	29.15	28.59	84	3.1	193
15:45:00	30.73	29.33	28.99	84	3.1	192
16:00:00	30.41	29.2	28.8	79	3.1	149
16:15:00	30.93	29.18	28.1	78	3.1	149
16:30:00	30.4	29.53	29.28	79	3.2	148
16:45:00	30.3	30.39	29.08	79	3.3	149
17:00:00	29.75	30.1	29.82	94	1.3	96
17:15:00	29.21	30.63	29.21	94	1.3	97
17:30:00	29.39	30.9	30	94	1.3	97
17:45:00	29.59	28.33	30.02	94	1.3	96
18:00:00	29.85	27.62	30.4	94	3.1	36
18:15:00	29.4	27	30.84	93	3.1	36
18:30:00	27.61	27.19	30.4	94	3.2	35
18:45:00	27.6	27.1	30.34	94	3.1	33
19:00:00	27.45	27.28	30.6	93	2.2	
19:15:00	27.48	27.9	30.22	94	2.2	
19:30:00	27.77	28.03	28.24	94	2.2	
19:45:00	27.21	28.38	28.82	94	2.2	
20:00:00	27.52	28.1	28.95	90	1.3	
20:15:00	27.07	28.71	28.83	90	1.3	
20:30:00	27.2	28.59	28.45	90	1.3	
20:45:00	27.06	28.59	28.54	94	1.1	
21:00:00	27.22	28.13	28.12	93	2.2	
21:15:00	27.47	28.39	28.36	93	2.2	
21:30:00	25.31	26.35	26.43	93	2.2	
21:45:00	25.97	26.14	26.27	94	2.3	
22:00:00	25.61	26.95	26.07	94	1.3	
22:15:00	25.28	26.63	26.8	92	1.3	
22:30:00	25.93	26.45	26.58	94	1.3	
22:45:00	25.87	26.24	26.39	94	1.2	
23:00:00	25.69	26.05	26.23	94	0.9	
23:15:00	25.45	26.84	26.04	94	0.9	
23:30:00	25.52	25.75	25.96	93	0.8	
23:45:00	25.47	25.72	25.89	93	0.9	
00:00:00	25.52	25.68	25.81	94	0.9	
00:15:00	25.46	25.7	25.85	94	0.6	
00:30:00	25.46	25.63	25.78	94	0.7	
00:45:00	25.53	25.61	25.76	94	0.9	
01:00:00	25.38	25.59	25.4	97	0	
01:15:00	25.27	25.48	25.62	98	0	
01:30:00	25.17	25.44	25.5	98	0	
01:45:00	25.15	25.4	25.44	97	0	
02:00:00	27.1	25.32	25.41	97	0	
02:15:00	25.13	25.5	25.38	94	0	
02:30:00	26.05	26.21	25.34	94	0	
02:45:00	26.04	26.18	25.33	94	0	
03:00:00	26.05	26.17	25.2	100	0	
03:15:00	26.01	26.27	25.24	100	0	
03:30:00	26.13	26.15	25.23	99	0	
03:45:00	26.11	26.18	25.43	100	0	
04:00:00	26.3	26.16	25.5	97	0.9	
04:15:00	26.04	26.4	25.19	97	0.9	
04:30:00	26.08	25.17	25.19	97	0.8	
04:45:00	26.08	25.11	25.15	98	0.8	
05:00:00	26.92	25.09	25.06	94	0.9	
05:15:00	26.94	25.05	25.96	90	0.5	
05:30:00	26.8	26.72	25.1	94	0.5	

B4 Experimental Temperatures for $BaSO_4$ and MPEA in Afikpo on 10-13/08/22022

Time	T_amb	T_BaSO4	T_mpea	Rel. Hum	V_Wind	Solar Rad.
06:00:00	25.87	26.77	26.43	94	0	
06:15:00	25.87	26.55	26.31	94	0	
06:30:00	25.44	26.92	26.91	94	0	
06:45:00	25.38	26.71	26.62	94	0	
07:00:00	25.31	26.66	26.54	94	0	26
07:15:00	25.43	26.69	26.55	93	0	26
07:30:00	25.13	26	26.8	93	0	26
07:45:00	25.66	26.98	26.64	93	0	26
08:00:00	25	26.41	26.79	94	0	178
08:15:00	25.92	26.33	26.36	96	0	178
08:30:00	26.89	26.33	26.8	95	0	179
08:45:00	26.73	26.09	26.74	96	0	18
09:00:00	26.5	26.25	26.1	89	0.9	320
09:15:00	26.07	26.53	26.34	89	0.8	321
09:30:00	26.74	26.63	25.94	90	0.8	321
09:45:00	26.44	26.98	25.08	89	0.9	321
10:00:00	26.18	26.94	25.76	89	0.5	503
10:15:00	26.08	26.08	25.33	89	0.3	503
10:30:00	27.02	26.53	25.7	90	0.4	503
10:45:00	27.96	26.6	25.21	90	0.7	503
11:00:00	27.19	26.1	25	90	2.2	666
11:15:00	27.7	26.82	25.97	94	2.2	667
11:30:00	27.63	26.23	25.4	95	2.2	668
11:45:00	27.61	26.52	25.49	89	2.1	667
12:00:00	27.87	26.03	25.81	84	2.3	649
12:15:00	27.55	26.87	25.5	84	2.2	649
12:30:00	27.36	26.73	25.08	84	2.3	649
12:45:00	27.03	26.92	25.2	84	2.1	648
13:00:00	27.53	26.97	25.45	84	2.4	567
13:15:00	27.07	26.37	25.7	84	2.1	567
13:30:00	28.03	27.03	25.03	83	2.1	567
13:45:00	28.03	27.47	25.71	83	2.2	566
14:00:00	28.76	27.42	25.81	81	2.2	644
14:15:00	28.5	27.42	25.97	81	2.2	644
14:30:00	27.49	27.79	26.58	84	2.1	644
14:45:00	27.16	27.55	26.57	84	2.1	645
15:00:00	27.94	27.11	25.12	84	2.3	614
15:15:00	27.53	27.77	25.66	84	2.2	614
15:30:00	27.89	27.39	26.5	84	2.2	613
15:45:00	27.38	27.08	26.33	84	2.2	614
16:00:00	27.49	27.91	26.12	84	4	230
16:15:00	27.25	27.76	26.5	87	3.6	230
16:30:00	27.77	27.53	27.29	87	3.9	230
16:45:00	27.17	27.21	27.1	87	3.7	231
17:00:00	27.56	27.66	27.68	89	3.8	103
17:15:00	27.22	27.29	27.28	89	3.9	103
17:30:00	26.9	27.98	27.94	89	4	103
17:45:00	26.63	27.72	27.73	88	4	103
18:00:00	26.27	27.48	27.47	89	3.1	44
18:15:00	26.09	27.17	27.12	90	3.1	44
18:30:00	26.87	27.89	27.68	89	3.1	44
18:45:00	26.63	27.74	27.69	89	3.2	43
19:00:00	26.51	27.58	27.44	89	2.1	
19:15:00	26.47	27.48	27.33	87	2.1	
19:30:00	25.44	26.44	27.27	87	2.1	
19:45:00	25.42	26.31	26.96	87	2.2	
20:00:00	25.35	26.28	25.75	94	2.2	
20:15:00	25.36	26.17	25.65	94	2.2	
20:30:00	25.34	26.17	24.58	94	2.2	
20:45:00	25.25	25.13	24.58	93	2.4	
21:00:00	25.29	25.1	24.5	94	0	
21:15:00	25.27	25.12	24.57	94	0	
21:30:00	25.3	25.13	24.56	94	0	
21:45:00	25.38	25.13	24.6	95	0	
22:00:00	25.38	25.23	24.7	94	0	
22:15:00	25.4	25.33	24.82	94	0	
22:30:00	25.38	25.32	24.82	94	0	
22:45:00	25.34	25.31	24.81	94	0	
23:00:00	25.38	25.27	24.74	94	0	
23:15:00	25.46	25.32	24.8	93	0	
23:30:00	25.41	25.36	24.87	93	0	
23:45:00	25.45	25.36	24.82	93	0	
00:00:00	25.5	25.31	24.85	94	0	
00:15:00	25.46	25.37	24.92	97	0	
00:30:00	24.35	24.33	24.81	97	0	
00:45:00	24.29	24.25	24.74	97	0	
01:00:00	24.36	24.25	24.7	94	0	
01:15:00	24.41	24.26	24.74	97	0	
01:30:00	24.5	24.35	24.75	94	0	
01:45:00	24.34	24.3	24.84	94	0	
02:00:00	24.24	24.33	24.83	94	0	
02:15:00	24.3	24.29	24.82	93	0	
02:30:00	24.23	24.24	24.83	90	0	
02:45:00	24.28	24.21	24.8	90	0	
03:00:00	24.19	24.2	24.76	100	0	
03:15:00	24.08	24.11	24.69	100	0	
03:30:00	25.02	25.04	24.67	100	0	
03:45:00	25.7	25.03	24.63	100	0	
04:00:00	25.05	25.03	24.58	100	0	
04:15:00	25.86	25.97	24.52	100	0	
04:30:00	25.86	25.85	25.39	99	0	
04:45:00	25.9	25.84	25.32	99	0	
05:00:00	25.92	25.91	25.32	94	0	
05:15:00	25.84	25.81	25.32	94	0	
05:30:00	24.92	24.84	24.3	94	0	
05:45:00	24.96	24.89	25.31	94	0	
06:00:00	24.01	24	25.38	94	0	

06:00:00	24.01	24	25.38	94	0	
06:15:00	24.01	24.98	25.41	92	0	
06:30:00	24.99	24.95	24.44	92	0	
06:45:00	24.04	24.96	24.35	93	0	
07:00:00	24.15	24.1	25.42	100	0	26
07:15:00	24.17	24.09	25.51	100	0	26
07:30:00	24.63	24.12	25.53	99	0	26
07:45:00	24.12	24.47	25.02	99	0	27
08:00:00	24.29	24.26	25.85	94	0	87
08:15:00	24.63	24.55	25.98	94	0	87
08:30:00	25.92	24.81	25.08	94	0	87
08:45:00	25.3	24.24	25.12	94	0	87
09:00:00	25.24	24.93	25.4	94	2.1	141
09:15:00	25.87	24.53	25.74	94	2.1	141
09:30:00	25.95	24.27	24.36	94	2.2	142
09:45:00	25.94	24.53	24.39	92	0.2	142
10:00:00	25.8	24.14	24.84	91	2.2	275
10:15:00	25.98	24.66	24.58	91	2.3	275
10:30:00	27.01	26.82	25.61	90	2.3	275
10:45:00	27.29	26.11	25.74	90	2.3	276
11:00:00	27.15	26.41	25.83	84	2.3	282
11:15:00	27.03	26.04	25.69	84	2.2	282
11:30:00	27.34	26.19	25.76	84	2.2	282
11:45:00	27.23	26.59	25.98	83	2.2	283
12:00:00	27.21	26.09	25.18	83	1.3	595
12:15:00	27.07	26.08	25.68	84	1.3	595
12:30:00	27.21	25.45	25.29	84	1.2	598
12:45:00	27.3	25.01	25.76	84	1.1	595
13:00:00	27.49	25.93	25.65	89	1.3	639
13:15:00	27.2	25.73	25.79	89	1.3	639
13:30:00	27.31	25.81	25	89	1.4	638
13:45:00	27.13	25.3	25.67	89	1.3	639
14:00:00	27.23	25.85	25.14	90	2.2	655
14:15:00	27.34	25.38	25.03	90	2.2	655
14:30:00	26.36	25.59	25.53	90	2.2	655
14:45:00	26.88	25.51	25.43	87	2.1	656
15:00:00	26.55	25.39	25.75	94	2.2	599
15:15:00	26.32	25.36	25.8	94	2.2	599
15:30:00	26.03	25.96	25.23	94	2.2	589
15:45:00	26.03	25.47	25.6	94	2.3	589
16:00:00	26.26	25.16	25.21	94	1.3	491
16:15:00	26.23	25.95	25.88	91	1.3	491
16:30:00	25.14	25.85	25.74	91	1.2	490
16:45:00	25.24	25.87	25.74	90	1.3	490
17:00:00	25.24	25.85	25.74	94	2.2	261
17:15:00	25.02	25.87	25.67	93	2.2	261
17:30:00	25.77	25.7	25.44	93	2.2	261
17:45:00	25.38	25.43	25.24	93	2.1	260
18:00:00	25.18	25.2	25.01	84	2.1	69
18:15:00	25.93	25.12	25.73	84	2.1	69
18:30:00	25.79	25.65	25.7	84	2.2	68
18:45:00	25.61	25.78	25.55	84	2.2	68
19:00:00	25.38	25.6	25.39	84	2.3	
19:15:00	25.16	25.33	25.24	87	2.3	
19:30:00	25.28	25.37	25.06	87	2.3	
19:45:00	25.17	25.31	25.99	87	2.2	
20:00:00	25.09	25.28	25.8	94	2.1	
20:15:00	25.87	25.17	25.7	94	2.1	
20:30:00	25.81	26.11	25.53	94	2.2	
20:45:00	25.76	26.07	25.57	93	2.3	
21:00:00	25.79	26.16	25.54	94	0.9	
21:15:00	25.69	26.03	25.56	93	0.9	
21:30:00	25.7	25.89	25.48	93	0.8	
21:45:00	25.66	25.93	25.44	93	0.8	
22:00:00	25.61	25.91	25.44	94	0	
22:15:00	25.57	25.92	25.44	94	0	
22:30:00	25.44	25.83	25.39	94	0	
22:45:00	25.33	25.74	25.36	94	0	
23:00:00	25.16	25.64	25.24	100	0	
23:15:00	25.09	25.56	25.16	100	0	
23:30:00	24.06	24.55	24.09	100	0	
23:45:00	24.07	24.45	24.04	99	0	
00:00:00	24.99	24.39	24.03	100	0	
00:15:00	24.04	24.37	24.15	99	0	
00:30:00	24.99	24.35	24.6	99	0	
00:45:00	24.02	24.32	24.04	100	0	
01:00:00	24.93	24.34	24.06	100	0	
01:15:00	24.1	24.31	24.04	100	0	
01:30:00	24	25.21	25.1	100	0	
01:45:00	24.96	25.26	25.01	99	0	
02:00:00	24.87	25.23	25.02	97	0	
02:15:00	24.89	25.17	25.09	97	0	
02:30:00	24.98	25.15	25.03	97	0	
02:45:00	24.9	25.17	25.05	99	0	
03:00:00	24.9	25.2	25.06	94	0	
03:15:00	24.76	25.15	25.06	94	0	
03:30:00	24.01	24.08	24.12	94	0	
03:45:00	24.09	24.05	24.11	93	0	
04:00:00	24.91	24.09	24.18	100	0	
04:15:00	24.93	24.96	24.2	100	0	
04:30:00	25	24.93	25.21	100	0	
04:45:00	25.01	24.94	25.23	99	0	
05:00:00	25.96	24.96	25.2	94	0	
05:15:00	25.93	24.94	25.18	94	0	
05:30:00	25.95	25.92	25.2	94	0	
05:45:00	25.94	25.93	25.19	93	0	
06:00:00	25.94	25.91	25.19	94	0	

06:00:00	25.94	25.91	25.19	94	0	
06:15:00	25.91	25.92	25.13	93	0	
06:30:00	25.97	25.28	25.88	94	0	
06:45:00	25.63	25.05	25.69	94	0	
07:00:00	25.1	25.48	24.82	94	0	50
07:15:00	25.02	26.05	24.59	81	0	50
07:30:00	26.63	26.92	24.04	90	0	49
07:45:00	26.63	26.23	24.56	90	0	49
08:00:00	26.07	26.48	24.06	94	0	180
08:15:00	26.9	26.02	24.28	94	0	181
08:30:00	26.81	26.32	24.49	94	0	183
08:45:00	26.42	26.8	24.43	94	0	186
09:00:00	26.92	26.22	24.66	89	0	161
09:15:00	26.37	26.25	24.27	87	0	161
09:30:00	26.05	25.29	24.75	87	0	161
09:45:00	26.94	25.9	24.73	87	0	162
10:00:00	26.9	25.72	24.18	89	0	178
10:15:00	26.75	25.22	24.49	89	0	178
10:30:00	27.9	26.31	24.06	89	0	178
10:45:00	27.7	26.98	24.06	90	0	179
11:00:00	27.32	26.84	24.98	84	0	209
11:15:00	27.61	26.58	24.44	84	0	209
11:30:00	27.85	26.83	25.14	84	0	210
11:45:00	27.92	26.43	25.65	84	0	209
12:00:00	27.59	26.4	25.42	94	1.3	227
12:15:00	27.5	26.4	25.74	94	1.3	227
12:30:00	28.69	26.82	25	94	1.3	228
12:45:00	28.05	26.95	25.97	94	1.2	227
13:00:00	28.09	26.06	25.07	94	1.3	229
13:15:00	28.75	26.99	25.01	90	1.3	229
13:30:00	28.96	27.88	26.89	90	1.2	229
13:45:00	28.36	27.1	26.03	90	1.1	229
14:00:00	28.72	27.4	26.33	94	2.2	215
14:15:00	28.24	27.73	26.64	94	2.2	215
14:30:00	29.38	27.15	26.01	94	2.2	216
14:45:00	29.21	27.18	26.22	93	2.2	212
15:00:00	29.19	27.85	26.95	94	3.1	187
15:15:00	29.35	27.49	26.59	94	3.1	187
15:30:00	29.07	27.17	26.27	94	3.1	187
15:45:00	29.33	27.22	26.48	94	3.1	178
16:00:00	28.63	27.81	26.59	94	3.1	146
16:15:00	28.75	27.98	26.78	93	3.2	146
16:30:00	28.3	27.61	27.38	93	3.2	138
16:45:00	28.19	27.88	27.99	93	3	138
17:00:00	28.97	27.96	27.12	89	2.8	96
17:15:00	28.19	27.27	27.4	90	2.8	95
17:30:00	28	27.8	27.91	89	2.9	95
17:45:00	28.34	27.61	27.68	89	2.9	91
18:00:00	28.58	27.89	27.07	94	2.2	39
18:15:00	27.89	27.06	27.37	94	2.2	39
18:30:00	27.8	27.55	27.83	94	2.2	34
18:45:00	27.73	27.17	27.47	94	2.2	33
19:00:00	27.57	27.21	27.2	94	1.3	
19:15:00	26.75	27.45	26.46	96	1.3	
19:30:00	26.11	27.77	26.72	95	1.1	
19:45:00	26.05	27.77	26.61	95	1.3	
20:00:00	26.22	27.69	26.51	94	1.3	
20:15:00	26.93	27.69	26.65	97	1.3	
20:30:00	26.58	27.31	26.39	95	1.3	
20:45:00	26.38	26.98	26.04	95	1.2	
21:00:00	26.13	26.8	26.87	100	0	
21:15:00	26.02	26.61	26.83	100	0	
21:30:00	26.95	26.58	26.76	100	0	
21:45:00	26.85	26.61	26.79	99	0	
22:00:00	26.79	26.54	26.78	94	0	
22:15:00	25.76	25.42	25.68	94	0	
22:30:00	25.71	25.33	25.65	94	0	
22:45:00	25.68	25.33	25.6	93	0	
23:00:00	25.69	25.28	25.59	100	0	
23:15:00	25.61	25.26	25.58	99	0	
23:30:00	25.57	25.21	25.56	99	0	
23:45:00	25.53	25.09	25.53	97	0	
00:00:00	25.5	25.03	25.48	100	0	
00:15:00	25.43	25.94	25.43	98	0	
00:30:00	25.44	25.9	25.34	98	0	
00:45:00	25.35	25.91	25.32	97	0	
01:00:00	25.39	25.85	25.35	100	0	
01:15:00	25.32	25.81	25.28	100	0	
01:30:00	24.31	23.81	25.27	100	0	
01:45:00	24.3	23.72	25.24	100	0	
02:00:00	24.28	23.73	25.27	100	0	
02:15:00	24.22	23.69	25.27	100	0	
02:30:00	24.19	24.69	24.25	100	0	
02:45:00	24.13	24.6	24.23	100	0	
03:00:00	24.14	24.55	24.2	97	0	
03:15:00	24.14	24.49	24.17	97	0	
03:30:00	25.11	24.49	24.14	97	0	
03:45:00	25.14	24.49	24.13	95	0	
04:00:00	25.1	24.51	24.13	97	0	
04:15:00	25.04	24.4	24.07	96	0	
04:30:00	25.08	24.35	24.07	96	0	
04:45:00	25.16	24.43	24.1	96	0	
05:00:00	25.14	24.4	24.13	100	0	
05:15:00	25.18	24.44	24.16	100	0.5	
05:30:00	25.2	24.48	24.21	100	0.5	
05:45:00	25.19	24.49	24.22	100	0.6	
06:00:00	25.22	24.48	24.12	94	0.6	

B5 Experimental Temperatures for $BaSO_4$ and MPEA in Owerri on 12-15/07/22022

TIME	Tamb	Tbs	Tmpea	Rel. Hum	V_wind	Solar Rad
06:00	25.42	25.23	25.52	94	0	
06:15	25.23	24.74	25.05	94	0	
06:30	24.8	24.31	24.58	94	0	
06:45	25.03	24.23	24.38	93	0	
07:00	25.2	24.35	24.39	100	0	26
07:15	25.89	24.52	24.47	100	0	26
07:30	25.27	25.11	24.8	99	0	26
07:45	25.05	26.18	25.47	100	0	28
08:00	25.43	25.55	24.27	94	0	128
08:15	25.66	25.32	24.26	94	0	128
08:30	25.28	25.31	24.5	94	0	129
08:45	25.84	25.16	24.36	93	0	128
09:00	26.12	25.35	24.54	94	3.8	134
09:15	26.72	25.26	24.23	93	3.8	134
09:30	25.72	25.85	24.83	93	3.8	134
09:45	25.33	25.37	24.57	94	3.8	135
10:00	26.23	25.86	24.8	94	2.7	178
10:15	26.39	25.38	24.16	93	2.7	178
10:30	26.3	25.68	24.84	93	2.6	179
10:45	26.99	25.2	24.18	93	2.7	178
11:00	28.78	26.18	24.18	94	1.3	209
11:15	28.61	26.47	24.93	90	1.3	209
11:30	28.1	26.25	24.55	90	1.3	210
11:45	28.17	26.26	24.28	90	1.3	209
12:00	29.07	27.42	25.85	94	3.1	227
12:15	29.86	27.66	25.77	89	3.1	227
12:30	29.1	27.54	25.25	90	3.1	227
12:45	29.91	27.34	25.68	90	3.1	228
13:00	29.83	27.96	27.53	94	2.7	229
13:15	29.9	27.3	27.2	94	2.7	229
13:30	29.41	27.08	27.36	94	2.7	230
13:45	29.38	28.84	27.57	94	2.8	229
14:00	30.39	29.12	28.22	89	2.2	215
14:15	30.4	29.46	28.49	89	2.2	215
14:30	30.26	29.17	28.88	89	2.2	215
14:45	30.26	29.97	28.88	90	2.2	219
15:00	30.77	29.25	26.67	89	2.2	187
15:15	30.7	29.58	26.22	87	2.3	187
15:30	30.48	29.4	26.28	87	2.3	187
15:45	30.42	29.9	26.94	88	2.1	187
16:00	29.87	29.54	26.28	79	2.1	147
16:15	29.24	29.21	26.13	79	2.1	147
16:30	29.55	29.02	26.52	79	2.2	147
16:45	29.59	29.84	26.55	81	2.2	148
17:00	28.71	29.1	26.95	79	2.6	96
17:15	28.93	29.56	26.07	79	2.6	96
17:30	28.96	29.9	26.14	79	2.6	97
17:45	28.14	29.34	26.5	83	2.7	96
18:00	28.64	29.67	27.96	79	2.5	39
18:15	28.94	29.86	27.18	79	2.5	39
18:30	28.31	29.09	27.9	79	2.7	38
18:45	28.76	29.46	27.12	82	2.7	39
19:00	28.13	29.33	28.45	79	2.2	
19:15	28.81	29.1	28.01	82	2.2	
19:30	28.72	29.04	27.71	82	2.2	
19:45	28.23	29.17	27.36	82	2.2	
20:00	27.03	28.45	25.85	79	2.2	
20:15	27.58	28.02	25.1	79	2.1	
20:30	27.51	28.14	24.79	79	2.1	
20:45	27.17	28.2	24.54	79	2.1	
21:00	27.04	26.95	24.32	89	1.3	
21:15	27.25	26.74	24.24	89	1.3	
21:30	27.64	26.66	24.7	89	1.3	
21:45	27.71	26.26	25.24	89	1.5	
22:00	26.44	26.2	25.26	94	0.9	
22:15	26.34	26.61	25.8	94	0.9	
22:30	26.06	26.22	25.04	94	0.7	
22:45	26.63	26.88	25.59	93	0.8	
23:00	26.8	26.06	24.83	94	0	
23:15	26.87	26.13	24.97	94	0	
23:30	26.85	26.18	24.01	94	0	
23:45	26.86	26.03	24.96	94	0	
00:00	25.84	26.06	25.15	94	0	
00:15	25.75	26.97	25.86	93	0	
00:30	25.85	26.94	25.88	93	0	
00:45	25.78	26.86	25.37	93	0	
01:00	25.67	24.88	24.7	100	0	
01:15	25.7	24.78	24.8	100	0	
01:30	25.6	24.76	24.78	100	0	
01:45	25.57	24.68	24.7	100	0	
02:00	25.54	24.52	24.42	94	0	
02:15	25.33	25.43	24.5	94	0	
02:30	25.44	25.27	24.41	94	0	
02:45	25.24	25.18	24.43	94	0	
03:00	26.31	25.21	24.21	94	0	
03:15	26.31	25.09	25.41	92	0	
03:30	26.24	25.07	25.36	92	0	
03:45	26.25	25.05	25.26	92	0	
04:00	26.17	25.04	25.25	98	0	
04:15	26.15	25.97	25.15	98	0	
04:30	26.17	25.94	25.11	97	0	
04:45	26.08	25.77	25.01	97	0	
05:00	26.71	25.7	24.94	98	0	
05:15	26.53	25.74	24.3	95	0	
05:30	26.52	25.23	24.67	95	0	
05:45	26.76	25.97	25.6	97	0	
06:00	26.69	26.18	25.98	98	0	

06:00	26.69	26.18	25.98	98	0	
06:15	26.21	26.75	25.43	97	0	
06:30	26.37	26.07	25.65	97	0	
06:45	26.51	26.07	25.61	98	0	
07:00	25.55	26.66	23.76	100	0	26
07:15	25.57	26.9	23.24	100	0	26
07:30	25.29	26.18	23.37	100	0	26
07:45	25.78	26.91	23.91	99	0	27
08:00	25.37	26.14	23.6	79	0	201
08:15	25.02	26.93	23.61	79	0	201
08:30	25.48	26	23.48	81	0	202
08:45	25.74	26.68	23.25	81	0	201
09:00	26.72	24.78	23.33	79	2.7	222
09:15	26.34	24.12	23.63	79	2.7	222
09:30	26.58	24.76	23.31	79	2.7	222
09:45	26.19	24.01	23.84	79	2.6	223
10:00	26.59	25	24.73	74	2.2	178
10:15	26.88	25.52	24.88	74	2.2	178
10:30	26.27	25.14	24.71	74	2.3	178
10:45	26.69	25.47	24.31	74	2.2	179
11:00	27.42	25.02	24.29	79	1.3	209
11:15	27.53	25.15	24.13	79	1.3	209
11:30	29.21	25.98	24.36	79	1.3	210
11:45	29.19	25.96	24.5	79	1.4	209
12:00	29.13	27.67	26.83	84	1.8	531
12:15	29.83	28.09	26.69	84	1.7	531
12:30	29.87	28.13	26.88	84	1.8	531
12:45	29.74	28.17	26.78	84	1.8	533
13:00	29.29	27.5	25.03	84	1.3	252
13:15	29.99	27.12	25.03	83	1.5	252
13:30	29.44	27.27	25.29	83	1.3	252
13:45	29.33	27.56	25.33	83	1.4	255
14:00	30.38	27.03	25.45	86	1.8	258
14:15	30.33	27.4	25.63	86	1.8	258
14:30	30.67	27.89	25.91	86	1.9	258
14:45	30.95	27.23	25.84	86	1.7	259
15:00	30.8	28.48	25.92	74	1.3	187
15:15	30.12	28.41	25.51	74	1.3	187
15:30	30.88	28.23	25.54	74	1.3	187
15:45	30.1	28.32	25.82	74	1.3	186
16:00	30.59	28.03	26.89	84	5.4	279
16:15	30.64	28.25	26.13	83	5.4	279
16:30	30.83	28.71	26.83	84	5.1	279
16:45	30.69	28.24	26.99	84	5.1	278
17:00	28.79	28.23	26.17	79	4	151
17:15	28.4	28.15	26.54	79	4.1	151
17:30	28.79	28.43	26.22	79	4.1	152
17:45	28.09	28.31	26.39	79	4	151
18:00	28.48	28.78	28.04	84	3.1	47
18:15	28.89	28.96	28.31	84	3.1	47
18:30	28.51	28.5	28.85	84	3.2	47
18:45	28.06	28.1	28.45	82	3.3	46
19:00	28.44	28.5	28.03	84	2.2	
19:15	28.17	28.22	28.03	82	2.2	
19:30	28.61	28.21	28.73	82	2.2	
19:45	27.54	26.29	27.81	84	2.2	
20:00	27.65	26.03	27.62	89	1.3	
20:15	27.26	26.01	27.57	89	1.2	
20:30	27.04	25.76	27.35	89	1.3	
20:45	26.34	25.27	26.03	89	1.3	
21:00	26.12	24.92	26.83	79	3.1	
21:15	26.7	24.92	26.65	79	3.1	
21:30	26.22	26.13	26.38	79	3.1	
21:45	26.59	26.64	26.82	79	3.1	
22:00	26.7	26.87	26.05	79	2.2	
22:15	26.74	26.87	26.87	81	2.3	
22:30	26.77	26.72	26.72	81	2.2	
22:45	26.78	26.67	26.97	81	2.2	
23:00	26.66	26.6	26.96	94	1.3	
23:15	26.63	26.63	26.93	94	1.3	
23:30	26.71	26.57	26.21	94	1.3	
23:45	26.7	26.47	26.86	94	1.1	
00:00	26.68	26.35	26.86	100	0	
00:15	25.73	26.28	26.79	100	0	
00:30	25.72	25.93	26.75	100	0	
00:45	25.69	25.7	26.6	99	0	
01:00	25.73	25.5	26.49	94	0	
01:15	25.69	25.4	25.48	94	0	
01:30	25.62	25.4	25.5	94	0	
01:45	25.56	25.29	25.46	94	0	
02:00	25.48	25.25	25.46	93	0	
02:15	25.47	25.24	25.41	93	0	
02:30	25.44	25.21	25.31	93	0	
02:45	25.35	25.27	25.35	94	0	
03:00	25.34	25.17	25.29	94	0	
03:15	25.47	25.12	25.23	94	0	
03:30	25.25	25.03	25.21	94	0	
03:45	25.29	25.1	25.24	93	0	
04:00	25.21	25.18	25.35	98	0	
04:15	25.3	25.14	25.29	97	0	
04:30	25.9	25.18	25.29	97	0	
04:45	25.28	25.25	25.27	96	0	
05:00	25.1	25.28	25.28	94	0	
05:15	25.23	25.3	25.26	94	0	
05:30	25.34	25.3	25.33	94	0	
05:45	25.22	25.25	25.34	94	0	
06:00	25.2	25.32	25.34	94	0	

06:00	25.2	25.32	25.34	94	0	
06:15	25.14	25.23	26.25	93	0	
06:30	25.11	25.14	26.22	93	0	
06:45	25.07	25.04	26.19	95	0	
07:00	25.4	25.03	26.16	100	0	23
07:15	24.08	25.12	26.21	100	0	23
07:30	24.33	25.05	26.27	100	0	23
07:45	24.81	25.07	26.44	100	0	25
08:00	24.96	25.35	26.6	94	3.6	81
08:15	24.6	26.44	25.79	94	3.6	81
08:30	24.89	26.39	25.6	94	3.5	81
08:45	24.77	26.37	25.51	94	3.5	83
09:00	24.65	26.4	25.41	94	2.7	308
09:15	25.8	26.53	25.56	93	2.7	308
09:30	25.75	26.73	25.66	93	2.6	309
09:45	25.49	27.03	25.74	93	2.6	308
10:00	25.31	27.76	25.32	94	1.3	178
10:15	26.68	27.61	24.82	93	1.3	178
10:30	26.51	27.65	24.59	93	1.3	178
10:45	26.06	27.48	24.36	94	1.2	179
11:00	26.78	27.72	24.91	84	3.1	209
11:15	26.83	27.1	24.19	84	3.1	209
11:30	26.2	27.15	24.52	84	3.1	209
11:45	26.26	27.4	24.73	84	3.2	210
12:00	26.69	27.78	24.84	89	2.2	227
12:15	26.95	25.95	23.95	89	2.2	227
12:30	26.59	25.97	23.18	89	2.2	227
12:45	26.47	25.49	23.63	89	2.1	227
13:00	26.67	25.73	23.67	89	2.2	318
13:15	26.22	25.51	23.34	87	2.2	318
13:30	26.57	25.26	23.09	87	2.3	318
13:45	26.32	25.3	23.14	87	2.3	319
14:00	26.82	25.33	23.65	89	2.7	237
14:15	26.63	25.48	25.12	87	2.7	237
14:30	26.55	25.54	25.45	87	2.6	237
14:45	26.67	25.79	25.68	87	2.6	238
15:00	26.81	25.23	25.87	79	2.7	188
15:15	28.02	26.02	25.63	79	2.7	188
15:30	28.02	26.01	25.81	79	2.6	187
15:45	28.24	26.22	25.54	79	2.7	187
16:00	28.25	26.25	25.16	79	3.6	147
16:15	28.09	26.95	25.03	78	3.6	147
16:30	28.2	26.92	25.03	78	3.6	145
16:45	27.65	26.12	25.32	78	3.7	145
17:00	27.47	26.27	25.41	79	3.1	142
17:15	25.95	26.26	25.9	78	3.1	142
17:30	25.28	26.28	25.51	77	3.1	142
17:45	25.54	26.63	25.94	77	3.2	142
18:00	25.9	26.41	25.57	79	3.2	112
18:15	25.42	26.42	25.91	79	3.2	112
18:30	25.41	26.23	25.91	79	3.1	112
18:45	25.3	26.23	25.61	79	3.1	110
19:00	25.92	26.25	25.78	79	2.7	
19:15	25.69	26.41	25.15	76	2.7	
19:30	25.21	26.38	25.16	76	2.7	
19:45	25.11	26.81	25.4	77	2.6	
20:00	25.78	26.59	25.11	89	2.5	
20:15	25.91	26.29	25.77	89	2.5	
20:30	25.79	26.12	25.62	89	2.6	
20:45	25.78	26.98	25.48	89	2.7	
21:00	25.83	26.85	25.35	84	1.3	
21:15	25.55	26.69	26.78	84	1.3	
21:30	25.32	26.64	26.74	84	1.1	
21:45	25.48	26.06	26.15	84	1.2	
22:00	25.22	26.19	26.25	94	0.9	
22:15	25.27	26.01	26.05	94	0.9	
22:30	25.3	26.81	26.8	94	0.8	
22:45	25.27	26.65	26.55	94	0.9	
23:00	25.41	26.59	26.41	94	0	
23:15	25.42	26.49	26.39	93	0	
23:30	25.34	26.47	26.33	93	0	
23:45	25.35	26.48	26.43	93	0	
00:00	25.13	26.44	26.37	100	0	
00:15	24.96	24.1	24.04	100	0	
00:30	24.14	24.7	24.71	99	0	
00:45	24.18	24.48	24.57	100	0	
01:00	24.01	24.64	24.53	94	0	
01:15	25.26	24.46	24.61	94	0	
01:30	25.1	24.4	24.67	93	0	
01:45	25.08	24.39	24.6	94	0	
02:00	25.98	24.39	24.55	94	0	
02:15	25.92	24.33	24.47	93	0	
02:30	25.9	24.35	24.47	93	0	
02:45	25.89	24.27	24.48	93	0	
03:00	25.88	24.28	24.54	90	0	
03:15	24.78	24.12	24.34	90	0	
03:30	24.72	24.1	24.4	90	0	
03:45	24.72	24.06	24.38	90	0	
04:00	24.68	24.9	24.24	90	0	
04:15	24.46	24.95	24.3	89	0	
04:30	24.62	24.82	24.19	89	0	
04:45	24.67	24.89	24.23	89	0	
05:00	24.3	24.95	24.25	94	0	
05:15	24.61	24.9	23.33	93	0	
05:30	24.59	24.75	23.34	93	0	
05:45	24.53	24.78	23.4	93	0	
06:00	24.21	24.63	23.26	94	0	

B6 Experimental Temperatures for $BaSO_4$ and MPEA in Owerri on 14-17/08/2202

TIME	Tamb	Tbs	Tmpea	Rel. Hum	V_speed	Solar Rad
06:00	22.38	22.58	23.4	94	0	
06:15	22.66	22.07	23.53	94	0	
06:30	22.33	22.73	23.48	94	0	
06:45	22.17	22.94	23.76	94	0	
07:00	24.04	24.63	25.41	94	0	38
07:15	24.01	24.45	25.26	93	0	38
07:30	24.09	24.36	25.21	93	0	38
07:45	24.71	24.41	25.26	93	0	38
08:00	25.37	25.2	25.33	89	0	167
08:15	25.42	25.55	25.41	89	0	167
08:30	25.53	25.64	25.45	89	0	167
08:45	25.57	25.65	25.58	89	0	168
09:00	25.15	25.87	25.7	89	0	356
09:15	24.31	25.27	25.98	90	0	356
09:30	24.52	25.4	25.17	90	0	357
09:45	24.82	25.69	25.42	90	0	356
10:00	24.88	25.4	24.73	89	0	661
10:15	24.04	25.4	24.13	89	0	661
10:30	24.46	25.64	24.49	89	0	663
10:45	24.8	25.21	24.01	87	0	663
11:00	24.55	24.21	24.13	89	0	623
11:15	24.9	24.37	24.08	87	0	623
11:30	24.5	24.29	24.37	87	0	623
11:45	24.11	24.24	24.13	89	0	621
12:00	25.31	24.33	24.91	74	0	547
12:15	25.63	24.28	24.73	75	0	547
12:30	25.2	24.38	24.89	75	0	547
12:45	25.34	24.43	24.78	74	0	544
13:00	25.84	24.2	24.69	75	0	289
13:15	25.76	24.32	24.66	75	0	289
13:30	25.47	24.46	24.94	75	0	289
13:45	25.73	24.21	24.25	75	0	287
14:00	25.56	24.85	25.86	74	1.3	280
14:15	25.59	24.14	25.98	74	1.3	280
14:30	25.82	24.55	25.46	74	1.2	280
14:45	25.81	24.25	25.15	74	1.3	278
15:00	25.61	25.12	25.99	66	2.7	440
15:15	25.52	25.92	25.87	66	2.7	440
15:30	25.41	25.85	25.81	66	2.6	441
15:45	25.47	25.83	25.76	67	2.7	441
16:00	25.8	25.89	25.8	68	2.6	486
16:15	25.75	25.02	25.92	66	2.6	486
16:30	25.8	25.37	25.03	66	2.5	487
16:45	25.88	25.71	25.85	67	2.7	484
17:00	26.83	26.38	25.52	79	1.3	272
17:15	26.49	26.07	25.34	79	1.3	272
17:30	26.39	26.84	25.11	79	1.3	273
17:45	26.05	26.58	25.96	79	1.1	272
18:00	26.9	25.94	25.78	79	1.3	86
18:15	26.77	25.04	25.66	81	1.3	86
18:30	26.53	25.92	25.63	81	1.2	87
18:45	26.42	25.74	25.43	81	1.2	86
19:00	25.33	25.8	25.29	84	1.8	
19:15	25.29	25.53	25.19	84	1.8	
19:30	25.18	25.45	25.11	84	1.6	
19:45	25.11	25.42	25.12	83	1.6	
20:00	25.16	25.39	25.04	94	5.4	
20:15	25.08	25.38	25.02	94	5.3	
20:30	26.13	25.37	25.09	94	5.4	
20:45	26.08	25.36	25.08	94	5.4	
21:00	26.88	26.37	25.05	94	2.2	
21:15	26.71	26.22	25.93	95	0.2	
21:30	26.67	26.16	25.81	93	2.2	
21:45	26.65	26.05	25.7	93	2.1	
22:00	26.55	26.99	25.62	94	3.1	
22:15	26.51	26.97	25.6	93	3.1	
22:30	26.3	26.98	25.61	93	3.2	
22:45	26.39	26.88	25.64	94	3.1	
23:00	26.42	26.85	25.61	89	2.2	
23:15	26.4	26.82	25.58	89	2.2	
23:30	26.36	26.8	25.55	89	2.1	
23:45	26.25	26.73	25.56	89	2.1	
00:00	25.2	25.72	25.53	94	0	
00:15	25.14	25.69	25.45	94	0	
00:30	25.15	25.58	25.49	94	0	
00:45	25.08	25.53	25.39	94	0	
01:00	25.04	24.45	25.44	94	0	
01:15	25.05	24.1	25.39	94	0	
01:30	25.05	24.32	25.39	94	0	
01:45	25.02	24.3	25.39	94	0	
02:00	24.94	24.21	25.33	94	0	
02:15	24.83	24.76	25.28	90	0	
02:30	24.79	24.14	25.2	90	0	
02:45	24.82	24.12	25.15	90	0	
03:00	24.75	24.07	25.15	94	0	
03:15	24.8	24	25.16	93	0	
03:30	24.75	24.19	25.13	93	0	
03:45	24.78	24.6	25.11	94	0	
04:00	24.71	24.06	25.1	94	0	
04:15	24.71	24.03	25.13	94	0	
04:30	24.6	24.1	25.01	94	0	
04:45	24.62	24.02	24.99	94	0	
05:00	24.57	24.12	24.95	94	0	
05:15	24.58	24.91	24.95	95	0	
05:30	24.48	24.84	24.92	95	0	
05:45	24.51	24.83	24.87	95	0	
06:00	24.5	24.77	24.91	94	0	

06:00	24.5	24.77	24.91	94	0	
06:15	24.48	24.75	24.87	93	0	
06:30	24.51	23.77	24.86	93	0	
06:45	24.55	23.85	24.96	93	0	
07:00	24.66	23.89	24.97	94	0.9	22
07:15	24.8	24.05	24.05	94	0.9	22
07:30	24.88	24.19	24.12	94	0.8	22
07:45	25.02	24.27	24.22	94	0.9	25
08:00	25.18	24.89	24.08	94	1.3	83
08:15	25.05	25.53	24.85	95	1.3	83
08:30	25.62	25.44	24.94	95	1.2	83
08:45	25.69	25.41	24.85	95	1.3	87
09:00	25.72	24	24.82	94	1.3	138
09:15	25.57	24.79	24.83	94	1.3	138
09:30	25.11	24.03	24.5	94	1.2	138
09:45	25.96	24.8	24.01	94	1.1	139
10:00	26.39	25.76	24.89	94	0.5	220
10:15	26.84	25.72	24.78	93	0.5	220
10:30	26.45	25.28	24.05	93	0.5	221
10:45	26.88	25.59	24.34	95	0.7	221
11:00	28.48	25.9	24.67	94	0.6	280
11:15	28.89	25.9	24.59	95	0.6	280
11:30	28.18	25.58	24.24	95	0.7	280
11:45	28.85	25.26	24.64	95	0.6	281
12:00	30.13	27.99	25.47	84	0.5	234
12:15	30.25	27.34	25.01	83	0.5	234
12:30	30.34	27.95	25.25	83	0.4	234
12:45	30.73	27.22	25.39	83	0.5	235
13:00	30.97	28.52	26.06	84	0.4	235
13:15	30.31	28.18	26.83	84	0.3	235
13:30	30.28	28.23	26.68	84	0.4	237
13:45	30.06	28.38	25.49	84	0.4	235
14:00	30.45	28.03	25.77	84	0.5	562
14:15	30.93	28.97	25.96	83	0.6	562
14:30	30.13	28.6	25.41	83	0.6	562
14:45	30.44	28.52	26.32	83	0.5	563
15:00	31.12	28.87	26.05	84	2.7	531
15:15	31.13	29.04	26.78	86	2.7	531
15:30	31.22	29.54	26.75	86	2.7	533
15:45	31.11	29.2	26.31	86	2.6	531
16:00	31.32	29.65	26.99	74	2.7	514
16:15	31.16	29.66	26.67	74	2.7	514
16:30	31.64	29.52	25.66	74	2.8	515
16:45	31.51	29.28	25.95	74	2.7	514
17:00	30.11	29.51	25.47	84	1.3	358
17:15	30.7	29.31	25.84	84	1.3	358
17:30	30.04	29.47	25.62	84	1.2	358
17:45	30.35	29.64	25.9	84	1.2	359
18:00	30.82	29.07	25.36	84	1.3	135
18:15	30.25	29.07	25.86	83	1.3	135
18:30	30.87	29.21	25.46	83	1.3	135
18:45	29.53	29.78	24.999	83	1.5	133
19:00	28.26	29.31	24.77	84	2.2	
19:15	28.29	29.32	24.63	82	2.2	
19:30	28.35	29.98	24.69	82	2.2	
19:45	28.99	29.25	24.99	84	2.1	
20:00	26.74	28.71	24.52	84	5.4	
20:15	26.79	28.45	24.43	84	5.4	
20:30	26.53	28.42	24.41	83	5.3	
20:45	26.57	28.34	24.85	83	5.5	
21:00	26.01	28.03	24.83	84	2.2	
21:15	26.07	28.01	24.57	84	2.2	
21:30	26.84	28.27	24.89	84	2.2	
21:45	26.2	26.09	24.94	84	2.2	
22:00	25.24	25.1	24.72	89	3.1	
22:15	25.32	25.2	24.83	89	3.1	
22:30	25.65	25.13	24.24	89	3.1	
22:45	25.92	25.57	24.67	89	3.1	
23:00	25.94	25.69	24.8	94	3.1	
23:15	25.93	25.69	24.83	94	3.2	
23:30	25.86	25.66	24.4	94	3.3	
23:45	25.83	25.64	24.82	94	3.1	
00:00	25.73	25.58	24.78	94	0	
00:15	25.65	25.49	24.71	95	0	
00:30	25.73	25.51	24.62	95	0	
00:45	25.68	25.53	24.54	95	0	
01:00	25.51	25.43	24.51	94	0	
01:15	25.41	25.36	24.33	94	0	
01:30	25.4	25.31	25.26	94	0	
01:45	25.36	25.25	25.27	94	0	
02:00	25.34	25.16	25.28	94	0	
02:15	25.32	25.19	25.31	93	0	
02:30	25.35	25.2	25.21	93	0	
02:45	25.34	25.19	25.17	93	0	
03:00	25.43	25.19	25.26	94	0	
03:15	25.49	25.3	25.32	95	0	
03:30	25.5	25.32	25.43	95	0	
03:45	25.42	25.33	25.34	95	0	
04:00	25.41	25.25	25.31	94	0	
04:15	25.41	25.2	25.36	94	0	
04:30	25.29	25.15	25.26	94	0	
04:45	25.41	25.18	25.31	94	0	
05:00	25.54	25.23	25.44	94	0	
05:15	25.53	25.24	25.6	96	0	
05:30	25.65	25.31	25.57	97	0	
05:45	25.6	25.34	25.65	97	0	
06:00	25.59	25.33	25.61	94	0	

06:15	25.56	25.36	25.6	93	0	
06:30	25.51	25.29	25.55	93	0	
06:45	25.57	25.25	25.59	93	0	
07:00	25.52	25.23	25.51	94	1.3	25
07:15	25.44	25.22	25.53	93	1.3	25
07:30	25.56	25.21	25.53	93	1.4	25
07:45	25.69	25.27	25.58	93	1.3	27
08:00	25.92	25.41	25.67	100	1.3	152
08:15	26.04	25.61	25.85	100	1.2	152
08:30	26.07	25.71	25.92	100	1.2	152
08:45	26.38	25.78	26.01	100	1.1	155
09:00	26.57	25.97	26.15	100	1.3	166
09:15	26.67	26.1	26.29	99	1.3	166
09:30	26.86	26.24	26.48	99	1.4	166
09:45	27.83	26.74	26.72	99	1.3	167
10:00	27.81	26.96	26.03	94	1.3	184
10:15	27.83	27.11	26.17	94	1.3	184
10:30	27.29	27.2	26.22	94	1.2	184
10:45	27.34	27.87	26.55	94	1.2	182
11:00	26.4	25.89	25.21	94	1.3	216
11:15	26.58	25.54	25.66	93	1.4	216
11:30	26.58	25.77	25.95	93	1.4	217
11:45	26.85	25.3	25.34	93	1.3	217
12:00	28.78	26.78	25.4	79	1.3	234
12:15	28.05	26.71	25.15	79	1.2	234
12:30	28.73	26.95	26.47	79	1.3	234
12:45	28.15	26.32	26.1	79	1.4	235
13:00	28.11	26.49	27.2	70	1.3	236
13:15	29.17	26.63	27.82	70	1.3	236
13:30	29.42	26.08	27.79	70	1.4	236
13:45	29.98	26.72	27.71	70	1.4	233
14:00	29.54	29.12	28.08	84	1.3	222
14:15	29.57	29.17	28.5	84	1.3	222
14:30	29.12	29.32	28.61	84	1.4	223
14:45	29.39	29.9	29.03	84	1.5	221
15:00	30.29	29.58	29.03	84	1.6	211
15:15	30.31	29.14	29.13	83	1.6	211
15:30	30.6	29.19	29.06	83	1.7	211
15:45	30.59	29.34	29.17	83	1.6	210
16:00	30.43	30.72	28.49	84	1.5	149
16:15	30.21	30.39	28.17	84	1.5	149
16:30	30.64	30.33	28.69	84	1.6	149
16:45	30.22	30.56	28.19	84	1.8	148
17:00	28.21	30.34	28.15	94	3.6	96
17:15	28.82	30.83	28.24	94	3.6	96
17:30	28.82	30.14	28.1	94	3.6	96
17:45	28.49	30.47	28.64	94	3.7	94
18:00	28.11	30.09	28.2	94	3.6	36
18:15	27.78	28.72	27.84	93	3.6	36
18:30	27.49	28.3	27.46	93	3.7	36
18:45	26.62	28.65	27.06	93	3.8	33
19:00	25.93	25.68	26.07	94	3.6	
19:15	25.72	25.26	25.19	94	3.6	
19:30	25.65	25.3	25.59	94	3.8	
19:45	25.64	25.15	25.53	94	3.7	
20:00	25.66	25.22	25.54	94	3.1	
20:15	25.57	25.18	25.51	93	3.1	
20:30	25.67	25.81	25.54	93	3.1	
20:45	25.73	25.23	25.58	93	3.3	
21:00	25.63	25.45	25.67	94	3.6	
21:15	25.72	25.32	25.72	94	3.5	
21:30	25.85	25.4	25.73	94	3.6	
21:45	25.88	25.43	25.83	94	3.6	
22:00	25.89	25.49	25.91	94	2.2	
22:15	25.76	25.59	25.89	89	2.2	
22:30	25.57	25.37	25.78	89	2.2	
22:45	25.66	25.91	25.66	89	2.1	
23:00	25.58	25.3	25.65	94	1.3	
23:15	25.66	25.2	25.7	93	1.3	
23:30	25.55	25.23	25.64	93	1.3	
23:45	25.47	25.11	25.61	93	1.3	
00:00	25.39	25.04	25.47	94	0	
00:15	25.28	24.99	25.44	94	0	
00:30	25.28	24.92	25.4	94	0	
00:45	25.36	24.92	25.38	94	0	
01:00	25.49	24.98	25.41	94	0	
01:15	25.52	25.03	25.48	93	0	
01:30	25.53	25.04	25.53	93	0	
01:45	25.67	25.09	25.53	93	0	
02:00	25.67	25.08	25.63	94	0	
02:15	25.63	25.16	25.59	93	0	
02:30	25.66	25.13	25.6	93	0	
02:45	25.52	25.17	25.6	93	0	
03:00	25.58	25.04	25.6	100	0	
03:15	25.64	25.06	25.69	100	0	
03:30	25.66	25.09	25.69	100	0	
03:45	25.76	25.06	25.78	99	0	
04:00	25.74	25.15	25.77	100	0	
04:15	25.76	25.24	25.75	100	0	
04:30	25.69	25.18	25.82	100	0	
04:45	25.74	25.21	25.74	100	0	
05:00	25.64	25.19	25.67	94	0	
05:15	25.41	25.14	25.63	94	0	
05:30	25.3	25	25.5	94	0	
05:45	25.16	24.83	25.35	94	0	
06:00	25.21	24.82	25.26	94	0.5	
06:15	25.07	24.8	25.23	93	0.5	
06:30	25	24.68	25.16	93	0.5	
06:45	25.03	24.7	25.2	93	0.6	
07:00	26.21	24.79	25.26	94	0.9	
07:15	26.38	24.91	25.38	94	0.9	
07:30	26.59	25.1	25.51	94	0.9	
07:45	26.69	25.24	25.67	94	0.7	
08:00	25.99	25.43	25.84	94	0.9	

Appendix C Numerical Temperatures for $BaSO_4$ and MPEA

C1 Experimental and Numerical Temperatures for $BaSO_4$ and MPEA in Abuja on 19/05/22022

Time	Tamb_Exp	Tbs_Expt	Tmpea_Ex	Tamb_mo	Tmpea_m	Tbs_mode
07:00:00	26.54	26.9	26.19	24.46	23.82	23.85
07:15:00	27.48	27.64	27.74	24.62	23.85	23.88
07:30:00	27.17	26.87	27.11	24.83	23.88	23.94
07:45:00	27.74	27.18	27.62	25.24	23.94	23.97
08:00:00	27.53	27.11	27.74	25.5	24.02	24.07
08:15:00	27.79	27.91	27.09	25.88	24.1	24.11
08:30:00	27.78	27.56	27.98	26.08	24.12	24.16
08:45:00	27.48	27.54	27.83	26.7	24.25	24.26
09:00:00	29.55	26.49	25.66	26.83	24.39	24.31
09:15:00	29.98	26.64	27.27	27.35	24.5	24.52
09:30:00	29.35	26.51	27.02	27.48	24.63	24.71
09:45:00	29.72	26.02	27.09	27.78	24.78	24.84
10:00:00	29.86	26.88	27.86	28.24	24.93	25.07
10:15:00	29.39	26.38	27.83	28.43	25.14	25.33
10:30:00	29.86	26.57	27.28	28.65	25.26	25.48
10:45:00	29.32	26.58	27.76	28.89	25.42	25.68
11:00:00	30.43	27.43	26.38	29.29	25.64	25.94
11:15:00	30.53	27.63	26.34	29.54	25.79	26.21
11:30:00	30.98	27.79	26.27	29.91	26.06	26.44
11:45:00	30.68	27.62	26.48	29.98	26.19	26.58
12:00:00	31.76	27.58	27.25	30.5	26.49	26.96
12:15:00	31.81	27.88	27.81	30.61	26.6	27.12
12:30:00	31.73	27.46	27.6	31.04	26.94	27.51
12:45:00	31.8	27.32	27.14	31.43	27.09	27.88
13:00:00	32.87	28.73	27.62	31.53	27.39	28.06
13:15:00	32.81	28.57	27.01	31.77	27.64	28.18
13:30:00	32.32	28.87	27.87	31.97	27.86	28.6
13:45:00	32.48	28.34	27.66	32.01	27.91	28.92
14:00:00	33.74	30.69	28.26	32.33	28.25	29.12
14:15:00	33.57	30.72	28.74	32.49	28.37	29.23
14:30:00	33.24	30.02	28.26	32.62	28.64	29.61
14:45:00	33.09	30.1	28.37	32.75	28.87	29.79
15:00:00	34.99	30.91	29.55	32.82	29	30.04
15:15:00	34.49	30.16	29.64	32.91	29.15	30.3
15:30:00	34.85	30.46	29.29	32.96	29.31	30.44
15:45:00	34.15	30.74	29.58	33	29.44	30.86
16:00:00	34.69	31.86	30.97	33.29	29.56	31.06
16:15:00	34.58	31.01	30.66	33.45	27.67	31.11
16:30:00	34.06	31.32	30.24	32.96	29.77	31.27
16:45:00	34.23	31.21	30.01	32.88	29.83	31.32
17:00:00	31.06	29.37	27.7	32.82	29.91	31.42
17:15:00	31.98	29.32	27.07	32.79	29.98	31.28
17:30:00	31.84	29.63	27.32	32.61	30	31.5
17:45:00	31.73	29.31	27.11	32.51	30.03	31.52
18:00:00	28.42	27.14	26.31	32.33	30.05	31.53
18:15:00	28.49	27.27	26.82	32.2	30.06	31.53
18:30:00	28.27	27.39	26.99	31.97	30.08	31.54
18:45:00	28.5	27.4	26.51	31.76	30.08	31.54
19:00:00	28.51	27.46	27.38	31.53	30.09	31.54
19:15:00	28.17	28.17	27.16	31.47	30.1	31.54
19:30:00	28.26	28.26	27.32	31.04	30.1	31.54
19:45:00	28.16	28.16	27.25	30.92	30.1	31.54
20:00:00	27.98	29.65	31.04	30.53	30.1	31.54
20:15:00	28.06	30.57	31.04	30.32	30.1	31.54
20:30:00	27.63	30.12	30.51	29	30.1	31.54
20:45:00	27.27	29.78	30.22	29.86	30.1	31.5
21:00:00	26.89	29.33	29.57	28.49	30.1	31.49
21:15:00	27.08	29.35	29.72	28.31	30.1	31.46
21:30:00	26.2	28.68	28.97	28.02	30.1	31.42
21:45:00	25.92	28.3	28.66	27.87	30	31.39
22:00:00	25.8	28.15	28.58	27.62	30	31.31
22:15:00	25.63	27.89	28.33	27.4	29.99	31.25
22:30:00	25.43	27.64	28.08	26.81	29.98	31.15
22:45:00	25.18	27.31	27.78	26.72	29.91	31.06
23:00:00	25.07	27.19	27.6	26.08	29.87	30.93
23:15:00	24.67	26.88	27.3	26	29.76	30.85
23:30:00	24.76	26.78	27.16	25.94	29.67	30.65
23:45:00	24.65	26.61	26.91	25.88	29.5	30.55
00:00:00	24.46	26.45	26.82	25.51	29.46	30.32
00:15:00	24.25	26.2	26.5	25.47	29.41	30.2
00:30:00	24.23	26.14	26.41	24.79	29.32	29.96
00:45:00	24.04	25.9	26.2	24.6	29.21	29.81
01:00:00	24.06	25.86	26.13	24.25	29.17	29.55
01:15:00	24	25.76	25.99	24.01	29.07	29.4
01:30:00	23.89	25.61	25.85	23.78	28.84	29.17
01:45:00	24	25.61	25.84	23.66	28.73	29.09
02:00:00	24.13	25.65	26.02	23.45	28.52	28.78
02:15:00	24.13	25.51	25.8	23.34	28.36	28.63
02:30:00	24.25	25.65	25.99	23.22	28.23	28.41
02:45:00	24.11	25.44	25.77	23.12	28.18	28.33
03:00:00	23.77	25.29	25.6	23.08	27.97	28.05
03:15:00	23.53	25.03	25.31	23.05	27.87	27.8
03:30:00	23.86	25.1	25.4	23.01	27.84	27.72
03:45:00	25.22	25.8	26.05	23	27.76	27.69
04:00:00	25.7	26.28	26.5	23.01	27.75	27.42
04:15:00	25.04	26.02	26.37	23.08	27.74	27.34
04:30:00	25.1	25.9	26.15	23.1	27.73	27.16
04:45:00	25.17	26.02	26.28	23.17	27.69	27.01
05:00:00	24.79	25.68	25.89	23.22	27.52	26.94
05:15:00	24.16	25.25	25.5	23.45	27.47	26.87
05:30:00	24.36	25.3	25.53	24.46	27.35	26.72
05:45:00	23.74	24.92	25.2	24.73	27.25	26.6
06:00:00	23.48	24.69	24.99	25.24	27.13	26.56

C2 Experimental and Numerical Temperatures for $BaSO_4$ and MPEA in Afikpo on 13/07/22022

Time	Tamb_exp	T_BaSO4_	Tmpea_ex	Tamb_mo	T_BaSO4_	Tmpea_m
07:00:00	25.1	25.48	24.82	25.63	25.14	25.15
07:30:00	26.63	26.92	24.04	25.86	25.22	25.21
08:00:00	26.07	26.48	24.06	26.5	25.37	25.25
08:30:00	26.81	26.32	24.49	26.66	25.51	25.34
09:00:00	26.92	26.22	24.66	27.09	25.83	25.55
09:30:00	26.05	25.29	24.75	27.54	26.12	25.74
10:00:00	26.9	25.72	24.18	28	26.44	25.96
10:30:00	27.9	26.31	24.06	28.45	26.81	26.21
11:00:00	27.32	26.84	24.98	28.91	27.18	26.47
11:30:00	27.85	26.83	25.14	29.33	27.58	26.75
12:00:00	27.59	26.4	25.42	29.75	27.99	27.04
12:30:00	28.69	26.82	25	30.13	28.41	27.35
13:00:00	28.09	26.06	25.07	30.47	28.81	27.64
13:30:00	28.96	27.88	26.89	30.77	29.19	27.93
14:00:00	28.72	27.4	26.33	31.03	29.56	28.21
14:30:00	29.38	27.15	26.01	31.23	29.98	28.47
15:00:00	29.19	27.85	26.95	31.38	30.2	28.71
15:30:00	29.07	27.17	26.27	31.47	30.46	28.91
16:00:00	28.63	27.81	26.59	31.5	30.67	29.08
16:30:00	28.3	27.61	27.38	31.47	30.84	29.21
17:00:00	28.97	27.96	27.12	31.38	30.96	29.31
17:30:00	28	27.8	27.91	31.23	31.02	29.36
18:00:00	28.58	27.89	27.07	31.03	31.04	29.39
18:30:00	27.8	27.55	27.83	30.77	31.05	29.4
19:00:00	27.57	27.21	27.2	30.47	31.06	29.41
19:30:00	26.11	27.77	26.72	30.13	31.05	29.42
20:00:00	26.22	27.69	26.51	29.75	31.04	29.42
20:30:00	26.58	27.31	26.39	29.35	31.03	29.41
21:00:00	26.13	26.8	26.87	28.83	31	29.41
21:30:00	26.95	26.58	26.76	28.28	30.94	29.41
22:00:00	26.79	26.54	26.78	27.73	30.84	29.39
22:30:00	25.71	25.33	25.65	27.19	30.68	29.37
23:00:00	25.69	25.28	25.59	26.66	30.48	29.36
23:30:00	25.57	25.21	25.56	26.45	30.31	29.31
00:00:00	25.5	25.03	25.48	26.17	30.23	29.3
00:30:00	25.44	25.9	25.34	25.72	29.94	29.23
01:00:00	25.39	25.85	25.35	25.33	29.62	29.19
01:30:00	24.31	23.81	25.27	25.04	29.32	29.1
02:00:00	24.28	23.73	25.27	24.82	29.05	29.05
02:30:00	24.19	24.69	24.25	24.65	28.78	28.93
03:00:00	24.14	24.55	24.2	24.54	28.54	28.84
03:30:00	25.11	24.49	24.14	24.5	28.32	28.67
04:00:00	25.1	24.51	24.13	24.47	28.13	28.59
04:30:00	25.08	24.35	24.07	24.31	27.95	28.44
05:00:00	25.14	24.4	24.13	25.17	27.56	28.36
05:30:00	25.2	24.48	24.21	25.28	27.46	28.23
06:00:00	25.22	24.48	24.12	25.87	27.35	28.18

C3 Experimental and Numerical Temperatures for $BaSO_4$ and MPEA in Owerri on xx/07/22022

Time	Tamb_exp	T_BaSO4_	Tmpea_ex	Tamb_mo	T_BaSO4_	Tmpea_m
07:00	25.2	24.35	24.39	24.89	23.43	23.37
07:30	25.27	25.11	24.8	25.26	23.51	23.42
08:00	25.43	25.55	24.27	25.57	23.6	23.48
08:30	25.28	25.31	24.5	26.76	23.74	23.58
09:00	26.12	25.35	24.54	27.24	24.12	23.84
09:30	25.72	25.85	24.83	27.48	24.37	24.11
10:00	26.23	25.86	24.8	27.71	24.94	24.44
10:30	26.3	25.68	24.84	28.12	25.43	24.82
11:00	28.78	26.18	24.18	29.1	25.97	25.25
11:30	28.1	26.25	24.55	29.74	26.52	25.72
12:00	29.07	27.42	25.85	30.89	27.09	26.19
12:30	29.1	27.54	25.25	31.36	27.64	26.67
13:00	29.83	27.96	27.53	31.76	28.18	27.14
13:30	29.41	27.08	27.36	32.08	28.66	27.59
14:00	30.39	29.12	28.22	31.31	29.12	27.99
14:30	30.26	29.17	28.88	32.45	29.62	28.35
15:00	30.77	29.25	26.67	32.5	29.86	28.67
15:30	30.48	29.4	26.28	32.45	30.15	28.93
16:00	29.87	29.54	26.28	32.31	30.38	29.14
16:30	29.55	29.02	26.52	32.08	30.55	29.3
17:00	28.71	29.1	26.95	31.76	30.67	29.4
17:30	28.96	29.9	26.14	31.36	30.73	29.46
18:00	28.64	29.67	27.96	30.88	30.75	29.48
18:30	28.31	29.09	27.9	30.38	30.75	29.49
19:00	28.13	29.33	28.45	29.17	30.75	29.5
19:30	28.72	29.04	27.71	28.44	30.71	29.5
20:00	27.03	28.45	25.85	27.68	30.64	29.49
20:30	27.51	28.14	24.79	26.91	30.58	29.46
21:00	27.04	26.95	24.32	26.31	30.5	29.4
21:30	27.64	26.66	24.7	25.37	30.28	29.37
22:00	26.44	26.2	25.26	24.64	29.96	29.3
22:30	26.06	26.22	25.04	23.97	29.56	29.13
23:00	26.8	26.06	24.83	23.35	29.08	28.9
23:30	26.85	26.18	24.01	23.12	28.56	28.61
00:00	25.84	26.06	25.15	22.8	28.01	28.27
00:30	25.85	26.94	25.88	22.38	27.51	27.89
01:00	25.67	24.88	24.7	22.03	27.02	27.54
01:30	25.6	24.76	24.78	21.77	27.78	27.21
02:00	25.54	24.52	24.42	21.59	26.57	26.9
02:30	25.44	25.27	24.41	21.51	26.23	26.61
03:00	26.31	25.21	24.21	21.52	25.82	26.34
03:30	26.24	25.07	25.36	21.55	25.68	26.22
04:00	26.17	25.04	25.25	21.57	25.53	26.11
04:30	26.17	25.94	25.11	22.88	25.42	26.03
05:00	26.71	25.7	24.94	22.67	25.25	25.91
05:30	26.52	25.23	24.67	22.79	25.2	25.79
06:00	26.69	26.18	25.98	23.56	25.17	25.63

C4 Numerical Temperatures for $BaSO_4$ and MPEA in Adamawa on xxx/09/22022

Time	Tamb_Mo	T_BaSO4_	Tmpea_M
06:00:00	26.47	25.44	25.29
06:30:00	26.73	25.51	25.48
07:00:00	26.96	25.59	25.5
07:30:00	27.31	25.78	25.57
08:00:00	28.02	26.03	25.77
08:30:00	28.26	26.31	25.61
09:00:00	28.52	26.63	25.96
09:30:00	29.03	26.99	26.2
10:00:00	30.27	27.38	26.45
10:30:00	30.43	27.79	26.73
11:00:00	30.82	28.19	27.04
11:30:00	31.17	28.6	27.67
12:00:00	31.46	29	27.99
12:30:00	31.69	29.38	28.29
13:00:00	31.86	29.73	28.58
13:30:00	31.97	30	28.84
14:00:00	32	30.33	29.07
14:30:00	31.97	30.57	29.26
15:00:00	31.86	30.76	29.42
15:30:00	31.7	30.91	29.54
16:00:00	31.46	31.02	29.62
16:30:00	31.17	31.08	29.67
17:00:00	30.82	31.09	29.69
17:30:00	30.43	31.1	29.69
18:00:00	30.31	31.09	29.7
18:30:00	29.53	31.06	29.69
19:00:00	29.03	31.03	29.69
19:30:00	28.62	30.97	29.69
20:00:00	28.09	30.87	29.67
20:30:00	27.57	30.72	29.62
21:00:00	27.05	30.52	29.58
21:30:00	26.55	30.29	29.54
22:00:00	26.07	30.02	29.44
22:30:00	25.63	29.71	29.25
23:00:00	25.22	29.39	29.03
23:30:00	24.87	29.08	28.95
00:00:00	24.54	28.77	28.77
00:30:00	24.34	28.48	28.65
01:00:00	24.05	28.22	28.49
01:30:00	24.01	28.15	28.34
02:00:00	24	27.98	28.26
02:30:00	24.07	27.05	28.18
03:00:00	24.13	26.78	27.64
03:30:00	24.21	26.57	27.53
04:00:00	24.25	26.6	27.05
04:30:00	24.43	25.1	26.89
05:00:00	25.85	25.24	26.67

C5 Numerical Temperatures for $BaSO_4$ and MPEA in Ekiti on xxx/09/22022

Time	Tamb_mo	T_BaSO4_	Tmpea_m
06:00:00	22.56	21.76	21.71
06:30:00	22.79	21.83	21.75
07:00:00	23	21.9	21.8
07:30:00	23.31	22.08	21.88
08:00:00	23.96	22.3	22.06
08:30:00	24.47	22.57	22.24
09:00:00	25.22	22.86	22.45
09:30:00	25.52	23.2	22.69
10:00:00	26.03	23.57	22.97
10:30:00	26.53	23.95	23.25
11:00:00	27.24	24.36	23.58
11:30:00	27.43	24.77	23.9
12:00:00	27.82	25.16	24.22
12:30:00	28.17	25.55	24.55
13:00:00	28.46	25.92	24.87
13:30:00	28.69	26.25	25.15
14:00:00	28.86	26.56	25.42
14:30:00	28.96	26.81	25.66
15:00:00	29.03	27.02	25.86
15:30:00	28.96	27.19	26.02
16:00:00	28.86	27.31	26.14
16:30:00	28.69	27.37	26.21
17:00:00	28.46	27.4	26.26
17:30:00	28.17	27.41	26.28
18:00:00	27.91	27.41	26.3
18:30:00	27.82	27.42	26.31
19:00:00	27.27	27.42	26.31
19:30:00	26.54	27.42	26.31
20:00:00	25.94	27.42	26.31
20:30:00	25.3	27.41	26.3
21:00:00	24.66	27.4	26.29
21:30:00	24.09	27.37	26.2
22:00:00	23.54	27.3	26.17
22:30:00	23.02	27.2	26.12
23:00:00	22.55	27.04	26.03
23:30:00	22.43	26.83	25.91
00:00:00	22.11	26.58	25.84
00:30:00	21.76	26.28	25.74
01:00:00	21.5	25.99	25.61
01:30:00	21.29	25.7	25.58
02:00:00	21.13	25.42	25.26
02:30:00	21.09	25.16	25.2
03:00:00	21.03	24.92	25.13
03:30:00	21.02	24.74	25.07
04:00:00	21	24.7	24.92
04:30:00	21.84	25.22	24.56
05:00:00	22.01	25.64	24.43

C6 Numerical Temperatures for $BaSO_4$ and MPEA in Kaduna on xxx/09/22022

Time	Tamb_mo	TBaSO4_m	Tmpea_m
06:00:00	25.17	24.62	24.56
06:30:00	25.34	24.68	24.6
07:00:00	25.5	24.75	24.65
07:30:00	25.85	24.87	24.76
08:00:00	26.22	25.14	24.9
08:30:00	26.6	25.39	25.07
09:00:00	27.25	25.67	25.25
09:30:00	27.39	25.98	25.46
10:00:00	27.77	26.31	25.68
10:30:00	28.14	26.65	25.92
11:00:00	28.5	27	26.16
11:30:00	28.82	27.25	26.41
12:00:00	29.12	27.69	26.66
12:30:00	29.38	28.02	26.9
13:00:00	29.59	28.34	27.13
13:30:00	29.77	28.63	27.35
14:00:00	29.89	28.89	27.54
14:30:00	29.97	29.11	27.71
15:00:00	30	29.3	27.86
15:30:00	29.97	29.44	27.97
16:00:00	29.89	29.54	28.05
16:30:00	29.77	29.6	28.09
17:00:00	29.59	29.61	28.11
17:30:00	29.38	29.62	28.12
18:00:00	29.12	29.62	28.13
18:30:00	28.98	29.62	28.13
19:00:00	28.5	29.62	28.14
19:30:00	28.15	29.61	28.14
20:00:00	27.21	29.58	28.13
20:30:00	27.72	29.54	28.13
21:00:00	26.72	29.46	28.12
21:30:00	26.25	29.35	28.11
22:00:00	25.79	29.2	28.08
22:30:00	25.58	29.14	28.03
23:00:00	25.36	29	28
23:30:00	24.98	28.78	27.9
00:00:00	24.65	28.53	27.87
00:30:00	24.45	28.37	27.76
01:00:00	24.39	28.28	27.72
01:30:00	24.3	28.16	27.61
02:00:00	24.21	28.05	27.54
02:30:00	24.19	27.94	27.49
03:00:00	24.08	27.83	27.37
03:30:00	24.05	27.77	27.33
04:00:00	24.01	27.63	27.22
04:30:00	24.01	27.45	27.18
05:00:00	24	27.29	27.1

C7 Numerical Temperatures for $BaSO_4$ and MPEA in Warri on xxx/09/22022

Time	Tamb_mo	TBaSO4_m	Tmpea_m
06:00:00	23.17	22.61	22.56
06:30:00	23.34	2.68	22.6
07:00:00	23.5	22.74	22.64
07:30:00	23.85	22.86	22.71
08:00:00	24.22	22.92	22.75
08:30:00	24.61	23.13	22.89
09:00:00	25	23.65	23.06
09:30:00	25.39	23.95	23.23
10:00:00	25.77	24.27	23.66
10:30:00	26.14	24.6	23.89
11:00:00	26.5	24.94	24.13
11:30:00	26.82	25.29	24.38
12:00:00	27.12	25.62	24.63
12:30:00	27.38	25.94	24.87
13:00:00	27.59	26.26	25.1
13:30:00	27.77	26.54	25.31
14:00:00	27.89	26.71	25.51
14:30:00	27.97	27.01	25.68
15:00:00	28.27	27.2	25.82
15:30:00	27.97	27.43	25.93
16:00:00	27.89	27.44	26.01
16:30:00	27.77	27.49	26.06
17:00:00	27.59	27.51	26.08
17:30:00	27.38	27.51	26.09
18:00:00	27.17	27.52	26.1
18:30:00	27.12	27.51	26.11
19:00:00	26.89	27.51	26.11
19:30:00	26.83	27.5	26.11
20:00:00	26.5	27.49	26.11
20:30:00	26.15	27.44	26.11
21:00:00	25.69	27.37	26.09
21:30:00	25.21	27.26	26.07
22:00:00	24.72	27.11	26.05
22:30:00	24.25	26.91	26.01
23:00:00	23.79	26.69	25.96
23:30:00	23.36	26.44	25.89
00:00:00	22.98	26.19	25.84
00:30:00	22.78	26.05	25.71
01:00:00	22.39	25.97	25.67
01:30:00	22.21	25.83	25.55
02:00:00	22.08	25.75	25.49
02:30:00	22.01	25.6	25.39
03:00:00	22	25.55	25.31
03:30:00	23.09	25.42	25.25
04:00:00	23.53	25.37	25.17
04:30:00	23.86	25.31	25.06
05:00:00	24.32	25.22	25.04

Appendix D Cooling Power of $BaSO_4$ and MPEA in the seven test locations

D1 Cooling Power of $BaSO_4$ and MPEA in Abuja

Time	BaSO4	MPEA
7:00AM	40.44	40.12
7:30AM	47.98	47.44
8:00AM	54.36	53.56
8:30AM	63.21	61.89
8:45AM	67.44	65.83
9:00AM	79.47	76.76
9:30AM	90.3	86.23
10:00AM	99.75	94.14
10:30AM	107.64	100.44
11:00AM	113.79	105.07
11:30AM	118.05	107.97
12:00PM	120.25	109.09
12:30PM	120.29	108.34
1:00PM	118.11	105.67
1:30PM	113.67	101.06
2:00PM	107	94.51
2:30PM	98.2	86.1
3:00PM	87.41	75.93
3:30PM	74.83	64.17
4:00PM	60.7	50.04
4:30PM	45.3	36.79
5:00PM	28.96	21.71
5:30PM	12.02	6.11

D2 Cooling Power of $BaSO_4$ and MPEA in Adamawa

Time	Pcool-BS	Pcool-MPE
07:00	28.85	31.12
07:30	31.41	36.75
08:00	37.23	41.45
08:30	48.96	50.87
09:00	52.22	59.27
09:30	61.49	65.57
10:00	69.83	72.72
10:30	77.1	77.65
11:00	83.18	81.32
11:30	87.89	83.67
12:00	91.14	84.64
12:30	92.79	84.18
13:00	92.77	82.25
13:30	91.02	78.83
14:00	87.54	73.94
14:30	82.35	67.64
15:00	75.51	60
15:30	67.16	51.17
16:00	57.42	41.28
16:30	46.5	30.52
17:00	34.6	19.09
17:30	21.95	7.19

D3 Cooling Power of $BaSO_4$ and MPEA in Afikpo

Time	Pcool_BS	Pcool_MPI
07:00:00	36.11	36
07:30:00	42.89	42.63
08:00:00	56.61	55.99
08:30:00	60.42	59.66
09:00:00	71.25	69.98
09:30:00	80.95	79.03
10:00:00	89.34	86.68
10:30:00	96.26	92.79
11:00:00	101.55	97.28
11:30:00	105.07	100.05
12:00:00	106.74	101.06
12:30:00	106.46	100.26
13:00:00	104.22	97.64
13:30:00	100	93.24
14:00:00	93.88	87.1
14:30:00	85.93	79.31
15:00:00	76.3	69.99
15:30:00	65.16	59.32
16:00:00	52.73	47.48
16:30:00	39.25	34.7
17:00:00	25	21.23
17:30:00	10.27	7.31

D4 Cooling Power of $BaSO_4$ and MPEA in Ekiti

Time	Pcool_BaS	Pcool_MPI
07:00	29.97	29.74
07:30	35.52	35.14
08:00	40.22	39.66
08:30	46.69	45.78
09:00	49.78	48.66
09:30	50.53	56.61
10:00	66.33	63.39
10:30	73.07	68.95
11:00	78.63	73.24
11:30	82.89	76.24
12:00	85.77	77.94
12:30	87.16	78.31
13:00	87.01	77.34
13:30	85.27	75.03
14:00	81.93	71.37
14:30	77.03	66.39
15:00	70.62	60.14
15:30	62.8	52.7
16:00	53.72	44.18
16:30	43.55	34.74
17:00	32.47	12.77
17:30	8.53	2.64

D5 Cooling Power of $BaSO_4$ and MPEA in Kaduna

Time	Pcool_BaS	Pcool_MPI
07:00:00	31.49	31.37
07:30:00	37.4	37.2
08:00:00	42.4	42.12
08:30:00	49.33	48.87
09:00:00	52.65	52.08
09:30:00	62.05	61.09
10:00:00	70.45	69
10:30:00	77.69	75.67
11:00:00	83.63	80.99
11:30:00	88.15	84.87
12:00:00	91.13	87.26
12:30:00	92.49	88.09
13:00:00	92.17	87.32
13:30:00	90.16	84.99
14:00:00	86.45	81.09
14:30:00	81.1	75.69
15:00:00	74.19	68.88
15:30:00	65.85	60.76
16:00:00	56.21	51.47
16:30:00	45.47	41.19
17:00:00	33.84	30.11
17:30:00	21.56	18.43
	8.86	6.38

D6 Cooling Power of $BaSO_4$ and MPEA in Owerri

Time	Pcool_BaS	Pcool_MPI
07:00	30.76	30.18
07:30	36.29	35.3
08:00	47.38	45.05
08:30	56.43	52.43
09:00	64.77	54.63
09:30	67.37	60.64
10:00	74.12	65.75
10:30	80.86	70.02
11:00	85.94	73.45
11:30	89.67	75.94
12:00	91.88	77.34
12:30	92.45	77.53
13:00	91.27	76.35
13:30	88.29	73.73
14:00	83.51	69.62
14:30	76.99	64.05
15:00	68.82	57.07
15:30	59.14	48.81
16:00	48.12	39.42
16:30	35.96	29.08
17:00	22.91	17.97
17:30	9.22	6.31

D7 Cooling Power of $BaSO_4$ and MPEA in Warri

Time	Pcool_BaS	Pcool_MPI
07:00	30.58	30.46
07:30	36.31	36.1
08:00	47.89	47.39
08:30	51.1	50.48
09:00	60.22	59.18
09:30	68.37	66.79
10:00	75.4	73.19
10:30	81.17	78.29
11:00	85.56	81.99
11:30	88.47	84.24
12:00	89.81	84.99
12:30	89.52	84.22
13:00	87.58	81.92
13:30	84	78.13
14:00	78.83	72.9
14:30	72.14	66.3
15:00	64.04	58.44
15:30	54.69	49.46
16:00	44.26	39.51
16:30	32.96	28.79
17:00	21.01	17.49
17:30	8.66	5.83

D8 Cooling Power of $BaSO_4$ in all the seven test locations

Time	Pcool_Abj	Pcool_Ada	Pcool_Afk	Pcool_Ekt	Pcool_Kad	Pcool_Ow	Pcool_Wa
07:00	40.44	28.85	36.11	29.97	31.49	30.76	30.58
07:30	47.98	31.41	42.89	35.52	37.4	36.29	36.31
08:00	54.36	37.23	56.61	40.22	49.33	47.38	47.89
08:30	67.44	48.96	60.42	46.69	52.65	56.43	51.1
09:00	79.47	52.22	71.25	49.78	62.05	64.77	60.22
09:30	90.3	61.49	80.95	50.53	70.45	67.37	68.37
10:00	99.75	69.83	89.34	66.33	77.69	74.12	75.4
10:30	107.64	77.1	96.26	73.07	83.63	80.86	81.17
11:00	113.79	83.18	101.55	78.63	88.15	85.94	85.56
11:30	118.05	87.89	105.07	82.89	91.13	89.67	88.47
12:00	120.25	91.14	106.74	85.77	92.49	91.88	89.81
12:30	120.29	92.79	106.46	87.16	92.17	92.45	89.52
13:00	118.11	92.77	104.22	87.01	90.16	91.27	87.58
13:30	113.67	91.02	100	85.27	86.45	88.29	84
14:00	107	87.54	93.88	81.93	81.1	83.51	78.83
14:30	98.2	82.35	85.93	77.03	74.19	76.99	72.14
15:00	87.41	75.51	76.3	70.62	65.85	68.82	64.04
15:30	74.83	67.16	65.16	62.8	56.21	59.14	54.69
16:00	60.7	57.42	52.73	53.72	45.47	48.12	44.26
16:30	45.3	46.5	39.25	43.55	33.84	35.96	32.96
17:00	28.96	34.6	25	32.47	21.56	22.91	21.01
17:30	12.02	21.95	10.27	8.53	8.86	9.22	8.66

D9 Cooling Power of MPEA in all the seven test locations

Time	Pcool_Abj	Pcool-Ada	Pcool_Afk	Pcool_Ekt	Pcool_Kad	Pcool_Ow	Pcool_Wa
07:00	40.12	31.12	36	29.74	31.37	30.18	30.46
07:30	47.44	36.75	42.63	35.14	37.2	35.3	36.1
08:00	53.56	41.45	55.99	39.66	48.87	45.05	47.39
08:30	65.83	50.87	59.66	45.78	52.08	52.43	50.48
09:00	76.76	59.27	69.98	48.66	61.09	54.63	59.18
09:30	86.23	65.57	79.03	56.61	69	60.64	66.79
10:00	94.14	72.72	86.68	63.39	75.67	65.75	73.19
10:30	100.44	77.65	92.79	68.95	80.99	70.02	78.29
11:00	105.07	81.32	97.28	73.24	84.87	73.45	81.99
11:30	107.97	83.67	100.05	76.24	87.26	75.94	84.24
12:00	109.09	84.64	101.06	77.94	88.09	77.34	84.99
12:30	108.34	84.18	100.26	78.31	87.32	77.53	84.22
13:00	105.67	82.25	97.64	77.34	84.99	76.35	81.92
13:30	101.06	78.83	93.24	75.03	81.09	73.73	78.13
14:00	94.51	73.94	87.1	71.37	75.69	69.62	72.9
14:30	86.1	67.64	79.31	66.39	68.88	64.05	66.3
15:00	75.93	60	69.99	60.14	60.76	57.07	58.44
15:30	64.17	51.17	59.32	52.7	51.47	48.81	49.46
16:00	50.04	41.28	47.48	44.18	41.19	39.42	39.51
16:30	36.79	30.52	34.7	34.74	30.11	29.08	28.79
17:00	21.71	19.09	21.23	12.77	18.43	17.97	17.49
17:30	6.11	7.19	7.31	2.64	6.38	6.31	5.83

Appendix E Temperatures of $BaSO_4$ and MPEA at varying thicknesses, Number of windscreens and angles of inclination

E1 Temperatures of $BaSO_4$ at varying thicknesses

Time	T_BaSO4@	T_BaSO4@	T_BaSO4@	T_BaSO4(	T_BaSO4@	T_BaSO4@	T_BaSO4@	T_BaSO4@
06:00:00	22.35	22.37	22.36	22.36	22.35	22.35	22.35	22.35
06:30:00	22.42	22.39	22.37	22.37	22.36	22.35	22.35	22.35
07:00:00	22.48	22.4	22.38	22.37	22.36	22.35	22.35	22.35
07:30:00	22.7	22.42	22.39	22.38	22.37	22.35	22.36	22.35
08:00:00	22.81	22.45	22.41	22.39	22.38	22.35	22.36	22.36
08:30:00	23.34	22.47	22.43	22.41	22.39	22.36	22.37	22.36
09:00:00	23.48	22.52	22.46	22.43	22.42	22.36	22.38	22.37
09:30:00	24.27	22.68	22.51	22.46	22.44	22.37	22.39	22.38
10:00:00	24.44	22.74	22.57	22.52	22.48	22.38	22.42	22.5
10:30:00	25.02	22.95	22.61	22.55	22.51	22.39	22.43	22.41
11:00:00	25.63	23.21	22.76	22.66	22.6	22.4	22.48	22.45
11:30:00	26.27	23.54	22.95	22.81	22.72	22.43	22.54	22.51
12:00:00	26.93	23.92	23.19	23	22.88	22.48	22.63	22.57
12:30:00	27.58	24.35	23.49	23.24	23.09	22.54	22.74	22.67
13:00:00	28.22	24.83	23.83	23.53	23.34	22.62	22.89	22.79
13:30:00	28.82	25.34	24.22	23.87	23.63	22.72	23.07	22.95
14:00:00	29.39	25.86	24.65	24.24	23.96	22.85	23.29	23.12
14:30:00	29.9	26.38	25.11	24.64	24.32	23.01	23.53	23.33
15:00:00	30.35	26.89	25.57	25.07	24.71	23.19	23.79	23.56
15:30:00	30.74	27.37	26.04	25.49	25.1	23.39	24.08	23.81
16:00:00	31.05	27.82	26.48	25.91	25.48	23.62	24.37	24.08
16:30:00	31.3	28.22	26.9	26.3	25.86	23.85	24.67	24.33
17:00:00	31.46	28.56	27.28	26.67	26.21	24.09	24.94	24.6
17:30:00	31.55	28.85	27.62	26.99	26.53	24.33	25.21	24.84
18:00:00	31.58	29.08	27.9	27.27	26.81	24.55	25.46	25.07
18:30:00	31.59	29.24	28.13	27.51	27.05	24.77	25.68	25.28
19:00:00	31.59	29.35	28.31	27.7	27.24	24.96	25.86	25.45
19:30:00	31.59	29.41	28.44	27.84	27.38	25.13	26.01	25.6
20:00:00	31.57	29.43	28.52	27.93	27.49	25.27	26.13	25.72
20:30:00	31.53	29.44	28.57	27.99	27.55	25.39	26.21	25.79
21:00:00	31.45	29.45	28.6	28.03	27.59	25.46	26.28	25.87
21:30:00	31.29	29.46	28.61	28.05	27.63	25.54	26.34	25.94
22:00:00	31.04	29.46	28.62	28.07	27.65	25.61	26.37	25.97
22:30:00	30.69	29.46	28.63	28.08	27.66	25.65	26.39	25.99
23:00:00	30.11	29.44	28.63	28.09	27.67	25.67	26.4	26
23:30:00	29.42	29.39	28.63	28	27.67	25.68	26.4	26
00:00:00	28.67	29.28	28.63	28.08	27.67	25.68	26.4	26
00:30:00	27.98	29.12	28.61	28.07	27.66	25.68	26.4	26
01:00:00	27.34	28.9	28.58	28.04	27.64	25.68	26.4	26
01:30:00	26.75	28.61	28.51	27.97	27.6	25.68	26.39	26
02:00:00	26.21	28.26	28.4	27.88	27.54	25.68	26.37	25.99
02:30:00	25.73	27.85	28.24	27.75	27.45	25.68	26.34	25.97
03:00:00	25.33	27.49	28.04	27.59	27.33	25.67	26.31	25.95
03:30:00	25.28	27.14	27.79	27.4	27.16	25.65	26.24	25.91
04:00:00	24.89	26.81	27.51	27.19	26.95	25.63	26.16	25.87
04:30:00	24.76	26.51	27.22	26.97	26.75	25.61	25.89	25.81
05:00:00	24.67	26.23	26.95	26.76	26.57	25.52	25.67	25.73
05:30:00	24.43	25.98	26.69	26.55	26.41	25.35	25.54	25.65
06:00:00	24.2	25.77	26.45	26.37	26.28	25.21	25.43	25.46

E2 Temperatures of MPEA at varying thicknesses

Time	T_MPEA@	T_MPEA@	T_MPEA@	T_MPEA@	T_MPEA@	T_MPEA@
06:00:00	23.28	23.28	23.27	23.27	23.27	23.27
06:30:00	23.3	23.29	23.28	23.27	23.27	23.27
07:00:00	23.31	23.3	23.29	23.28	23.27	23.27
07:30:00	23.32	23.31	23.3	23.29	23.28	23.28
08:00:00	23.35	23.33	23.32	23.3	23.29	23.28
08:30:00	23.37	23.34	23.33	23.31	23.3	23.29
09:00:00	23.42	23.38	23.36	23.33	23.31	23.3
09:30:00	23.38	23.43	23.39	23.35	23.33	23.31
10:00:00	23.58	23.51	23.45	23.39	23.36	23.34
10:30:00	23.63	23.55	23.49	23.42	23.38	23.35
11:00:00	23.77	23.71	23.62	23.51	23.45	23.41
11:30:00	23.85	23.93	23.81	23.64	23.55	23.49
12:00:00	24.11	24.2	24.03	23.81	23.68	23.6
12:30:00	24.45	24.52	24.31	24.01	23.84	23.74
13:00:00	24.82	24.88	24.63	24.25	24.04	23.91
13:30:00	25.25	25.29	24.99	24.53	24.28	24.1
14:00:00	25.72	25.71	25.37	24.84	24.53	24.32
14:30:00	26.2	26.14	25.76	25.17	24.81	24.57
15:00:00	26.67	26.57	26.16	25.51	25.1	24.82
15:30:00	27.15	26.98	26.55	25.84	25.39	25.09
16:00:00	27.59	27.36	26.91	26.16	25.68	25.34
16:30:00	27.99	27.71	27.23	26.45	25.95	25.59
17:00:00	28.36	28	27.52	26.72	26.2	25.81
17:30:00	28.67	28.26	27.77	26.95	26.41	26.02
18:00:00	28.93	28.47	27.97	27.14	26.59	26.2
18:30:00	29.14	28.62	28.13	27.3	26.75	26.34
19:00:00	29.3	28.73	28.24	27.42	26.87	26.46
19:30:00	29.41	28.79	28.31	27.5	26.95	26.54
20:00:00	29.46	28.83	28.35	27.55	27	26.6
20:30:00	29.49	28.84	28.37	27.57	27.04	26.64
21:00:00	29.49	28.85	28.38	27.59	27.06	26.66
21:30:00	29.5	28.85	28.38	27.59	27.07	26.67
22:00:00	29.5	28.85	28.39	27.6	27.08	26.68
22:30:00	29.5	28.84	28.39	27.6	27.08	26.68
23:00:00	29.49	28.84	28.39	27.61	27.08	26.69
23:30:00	29.47	28.83	28.38	27.6	27.08	26.69
00:00:00	29.41	28.79	28.36	27.59	27.07	26.69
00:30:00	29.3	28.73	28.32	27.58	27.07	26.68
01:00:00	29.13	28.62	28.26	27.56	27.06	26.67
01:30:00	28.91	28.47	28.16	27.51	27.03	26.66
02:00:00	28.62	28.27	28.03	27.44	26.99	26.64
02:30:00	28.28	28.02	27.84	27.35	26.93	26.61
03:00:00	27.89	27.73	27.63	27.21	26.85	26.55
03:30:00	27.55	27.43	27.41	27.04	26.74	26.47
04:00:00	27.21	27.15	27.16	26.85	26.61	26.38
04:30:00	26.9	26.87	26.92	26.68	26.49	26.3
05:00:00	26.61	26.62	26.69	26.53	26.38	26.22
05:30:00	26.34	26.39	26.49	26.41	26.29	26.15
06:00:00	26.11	26.2	26.32	26.31	26.22	26.1

E3 Temperatures of $BaSO_4$ at varying Number of windscreens

Time	T_BaSO4@	T_BaSO4@	T_BaSO4@	T_BaSO4@	T_BaSO4@
06:00:00	22.39	22.4	22.38	22.36	22.36
06:30:00	22.42	22.42	22.39	22.37	22.36
07:00:00	22.44	22.44	22.42	22.39	22.37
07:30:00	22.48	22.49	22.44	22.41	22.38
08:00:00	22.55	22.56	22.48	22.43	22.4
08:30:00	22.7	22.6	22.54	22.46	22.42
09:00:00	22.81	22.71	22.68	22.51	22.45
09:30:00	23	22.82	22.78	22.65	22.5
10:00:00	23.1	23.02	22.95	22.74	22.54
10:30:00	23.34	23.12	23.05	22.89	22.62
11:00:00	23.48	23.48	23.37	22.98	22.7
11:30:00	23.77	23.91	23.76	23.28	22.85
12:00:00	23.92	24.39	24.2	23.62	22.92
12:30:00	24.26	24.93	24.68	24.02	23.19
13:00:00	24.44	25.51	25.2	24.46	23.51
13:30:00	25.02	26.12	25.75	24.94	23.87
14:00:00	25.63	26.75	26.32	25.43	24.27
14:30:00	26.27	27.37	26.9	25.95	24.71
15:00:00	26.93	27.99	27.46	26.48	25.16
15:30:00	27.58	28.58	28.01	27	25.64
16:00:00	28.22	29.14	28.53	27.05	26.13
16:30:00	28.83	29.65	29.01	27.98	26.61
17:00:00	29.39	30.11	29.44	28.43	27.08
17:30:00	29.9	30.51	29.81	28.83	27.52
18:00:00	30.35	30.83	30.11	29.17	27.94
18:30:00	30.74	31.08	30.34	29.46	28.31
19:00:00	31.05	31.25	30.51	29.68	28.64
19:30:00	31.29	31.35	30.6	29.83	28.91
20:00:00	31.46	31.38	30.63	29.93	29.12
20:30:00	31.55	31.39	30.64	29.96	29.26
21:00:00	31.58	31.39	30.64	29.97	29.35
21:30:00	31.59	31.39	30.64	29.97	29.38
22:00:00	31.59	31.38	30.64	29.97	29.4
22:30:00	31.59	31.33	30.63	29.97	29.41
23:00:00	31.57	31.2	30.58	29.97	29.41
23:30:00	31.53	30.92	30.46	29.95	29.41
00:00:00	31.45	30.48	30.23	29.9	29.41
00:30:00	31.29	29.87	29.87	29.78	29.4
01:00:00	31.04	29.14	29.39	29.57	29.37
01:30:00	30.68	28.36	28.83	29.26	29.28
02:00:00	30.11	27.68	28.24	28.87	29.08
02:30:00	29.42	27.1	27.68	28.43	28.77
03:00:00	28.67	26.59	27.19	27.99	28.39
03:30:00	27.97	26.19	26.8	27.59	28.25
04:00:00	27.34	25.83	26.47	27.25	27.85
04:30:00	26.74	25.67	26.13	26.95	27.53
05:00:00	26.21	25.44	25.76	26.79	26.83
05:30:00	25.73	25.3	25.55	26.54	26.32
06:00:00	25.33	25.17	25.31	25.74	25.5

E4 Temperatures of MPEA at varying Number of windscreens

Time	T_MPEA@	T_MPEA@	T_MPEA@	T_MPEA@	T_MPEA@
06:00:00	23.28	23.28	23.28	23.27	23.27
06:30:00	23.29	23.3	23.29	23.28	23.27
07:00:00	23.31	23.31	23.3	23.29	23.28
07:30:00	23.33	23.33	23.32	23.3	23.29
08:00:00	23.35	23.36	23.35	23.31	23.29
08:30:00	23.37	23.37	23.36	23.34	23.31
09:00:00	23.42	23.42	23.41	23.35	23.33
09:30:00	23.48	23.48	23.45	23.39	23.35
10:00:00	23.58	23.57	23.53	23.44	23.38
10:30:00	23.63	23.62	23.58	23.51	23.42
11:00:00	23.77	23.8	23.73	23.55	23.48
11:30:00	23.81	24.02	23.92	23.68	23.52
12:00:00	24.11	24.28	24.15	23.85	23.64
12:30:00	24.45	24.59	24.41	24.05	23.79
13:00:00	24.83	24.93	24.69	24.27	23.97
13:30:00	25.26	25.3	25	24.52	24.17
14:00:00	25.72	25.68	25.33	24.79	24.39
14:30:00	26.2	26.08	25.67	25.07	24.64
15:00:00	26.67	26.48	26.01	25.37	24.88
15:30:00	27.14	26.86	26.34	25.67	25.15
16:00:00	27.58	27.22	26.66	25.96	25.41
16:30:00	27.99	27.55	26.95	26.24	25.67
17:00:00	28.35	27.84	27.21	26.51	25.93
17:30:00	28.67	28.09	27.45	26.75	26.17
18:00:00	28.93	28.3	27.63	26.95	26.38
18:30:00	29.14	28.45	27.78	27.13	26.57
19:00:00	29.3	28.56	27.88	27.27	26.73
19:30:00	29.4	28.63	27.95	27.37	26.86
20:00:00	29.46	28.66	27.98	27.43	26.95
20:30:00	29.49	28.67	27.99	27.46	27.02
21:00:00	29.49	28.67	28	27.47	27.05
21:30:00	29.5	28.68	28	27.48	27.06
22:00:00	29.5	28.68	28	27.49	27.07
22:30:00	29.5	28.67	28.01	27.49	27.08
23:00:00	29.49	28.65	28	27.49	27.08
23:30:00	29.46	28.59	27.98	27.49	27.09
00:00:00	29.4	28.47	27.93	27.47	27.08
00:30:00	29.3	28.26	27.83	27.44	27.07
01:00:00	29.13	27.99	27.69	27.37	27.05
01:30:00	28.9	27.67	27.47	27.25	27
02:00:00	28.61	27.34	27.25	27.11	26.92
02:30:00	28.27	27.06	26.84	26.88	26.82
03:00:00	27.89	26.82	26.64	26.75	26.73
03:30:00	27.55	26.63	26.55	26.53	26.58
04:00:00	27.21	26.52	26.35	26.32	26.35
04:30:00	26.9	26.43	26.12	25.9	26.05
05:00:00	26.6	25.96	25.94	25.76	25.82
05:30:00	26.34	25.84	25.87	25.56	25.64
06:00:00	26.11	25.56	25.65	25.43	25.25

E5 Temperatures of $BaSO_4$ at varying angles of inclination

Time	T_BaSO4@	T_BaSO4@	T_BaSO4@	T_BaSO4@	T_BaSO4@	T_BaSO4@
06:00:00	22.39	22.39	22.4	22.38	22.38	22.36
06:30:00	22.42	22.42	22.43	22.39	22.41	22.37
07:00:00	22.44	22.43	22.45	22.42	22.44	22.38
07:30:00	22.48	22.48	22.5	22.44	22.49	22.39
08:00:00	22.55	22.54	22.57	22.48	22.52	22.42
08:30:00	22.59	22.58	22.61	22.55	22.6	22.43
09:00:00	22.7	22.68	22.73	22.59	22.68	22.48
09:30:00	22.82	22.79	22.86	22.69	22.82	22.53
10:00:00	23.11	22.97	23.07	22.81	22.9	22.61
10:30:00	23.35	23.07	23.18	22.99	23.2	22.67
11:00:00	23.49	23.3	23.58	23.1	23.42	22.79
11:30:00	23.78	23.43	24.06	23.33	23.55	22.86
12:00:00	23.94	23.71	24.6	23.46	23.83	23.03
12:30:00	24.28	23.86	25.21	23.75	23.99	23.15
13:00:00	24.46	24.19	25.85	23.91	24.31	23.36
13:30:00	25.03	24.36	26.51	24.24	24.48	23.5
14:00:00	25.65	24.73	27.19	24.41	25.03	23.83
14:30:00	26.3	24.92	27.87	24.78	25.61	23.93
15:00:00	26.95	25.53	28.53	24.97	26.2	24.32
15:30:00	27.61	26.15	29.16	25.58	26.81	24.43
16:00:00	28.25	26.8	29.75	26.22	27.39	24.86
16:30:00	28.86	27.44	30.29	27.52	27.95	24.97
17:00:00	29.42	28.07	30.77	28.14	28.47	25.42
17:30:00	29.94	28.66	31.18	28.74	28.94	25.53
18:00:00	30.39	29.22	31.52	29.31	29.36	25.99
18:30:00	30.78	29.72	31.78	29.82	29.71	26.11
19:00:00	31.1	30.16	31.96	30.26	30	26.56
19:30:00	31.34	30.53	32.06	30.65	30.22	26.67
20:00:00	31.5	30.84	32.09	30.96	30.37	27.11
20:30:00	31.59	31.08	32.1	31.21	30.46	27.21
21:00:00	31.62	31.24	32.08	31.37	30.49	27.61
21:30:00	31.63	31.33	32.02	31.46	30.5	27.72
22:00:00	31.63	31.36	31.87	31.49	30.51	28.17
22:30:00	31.63	31.37	31.62	31.5	30.51	28.57
23:00:00	31.62	31.37	31.23	31.5	30.5	28.92
23:30:00	31.57	31.37	30.7	31.5	30.48	29.2
00:00:00	31.48	31.36	30.05	31.49	30.43	29.42
00:30:00	31.32	31.33	29.33	31.46	30.31	29.58
01:00:00	31.06	31.27	28.56	31.38	30.11	29.69
01:30:00	30.7	31.13	27.86	31.24	29.82	29.75
02:00:00	30.13	30.91	27.2	31.02	29.43	29.78
02:30:00	29.43	30.59	26.58	30.69	28.96	29.79
03:00:00	28.66	30.18	26.04	30.16	28.44	29.8
03:30:00	27.97	29.68	25.58	29.5	27.88	29.8
04:00:00	27.34	29.11	25.46	28.76	27.33	29.8
04:30:00	26.75	28.51	25.3	28.07	26.79	29.78
05:00:00	26.2	27.9	25.22	27.43	26.3	29.71
05:30:00	25.72	27.31	25.17	26.83	25.85	29.57
06:00:00	25.33	26.74	25	26.28	25.47	29.34

E6 Temperatures of MPEA at varying angles of inclination

Time	T_MPEA@	T_MPEA@	T_MPEA@	T_MPEA@	T_MPEA@	T_MPEA@
06:00:00	23.28	23.28	23.29	23.28	23.28	23.27
06:30:00	23.29	23.29	23.3	23.29	23.28	23.27
07:00:00	23.31	23.3	23.31	23.3	23.29	23.28
07:30:00	23.33	23.32	23.33	23.32	23.31	23.29
08:00:00	23.35	23.35	23.36	23.35	23.33	23.3
08:30:00	23.37	23.37	23.38	23.37	23.34	23.31
09:00:00	23.43	23.42	23.44	23.42	23.38	23.33
09:30:00	23.48	23.47	23.5	23.48	23.42	23.35
10:00:00	23.58	23.56	23.6	23.57	23.5	23.4
10:30:00	23.64	23.62	23.66	23.63	23.54	23.43
11:00:00	23.77	23.74	23.88	23.83	23.65	23.52
11:30:00	23.85	23.82	24.17	24.09	23.71	23.56
12:00:00	24.12	24.08	24.5	24.41	23.85	23.67
12:30:00	24.45	24.4	24.89	24.78	23.93	23.74
13:00:00	24.83	24.77	25.32	25.2	24.22	23.9
13:30:00	25.2	25.2	25.78	25.65	24.56	23.98
14:00:00	25.73	25.65	26.26	26.12	24.94	24.29
14:30:00	26.21	26.12	26.74	26.58	25.37	24.65
15:00:00	26.69	26.59	27.21	27.05	25.81	25.05
15:30:00	27.16	27.05	27.66	27.48	26.27	25.47
16:00:00	27.6	27.49	28.07	27.88	26.71	25.91
16:30:00	28.01	27.89	28.43	28.25	27.13	26.33
17:00:00	28.37	28.35	28.76	28.55	27.52	26.74
17:30:00	28.65	28.57	29.02	28.82	27.87	27.12
18:00:00	28.95	28.83	29.23	29.03	28.18	27.46
18:30:00	29.16	29.04	29.39	29.19	28.43	27.76
19:00:00	29.31	29.2	29.5	29.29	28.64	28.01
19:30:00	29.42	29.3	29.56	29.35	28.79	28.21
20:00:00	29.48	29.36	29.58	29.38	28.89	28.37
20:30:00	29.5	29.38	29.59	29.38	28.96	28.48
21:00:00	29.51	29.39	29.59	29.39	28.99	28.55
21:30:00	29.52	29.39	29.59	29.39	29	28.59
22:00:00	29.51	29.4	29.59	29.39	29	28.6
22:30:00	29.51	29.4	29.58	29.38	29.01	28.61
23:00:00	29.51	29.39	29.56	29.35	29.01	28.62
23:30:00	29.48	29.37	29.49	29.28	29	28.62
00:00:00	29.422	29.33	29.38	29.17	29	28.62
00:30:00	29.31	29.26	29.21	28.99	28.97	28.61
01:00:00	29.15	29.13	28.96	28.76	28.92	28.6
01:30:00	28.92	28.93	28.65	28.46	28.82	28.56
02:00:00	28.63	28.68	28.29	28.1	28.67	28.49
02:30:00	28.29	28.37	27.89	27.72	28.47	28.37
03:00:00	27.91	28.03	27.54	27.38	28.21	28.21
03:30:00	27.56	27.67	27.21	27.08	27.91	27.98
04:00:00	27.23	27.34	26.91	26.78	27.58	27.72
04:30:00	26.91	27.03	26.62	26.51	27.27	27.42
05:00:00	26.61	26.72	26.36	26.27	26.97	27.1
05:30:00	26.35	26.44	26.14	26.07	26.69	26.82
06:00:00	26.11	26.2	25.95	25.86	26.44	26.56

Appendix F Cooling Powers of BaSO4 and MPEA at varying thicknesses

F1 Cooling Power of $BaSO_4$ at varying thicknesses

Time	P_cool_Ba	P_cool_Ba	P_cool_Ba	P_cool_Ba	P_cool_Ba	P_cool_Ba	P_cool_Ba	P_cool_Ba
06:00:00	14.6	14.56	14.55	14.54	14.54	14.53	14.53	14.53
06:30:00	17.78	17.7	17.67	17.66	17.65	17.64	17.63	17.63
07:00:00	19.98	19.88	19.84	19.82	19.8	19.78	19.78	19.77
07:30:00	23.88	23.69	23.62	23.58	23.56	23.53	23.51	23.5
08:00:00	28.68	28.35	28.21	28.15	28.1	28.04	28.01	27.99
08:30:00	31.23	30.79	30.62	30.52	30.47	30.39	30.35	30.33
09:00:00	37.04	36.31	36	35.84	35.73	35.59	35.52	35.48
09:30:00	41.97	40.91	40.45	40.2	40.04	39.82	39.7	39.63
10:00:00	48.83	47.15	46.4	45.97	45.69	45.32	45.12	44.99
10:30:00	52.14	50.09	49.15	48.62	48.27	47.78	47.52	47.37
11:00:00	58.55	58.29	56.64	55.67	55.03	54.1	53.61	53.3
11:30:00	61.61	65.46	62.89	61.32	60.26	58.69	57.83	57.28
12:00:00	67.49	71.58	67.93	65.61	64	61.56	60.18	59.29
12:30:00	70.26	76.61	71.81	68.63	66.39	62.81	60.75	59.39
13:00:00	75.51	80.49	74.56	70.47	67.48	62.63	59.73	57.79
13:30:00	77.94	83.16	76.18	71.21	67.47	61.22	57.34	54.7
14:00:00	84.46	84.5	76.66	70.88	66.44	58.76	53.84	50.41
14:30:00	89.66	84.43	75.94	69.5	64.42	55.41	49.43	45.18
15:00:00	93.36	82.88	73.97	67.04	61.45	51.25	44.3	39.23
15:30:00	95.43	79.77	70.68	63.44	57.5	46.37	38.56	32.75
16:00:00	95.76	75.12	66.07	58.7	52.55	40.78	32.28	25.83
16:30:00	94.26	68.93	60.13	52.82	46.62	34.48	25.52	18.58
17:00:00	90.92	61.32	52.93	45.82	39.71	27.52	18.31	11.06
17:30:00	85.73	52.38	44.56	37.8	31.91	19.92	10.68	3.3
18:00:00	78.79	42.29	35.17	28.87	23.3	11.77	2.71	
18:30:00	70.19	31.24	24.92	19.17	14.02			
19:00:00	60.09	19.43	13.99	8.89	4.22			
19:30:00	48.68	7.12	2.62					

F2 Cooling Power of MPEA at varying thicknesses

Time	P_cool_M	P_cool_M	P_cool_M	P_cool_M	P_cool_M	P_cool_MI
06:00:00	14.56	14.55	14.55	14.55	14.55	14.54
06:30:00	17.64	17.63	17.62	17.6	17.59	17.59
07:00:00	19.75	19.74	19.72	19.7	19.99	19.69
07:30:00	23.44	23.39	23.37	23.34	23.32	23.31
08:00:00	27.87	27.79	27.75	27.69	27.66	27.64
08:30:00	30.18	30.08	30.01	29.93	29.89	29.86
09:00:00	35.29	35.12	35	34.85	34.77	34.73
09:30:00	39.48	39.21	39.03	38.79	38.68	38.6
10:00:00	45.05	44.58	44.28	43.87	43.66	43.52
10:30:00	47.62	47.03	46.65	46.12	45.85	45.68
11:00:00	52.42	53.55	52.85	51.85	51.31	50.98
11:30:00	54.63	58.9	57.74	56.03	55.09	54.51
12:00:00	60.63	63.22	61.48	58.83	57.34	56.37
12:30:00	65.75	66.63	64.23	60.44	58.23	56.77
13:00:00	70.02	69.21	66.1	61.05	57.99	55.94
13:30:00	73.45	70.93	67.16	60.82	56.84	54.11
14:00:00	75.93	71.71	67.38	59.83	54.93	51.48
14:30:00	77.34	71.45	66.66	58.09	52.35	48.21
15:00:00	77.52	70.01	64.92	55.57	49.11	44.35
15:30:00	76.34	67.31	62.07	52.2	45.21	39.94
16:00:00	73.72	63.28	58.03	47.94	40.61	34.98
16:30:00	69.62	57.92	52.79	42.75	35.28	29.45
17:00:00	64.04	51.29	46.38	36.62	29.21	23.34
17:30:00	57.07	43.47	38.88	29.61	22.44	16.68
18:00:00	48.81	34.61	30.41	21.79	15.02	9.49
18:30:00	39.42	24.85	21.11	13.29	7.03	1.86
19:00:00	29.07	14.39	11.15	4.24		
19:30:00	17.97	3.4	0.71			

F3 Cooling Power of BaSO4 and MPEA during peak solar radiation at 13:30 h

Thickness,	P_cool_M	P_cool_Ba
6	73.45	77.94
8	70.93	83.16
10	67.16	76.18
15	60.82	71.21
20	56.84	67.47
25	54.11	61.22
		57.34
		54.7

F4 Cooling Power of BaSO4 and MPEA during peak solar radiation at 15:00 h

Thickness,	P_cool_M	P_cool_Ba
2	77.52	93.36
4	70.01	82.88
6	64.92	73.97
8	58.09	67.04
10	49.11	61.45
15	44.35	55.41
20		44.3
25		39.23